Fragmentation of Block Copolymer Micelles in Ionic Liquids

A DISSERTATION

SUBMITTED TO THE FACULTY OF THE GRADUATE SCHOOL

OF THE UNIVERSITY OF MINNESOTA

BY

Julia Taylor Early

IN PARTIAL FULFILLMENT OF THE REQUIREMENTS

FOR THE DEGREE OF

DOCTOR OF PHILOSOPHY

Advised by:

Timothy P. Lodge

August 2021

Acknowledgements

First, I would like to thank my advisor, Prof. Tim Lodge, for his constant source of encouragement, guidance, support, and mentorship throughout my time in the group. I'm grateful for Tim giving me enough freedom with just the right amount of guidance to allow me to become an independent scientist. I feel a deep sense of pride in the work I've done in the Lodge group, where a project that was previously shelved turned into a wildly exciting area of research. Tim gave me the freedom to fail and allowed me to try just about any experiment. Tim fully supported me when I went to Brookhaven National Lab for four months in the middle of grad school to work on a somewhat promising TEM experiment, which ended up turning into the most interesting science I have ever done.

Additionally, I am forever grateful to Dr. Kevin Yager for agreeing to mentor me at BNL, for being a wonderful collaborator and co-author, and for getting me five uninterrupted days of synchrotron time. I had a wonderful experience mentoring an undergraduate student, Alison Block, through the MRSEC Summer REU program, and I appreciate all of her efforts in the work presented in Chapter 5.

I had the pleasure of serving as the laboratory safety officer with two excellent predecessors, Yaming Jiang and Aakriti Kharel, and I'm grateful to them for all of their safety wisdom. I'm pleased to have such excellent successors, Claire Seitzinger and Camila Perales, to fill this role as LSO.

The Lodge lodge has been a source of many wonderful friendships that I will carry with me for the rest of my life. Many thanks to the Lodge group members who mentored me,

trained me, and ultimately inspired me to do better science. Thanks to Aakriti Kharel for teaching me what a good mentor is, anything and everything to know about ionic liquids, and anionic polymerization. Thanks to Peter Schmidt for his help in the early developments of the liquid-phase TEM experiments. I'd also like to thank the past and present Lodge group members Sujay Chopade, Wenjia Zhang, Dan Zhao, Cecilia Hall, Ziang Li, Sveta Morozova, Piril Ertem, Yaming Jiang, Shuyi Xie, En Wang, Aaron Lindsay, Nick van Zee, Sanghee Yang, Liwen Chen, Supriya Gupta, Lucy Liberman, Michael Sims, Caini Zheng, Pranati Monkar, Donny Shen, Joe Hassler, Bo Zhang, Camila Perales, Sarah Seeger. Thanks to some of my dearest friends and group members, McKenzie Coughlin and Claire Seitzinger. I wouldn't have survived grad school without you two. Thank you to my partner, Colin Peterson, for being a constant source of love, support, encouragement, and many discussions of polymer physics. I do not think I would have made it this far if it weren't for him. Finally, thank you to my parents, for always telling me to go for it and never doubting me.

Dedication

For my parents, and Colin

Abstract

Block copolymers self-assemble into various micellar nanostructures in selective solvents and can be applied in a host of diverse technologies including drug delivery, viscosity modification, and nanoreactor design. To fully realize these practical uses, the mechanisms for micellization and equilibration must be elucidated. Micelle fragmentation, fusion, and chain exchange are all possible relaxation mechanisms. To date, fragmentation has not been studied in any detail. Block copolymer micelle fragmentation was studied using temperature-jump dynamic light scattering (*T*-jump DLS), synchrotron small-angle X-ray scattering (SAXS), and liquid-phase transmission electron microscopy (LP-TEM) to develop a quantitative understanding of micelle fragmentation kinetics in ionic liquids (ILs). The use of non-volatile IL solvents enables high temperature annealing and direct use of TEM.

Fragmentation of one molar mass of 1,2-polybutadiene-*b*-poly(ethylene oxide) (PB-PEO) was studied in five ILs to determine the effect of solvent selectivity. Then, fragmentation of PB-PEO was visualized directly for three molar masses in one IL using LP-TEM. The molar mass dependence of micelle fragmentation kinetics for six molar masses of PB-PEO in one IL were quantified by time-resolved SAXS and *T*-jump DLS. The effects of PB-PEO molar mass dispersity on micelle fragmentation was explored using hybrid micelles comprised of molar mass blends of PB-PEO. Finally, the swelling behavior of PB-PEO in an IL was explored using high temperature LP-TEM to determine how the solution preparation procedure used to make large, kinetically trapped micelles depends on the morphology of the bulk diblock copolymer. By combining these experimental

techniques, a detailed analysis of micelle fragmentation kinetics, along with the direct observation of intermediate structures during fragmentation events, was achieved.

Table of Contents

List of Figures

List of Tables

Chapter 1 – Introduction and background

1.1 – Introduction

Block copolymers (BCPs) consist of chemically distinct homopolymers that are covalently bonded together. Polymer blends typically undergo macrophase separation, under conditions estimated by the enthalpic and entropic contributions described by the Gibbs free energy of mixing. In contrast, BCPs undergo self-assembly or microphase separation in the bulk, as macrophase separation is suppressed due to the covalent linkage between the blocks. In solution, BCPs are known to self-assemble into a variety of micellar structures when placed in a block-selective solvent.[1,2] In the case of a diblock copolymer, which consists of two distinct A and B chains covalently linked together, a block selective solvent (S) for the A-block ($\chi_{SA} < \chi_{SB}$) will preferentially dissolve the A-block, which forms the micelle corona. The B-blocks will collapse into B-rich domains to minimize unfavorable contact with the solvent, and thereby form the micelle core. From the Flory-Huggins theory for the free energy of mixing, the polymer-solvent interaction parameter χ is defined as the exchange energy required to substitute one lattice site occupied by a polymer segment with a solvent molecule, normalized by the thermal energy, k_BT. With the addition of solvent, the interfacial tension between the B-block and the solvent, γ, drives

self-assembly from enthalpic contributions where B-blocks will minimize contacts with the solvent.

The self-assembly of BCPs in solution has been explored for numerous applications including drug or gene delivery,[3–6] nanoreactors for small molecule transformations,[7] nanolithography,[8] and viscosity modification.[9] Due to the versatility of block copolymer micelles from an applications perspective, there exists a large body of literature on the equilibrium structure of BCP micelles.[10–16] Most investigations of BCP micelles focus on the equilibrium structure as a function of polymer composition, architecture, molar mass, solvent selectivity, and temperature.

However, BCP micelles are not static structures. Micelles exist as dynamic assemblies in solution, and this dynamic behavior often complicates the location of the "true" equilibrium state. While much is understood about the equilibrium properties of BCP micelles, their dynamics and equilibration kinetics in solution are of interest, yet remain less well understood.[17–19] Historically, the equilibration of block copolymer micelles is thought to occur by two primary mechanisms, which were first described by Aniansson and Wall for low molar mass surfactants.[20] Specifically, Aniansson and Wall predict that micelle evolution and relaxation occurs via a combination of individual chain exchange and micelle fusion/fragmentation.[20] Chain exchange in block copolymer micelles has been explored in detail, and the exchange kinetics have been quantified by time-resolved small-angle neutron scattering (TR-SANS).[17–19,21–30] The influence of χ_{SB} and micelle core size on the chain exchange kinetics were recently reported, as described in Section 1.3.[17,19]

As predicted by Aniansson and Wall, single chain exchange is not the only process by which micelles attain equilibrium. If the micelle radius is large relative to the equilibrium size, fragmentation becomes more favorable. Similarly, if the micelles are too small, fusion becomes favorable; neither process has been studied in detail experimentally. Due to the fundamental lack of understanding of non-equilibrium micelle relaxation, this thesis is dedicated towards the systematic investigation of BCP micelle fragmentation. Due to the thermal stability and nonvolatility of ionic liquids (ILs), they are chosen as block-selective solvents.

1.2 – Micelle formation and thermodynamics

In recent years, studies on the self-assembly of diblock copolymers in IL solvents have revealed a variety of interesting behavior, lending polymer/IL systems to a broad variety of stimuli responsive applications. The following section outlines the thermodynamic origins of micellization, the theoretical models used to predict equilibrium parameters of a BCP micelle, experimental evidence for micelle polymorphism, and micellization in ILs.

1.2.1 – Thermodynamics of micellization

BCP micelles are self-assembled aggregates of amphiphilic macromolecules in a block selective solvent, where the soluble block forms the micelle corona, and the insoluble block forms a dense micelle core. BCP micelles are analogous to low molar mass surfactant

micelles, but the large molar mass of macromolecules leads to significant differences from classical surfactant micelles, in both the thermodynamics and relaxation kinetics.

In the simplest case of a sphere-forming AB diblock copolymer diluted with a block selective solvent, the formation of micelles is reflected in two thermodynamic quantities, the critical micelle concentration (CMC) and the critical micelle temperature (CMT). A schematic illustration of the phase behavior of a sphere-forming diblock copolymer with a UCMT as a function of temperature and concentration is depicted in Figure 1.1. Significant micellization occurs for concentrations at or above the CMC; at more dilute concentrations (*i.e.*, below the CMC), the chains are essentially all dissolved as unimers, as shown in Figure 1.1. In micelle-forming BCPs, the solution phase behavior can lead to two micellization scenarios as a function of temperature depending on the thermoresponsive nature of the core-forming block: 1) an upper critical solution temperature (UCST) system forms micelles upon cooling below the CMT (*i.e.*, the UCMT), or 2) a lower critical solution temperature (LCST) system where micelle formation occurs upon heating above the CMT (*i.e.*, the LCMT). For a UCST system above the CMC, polymer chains are well dissolved as unimers at high temperatures and self-assemble into micelles at low temperatures. For an LCST system, the opposite is true, and micelles will form at elevated temperatures and the polymer chains will exist as unimers at low temperatures.

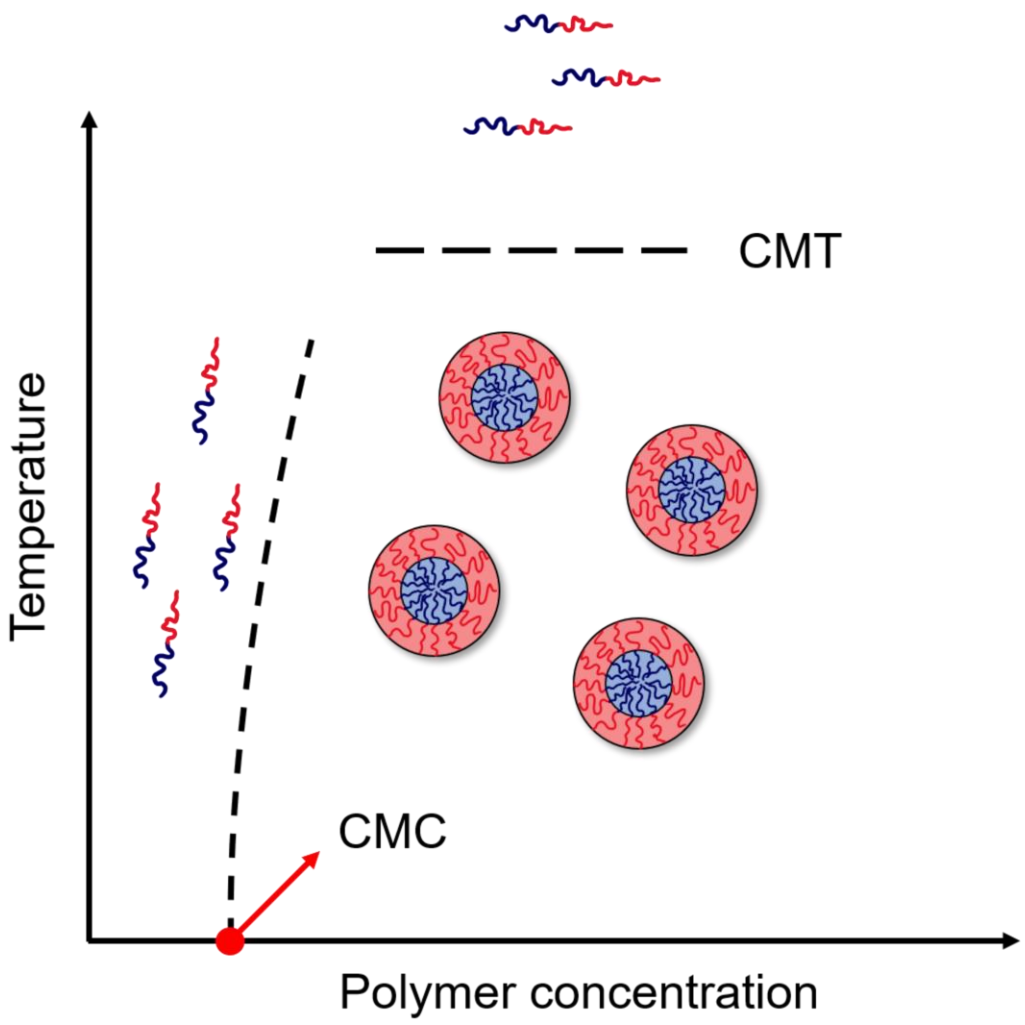

Figure 1.1: Schematic illustration of the critical micelle concentration (CMC) and critical micelle temperature (CMT) in a USCT core-block/solvent system.

Above the CMC, there are two relevant micelle concentration regimes to note. The first is the dilute regime, where the micelle concentration is below the overlap concentration, and micelles are discrete, non-interacting spheres. Further increase of polymer, and therefore micelle, concentration results in a crossover to the second regime where micelle

aggregation and eventually, packing onto a periodic lattice (body-centered cubic, face-centered cubic, etc.), begins to occur.[31]

1.2.2 – Theoretical depiction of micelles

Early theoretical treatments on the thermodynamics of sphere-forming block copolymer micelles in solution were pioneered by de Gennes,[32] Leibler et al.,[33] Noolandi and Hong,[34] and others.[35–37] Many theoretical depictions for predicting the structure of diblock copolymer micelles in solution were developed using scaling relations[31–33,35–37] and self-consistent mean-field theory (SCFT) calculations.[38–41] In general, the equilibrium structure of a micelle is determined by the free energy of the micelle in solution. This free energy is dependent on parameters related to micelle size such as the aggregation number or the total number of chains per micelle (Q), total micelle radius or hydrodynamic radius (R_h), core radius (R_{core}), and corona thickness (L_{corona}). These parameters are obtainable from experimental techniques such as dynamic light scattering (DLS), static light scattering (SLS), small-angle X-ray scattering (SAXS), and transmission electron microscopy (TEM).

It is well known that the free energy per chain of a micelle in solution, F_{mic}, is described by the sum of the free energy contributions from the core chains (F_{core}), corona chains (F_{corona}), and the micelle interface (F_{int}), as shown in Equation 1.1,

$$F_{mic} = F_{core} + F_{corona} + F_{int} \tag{1.1}$$

where F_{core} is governed by the core chain stretching, F_{corona} is related to the excluded volume interactions between solvated corona chains, and F_{int} arises from the interfacial tension between the core-forming block and the solvent. Equilibrium scaling relations of micelle properties as a function of block copolymer characteristics, such as molar mass, are estimated by minimizing F_{mic} with respect to Q or R_{core}.

de Gennes proposed a simplified scaling relation for spherical BCP micelles in the limit where $N_{core} >> N_{corona}$, where N is the total degree of polymerization of the core- and corona-forming blocks, respectively.[32] This limit is the so-called "crew-cut" micelle regime. Using the analogy of tethered polymer brushes on a flat surface, de Gennes proposed the radial density profile of the micelle corona is described by a step function. In the "star-like" micelle regime, where $N_{core} << N_{corona}$, the interfacial curvature becomes more pronounced, and the radial density profile of the micelle corona is then a function of the distance from the micelle core. The model was improved by Daoud and Cotton who focused on star-like micelles in dilute and semi-dilute conditions. To expand upon the model for corona chain conformations in a micelle, they proposed a radial variation of monomer concentration in the micelle corona, introducing the blob concept.[42] Because the corona chains are covalently tethered to the core chains in a BCP micelle, the local concentration of monomers in the corona will increase as the distance from the micelle

core is decreased. Conversely, monomer units further away from the core-corona interface will have a decreased local concentration as the distance from the core is increased. This eventually leads to a single linear chain problem toward the outside of the corona region, where different corona chains can be considered relatively well separated. The size (ξ) scale where this occurs is defined as a blob, which depends only on the monomer concentration.

Table 1.1: Scaling relations of Q, R_{core}, L_{corona}, and R_h for crew-cut and star-like micelles.

	Crew-cut ($N_{core} >> N_{corona}$)	Star-like ($N_{core} << N_{corona}$)
Q	$\sim \gamma N_{core}$	$\sim \gamma^{6/5} N_{core}^{4/5}$
R_{core}	$\sim N_{core}^{2/3}$	$\sim N_{core}^{3/5}$
L_{corona}	$\sim N_{corona}$	$\sim Q^{1/5} N_{corona}^{3/5}$
R_h	$\sim N_{core}^{2/3}$	$\sim N_{core}^{3/5} N_{corona}^{4/25}$

The blob concept is illustrated in Figure 1.2 for a spherical micelle. The introduction of the blob allowed for predictions of corona chain conformation in a good solvent (the swollen region), as well as for the theta condition, which gave additional insights into the scaling predictions of BCP micelles at equilibrium. Halperin utilized this blob picture in further developments of the scaling relations for star-like micelles to give an equilibrium scaling relation for the micelle core radius as a function of N_{core} and the total micelle radius as a function of N_{core} and N_{corona}.[37] In this work, Halperin derived an explicit form for the

radial density profile in the corona, $\varphi(r)$, for dilute solutions where F_{mic} is more accurately described as the free energy *per chain* in a single micelle.

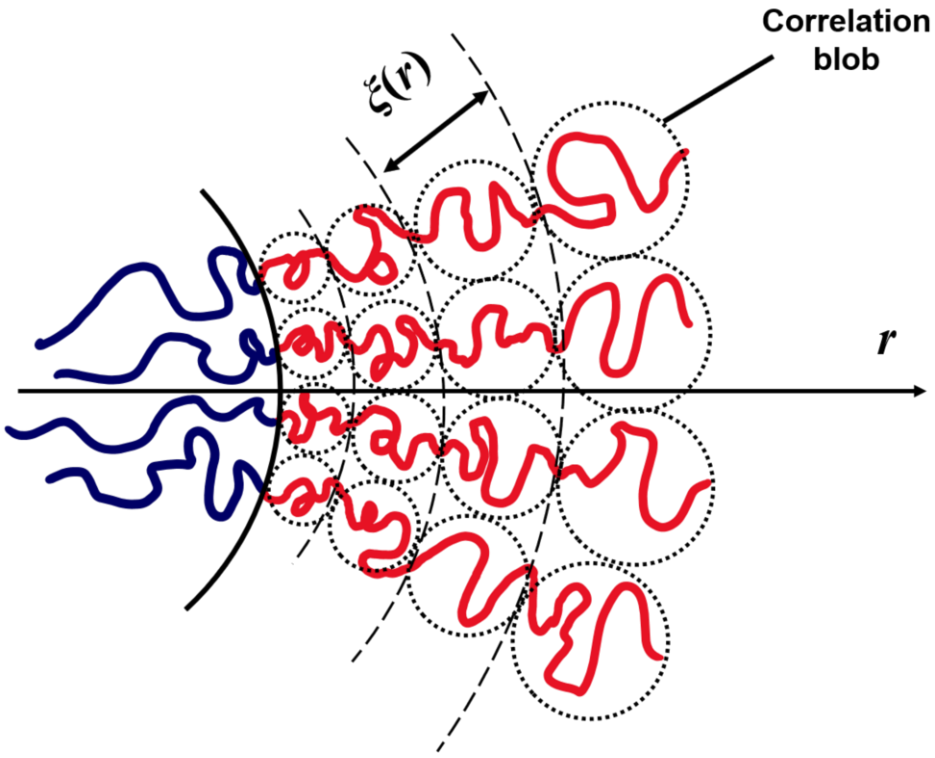

Figure 1.2: Schematic illustration of the correlation blob concept for a spherical diblock copolymer micelle, where the blue chains represent the core and the red chains are the corona, presented by Daoud and Cotton to represent the concentration dependence of the radial density profile of monomer units in a micelle corona.

Zhulina and Birshtein used the scaling approach to derive analytical expressions for three different BCP micelle morphologies, namely, spheres, cylinders, and lamellae.[31] They extended the concepts of tethered layers on curved surfaces to derive the free energy per chain in a micelle of each morphology, and gave some equilibrium scaling relationships

for micelle size as a function of concentration, surface tension (γ), and molar mass. Zhulina *et al*. expanded these models to quantify the free energy of spherical, cylindrical, and bilayer structures in solution as a function of N.[36] They estimate regions of thermodynamic stability (*i.e*., morphological transitions), along with expressions to estimate the equilibrium size and aggregation numbers for micelles of each morphology. Most notably they predict the equilibrium scaling with N for micelles of various morphologies in both the crew-cut ($N_{core} >> N_{corona}$) and star-like ($N_{core} << N_{corona}$) micelle regimes.

Table 1.2: Scaling of ξ, $\varphi(r)$, and F_{corona}/kT for various micelle geometries in a good solvent, where a is the monomer size and d is the domain size.[1]

	Spherical	Cylinders	Bilayers
ξ	$\sim r/Q^{1/2}$	$\sim (rL_{corona}/Q)^{1/2}$	$\sim d$
$\varphi(r)$	$\sim Q^{2/3}(a/r)^{4/3}$	$\sim (Qa^2/rL_{corona})^{2/3}$	$\sim (a/d)^{4/3}$
F_{corona}/kT	$\sim Q^{1/2}$	$\sim N_{corona}^{3/8}(Qa/L_{corona})^{5/8}$	$\sim N_{corona}(a/d)^{5/3}$

In summary, there are several scaling methods used to predict the equilibrium properties of BCP micelles in solution, which are summarized in Tables 1.1 and 1.2. In addition to scaling relations, SCFT computations have been widely employed to give more accurate values of micelle size in combination with scaling relations.[38–41]

1.2.3 – Polymorphism of BCP micelles

In addition to theoretical predictions of polymorphism in micelle-forming BCPs, there is extensive experimental evidence showing that diblock copolymers can form a variety of self-assembled structures in solution. Several reports on the morphology of A-B diblocks, A-B-A and A-B-C triblocks, and numerous other block copolymers exist to date.[43–51] An interesting characteristic of micelle-forming block copolymers is their ability to adopt various structures when the solvent selectivity, concentration, or block lengths are altered.

Transitions from spherical to cylindrical (worm-like) micelles, or from cylindrical micelles to bilayer vesicles have been reported for various polymer/solvent systems including 1,2-polybutadiene-*block*-poly(ethylene oxide) (PB-PEO)[46,47] and polystyrene-*block*-poly(acrylic acid) (PS-PAA)[44,49,52,53] in various polar solvents. One way to anticipate the resulting morphology of a micelle is through the critical packing parameter, p. The critical packing parameter is defined by Equation 1.2, where a_0 is the effective surface area of the solvophilic heads in the micelle, v is the volume of the solvophobic tails, and l_c is the contour length of the hydrophobic tails.

$$p = \frac{v}{l_c a_0} \tag{1.2}$$

This parameter is commonly used for the analogous low molar mass surfactants, and the specific value of p can be used to predict the morphology in micelle-forming systems. Spherical micelles form for values of $p \leq 1/2$, and the transition from spherical to

cylindrical micelles occurs for values of $1/3 < p \leq 1/2$. Polymer aggregation into bilayer membrane structures (such as "polymersomes") occurs for $p > ½$, *i.e*., for vesicle forming systems with low curvature.

Previous work has shown that changing the solvent selectivity and/or altering the core volume fraction, *f*, can lead to various transitions in micelle morphologies. The effect of core volume fraction on the packing parameter can be rationalized quite readily; increasing *f* will increase the volume of the hydrophobic tails along with the contour length from Equation 1.2, while a_0 remains constant. This results in an increase in *p*, and a transition from spherical to worm-like micelles is observed, as reported by Bates *et al.* who demonstrated that in aqueous solutions of PB-PEO, increasing the length of the PB block caused transitions from spherical micelles to worm-like micelles to bilayer vesicles.[54] This polymorphism was also observed by cryogenic TEM (cryo-TEM) for various values of *f* for PB-PEO in the IL 1-butyl-3-methylimidazolium hexafluorophosphate, [C_4mim][PF_6], as shown in the TEM micrographs in Figure 1.3a.[51]

The second approach used in manipulating micelle morphologies is to alter the solvent selectivity for the core forming block. As shown through numerous works by Eisenberg *et al.*,[44,49,52,53] a wide variety of micelle morphologies become accessible as the solvent selectivity is altered. The solvent selectivity dependence is largely due to the role of the interfacial tension, γ. When the solvent selectivity for the corona block is increased, the interfacial tension between the solvent and the core block is increased, and a decrease in the total interfacial area per chain is observed. This reduction in interfacial area gives rise

to a reduction in the curvature of the aggregates. This was observed experimentally via cryo-TEM for polystyrene-*block*-polyisoprene (PS-PI) in mixtures of dialkyl phthalate solvents, as shown in Figure 1.3b.[50] In the PS-PI system various compositions of dibuthyl phthalate (DBP), diethyl phthalate (DEP), and dimethyl phthalate (DMP) were used to selectively tune γ, which induced morphological transitions from spheres to coexisting spheres/worms to vesicles for a single PS-PI diblock.

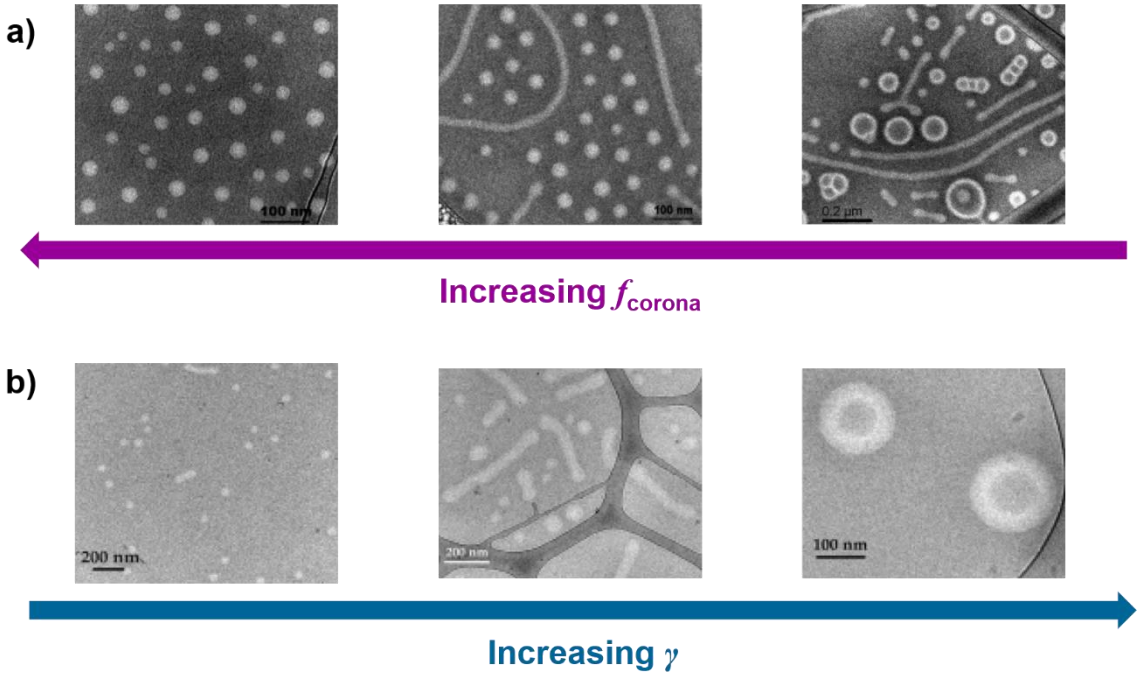

Figure 1.3: (a) TEM micrographs of PB-PEO micelles in [C_4mim][PF_6], where transitions from spheres to coexisting spheres/worms to coexistence of worms/vesicles is observed with decreasing f_{corona}. (b) TEM micrographs of polystyrene-*block*-polyisoprene (PS-PI) in mixtures of dialkyl phthalate solvents where increasing γ results in morphological transitions from spheres to coexisting spheres/worms to vesicles is observed. Reproduced from References 51 and 50, respectively.

By increasing solvent selectivity for the corona block, transitions from spherical micelles to bilayer vesicles can be achieved. Previous work by Lund *et al.* proposed a power law dependence of the aggregation number, *Q*, and the interfacial tension for poly(ethylene-*alt*-propylene)-*block*-poly(ethylene oxide) (PEP- PEO) in water/DMF. The dependence of aggregation number on interfacial tension was found to follow $Q \sim \gamma^{6/5}$, which agrees with the scaling relation from Table 1.1.[55]

1.2.4 – Diblock copolymer micelles in ionic liquids

The structure of BCP micelles in aqueous, organic, and IL solvents has been widely explored. Ionic liquids are salts with melting points at or below room temperature, and the thermodynamic principles of micellization in these solutions are the same as those discussed for organic and aqueous solvents. ILs, often referred to as "molten salts", have emerged as an intriguing class of solvents due to their desirable properties, namely, thermal stability, non-volatility, and conductivity. In these solvents, the IL cations and anions typically consist of bulky, charged small molecules. The bulkiness and flexibility of the ions prevents crystallization at room temperature; thus, the melting point of an IL is below room temperature. The structures of 1-alkyl-3-methylimidazolium bis(trifluoromethyl sulfonyl imide)-based ILs ([$C_x$mim][TFSI] where x = methyl, ethyl, butyl, hexyl, or octyl) used in this thesis are shown in Figure 1.4.

[C_1mim], x = 1
[C_2mim], x = 2
[C_4mim], x = 4
[C_6mim], x = 6
[C_8mim], x = 8

[TFSI]

Figure 1.4: Chemical structures of 1-alkyl-3-methylimidazolium bis(trifluoromethyl sulfonyl imide)-based ILs used in this thesis.

ILs are particularly interesting as a block selective solvent for polymer systems from an applications perspective, and they have found utility in polymer ion gels,[56–60] catalyst supports,[61,62] and dispersion media.[63–66] The solution phase behavior of polymers in ILs has been widely explored by Watanabe *et al.*,[67–70] where they have found a rich variety of polymer/IL solution phase behavior and the typical UCST behavior is observed for several polymer/IL combinations, but a number of LCST polymer/IL combinations have been identified as well.[58,69,70] Based on the selection of thermoresponsive blocks, BCPs in ILs have been reported to exhibit double thermoresponsivity.[58,71] From the perspective of micellization, ILs can be used to explore a wide range of temperature dependences for a diblock copolymer/IL system, where the IL is a good solvent for one block, and a poor solvent for the other block. The micellization temperature can be tuned by small changes to the IL structure, either the cation or anion, and micelles can be formed at high temperatures in a variety of LCST polymer/IL systems if desired.

Several reports on the equilibrium properties of diblock copolymer micelles in ILs have emerged in the last decade.[51,72–85] Simone and Lodge used cryo-TEM and DLS to explore the micellization of polystyrene-*block*-poly(methyl methacrylate) (PS-PMMA) in the IL [C_4mim][PF_6].[84] The authors report the morphological transition from spheres to cylinders with decreasing volume fraction of PMMA. Additionally, they note an inversion of TEM contrast due to the heavier atoms present in the ILs, where the micelle cores appear light and the IL medium is dark, as shown in Figure 1.3a.

Mok *et al*. explored the effects of diblock copolymer molar mass and composition on the CMC using IL solvents.[72] They studied two diblock copolymers, polystyrene-*block*-poly(ethylene oxide) (PS-PEO) and PS-PMMA, in [C_2mim][TFSI]. In these systems, [C_2mim][TFSI] is a poor solvent for PS and the micelle core is formed by the PS block, whereas [C_2mim][TFSI] is a good solvent for PMMA and PEO. For the PS-PEO molar mass series, N_{core} was fixed while N_{corona} was varied from 113 to 295. They found that the CMC decreased by a modest factor of approximately 1.5 with decreasing N_{corona}, which is well-described by SCFT calculations. However, the CMC decreased by 5 orders of magnitude in the PS-PMMA series as N_{core} was increased from 30 up to 110. This dependence of the CMC on N_{core} was much weaker than predicted by SCFT, and the authors discuss that kinetic limitations in these highly segregated systems could play a role.

The LCST phase behavior of poly(*n*-butyl methacrylate) (PnBMA) in mixtures of [C_2mim][TFSI] and [C_4mim][TFSI] was investigated previously by Hoarfrost, He, and Lodge.[77] They used a combination of transmittance, light scattering, and SANS to

demonstrate the tunability of the cloud point, spinodal, and theta temperatures with increasing content of [C4mim][TFSI].[77] It was found that the χ parameter varies linearly with increasing [C4mim][TFSI] content, and it was concluded that the increased enthalpic driving force for mixing dominates over the decreased entropic penalty of mixing leading to enhanced solubility of PnBMA in IL mixtures of [C2mim][TFSI]/[C4mim][TFSI] with increasing amounts of [C4mim]. Hoarfrost and Lodge explored the LCST phase behavior of a diblock copolymer, poly(ethylene oxide)-*block*- poly(*n*-butyl methacrylate) (PEO-PnBMA) in the same mixture of ILs, where PEO is well dissolved in the IL solvent mixtures.[83] In the diblock/IL system, it was found that PEO-PnBMA forms micelles above the CMT in [C2mim][TFSI]/[C4mim][TFSI] mixtures, and that the CMT depends on N_{core} as predicted by theory.

Ma and Lodge investigated the micellization of poly(methyl methacrylate)-*block*-poly(*n*-butyl methacrylate) (PMMA-PnBMA) diblocks in [C2mim][TFSI] with a particular focus on the scaling of the core and corona size with core block length.[79] In this system, the core-forming block is PnBMA, which exhibits an LCST in [C2mim][TFSI] as shown by Hoarfrost, He, and Lodge.[77] Using a combination of DLS and SAXS, they found that $R_{core} \sim N_{core}^{0.71\pm0.01}$ and $L_{corona} \sim N_{core}^{-0.04\pm0.05}$, which is only in partial agreement with the scaling model for star polymers proposed by Halperin *et al.*,[1,37] but in excellent agreement with predictions made by Nagarajan and Ganesh up to the hairy micelle limit where $L_{corona} >> R_{core}$.[35,86] The authors attribute this deviation from theory to the comparable dimensions of core and corona observed in their system. Additionally, they found that the core blocks

are significantly stretched in the micelle, which could cause deviations from equilibrium scaling theories.

PB-PEO is also known to form micelles in ionic liquids.[51,82,87–92] Micellization of PB-PEO in [C_4mim][PF_6] was studied by cryo-TEM and DLS, which showed morphological transitions from spheres to cylinders to vesicles with decreasing f_{PEO}.[82] It was found that the morphology of PB-PEO micelles were independent of temperature between 25 °C and 100 °C, which is consistent with the nonergodicity of PB-PEO micelles in water. PB-PEO also forms micelles in [C_2mim][TFSI] and exhibits the same morphological transitions from spheres to cylinders to vesicles with decreasing f_{PEO} reported for PB-PEO in [C_4mim][PF_6], as shown previously in Figure 1.3a. Phase diagrams of PB-PEO in [C_2mim][TFSI] and [C_4mim][PF_6] at 25 °C are shown in Figures 1.5a and 1.5b, respectively.[82]

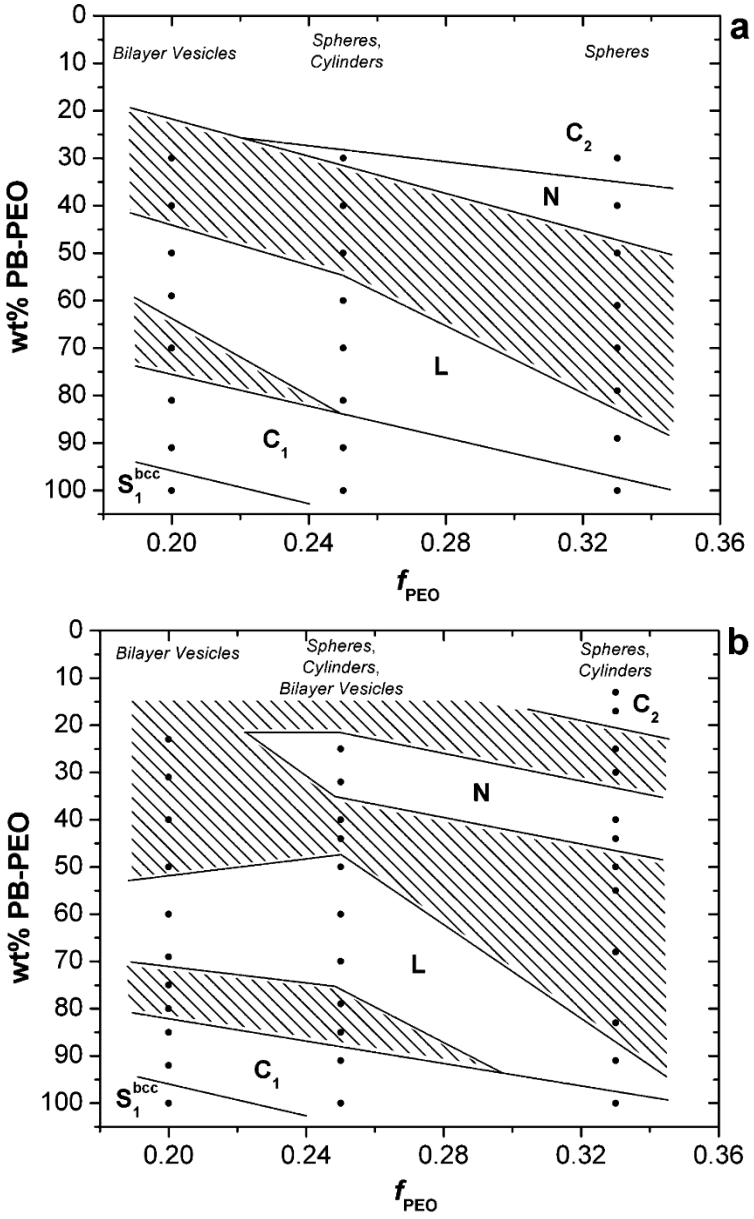

Figure 1.5: Phase diagram for PB-PEO in a) [C_2mim][TFSI] and b) [C_4mim][PF_6] at 25 °C. The *x*-axis is the volume fraction of PEO in the bulk diblock copolymers, and the *y*-axis represents the concentration by weight of PB-PEO in IL solutions. $\mathbf{S_1^{bcc}}$ is a cubic lattice of spheres with a PB core, $\mathbf{C_1}$ is hexagonally packed cylinders with PB a core, **L** is lamellae, **N** is a disordered network of cylinders, and $\mathbf{C_2}$ is hexagonally packed cylinders

with a PEO core. The dashed regions represent coexistence of microstructures. Reproduced from Reference 82.

BCPs in protic ILs have been explored extensively by Warr,[75] as well as López-Barrón, Wagner, *et al*.[73,74,81,85] Various examples in the literature demonstrate the micellization of diblocks[75] and triblocks[74,81,85] in protic ILs ethylammonium nitrate (EAN) and propylammonium nitrate (PAN). For the diblock copolymers, poly(ethylene oxide)-*block*-poly(ethyl glycidyl ether) (PEO-PEGE) and poly(ethylene oxide)-*block*-poly(glycidyl propyl ether) (PEO-PGPrE) in EAN and PAN exhibit the morphological transitions outlined previously with decreasing corona block length.[75] Additionally, triblock copolymers of poly(ethylene oxide)-*block*-poly(propylene oxide)-*block*- poly(ethylene oxide) (PEO-PPO-PEO) were found to exhibit thermoreversible gelation behavior in EAN.[85]

The experimental studies of diblock copolymers in organic solvents, aqueous media, and ILs are numerous. However, the current understanding of BCP micelles is most developed at equilibrium. In comparison to this large, comprehensive body of literature, papers on the dynamic behavior of micelles in solution are far more limited. Because of this, it is of critical importance to study the kinetics and equilibration mechanisms of BCP micelles in solution.

1.3 – Micelle dynamics

This section provides a brief history of micelle dynamics and equilibration kinetics. First, the traditional mechanisms of micelle equilibration, namely, chain exchange, fragmentation, fusion, formation, and annihilation, are discussed. Then, two theories of micelle equilibration kinetics, one proposed by Halperin and Alexander for micelles near equilibrium, and one by Dormidontova, who considered micelles that are far from equilibrium, are discussed. Finally, a review of experimental work in micelle dynamics and equilibration kinetics is presented.

1.3.1 – Mechanisms of equilibration

Although there are many predictions and experimental studies on the equilibrium properties of BCP micelles, there is an open question of great current interest. Exactly how do micelles attain equilibrium and how fast are these processes? To address this question, the mechanisms of micelle equilibration must be understood. In general, BCP micelle formation and equilibration occurs by similar pathways identified in small molecule surfactant micelles. The seminal papers from Aniansson and Wall describe mechanisms for BCP micellization and equilibration based on low molar mass surfactant micelles.[20,93,94] There are five primary processes thought to govern the formation, destruction, and equilibration of block copolymer micelles in solution, namely, (i) *chain exchange*, where individual copolymer chains are exchanged between micelles, (ii) *fragmentation*, where a micelle with aggregation number Q breaks up into smaller micelles, (iii) *fusion*, where two

micelles merge together, (iv) micelle *formation*, where individual chains nucleate a new micelle, and (v) *annihilation* of micelles, where a series of chain exchange/fragmentation/fusion events eliminates one micelle. These processes are illustrated in Figure 1.6.

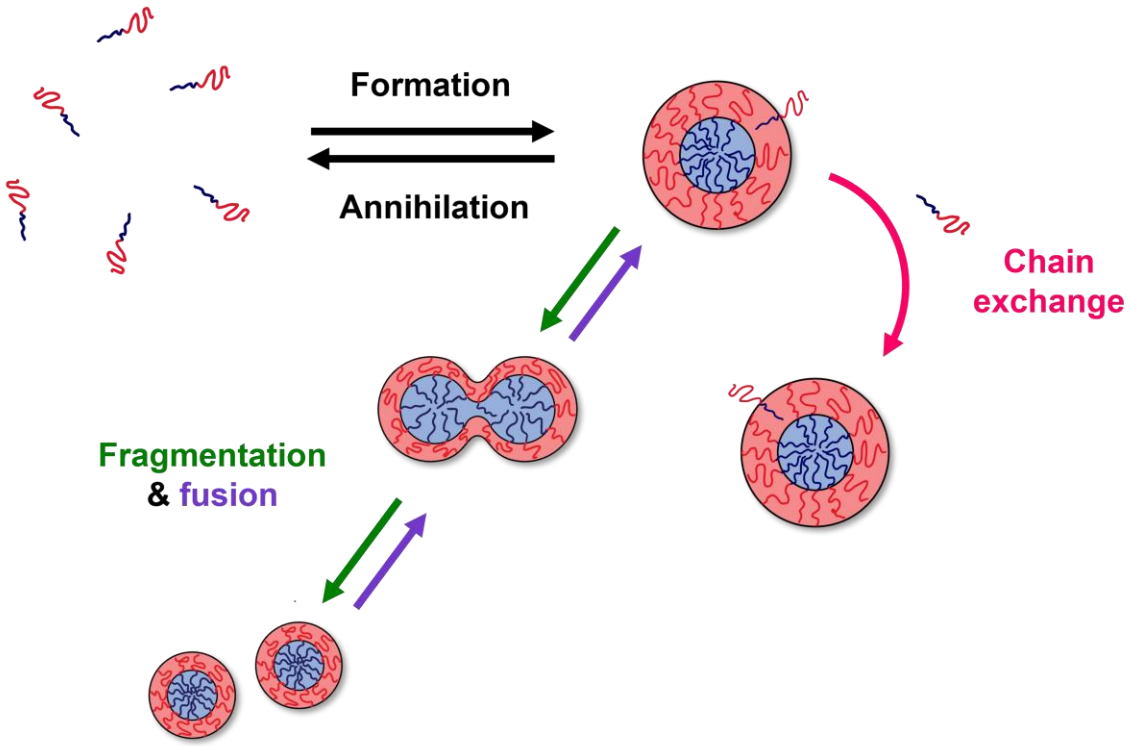

Figure 1.6: Illustration of micelle formation, annihilation, chain exchange, fragmentation, and fusion.

Experimentally, measurements of micelle kinetics in surfactants revealed two time constants, where the faster process is generally attributed to individual chain exchange.[95] However, the measurements of the time constants were for low molar mass surfactants,

and the kinetic analysis by Aniansson and Wall was restricted to nonionic detergents.[93,94] Kahlweit improved upon the Aniansson and Wall picture by extending micellization analyses to include ionic micelles, and suggested that micelles grow only via chain exchange at low counterion concentrations due to electrostatic repulsion of neighboring aggregates.[96] It was concluded that because nonionic systems lack this electrostatic repulsion both chain exchange and fusion/fragmentation pathways are in competition from the onset of the CMC and after.[96]

In general, the mechanisms of equilibration should be similar for BCP micelles and surfactant micelles, but the largest difference lies in the kinetics of these processes. In general, the large molar mass of diblock copolymers leads to equilibration kinetics that are orders of magnitude slower than for the surfactant case. This has led to significant interest in the kinetics of BCP micelle equilibration. Next, the theoretical framework for chain exchange, fragmentation, and fusion in BCP micelles is discussed.

1.3.2 – Theoretical approaches

The first detailed theory on diblock copolymer micelle equilibration kinetics was reported by Halperin and Alexander, who extended the predictions from Aniansson and Wall, as well as Kahlweit.[95] They consider the Aniansson-Wall framework for micelle equilibration to describe the kinetics of micelle relaxation in solution. In their theory, they consider only star-like spherical micelles that are at, or very close to, equilibrium. Based on this constraint, Halperin and Alexander propose that the dominant mechanism of

equilibration in BCP micelles is chain exchange. The authors suggest that fragmentation and fusion are not plausible mechanisms due to high activation energies from the interfacial tension in the former case and the strong steric repulsion of corona chains in the latter. They report that the exchange time, τ_{ex}, depends on the core and corona block lengths as

$$\tau_{ex} \sim N_{core}^{2/25} N_{corona}^{9/5} \exp(E_a / k_B T) \tag{1.3}$$

where k_B is the Boltzmann constant, T is the absolute temperature, and E_a is the activation barrier given by $\gamma N_{core}^{2/3} b^2$, where γ is the interfacial tension between the core block and the solvent and b is the monomer size of the core block.

Dormidontova proposed a scaling model to account for micellization in systems far from equilibrium, and assumed that micelle fragmentation proceeds by the reverse mechanism as micelle fusion.[97] The relaxation time for fusion, τ_{fus}, of two micelles with similar aggregation numbers ($Q_1 \leq Q_2$) scales with aggregation number and the degree of polymerization of the corona block as shown in Equation 1.4.

$$\tau_{fus} \sim N_{corona}^{17/5} Q_1^{14/5} Q_2 \tag{1.4}$$

The strong N_{corona} dependence on the characteristic time for fusion is attributed to the corona chain deformation during the merging process, where the corona chains of a smaller micelle penetrate into the corona region of a larger micelle. Based on this observation for micelle fusion, the fragmentation times for micelles with small aggregation numbers were

estimated to scale with $N_{corona}^{17/5}$ as well. For micelles with very large aggregation numbers $Q > (cV_{corona})^{5/2}N_{corona}^{2}$, where c is the micelle concentration and V_{corona} is the molar volume of a corona-forming chain, the fragmentation (τ_{frag}) and fusion times were proposed to scale with N_{corona} and Q as shown in Equation 1.5.

$$\tau_{frag} \sim N_{corona}^{9/5} Q^{13/5} \tag{1.5}$$

Halperin and Alexanders' model and Dormidontova's model present rate equations using the framework of Kramers rate theory for micellization kinetics. However, the primary conclusions from these works are contrasting in that Halperin and Alexander concluded, for micelles near equilibrium, that chain exchange is the only feasible mechanism in micelle formation and equilibration. Dormidontova considered systems that have been perturbed far from equilibrium, which was more relevant to experimental techniques used to study micellization kinetics at the time. Dormidontova concluded that in early stages of micellization, micelle fusion and fragmentation are the most favorable equilibration mechanisms, but as the system nears equilibrium, a crossover to chain exchange occurs. The free energy landscape for fusion, fragmentation, and chain exchange is summarized in Figure 1.7b.

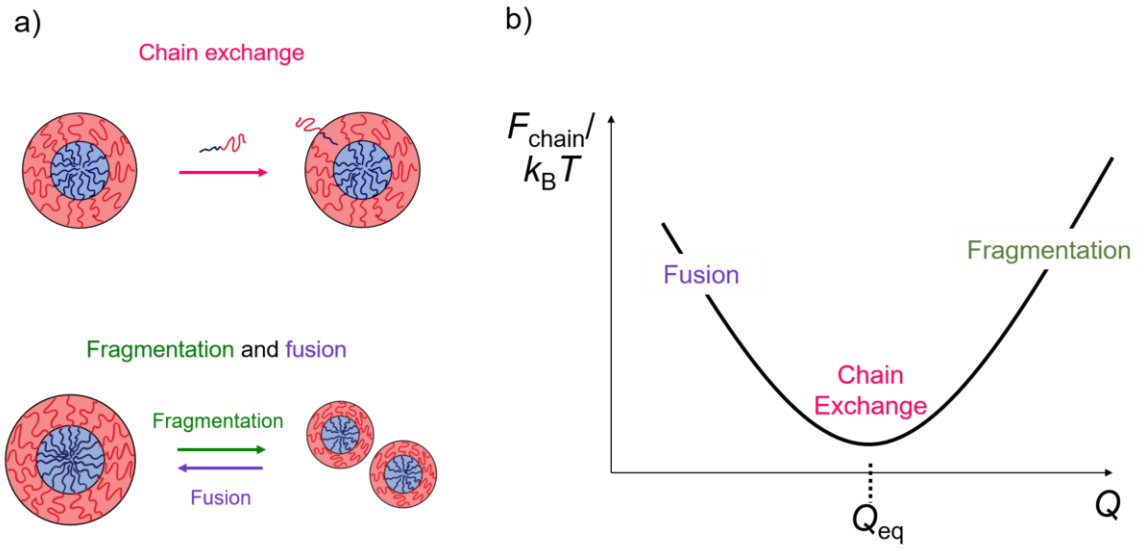

Figure 1.7: Schematic illustrations of a) micelle equilibration processes chain exchange, fragmentation, and fusion, and b) the free energy per chain in a micelle (F_{chain}/k_BT) versus aggregation number Q. The free energy regimes where each mechanism is proposed to contribute are shown according to Dormidontova's model.

1.3.3 – Experimental studies of micelle equilibration kinetics

This section focuses on micelle equilibration (*i.e.*, relaxation) experiments with a particular emphasis on the current understanding of micelle fragmentation and fusion. First, a brief history of early micellization experiments is discussed. Then, experimental results for micelle chain exchange are summarized, followed by a review of the experimental investigations of BCP micelle fragmentation and fusion.

To understand BCP micelle dynamics experiments, one must understand the terminology used to describe the experimental design in this field. Often, the terms

micellization and equilibration are seemingly used interchangeably; however, they are typically measuring very different phenomena. In micellization experiments, the kinetics of micelle formation from a solution of unimers are monitored. The micellization experiment typically probes the mechanisms of micelle formation and annihilation shown in Figure 1.6. In contrast, micelle equilibration/relaxation experiments are used to probe the dynamic behavior of metastable micelles in solution. The kinetic information is obtained during the application of some perturbation to the micelle solution, and the time scale for reaching an equilibrium size/morphology is monitored. In a micelle equilibration experiment, the mechanisms of relevance are chain exchange, fragmentation, and fusion. Typically perturbation experiments involve temperature-jumps (*T*-jumps)[89–92,98–105] or pH-jumps.[106–108] Following a perturbation, the kinetics are monitored using techniques such as light scattering,[89–91,104,109] X-ray scattering,[91,110–113] neutron scattering,[17–19,22,23,28,114–116] or excimer fluorescence spectroscopy.[117–120] Direct measurements of the evolution in micelle size has been achieved *ex-situ* by cryo-TEM,[121,122] and more recent *in-situ* observations were reported using liquid-phase TEM (LP-TEM).[92,123]

Studies of chain exchange kinetics are enabled by the development of TR-SANS experiments.[26] Several reports utilize this technique, and much has been discovered about the dependence of the exchange times on the molecular parameters of the system.[17,19,21,23,25,27,29,124] In a typical TR-SANS experiment, the contrast mechanism from a neutron scattering experiment is leveraged, where selective deuteration of the micelle core block is performed to give perdeuterated micelle cores. These *d*-micelles (deuterated

micelles) are then mixed with an identical solution of *h*-micelles (protonated core blocks), where the ratio of *h*- and *d*- micelles is deliberately chosen to contrast-match with the solvent upon complete redistribution of *h*- and *d*-chains in the micelles. The contrast in a SANS experiment results from the difference in the scattering length densities (SLDs) of the ^{1}H and ^{2}H nuclei. At the beginning of the experiment ($t_{mix} = 0$) there is a high scattering intensity as there is a large concentration of both *h*- and *d*-micelles, meaning chain exchange has yet to occur. As chain exchange occurs in the system, the *h*- and *d*- chains are distributed randomly among the micelles as a function of time, and the scattering intensity decreases monotonically as a function of the exchange time. This technique is powerful in that the dynamics of individual polymer chains can be followed due to this contrast matching approach, thus, the chain exchange time for a given diblock/solvent system can be assessed as a function of molecular parameters such as N_{core}, N_{corona}, χ, and Q.

Willner *et al*. were the first to report chain exchange measurements of PEP-PEO in dimethylformamide by TR-SANS.[24] It was found that the extent of chain exchange, also called the normalized relaxation function, $R(t)$, exhibits a logarithmic dependence with time, which contradicts Halperin and Alexander's theory. This logarithmic dependence was also observed for the chain exchange kinetics of polystyrene-*block*-1,4-polybutadiene (PS-PB) diblocks and PB-PS-PB triblocks in *n*-alkanes,[29] and for polystyrene-*block*-poly(ethylene-*alt*-propylene) (PS-PEP) micelles in squalene.[21] A quantitative model used

to interpret the logarithmic time dependence of chain exchange was presented by Choi *et al*.[21] In this model, $R(t)$ is described by Equation 1.6,

$$R(t) = \int P(N_{\text{core}}) \exp[-t \frac{6\pi^2 kT}{N_{\text{core}}^2 b^2 \zeta} \exp(-\alpha\chi N_{\text{core}})] \mathrm{d}N_{\text{core}} \tag{1.6}$$

where ζ is the monomer friction coefficient, b is the statistical segment length of the core block, and α is a parameter of order unity. The molar mass dispersity of N_{core} is accounted for using the Schulz-Zimm distribution function, $P(N_{\text{core}})$, given by Equation 1.7,

$$P(N_i) = \frac{z^{z+1}}{\Gamma(z+1)} \frac{N_i^{z-1}}{N_{\text{n}}^{z}} \exp\left(-\frac{zN_i}{N_{\text{n}}}\right) \tag{1.7}$$

where $z = (N_{\text{w}}/N_{\text{n}} - 1)^{-1}$, Γ is the gamma function, and N_{w} and N_{n} are the weight- and number-average degrees of polymerization of the core block, respectively. Choi's model accurately describes the logarithmic time dependence of $R(t)$ and demonstrates the hypersensitivity of chain exchange time on the length of the core block.

In Choi's model the activation barrier to chain exchange was assumed to depend on the The χ parameter between the core and the solvent as $E_{\text{a}} \sim \chi N_{\text{core}}$, but this does not accurately describe the situation of chain exchange in a system approaching the CMT. At the CMT, there should be no energy barrier to chain expulsion, however, $\chi \approx 0.5$ at the CMT, making this scaling invalid. The dependence of chain exchange time on $\chi_{\text{core-solvent}}$ was reported by

Ma and Lodge for PMMA-PnBMA micelles in mixtures of [C2mim][TFSI]/[C4mim][TFSI].[19] The authors proposed that $E_a \sim f(\chi)N_{core}$, where $f(\chi)$ is given by,

$$f(\chi) = \frac{v_2}{v_1}\left(\chi - \frac{v_2}{v_1}\right) + \frac{1}{a\chi^2 + b\chi + c} \tag{1.8}$$

where v_1 and v_2 are the molar volumes of the solvent and core block repeat unit, respectively, and a, b, and c are empirical constants. In this model, $f(\chi)$ is derived in the context of the Flory-Huggins theory, where the quantity of χ is converted by taking the volume of one core block repeat unit as the reference volume, and high segregation strength (*i.e.*, high χN_{core}) is assumed. The authors report good agreement between the modified function and the chain exchange kinetics of PMMA-PnBMA micelles in mixtures of [C2mim][TFSI]/[C4mim][TFSI].[19]

Wang *et al*. established the dependence of chain exchange time on N_{corona} for PS-PEP micelles in squalene.[23] For PS-PEP micelles where N_{core} is fixed at 255 and N_{corona} is varied from 256 – 2080, it was found that the rate of chain exchange was increased by 2 orders of magnitude when comparing the shortest corona to the longest. They proposed the following expression to describe the dependence of E_a on corona chain stretching, s_{corona},

$$E_a / k_B T = \alpha\chi N_{core} - \frac{3}{2}\left(\frac{R_g^2}{R_{g,0}^2}\right)_{corona} = \alpha\chi N_{core} - \frac{3}{2}s_{corona}^2 \quad (1.9)$$

where $R_g = L_{corona}/2$ is the radius of gyration of corona chains in the micelles and $R_{g,0}$ is the unperturbed value.

The significance of fusion/fragmentation processes in BCP micelles has been debated for some time.[95,97] Traditionally, fragmentation and fusion experiments are conducted using temperature perturbations, as described previously, where a *T*-jump is applied to a micelle solution, and relaxation is monitored by various detection methods, such as light scattering and fluorescence. Due to the indirect nature of scattering and spectroscopic techniques, and the complicated nature of BCP micelle equilibration, it was often inferred that fragmentation/fusion events occurred in BCP micelle systems, but this remained a topic of great debate for many years. *T*-jump light scattering in micelle relaxation experiments were pioneered by Honda and coworkers,[104,109] who used time-resolved static light scattering to monitor the micellization and equilibration kinetics of poly(*α*-methylstyrene)-*block*-poly(vinylphenethyl alcohol) (PMS-PVPA) in the PVPA-selective solvent benzyl alcohol. PMS-PVPA exhibits UCMT phase behavior with a CMT at approximately 29 °C. SLS was used to monitor the change in the apparent molar mass, $M_{w,app}$, of scatterers as a function of annealing time. First, they studied the unimer to micelle transition (a micellization experiment), by monitoring $M_{w,app}$ as a function of temperature.

This experiment revealed for temperatures below the CMT, a constant $M_{w,app}$ is obtained, consistent with the molar mass of the polymer chains dissolved in solution. The onset of micellization above the CMT was identified at 29 °C indicated by an orders-of-magnitude increase in $M_{w,app}$. The time evolution of micelle molar mass was studied as a function of concentration at 35 °C. The authors concluded that the formation of micelles proceeds by a fast process (~ 0.1 to 1 h), which was attributed to micelle chain exchange, and equilibration in size occurs very slowly (on the order of 10 h), most likely by micelle fragmentation and fusion.[104,109]

While many studies of micelle fragmentation and fusion are conducted by perturbing the system out of equilibrium, recent reports showed that fusion and fragmentation occurs in various micellization scenarios, and some systems even exhibit these phenomena at equilibrium.[120] There are several reports on fusion and fragmentation for low molar mass surfactants.[117,125] Rharbi and Winnik used a fluorescent pyrene-derived probe to monitor the kinetics of fusion and fragmentation in aqueous solutions of surfactant micelles, and found that a second-order kinetic process, identified as micelle fusion, occurs several orders of magnitude more slowly than a diffusion-controlled kinetic process.[118] The first report of fusion and fragmentation in BCP micelles at equilibrium was also conducted using excimer fluorescence, and the presence of both mechanisms in aqueous solutions of poly(ethylene oxide)-*b*-poly(propylene oxide)-*b*-poly(ethylene oxide) micelles was detected.[120] Additional work using excimer fluorescence spectroscopy to study

ionic/nonionic mixed micelles of Triton X-100 and sodium dodecyl sulfate provided a clearer picture of the fusion and fragmentation process.[126]

Eisenberg *et al.*,[44,127,128] and later Meli *et al.*,[89] demonstrated that the solution preparation method used to prepare BCP micelle solutions greatly affects their relaxation behavior. Eisenberg *et al*. studied the thermodynamic and kinetic aspects of the formation of crew-cut micelles prepared from PS-PAA diblocks in DMF/water mixtures and used two methods to prepare micelle solutions. In the first method, micellization was induced by the addition of water, a PAA-selective solvent, to polymer solutions that are well mixed in DMF. The second method was the direct dissolution (DD) of PS-PAA in mixtures of DMF/water. They found that increasing the polymer concentration results in morphological transitions from spheres to rods, to interconnected rods, and then to bilayers. Furthermore, increasing water content shifts the boundaries for formation of different morphologies to lower polymer concentrations. In the highest water concentration samples, kinetic limitations to the formation of rods and bilayers were observed. They concluded that the mechanism of micelle formation in the first method, later deemed the cosolvent method (CS), leads to thermodynamically stable micelles, that grow via a nucleation and growth type mechanism. The DD method leads to kinetically trapped micelles that are out of equilibrium, which most likely grow and relax via a combination of insertion/expulsion, and micelle fusion and fragmentation.

Meli *et al*.[89,90] utilized this approach reported by Eisenberg, and demonstrated that a range of micelle sizes could be obtained from a single block copolymer by changing the

solution preparation method. Meli *et al*. prepared PB-PEO micelles in ILs, [C_2mim][TFSI] or [C_4mim][TFSI], by different dissolution methods. It was found that micelles formed by direct dissolution (DD) of PB-PEO into the IL formed large, polydisperse spherical aggregates, which decreased in size when subjected to annealing at elevated temperatures.[89,90] They showed that PB-PEO micelle relaxation in [C_2mim][TFSI] and [C_4mim][TFSI] was heavily dependent on temperature, but the timescale for micelle equilibration at 170 °C remained on the order of 10^3 seconds when changing the solvent from [C_2mim][TFSI] to [C_4mim][TFSI]. Analysis of this system by TR-SANS revealed that chain exchange did not occur up to at least 200 °C,[90] indicating that micelle equilibration must take place through some other mechanism(s). It was also found that the decay in PB-PEO micelle size is well described by a compressed exponential with $n = 2$ in both ionic liquids and at various annealing temperatures.[90] However, a physical interpretation for this compressed exponential behavior remains elusive. Although these results suggest that the primary relaxation mechanism in PB-PEO/[C_2mim][TFSI] is micelle fragmentation, there are several questions that remain unanswered, including the dependence on solvent selectivity, initial micelle size, N_{core}, and N_{corona} in the fragmentation kinetics.

Previous work on micelle equilibration kinetics relied on indirect detection methods, primarily scattering and spectroscopic methods. Cryo-TEM imaging provides additional insight into the micelle core size *ex-situ*. For kinetically trapped micelle systems, the change in micelle size and size distributions can be monitored *ex-situ*, as demonstrated by

Esselink, Dormidontova, and Hadziioannou.[121,122] Another significant advance in the field of micelle relaxation kinetics is the development of LP-TEM techniques. The advent of *in-situ* LP-TEM has enabled the direct observation of the dynamics of nanoscale assemblies in solution.[91,92,123,129–132] A major portion of this thesis is dedicated to the development of *in-situ* LP-TEM for PB-PEO micelles in ionic liquids, which will be discussed in subsequent chapters.

Advances in the realm of liquid-phase microscopy of volatile solvents were enabled by liquid-cell TEM (LC-TEM). In an LC-TEM experiment, the solution must be hermetically sealed from the vacuum chamber of the electron microscope. This led to the fabrication of electron-transparent graphene and silicon nitride (SiN_x) membranes, which are used for preparing thin-films of polymer solutions in volatile organic solvents that can be viewed directly in the electron microscope. Parent *et al.* reported the first direct observation of micelle fusion events *in-situ* using LC-TEM,[123] for the micellization of an amphiphilic copolymer, designated as phenyl-*b*-peptide-*co*-hydroxyl, prepared by ring-opening metathesis polymerization of divinyltetrahydrocyclopentapyrrole-based monomers, which form micelles in water. They used SiN_x windows to hermetically seal the aqueous micelle solution, and used videography to observe micelle formation, and micelle fusion events, *in-situ*. Figure 1.8 shows TEM micrographs of a micelle fusion event observed during early times in the micellization process.

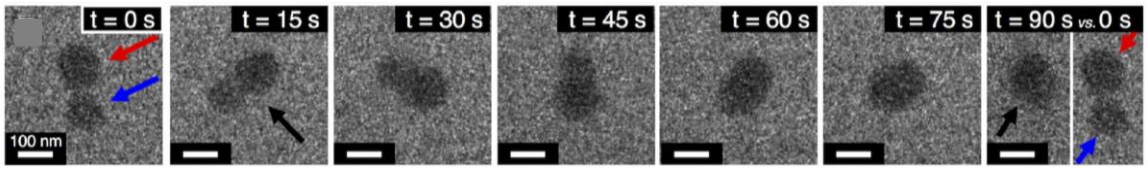

Figure 1.8: Micelle fusion event captured by LC-TEM where t = 0 s is the beginning of the fusion process, where two micelles diffusion within less than a distance R_h away from each other, followed by collision, merging, and relaxation to give a single, spherical micelle (t = 90 s). Reproduced from Reference 123.

A significant drawback to the LC-TEM experiment is that the viewing windows, *i.e.*, graphene and SiN_x, have been shown to influence the dynamics and motion of soft matter in solution.[123,131] This provides an exciting opportunity to exploit the non-volatility of ionic liquid solvents. A previous study used LP-TEM to study micelles formed by polystyrene-*block*-poly(2-vinyl pyridine) (PS-P2VP) in the ILs 1-ethyl-3-methylimidazolium ethylsulfate ([C_2mim][$ETOSO_3$]) and 1-butyl-3-methylimidazolium tetrafluoroborate ([C_4mim][BF_4]), both selective solvents for the P2VP blocks.[133] The authors demonstrated that ILs can be used to prepare stable, free-standing, thin-films on a traditional TEM grid, and the nonvolatility of the IL allows for direct observation of micelle motion in solution. This approach is advantageous in that the tedious fabrication and assembly of electron-transparent membranes is avoided, and the interaction of micelles with the membrane material is largely eliminated. However, both LC-TEM and LP-TEM experiments suffer from the same inherent issue, namely, the electron beam itself, which is known to influence the motion of particles in solution, and beam damage is of particular concern in soft matter

systems. Regardless, the development of these techniques has led to significant discoveries in the realm of micelle relaxation, which will be discussed throughout this thesis.

While there have been several reports implying that micelle fragmentation and fusion contribute to the process of micelle relaxation, current understanding of the fragmentation kinetics in diblock copolymer micelles is limited. Table 1.3 summarizes early reports on micelle fragmentation and fusion, but a quantitative understanding is desired, and direct observation of micelle fragmentation is necessary. This thesis aims to answer some fundamental open questions about micelle fragmentation, such as how do the kinetics depend on solvent selectivity and molar mass? Finally, what does the process of micelle fragmentation look like, in terms of micelle shape? To answer these questions, systematic investigations of the fragmentation behavior of PB-PEO micelles in [$C_x$mim][TFSI] ILs were conducted.

Table 1.3: Summary of the major findings related to micelle fusion and fragmentation from 1996 – 2017.

Date	Technique	System	Conclusion	Ref.
1996	*T*-jump SLS	PS-PVPA/benzyl alcohol	Fast micellization by unimer association; relaxation by micelle decomposition or fragmentation and reassociation by unimer addition.	104
1997	*T*-jump DLS & ultrasonic absorption	PEO-PPO-PEO/water	Two relaxation processes by chain exchange (fast) and formation and fragmentation (slow).	105
1998	Cryo-TEM	PS-P2VP/toluene	Early micelle formation by unimer aggregation, then fusion of micellar aggregates. Relaxation results in decreased micelle size by chain exchange.	121, 122
2010	*T*-jump DLS, TR-SANS	PB-PEO/ $[C_2mim][TFS]$ or $[C_4mim][TFS]$	PB-PEO micelles prepared by DD in ILs give large, kinetically trapped micelles that fragment at 170 °C. Kinetics are described by the Avrami equation where $n = 2$. No chain exchange is observed by TR-SANS.	89, 90
2012	Excimer Fluorescence	PEO-PPO-PEO/pyrene /water	First experimental evidence of micelle fusion and fragmentation at equilibrium.	120
2014	DLS, SAXS, Cryo-TEM	PB-PEO/ water/THF	PB-PEO micelles prepared by CS method with THF increase in size following THF removal and agitation by a bimodal pathway during a fusion-controlled growth process.	113
2017	LC-TEM	phenyl-*b*-peptide-*co*-hydroxyl /water	Direct observation of micelle fusion events during micelle growth by LC-TEM.	123

1.4 – Thesis outline

This thesis comprises eight chapters. This chapter serves as an introduction to the topic of micelle equilibration kinetics and serves as background for the experimental motivation of this work. Chapter 2 details the experimental methods used throughout, namely, the synthesis of PB-PEO diblocks by sequential anionic polymerization, IL synthesis, DLS, TR-SAXS, and LP-TEM techniques. Chapter 3 discusses the exploration of PB-PEO micelle fragmentation in five [$C_x$mim][TFSI]-based ILs, with the specific aim of understanding the influence of the solvent selectivity (*i.e.*, γ) on micelle fragmentation kinetics. Chapter 4 reports the first direct observation of micelle fragmentation *in-situ*, using high-temperature LP-TEM. Chapter 5 is the culmination of these early investigations of PB-PEO micelles in [C_2mim][TFSI], where the experimental efforts developed in Chapters 3 and 4 are utilized to explore the effect of diblock molar mass on fragmentation kinetics. Chapter 6 extends the molar mass study by exploring the fragmentation kinetics of hybrid PB-PEO micelles, prepared by blending molar masses of PB-PEO. Chapter 7 describes current efforts to image the DD mechanism of PB-PEO diblocks in [C_2mim][TFSI] via high-temperature LP-TEM. Finally, Chapter 8 summarizes the findings of this thesis and propose future areas of interest in the realm of micelle fragmentation and fusion.

Chapter 2 – Experimental methods*

In studying BCP micelle fragmentation, a model diblock copolymer should meet the following criteria to make these experiments feasible: (i) the core block should be rubbery at room temperature and above to prevent glassy core dynamics influencing the micelle fragmentation behavior, (ii) the χ parameter between the core-forming block and the solvent should be very large at temperatures ranging from 25 °C up to ~ 200 °C to prevent individual chain exchange and to kinetically trap nonergodic micelles, (iii) the corona block should be well dissolved in the ionic liquid of choice, and the χ parameter between the core and the corona should be large enough to induce microphase separation in the bulk, which will aid in the process of obtaining large, kinetically trapped micelles by the DD micelle preparation method. Because of these constraints, and previous studies by Meli *et al*.[90] confirming no chain exchange in this system, the diblock copolymer used in this thesis is PB-PEO in [$C_x$mim][TFSI] ILs. For this system, the micelle core is formed by PB and the corona is formed by PEO. The effects of the following molecular parameters on PB-PEO

* Reprinted in part with permission from Early, J. T.; Lodge, T. P. Fragmentation of 1,2-Polybutadiene-*block*-Poly(ethylene oxide) Micelles in Imidazolium-Based Ionic Liquids. *Macromolecules* **2019**, *52*, 7089 – 7101. Copyright © 2019 American Chemical Society, Early, J. T.; Yager, K. G.; Lodge, T. P. Direct Observation of Micelle Fragmentation via In Situ Liquid-Phase Transmission Electron Microscopy. *ACS Macro Lett.*, **2020**, *9*, 756 – 761. Copyright © 2020 American Chemical Society, and from Early, J. T.; Block, A.; Yager, K. G.; Lodge, T. P. Molecular Weight Dependence of Block Copolymer Micelle Fragmentation Kinetics. *J. Am. Chem. Soc.*, **2021**,*143*, 7748 – 7758. Copyright © 2021 American Chemical Society.

micelle fragmentation kinetics were studied in this thesis: 1) PB-PEO concentration in one IL, 2) solvent selectivity with respect to the core forming block for one molar mass of PB-PEO in five [$C_x$mim][TFSI] based ILs, 3) PB-PEO molar mass in [C_2mim][TFSI], where the total molar mass of the diblock was varied from 10^4 to 10^5 g mol^{-1} and nearly constant composition of $f_{PEO} \approx 0.4$, and 4) dispersity, where blends of different molar masses of PB-PEO were used to prepare micelle solutions in [C_2mim][TFSI]. Additionally, LP-TEM was used to achieve the direct observation of micelle fragmentation in an IL, and also to observe the swelling of a lamellar PB-PEO film in an IL, which aims to mimic the conditions of the DD preparation procedure.

This chapter describes the experimental techniques used in Chapters 3 – 7. The synthesis of linear PB-PEO diblock copolymers via two-step sequential anionic polymerization is introduced in Section 2.1. Polymer characterization by size exclusion chromatography (SEC) and proton nuclear magnetic resonance spectroscopy (^{1}H NMR) are provided in Section 2.1.2. The synthesis and purification of ILs is described in Section 2.2. Section 2.3 describes the DD method and co-solvent (CS) dissolution methods used to prepare PB-PEO micelle solutions in ILs, as well as the polymer blending procedure used to prepare hybrid micelles from PB-PEO molar mass blends. Dynamic light scattering (DLS) was used to characterize the total micelle radius R_h and the fragmentation kinetics, as discussed in Section 2.4. The change in micelle core radius during an annealing experiment was monitored by synchrotron small-angle X-ray scattering, as described in Section 2.5. Finally, the various types of TEM experiments used herein are described in

Section 2.6. From this information, a kinetic analysis of the change in micelle size during fragmentation is performed to obtain the fragmentation time of PB-PEO micelles in ILs.

2.1 – Polymer synthesis and characterization

PB-PEO diblock copolymers were synthesized by sequential anionic polymerization of 1,3-butadiene, followed by re-initiation with potassium naphthalenide (KNAP) to polymerize ethylene oxide. The polymerization scheme is shown in Figure 2.1.

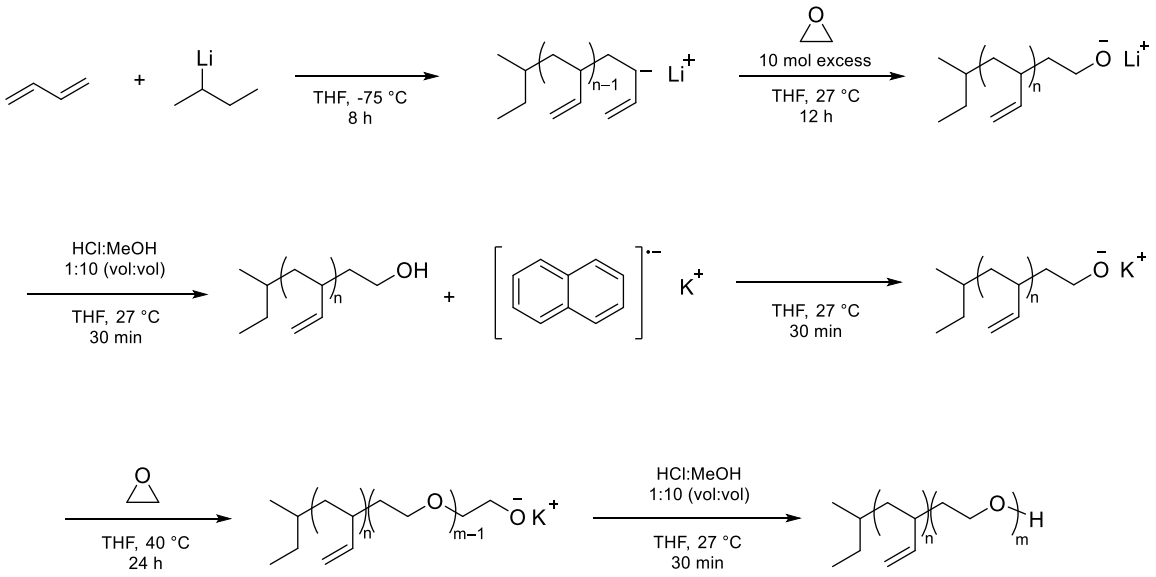

Figure 2.1: Synthesis of PB-PEO diblock copolymers by sequential anionic polymerization of 1,3-butadiene with *sec*-butyllithium in THF. Termination with one hydroxyl unit is achieved by the addition of excess (10 mol excess with respect to moles of PB-OH homopolymer) ethylene oxide at elevated temperatures. The hydroxyl end-group is re-initiated in the presence of KNAP, and polymerization of ethylene oxide is

conducted at 40 °C in THF to yield well-defined PB-PEO diblock copolymers with f_{PEO} = 0.4.

2.1.1 – Anionic polymerization

Anionic polymerization is a polymerization technique that enables the synthesis of block copolymers with well-defined structures, such as diblocks, triblocks, etc., and narrow molar mass distributions. Anionic polymerization follows chain-growth polymerization kinetics, with three basic steps: 1) initiation, where the initiator decomposes to give a reactive initiator species, followed by 2) propagation, where the reactive anion species generated from initiation reacts with a monomer, which continues to react and consecutively adds monomer units to the growing polymer chain, and finally 3) termination and transfer steps where living chain ends react, ideally in an irreversible fashion, to render the reactive chain ends effectively dead.[134] The potentially living nature of this polymerization allows for prediction of the molar mass of the polymer solely on the basis of the monomer-to-initiator ratio (assuming 100% initiation efficiency), where the degree of polymerization (N) is given by Equation 2.1,

$$N = \frac{[\mathrm{M}]_0}{[\mathrm{I}]_0} \tag{2.1}$$

where $[M]_0$ and $[I]_0$ are the monomer and initiator concentrations, respectively, at time zero. The kinetics of chain growth polymerizations can be used to estimate reaction times

when targeting nearly 100% conversion (*i.e.*, when $p \rightarrow 1$) of the monomer using Equation 2.2,

$$t = \frac{\ln(1-p)}{-k_p[\mathrm{I}]_0} \tag{2.2}$$

where k_p is the propagation rate constant and $0 \leq p \leq 1$ is the extent of reaction. An important consideration in the synthesis of low-dispersity polymers by anionic polymerization is the presence of impurities. Due to the reactivity of propagating anions in this technique, it is imperative to remove all impurities, air, and water from the system prior to the initiation step to maintain the living nature of this polymerization.

Several types of monomers are amenable to anionic polymerization techniques, including olefins like butadiene, styrene, isoprene, and ethylene, acrylates such as methyl methacrylate and methyl acrylate, and heterocycles, such as ethylene oxide.[135] In the case of vinyl monomers of type CH_2=CHX, the X group must be electron-withdrawing to stabilize the resulting carbanion. In the case of heterocyclic ring monomers, the ring must be amenable to a nucleophilic attack and result in a stable propagating anion. Examples of heterocyclic monomers amenable to anionic ring-opening polymerization include epoxides, cyclic siloxanes, lactones, and carbonates.

In anionic polymerization, many diblock copolymers are synthesized by sequential addition of a second monomer following full conversion of the first monomer to yield an AB diblock (*e.g.*, PS-PI or PS-PB). In preparation of diblock copolymers by anionic

polymerization, the living homopolymer chains will act as a macroinitiator for the polymerization of the second block, and after full conversion of the second monomer, the chain ends are terminated to give diblock copolymers. However, the drawback to this approach is that the reactivity of the second monomer must be similar to that of the first monomer under the reaction conditions employed. In other words, a critical constraint in synthesizing a diblock copolymer by sequential anionic polymerization is that the carbanion of the first block must be capable of initiating the polymerization of the second block. This means that the stability of the anion formed by polymerization of the second monomer must be greater than or equal to that of the first block. Other considerations for sequential anionic polymerization are that the solvent chosen for the reaction must be suitable for all blocks, and the counterion species must be suitable for the polymerization of both blocks.

These constraints limit the types of monomers that can be used in a sequential anionic polymerization. As 1,3-butadiene is ideally polymerized with alkyl lithium-based initiators, the polymerization of ethylene oxide (EO) by sequential addition is not possible due to the strong coordination between the alkoxide species (CH_2O^-) formed upon ring-opening of EO and Li^+ cations in solution. The reactivity of the alkoxide is less than that of the carbanion formed in the presence of Li^+ cations, and large molar masses of PEO cannot be achieved under these conditions. Thus, a two-step approach is used to synthesize PB-PEO, where polymerization of 1,3-butadiene in a polar, aprotic solvent at low temperatures favors the 1,2-addition mechanism, and the living PB polymer chains are end-

capped by the addition of EO at the end of the reaction, to yield mono-functionalized 1,2-polybutadiene-OH upon termination with acidic methanol.[136] The tight ion pair between the alkoxide end group and Li^+ ensures that mono-functionalization is achieved, as only one EO unit is added under these conditions, even with a 10-fold molar excess of EO added to the reactor. PB-OH homopolymer was purified by precipitation, characterized by ^1H NMR spectroscopy and SEC, and used as a macroinitiator in the polymerization of EO to yield PB-PEO diblocks.

For re-initiation of the PB-OH homopolymer, a potassium-based initiator is preferred for polymerization of EO, as the alkoxide species (CH_2O^-) formed upon ring-opening of ethylene oxide and K^+ forms a looser ion pairs in comparison to coordination of the alkoxide with Li^+.[136] With this in mind, the initiator must be a strong base so as to deprotonate the PB-OH homopolymer, but a weak nucleophile, so as to favor initiation by the homopolymer and not the initiator itself. Thus, the initiator commonly used in the synthesis of poly(alkane)-*block*-poly(ethylene oxide) diblocks is KNAP, as shown in Figure 2.1.[136]

In this work, six molar masses of PB-PEO diblock copolymers were synthesized by two-step sequential anionic polymerization with constant PEO composition ($f_{PEO} = 0.4$), as described here. The reaction setup used was described in previous reports.[136,137] 1,3-Butadiene (Sigma Aldrich, ≥ 99%) and ethylene oxide (Sigma Aldrich, ≥ 99.5%) were purified by stirring with vacuum-dried *n*-butyllithium (Sigma Aldrich, 2.5M in hexanes) twice for 30 min. Six molar masses (6 – 53 kg mol^{-1}) of hydroxyl-terminated 1,2-

polybutadiene were synthesized via anionic polymerization of 1,3-butadiene with *sec*-butyllithium (Sigma Aldrich, 1.4M in cyclohexane) in tetrahydrofuran (THF) at –75 °C for 8 h; the polymer chains were end-capped with a single ethylene oxide unit at 27 °C, and the polymerization was terminated by the addition of acidic methanol (1:10 HCl:methanol). Polymerization of 1,3-butadiene is known to favor 1,2-addition in low temperatures and polar, aprotic solvents, thus the reaction is run with THF as the solvent, and with the reactor submerged in a dry ice/isopropanol bath to maintain temperatures of –75 °C. A concentrated solution of PB-OH in dichloromethane was precipitated into an excess of cold methanol, isolated via vacuum filtration, and dried under vacuum (< 100 mTorr) at 40 °C for 72 h prior to use. PB-PEO diblocks with a nearly constant volume fraction of PEO (f_{PEO} ≈ 0.4) were prepared by subsequent anionic polymerization of ethylene oxide. The polymerization was performed in THF at 40 °C for 24 h in the presence of PB-OH with potassium naphthalenide. The polymerization was terminated by the addition of acidic methanol (1:10 HCl:methanol). PB-PEO diblocks were freeze-dried in benzene with 0.1 wt % BHT as an antioxidant under vacuum (< 100 mTorr) at 27 °C for 24 h prior to use. Explicit molar masses of PB-PEO diblocks are denoted BO(x-y), where x and y indicate the number- average molar mass of the PB and PEO blocks in kg mol^{-1}, respectively.

Table 2.1: Characteristics of BO(x-y) Diblock Copolymers.

Sample	$M_{n,PB}$ (kg mol^{-1})	$M_{n,PEO}$ (kg mol^{-1})	f_{PEO}	$Đ$
BO(6-5)	6.5	5.2	0.38	1.14
BO(8-6)[a]	8.4	6.4	0.37	1.10
BO(8-7)	9.4	7.6	0.38	1.07
BO(10-9)	10	9.4	0.43	1.05
BO(25-22)	25	22	0.41	1.09
BO(27-27)	27	27	0.43	1.06
BO(53-46)	53	46	0.40	1.05

^{1}H NMR spectroscopy in $CDCl_3$ was used to determine the number average molar mass (M_n) and volume fraction of PEO (f_{PEO}) using bulk densities ρ_{PB} = 0.87 g/cm^3 for PB, and ρ_{PEO} = 1.13 g/cm^3 for PEO. SEC with a multi-angle light scattering detector in THF was used to determine the weight average molar mass (M_w) and molar mass dispersity ($Đ = M_w/M_n$) of the diblocks.

[a]Synthesized previously by Dr. Luciana Meli.

2.1.2 Polymer characterization

SEC with a multi-angle light scattering detector (SEC-MALS) and refractive index (RI) detector is commonly used for the determination of number-average molar mass (M_n), weight-average molar mass (M_w), and dispersity ($Đ = M_w/M_n$). The packing material in the column consists of porous particles with some characteristic range of pore sizes, and the separation mechanism in this chromatography technique relies on the hydrodynamic

volume, V_h, of the polymer chains. The hydrodynamic volume is roughly proportional to the radius of gyration (R_g) cubed, thus the polymer chains in a sample with a smaller V_h (and therefore smaller R_g and N) can permeate the porous packing material and will elute later.[135] In contrast, larger N species will be excluded from smaller pores, and thus elute earlier.

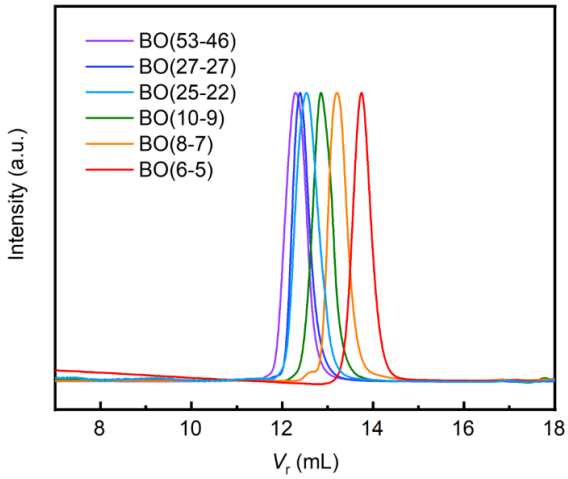

Figure 2.2: SEC RI traces of PB-PEO diblocks in THF. The d*n*/d*c* was estimated by the mass-weighted average of each block. Reproduced from Reference 139.

In this work, M_n, $Đ$, and f_{PEO} were determined by a combination of SEC-MALS (Wyatt Dawn Heleos II) in THF and ^{1}H nuclear magnetic resonance spectroscopy (^{1}H NMR) in $CDCl_3$ (^{1}H NMR, Varian Inova 500) as shown in Table 2.1. The refractive index detector traces from SEC in THF of BO(x-y) are shown in Figure 2.2. The refractive index increment (d*n*/d*c*) for a diblock was estimated as the weight average of the refractive index increments for PB in THF (d*n*/d*c* = 0.119 mL/g) and PEO in THF (d*n*/d*c* = 0.068 mL/g).[138]

^{1}H NMR spectroscopy was used to conduct end-group analysis of PB-PEO diblocks to determine the number-average molar mass M_n of each block, and the volume fraction of PEO. In an NMR spectrum, the various chemical shifts of each peak arise due to the local magnetic fields experienced by protons which is dependent on the local molecular structure. Figure 2.3 shows the ^{1}H NMR spectra for six PB-PEO diblocks in deuterated chloroform ($CDCl_3$),[139] where the chloroform peak is observed at 7.26 ppm.

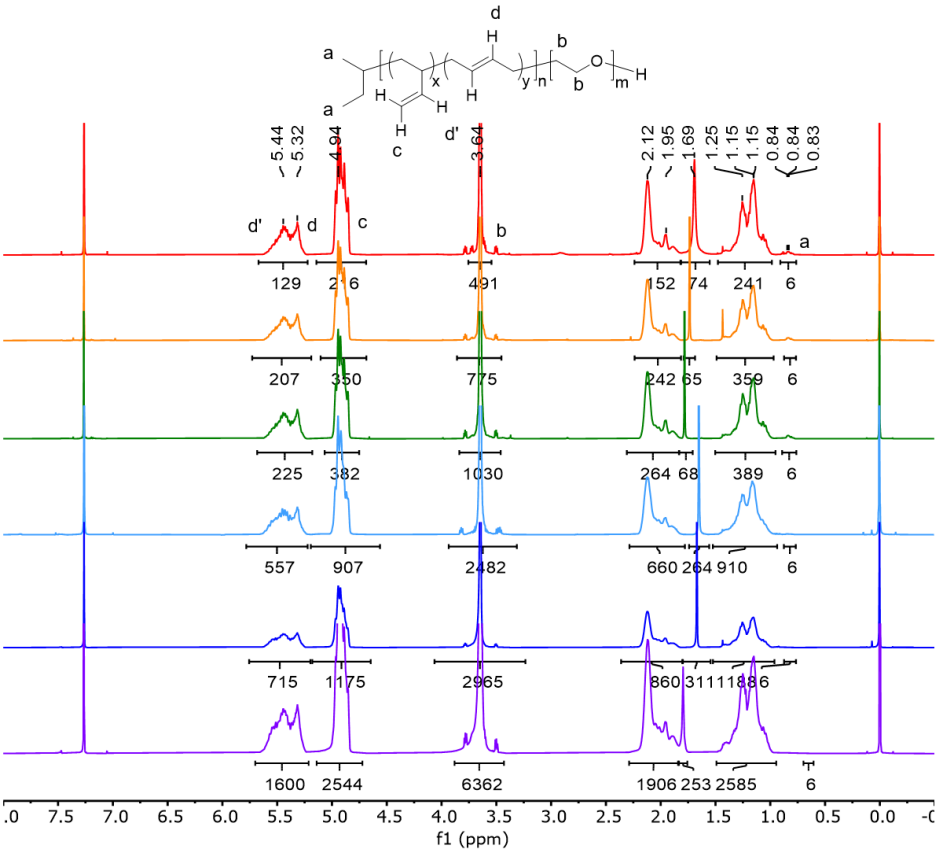

Figure 2.3: ^{1}H NMR spectra of BO(53-46) (bottom, purple), BO(27-27) (navy blue), BO(25-22) (light blue), BO(10-9) (green), BO(8-7) (orange), and BO(6-5) (top, red) in $CDCl_3$. Reproduced from Reference 139.

The integrated area (A) of the peaks corresponds to the relative number of hydrogen atoms, assuming the end group peak is well-defined and its chemical shift is known. For PB-PEO diblocks, methyl protons from the *sec*-BuLi initiator are observed at ~ 0.84 ppm and the area of this peak is normalized to 6 for end-group analysis. The percentage of 1,2 addition is determined by Equation 2.3,

$$f_{1,2} = \frac{A_c / 2}{A_c / 2 + [(A_{d'} + A_d) - A_c / 2] / 2} \tag{2.3}$$

where A_c is the integrated area for the terminal vinyl protons of the PB repeat unit with 1,2-regiochemistry (δ = 4.94 ppm), A_d is the integrated area for the alkene protons of the 1,4-PB repeat unit (δ = 5.32 ppm), and $A_{d'}$ is the integrated area for the alkene proton that is α to the terminal vinyl protons in the 1,2-PB repeating unit (δ = 5.44 ppm). Setting the integral area for the methyl end group protons, A_a (δ = 0.83 ppm), $M_{n,PB}$ is determined by Equation 2.4,

$$M_{n,PB} = \left(\frac{\frac{A_{d+d'} - A_c / 2}{2} + \frac{A_c}{2}}{\frac{A_a}{6}} \right) M_{0,B} \tag{2.4}$$

where $M_{0,B}$ = 54.1 g/mol is the molar mass of 1,3-butadiene. $M_{n,PEO}$ is determined by Equation 2.5,

$$M_{\mathrm{n,PEO}} = \frac{M_{\mathrm{n,PB}}\left(\frac{A_{\mathrm{b}}}{4}\right)M_{0,\mathrm{EO}}}{\left(\frac{A_{\mathrm{c}}/2}{f_{1,2}}\right)M_{0,\mathrm{B}}} \tag{2.5}$$

where $M_{0,\mathrm{EO}}$ = 44.1 g/mol is the molar mass of ethylene oxide and A_{b} is the integrated area for the methylene protons of the EO repeat unit (δ = 3.64 ppm). Finally, the volume fraction of PEO, f_{PEO}, is given by Equation 2.6.

$$f_{\mathrm{PEO}} = \frac{M_{\mathrm{n,PEO}} / \rho_{\mathrm{PEO}}}{M_{\mathrm{n,PEO}} / \rho_{\mathrm{PEO}} + M_{\mathrm{n,PB}} / \rho_{\mathrm{PB}}} \tag{2.6}$$

where ρ_i are the bulk densities ρ_{PB} = 0.87 g/cm^3 for PB, and ρ_{PEO} = 1.13 g/cm^3 for PEO.

2.2 – Ionic liquid synthesis

Ionic liquids have emerged as a unique class of so-called “designer” solvents due to their structural tunability from the selection of the cation and anion. The most useful characteristic of ILs leveraged in this work is their remarkable non-volatility and thermal stability.[140] These desirable properties allow for micelle fragmentation kinetics to be studied at elevated temperatures, making the temporal window for fragmentation accessible with traditional laboratory techniques. Additionally, the negligible vapor pressure of these ILs allows for facile observation of fragmentation *in-situ* via LP-TEM.

Using IL solvents for LP-TEM allows the direct observation of stable, free-standing IL-micelle films in the electron microscope, which is, comparatively, a more accessible method of solution observation in comparison to hermetically sealed LC-TEM methods. This section describes the synthesis and characterization of [$C_x$mim][TFSI]-based ILs through traditional ion exchange reactions, as described in a previous report.[141]

2.2.1 – Ion exchange reaction

The ILs 1,3-dimethylimidazolium bis(trifluoromethylsulfonyl)imide 99% ([C_1mim][TFSI]) and 1-hexyl-3-methylimidazolium TFSI ([C_6mim][TFSI]) 99.5% were purchased from IoLiTec. The ILs [C_2mim][TFSI], [C_4mim][TFSI], and [C_8mim][TFSI] were synthesized by anion exchange reactions.[141] The typical procedure for IL synthesis is as follows. For synthesis of [C_2mim][TFSI], shown in Figure 2.4, anion exchange between 1-ethyl-3-methylimidazolium bromide ([C_2mim][Br]) and lithium TFSI, both purchased from IoLiTec, was carried out in water at 70 °C for 24 h.

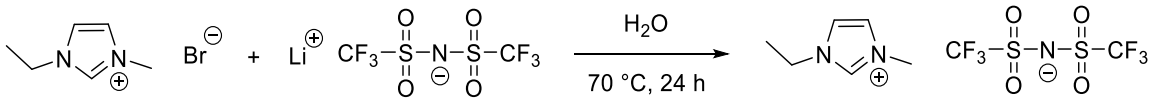

Figure 2.4: Anion exchange of [C_2mim][Br] and [Li][TFSI] in water to yield the IL [C_2mim][TFSI].

The reaction mixture was diluted with dichloromethane, the aqueous layer was removed, and the organic layer was washed with water three times. The organic layer was stirred in activated charcoal for 24 h before passing the solution through an alumina

column. Dichloromethane was removed *in vacuo*, and [C_2mim][TFSI] was dried under vacuum (< 100 mTorr) at 60 °C for 72 h. The same general procedure was used to synthesize [C_4mim][TFSI] and [C_8mim][TFSI], but [C_2mim][Br] was replaced with [C_4mim][Cl] (IoLiTec., 99%) and [C_8mim][Cl] (IoLiTec., 99%), respectively. All ILs were dried under vacuum (< 100 mTorr) at 60 °C for 72 h prior to use.

2.2.2 – Ionic liquid characterization

All ILs were characterized by ^{1}H, ^{13}C, and ^{19}F NMR spectroscopy in DMSO-d_6 (^{1}H NMR, Varian Inova 500). The ^{1}H and ^{13}C NMR spectra for all ILs are shown in Figures 2.5 – 2.9. In Figures 2.5 – 2.9, the DMSO protons are observed at δ = 2.50 ppm, and a trace amount of water can be observed at δ = 3.4 ppm. The water peak is most likely due to absorbed moisture in the NMR solvent itself, as the ILs are vacuum dried at elevated temperatures and stored in a vacuum desiccator when not in use. ^{19}F NMR spectra of all ILs used in this thesis are shown in Figure 2.10, where a single NMR peak is observed for all ILs resulting from the fluorine atoms in the TFSI anion. This peak in the ^{19}F NMR of [$C_x$mim][TFSI] based ILs appears at approximately δ = –79.0 ppm for all ILs, as shown in Figure 2.10.

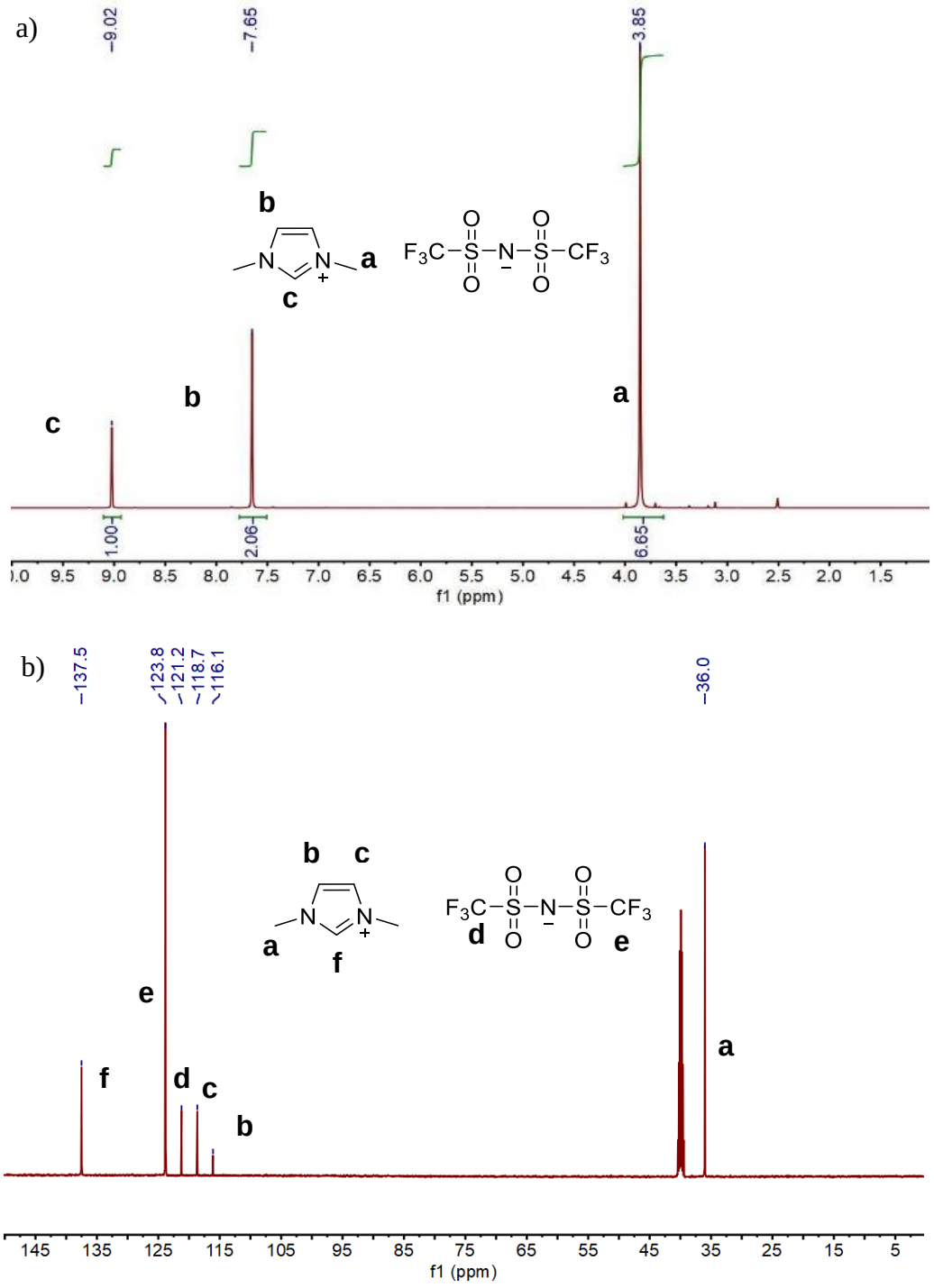

Figure 2.5: (a) ^{1}H NMR and (b) ^{13}C NMR spectra of [C_1mim][TFSI] in DMSO-d_6.

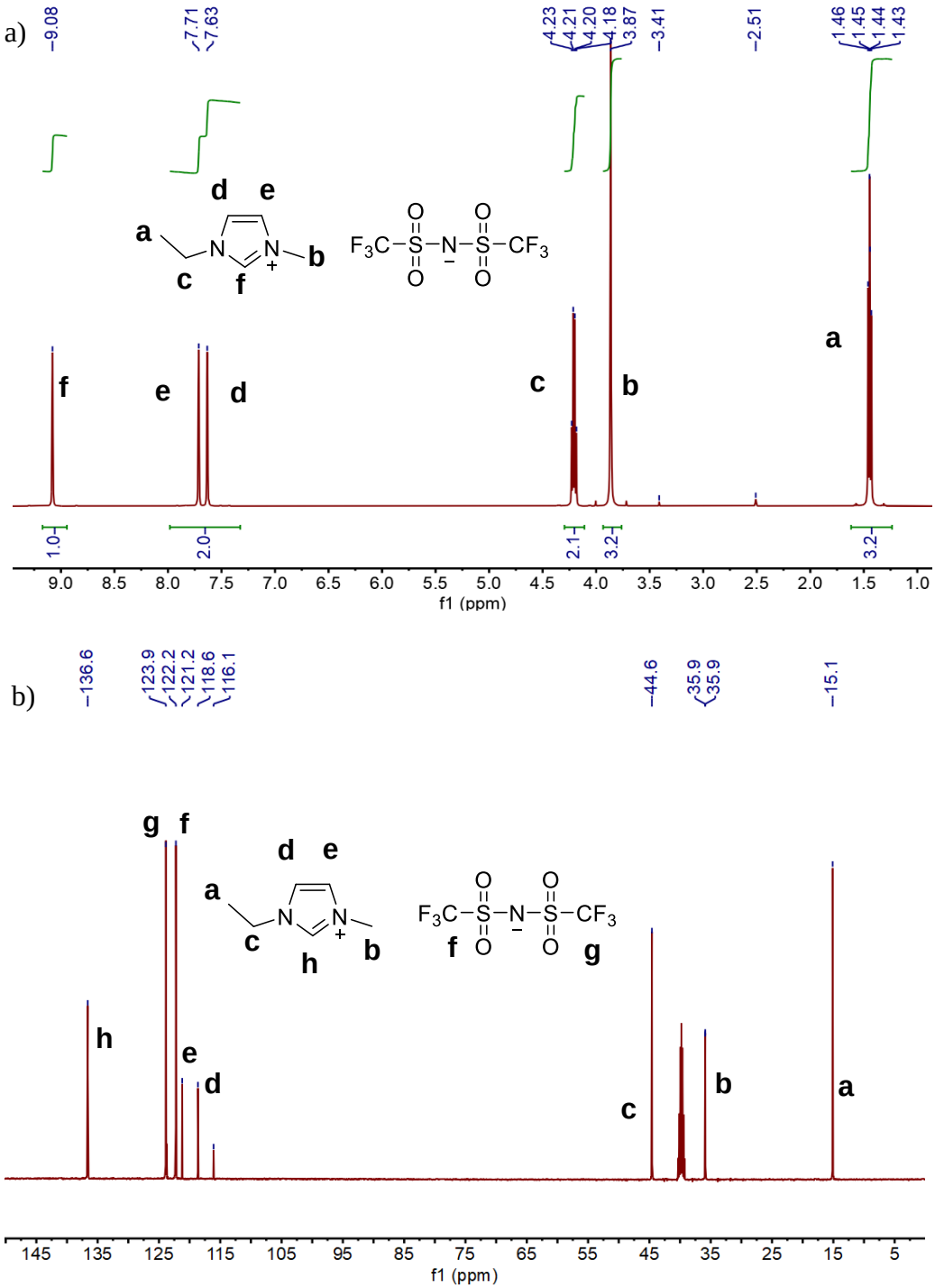

Figure 2.6: (a) ^{1}H NMR and (b) ^{13}C NMR spectra of [C_2mim][TFSI] in DMSO-d_6.

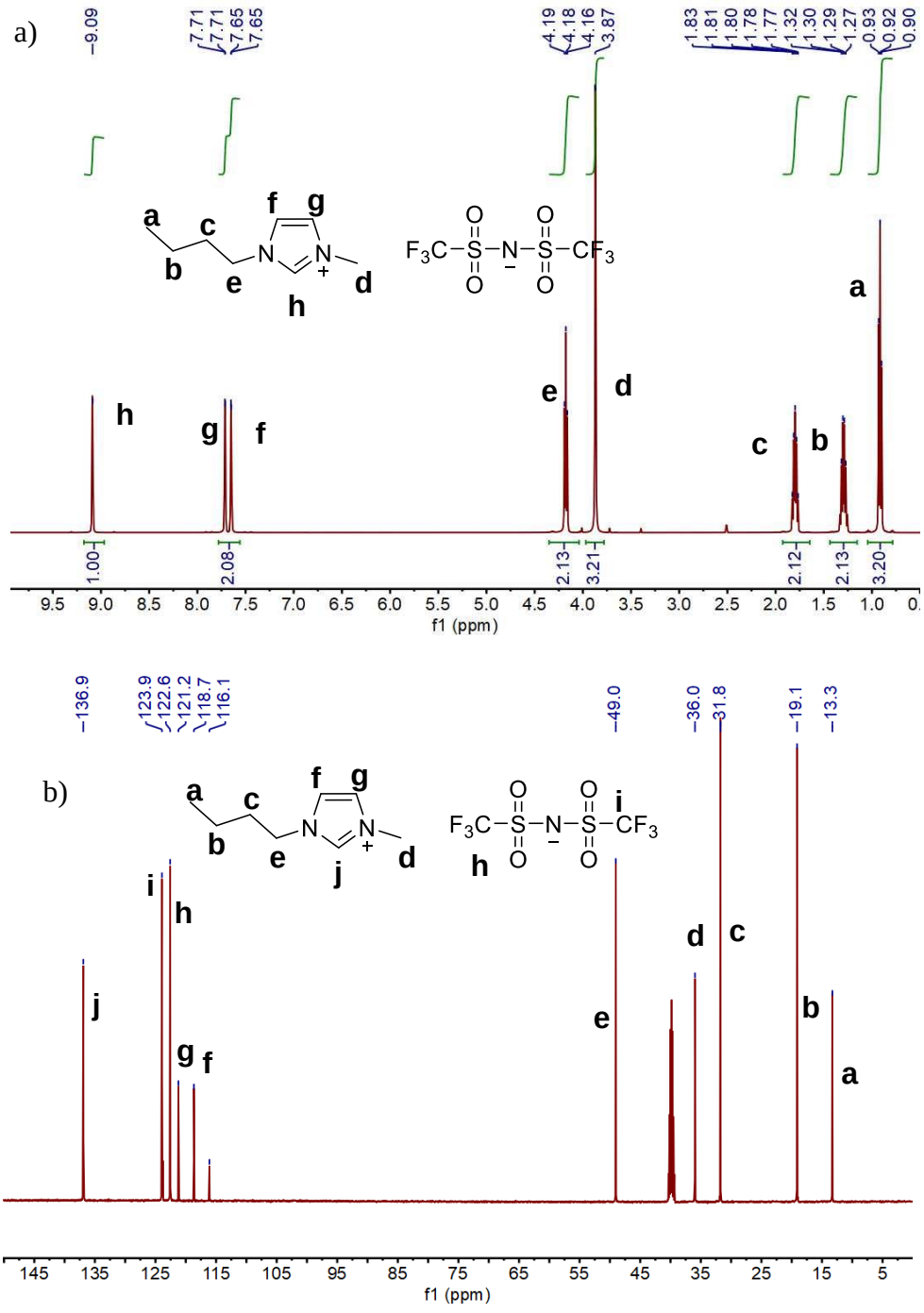

Figure 2.7: (a) ^{1}H NMR and (b) ^{13}C NMR spectra of [C$_4$mim][TFSI] in DMSO-d_6.

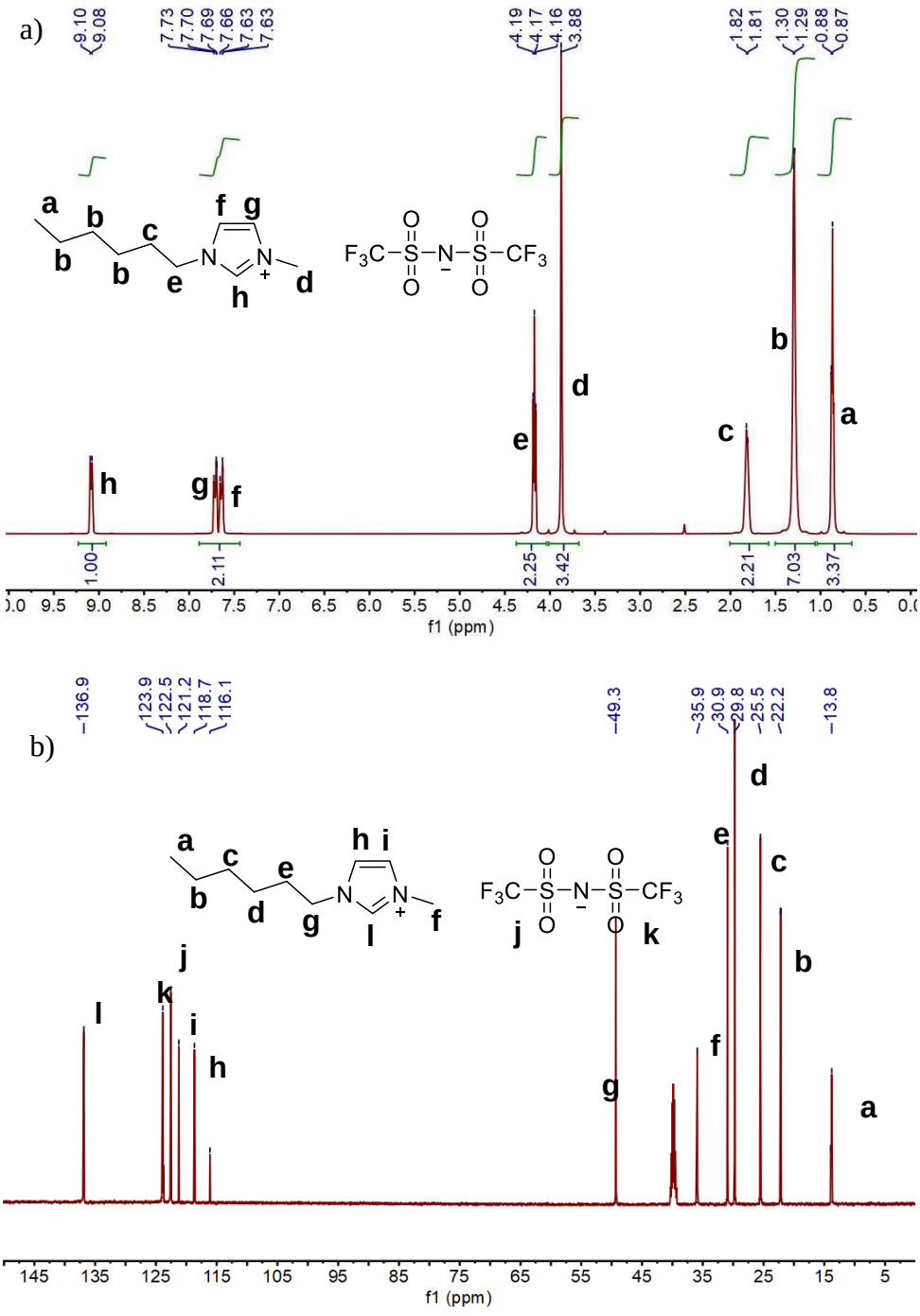

Figure 2.8: (a) ^{1}H NMR and (b) ^{13}C NMR spectra of [C$_6$mim][TFSI] in DMSO-*d*$_6$.

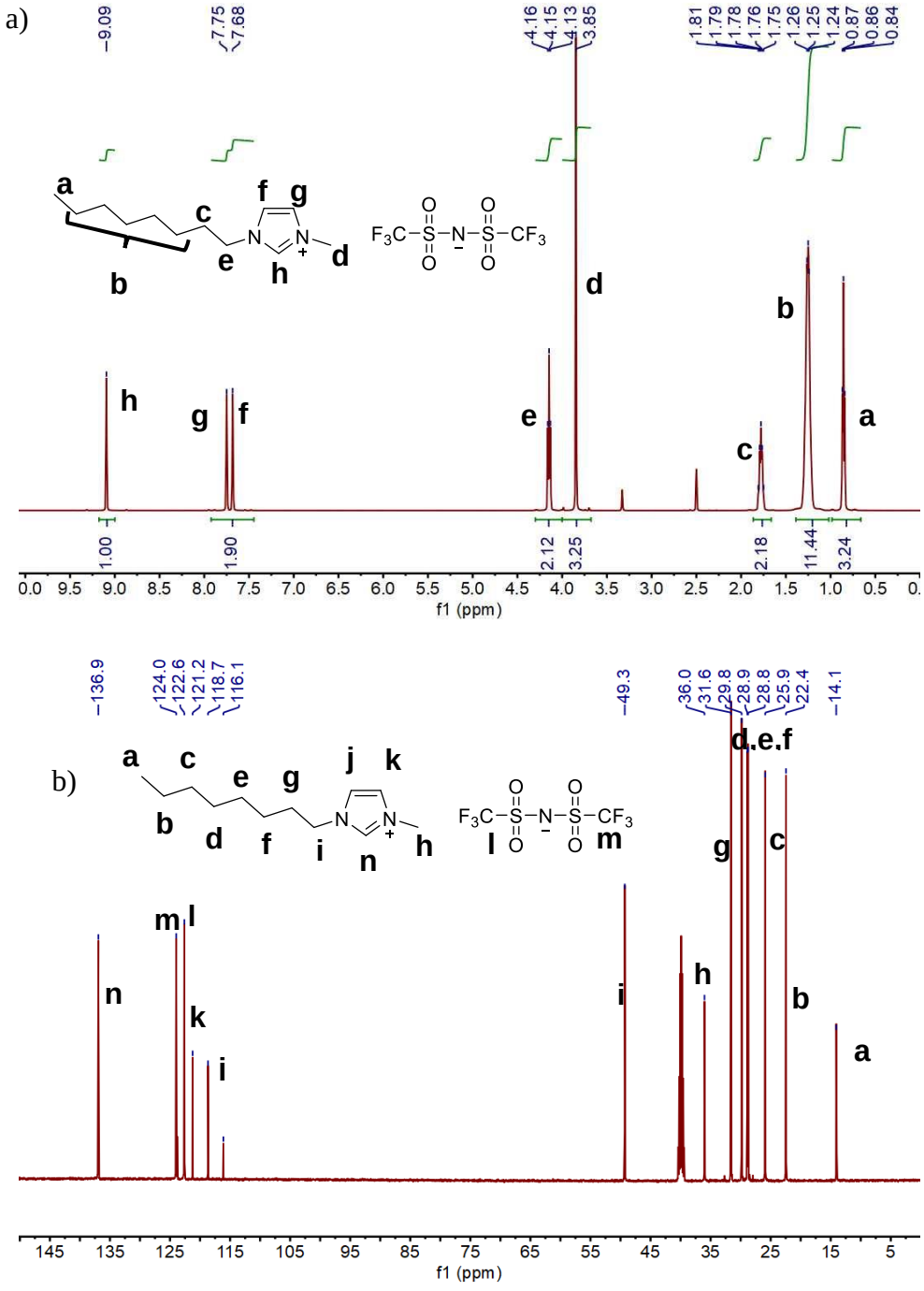

Figure 2.9: (a) ^{1}H NMR and (b) ^{13}C NMR spectra of [C$_8$mim][TFSI] in DMSO-*d*$_6$.

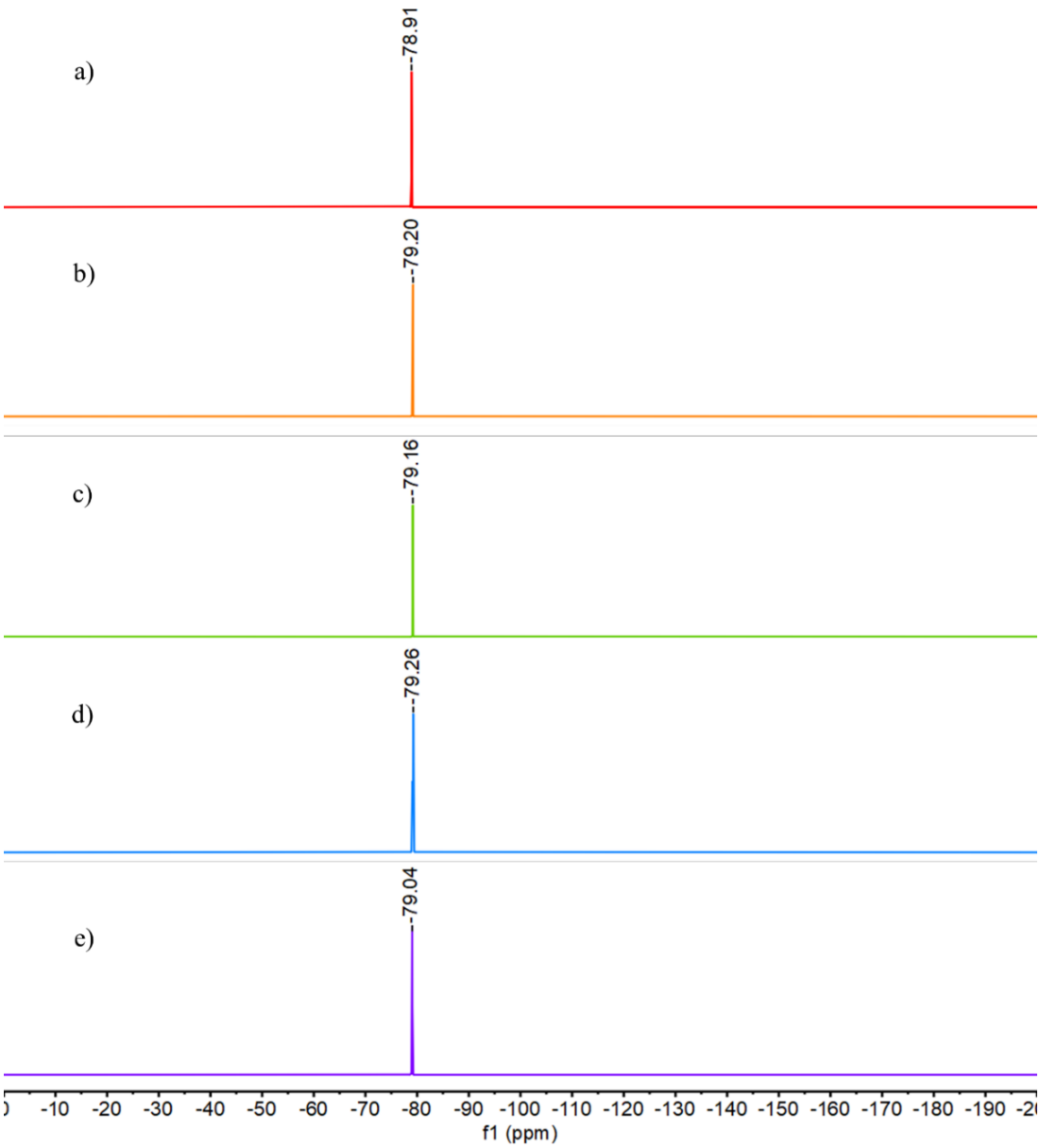

Figure 2.10: ^{19}F NMRs of (a) [C_1mim][TFSI], (b) [C_2mim][TFSI], (c) [C_4mim][TFSI], (d) [C_6mim][TFSI], and (e) [C_8mim][TFSI] in DMSO-d_6.

2.3 – Micelle solution preparation

It is well known that the method of preparation will affect the resulting size of micelles in solution. Eisenberg *et al.*,[44,127,128] and later Meli *et al.*,[89,90] demonstrated that the solution preparation method used to prepare BCP micelle solutions greatly affects their relaxation behavior. In this work, we exploit the approach used by Eisenberg *et al*.[44,127,128] and Meli *et al.*, [89,90] who showed that a range of micelle sizes could be obtained from a single block copolymer by changing the solution preparation method. Meli *et al*. prepared PB-PEO micelles in the ILs [C_2mim][TFSI] or [C_4mim][TFSI] by different dissolution methods. They noted that micelles formed by direct dissolution of PB-PEO into the IL formed large, polydisperse spherical aggregates, which decreased in size when subjected to annealing at elevated temperatures.[89,90]

2.3.1 – Direct dissolution (DD)

DD of BO(8-6) in [$C_x$mim][TFSI]

All micelle solutions were prepared by the DD method described here, unless noted otherwise. The desired amounts of BO(8-6) and IL were combined by weight in a 20 mL scintillation vial equipped with a stir bar to obtain the desired concentration. The vial was placed into an oil bath and stirred vigorously at 70 °C for 48 h. The resulting DD solutions were slightly blue-tinted in color when [C_1mim][TFSI], [C_2mim][TFSI], or [C_4mim][TFSI] was used as the solvent. Solutions prepared by DD in [C_6mim][TFSI] and [C_8mim][TFSI] were clear and colorless. Micelle fragmentation is expected to be a first-order kinetic

process with respect to polymer concentration, therefore, the concentration dependence of fragmentation was studied for BO(8-6) micelles prepared by DD in [C_2mim][TFSI]. For the concentration series of 0.5, 0.25, 0.1, and 0.05 wt % BO(8-6) in [C_2mim][TFSI], a 1 wt % solution was prepared by the DD protocol described previously, and subsequently diluted with additional [C_2mim][TFSI].

DD of BO(x-y) in [C_2mim][TFSI]

To study the molar mass dependence of micelle fragmentation, the DD protocol was also used to prepare large, kinetically trapped micelles in a single IL, namely, [C_2mim][TFSI], using the same protocol. Because larger molar mass polymers were used in this study, the concentration of polymer used for the molar mass study was 0.25 wt % to prevent any turbidity in the micelle solutions, as this would influence the light scattering results. The resulting DD solutions were slightly blue-tinged for BO(6-5), BO(8-7), BO(25-22), and BO(27-27) micelles, whereas those for BO(10-9) and BO(53-46) were white-tinged.

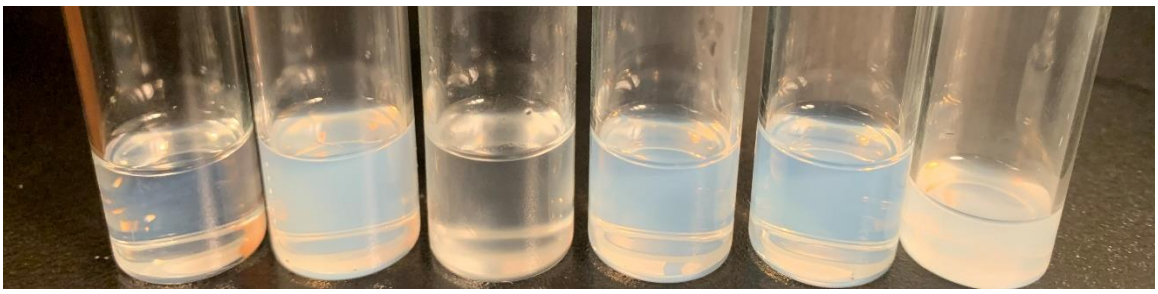

Figure 2.11: 0.25 wt % PB-PEO micelles as prepared by DD with increasing molar mass of PB-PEO from left to right.

2.3.2 – Cosolvent dissolution (CS)

In the CS dissolution method, a good solvent for the IL and PB-PEO blocks is added to the micelle solution and all components of the solution are well dissolved in the cosolvent. Then, the cosolvent is slowly removed through a gentle nitrogen purge over the course of 24 h, which induces micellization. The slow change in χ between the core block and the mixed solvent allows for thermodynamic control over the micelle formation process. This preparation procedure was shown to give small micelles with radii that are constant with annealing time, and these micelles typically do not undergo fragmentation in the PB-PEO/IL system. The desired amounts of PB-PEO and IL were combined by weight in a 20 mL scintillation vial equipped with a stir bar to obtain a 0.5 wt % solution. Dichloromethane, a common solvent for both blocks, was added to the vials with a 1:1 w/w IL-to-dichloromethane ration. After complete dissolution of the polymer, the cosolvent was gradually removed by stirring the solution under a nitrogen purge for 24 h to cause aggregation of the PB block.[82,84] The solutions were dried under vacuum (< 70 mTorr) at 60 °C for 24 h to remove trace amounts of remaining cosolvent.

2.3.3 – Preparation of hybrid micelles from PB-PEO blends

Previous work by Zhao *et al.*[142] demonstrated that the use of molar mass blends to prepare hybrid micelles can also change the initial micelle radius, and the equilibration kinetics. To further explore this effect in the PB-PEO/IL systems used previously, binary blends of the PB-PEO diblocks shown in Table 2.1 were prepared by freeze-drying in benzene. In this procedure, the desired amount of each molar mass were combined in a 100

mL glass jar, and the diblocks were dissolved in benzene. Then, the benzene was removed by freeze-drying process, where the polymer solution is frozen in liquid nitrogen, and the solvent is removed under vacuum (< 70 mTorr) at 27 °C for 24 h to give well-mixed PB-PEO blends. Then, the DD method in [C_2mim][TFSI] was used to give hybrid micelle solutions with c_{polymer} = 0.25 wt %.

The mole fraction of the longer block, $\bar{x}_{\text{L}}$, and the average degree of polymerization of the core and corona, $\langle N_{\text{core}} \rangle$ and $\langle N_{\text{corona}} \rangle$, for PB-PEO blends were calculated by Equations 2.7 and 2.8, respectively,[142]

$$\bar{x}_{\text{L}} = \frac{w_{\text{L}} / M_{\text{n,L}}}{w_{\text{L}} / M_{\text{n,L}} + (1 - w_{\text{L}}) / M_{\text{n,S}}} \tag{2.7}$$

$$\left\langle N_i \right\rangle = \bar{x}_{\text{L}} N_{i,\text{L}} + (1 - \bar{x}_{\text{L}}) N_{i,\text{S}} \tag{2.8}$$

where w_{L} is the weight fraction of the longer block, $M_{\text{n,L}}$ is the number-average molar mass of the longer block, $M_{\text{n,S}}$ is the number-average molar mass of the shorter block, and $\langle N_i \rangle$ where i = core or corona is the degree of polymerization of either the longer block, $N_{i,\text{L}}$, or the shorter block, $N_{i,\text{S}}$.

2.4 – Dynamic light scattering (DLS)

Dynamic light scattering (DLS) is frequently employed to characterize the radius of BCP micelles in solution.[17,79,89–91] Not only is DLS employed to characterize the equilibrium micelle radius, but the equilibration kinetics are commonly studied using high-temperature DLS.[90,91,100–102,142] Specifically, the hydrodynamic radius, R_h, is determined from DLS measurements, and this radius is assumed to be equal to the total micelle radius ($R_{mic} = R_h \approx R_{core} + L_{corona}$) for solutions that are well below the micelle overlap concentration. This section gives a brief description of the theory of DLS, followed by the experimental methods used to study PB-PEO micelle fragmentation in ILs. Three quantities are necessary to deduce quantitative information on the micelle fragmentation kinetics, namely, 1) the initial, as-prepared average micelle radius, $\langle R_h \rangle_0$, which is determined by multi-angle DLS at room temperature following the dissolution of PB-PEO in an IL, 2) the time-dependent micelle radius, $\langle R_h \rangle_t$, which is monitored during an annealing experiment at a single scattering angle, to determine the fragmentation kinetics, and 3) the steady-state micelle radius, $\langle R_h \rangle_f$, after fragmentation, which is determined using multi-angle DLS at room temperature. From this information, a kinetic analysis of the change in $\langle R_h \rangle$ is performed to obtain the fragmentation time of PB-PEO micelles in ILs.

2.4.1 – Theory

DLS is a widely utilized technique for the characterization of particle size distributions in solution. The particles, *e.g.*, micelles, move in solution via Brownian motion due to the

collisions of the particles with solvent molecules. This causes the particle position to be constantly changing, thus the intensity of scattered light is a function of the instantaneous spatial arrangement of the scattering particles. Light scattered from the particles can interfere more or less destructively, and the dynamics of the particle motion is reflected in the intensity autocorrelation function, $g_2(\tau)$, as shown in Equation 2.9,

$$g_2(\tau) = \frac{\langle I(t)I(t+\tau)\rangle}{\langle I(t)\rangle^2} \tag{2.9}$$

where τ is the delay time. For fast-moving small particles, this correlation in intensity decays more quickly, and this means that smaller particles will require less time than the larger particles in solution for $g_2(\tau)$ to decay to 1. At this point, $I(t)$ and $I(t+\tau)$ are uncorrelated, and particle size is directly related to τ. Then, $g_2(\tau)$ is converted to the electric field autocorrelation function, $g_1(\tau)$, via the Siegert relation,[143]

$$g_2(\tau) = 1 + \beta\left|g_1(\tau)\right|^2 \tag{2.10}$$

where β is a coherence factor that depends on the geometry and alignment of the laser. For a single population of scatterers, the electric field autocorrelation function can be fit to an exponential decay,

$$g_1(\tau) = \exp(-\Gamma\tau) \tag{2.11}$$

where Γ is the decay rate. The decay rate is related to the tracer diffusion coefficient, D_t, which is calculated from Equation 2.12

$$\Gamma = D_t q^2 \tag{2.12}$$

assuming dilute solutions where $D_t \approx D_m$. The magnitude of the scattering vector q is defined by Equation 2.13,

$$q = \frac{4\pi n}{\lambda_0} \sin\left(\frac{\theta}{2}\right) \tag{2.13}$$

where n is the refractive index of the solvent and λ_0 is the wavelength of light in a vacuum. For multi-angle light scattering experiments, D_m is estimated by taking the slope of the line in plots of Γ versus q^2 with zero intercept. For dilute solutions, D_m is used as an approximation of the tracer diffusion coefficient, D_t. This is used to calculate the hydrodynamic radius using the Stokes-Einstein equation,

$$R_h = \frac{kT}{6\pi\eta_s D_t} \tag{2.14}$$

where k is the Boltzmann constant, T is the temperature, and $\eta_s(T)$ is the solvent viscosity.

2.4.2 – Experimental details

DLS measurements were performed on two instrumental setups. The first is a home-built light scattering setup equipped with a Brookhaven BI-DS photomultiplier mounted to

an adjustable goniometer, a Lexel Ar^+ laser (λ = 488 nm), and a Brookhaven BI-9000 correlator. The second instrument is a commercially manufactured DLS instrument with a Brookhaven BI-200SM goniometer, a Brookhaven BI-9000AT correlator, and a mini-diode laser (λ = 637 nm). All annealing experiments were conducted on the home-built DLS instrument, and room-temperature multi-angle measurements were obtained on the commercial DLS, unless indicated otherwise. During a typical annealing experiment, the temperature was controlled with an index-matching high-temperature silicone oil bath to within ±0.1 °C. To verify the size of the micelles before and after annealing, multi-angle light scattering experiments were performed at T = 27 °C with a range of scattering angles θ from 60° to 120°. All micelle solutions were passed through 0.45 μm PTFE syringe filters to remove any dust, and subsequently flame-sealed under vacuum (≤ 70 mTorr) in a dust-free glass tube (I.D. 0.51 cm) to prevent degradation of the block copolymer and to avoid contact with moisture and dust. In an annealing experiment, the oil bath temperature was allowed to equilibrate for 30 min prior to introducing the sample. The electric field autocorrelation function, $g_1(\tau)$, was measured at θ = 90° as a function of time. For each time point, $g_1(\tau)$ was acquired for 90 sec. The electric field autocorrelation function was converted to the intensity autocorrelation function, $g_2(\tau)$, via Equation 2.10,[143] which was then fit to a second-order cumulant expansion shown in Equation 2.15.

$$g_2(\tau) = B + \beta \exp(-2\Gamma\tau)\left(1 + \frac{\mu_2\tau^2}{2!}\right)^2 \tag{2.15}$$

The solvent viscosity used to obtain R_h from Equation 2.14 is η_s(170 ºC) = 2.4 kPa·s for [C_2mim][TFSI].[87] The temperature dependence of the viscosity is well described by the Vogel-Fulcher-Tamman (VFT) equation for [C_2mim][TFSI] and many other ILs.[87,144–146] For [C_2mim][TFSI], the temperature dependence follows $\log[\eta(T)/\eta_\infty] = B/(T - T_0)$, where $\eta_\infty = 1.4 \times 10^{-4}$ Pa*s, B = 376 K, and T_0 = 145 K for [C_2mim].[87] VFT parameters for [C_4mim] were reported as $\eta_\infty = 1.7 \times 10^{-4}$ Pa*s, B = 763 K, and T_0 = 180 K.[144] For [C_6mim][TFSI], reported VFT parameters are $\eta_\infty = 1.0 \times 10^{-4}$ Pa*s, B = 819 K, and T_0 = 166 K.[145] The refractive index and viscosities of all ILs used to estimate R_h are summarized in Table 2.2.

Table 2.2: Summary of IL n at 27 °C, viscosity in cP at room temperature, η_s(27 ºC), and viscosity in cP at 170 °C, η_s(170 ºC) used to estimate $\langle R_h \rangle$ from Equation 2.14.

IL Cation	n	η_s(27 ºC) (cP)	η_s(170 ºC) (cP)
[C_1mim]	1.400	37.1	2.6
[C_2mim]	1.419	33.9	2.4
[C_4mim]	1.428	50.9	2.7
[C_6mim]	1.430	68.0	3.1
[C_8mim]	1.435	93.0	3.3

The temperature dependence of n was not established for all ILs, and instrumental limitations prevented direct measurement of n at this temperature, so the room temperature values of n for each IL, reported previously,[147–150] were used for all analyses. Because the

fragmentation kinetics were obtained by a normalization of $\langle R_h \rangle$, this is not expected to influence the time constants obtained for micelle fragmentation.

Additional analysis of the micelle size distribution was performed by applying the regularized positive exponential sum (REPES) Laplace inversion to the intensity autocorrelation function.[151] Application of this algorithm results in a decay rate distribution, $G(\Gamma)$, which can be expressed in terms of the hydrodynamic radius from Equation 2.14. When the REPES routine showed a sample with a bimodal distribution, $g_1(t)$ was fit to a double-exponential function, shown in Equation 2.16, to obtain the decay rates of each population.

$$g_1(\tau) = f_1 \exp(-\Gamma_1 \tau) + f_2 \exp(-\Gamma_2 \tau) \tag{2.16}$$

Representative REPES plots of 0.25 wt % BO(x-y) in [C_2mim][TFSI] are shown in Figure 2.12 (a) as prepared by DD and (b) after annealing at 170 °C. As evidenced by the figures, the total micelle radius decreases substantially after annealing, which is indicative of micelle fragmentation in this system.

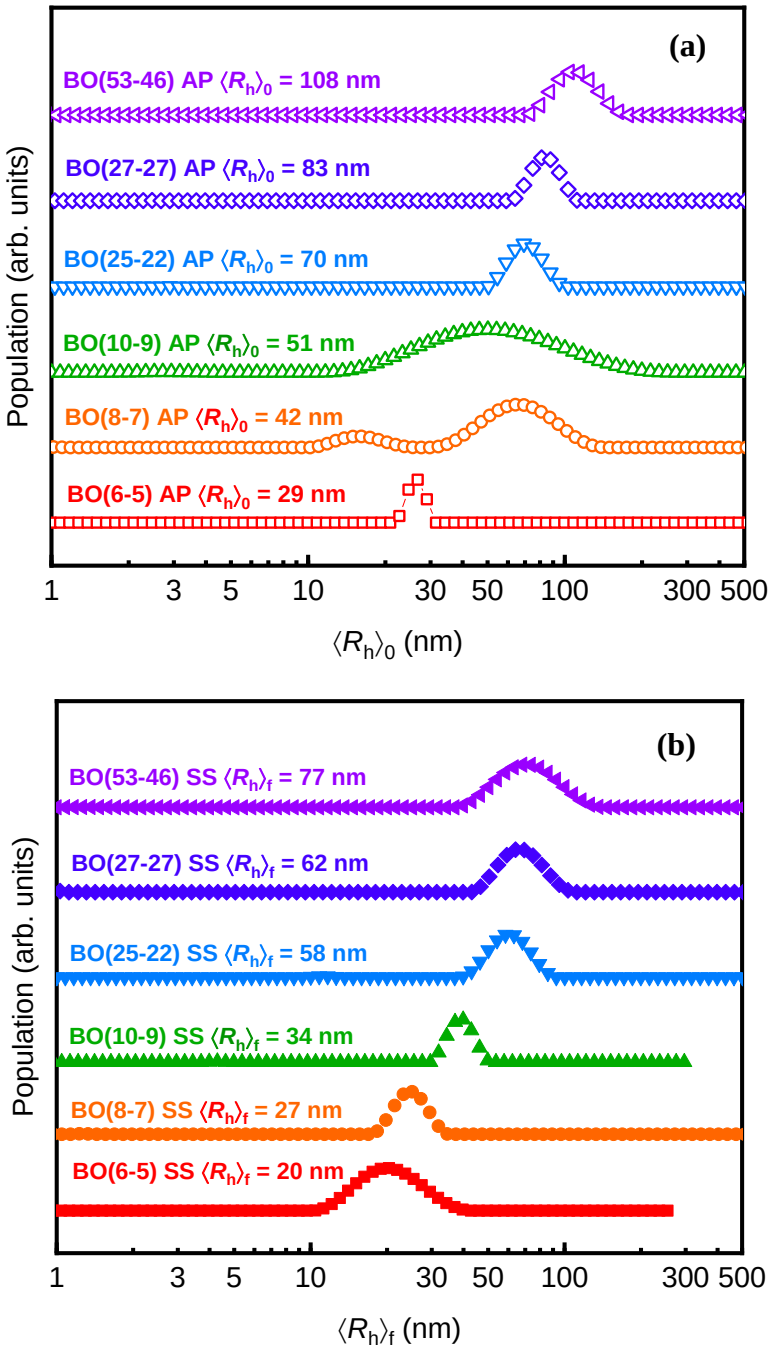

Figure 2.12: REPES results for 0.25 wt % PB-PEO in [C2mim][TFSI] (a) as-prepared by DD and (b) steady-state after annealing at 170 °C. Light scattering measurements were performed at a scattering angle of 90°. Reproduced from Reference 139.

In a high-temperature DLS experiment, $\langle R_h \rangle_t$ is measured at $\theta = 90°$. Because this is a single-angle measurement, the absolute value of R_h is not necessarily representative of the actual micelle radius as the scattering intensity is angle-dependent, and therefore Γ is angle-dependent as shown in Equation 2.12. Instead, the normalized change in radius, $R(t)$, is used to extract fragmentation time constants. $R(t)$ is calculated from Equation 2.17,

$$R(t) = \frac{\langle R_h \rangle_t - \langle R_h \rangle_f}{\langle R_h \rangle_0 - \langle R_h \rangle_f} \tag{2.17}$$

where $\langle R_h \rangle_0$ is the initial, as-prepared micelle radius and $\langle R_h \rangle_f$ is the steady-state micelle radius. Both $\langle R_h \rangle_0$ and $\langle R_h \rangle_f$ are measured using multi-angle DLS at room temperature before and after fragmentation, respectively. The fragmentation time, τ_{frag}, is determined by fitting $R(t)$ to a compressed exponential, shown in Equation 2.18,

$$R(t) = \exp[-(t / \tau_{frag})^n] \tag{2.18}$$

where t is the annealing time and n is the compression exponent. In this thesis and previous work of PB-PEO fragmentation in ILs, $n \approx 2$ is consistently obtained, as discussed in Chapters 3 – 6. Example data of the temperature dependence of $R(t)$ from high-temperature DLS experiment of 0.5 wt % BO(8-6) in [C_2mim][TFSI] is shown in Figure 2.13a.[91] The points represent the normalized change in R_h determined by Equation 2.17, and the solid lines represent fits to Equation 2.18. Figure 2.13b shows an Arrhenius plot of $\ln(\tau_{frag}/\eta)$ as

a function of inverse temperature, which is used to estimate the activation barrier for BO(8-6) micelle fragmentation.

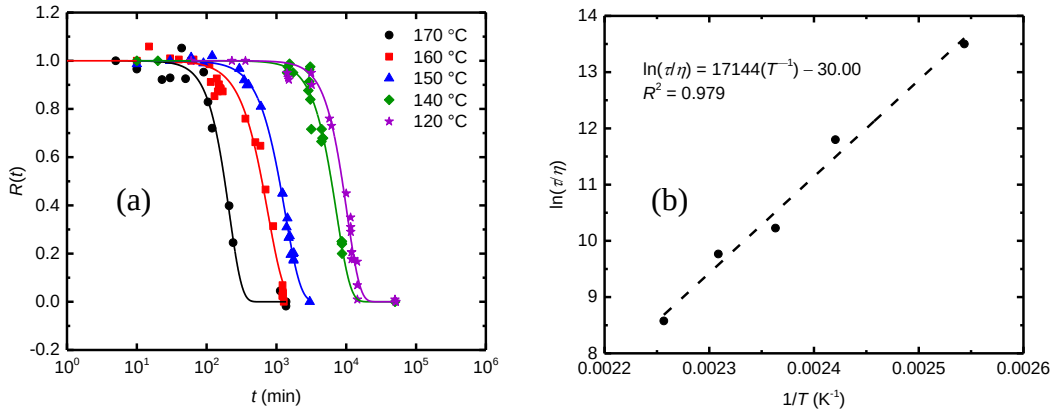

Figure 2.13: (a) High-temperature DLS results for 0.5 wt % BO(8-6) in [C_2mim][TFSI] at T = 170 °C (black circles), 160 °C (red squares), 150 °C (blue triangles), 140 °C (green diamonds), and 120 °C (purple stars). Solid lines represent the best fits to Equation 2.18 with n fixed at 2. All scattering measurements were obtained at θ = 90°. (b) Arrhenius plot for 0.5 wt % BO(8-6) in [C_2mim][TFSI]. The insert shows the equation obtained by best linear fit to the data, where the activation barrier, E_a, for fragmentation is 143 kJ/mol. Reproduced from Reference 91.

2.5 – Small-angle X-ray scattering (SAXS)

The use of light scattering in combination with SAXS allows for the determination of detailed molecular and structural information during the micelle relaxation process. When applying perturbations like T-jumps to the micelle system, it is critical to understand if any structural changes occur during this process.

2.5.1 – Theory

In SAXS, a collimated beam of X-rays hits the sample, and X-rays that are elastically scattered by the sample are detected at a fixed range of angles. This results in the formation of a scattering pattern. Contrast in SAXS arises from the differences in electron density; for a block copolymer in an IL solvent, each block, as well as the solvent, will have different contrast with respect to one another. The intensity, $I(q)$, of detected scattering for a given technique, be it light, X-rays, or neutrons, can be calculated via Equation 2.19

$$I(q) = \text{contrast}(S(q)) \tag{2.19}$$

$$\text{contrast(SAXS)} = V_{\text{ref}}\left[\left(\frac{b_1}{V_1}\right) - \left(\frac{b_2}{V_2}\right)\right]^2 \tag{2.20}$$

where the contrast is determined as shown in Equation 2.20 for X-ray scattering. In Equation 2.20, V_{ref} is the solvent reference volume, $b = \sum_{\text{atom}} z r_e$, where z is the atomic number, and r_e is the radius of an electron (2.81×10^{-13} cm), and V_1 and V_2 are the volumes of each block in the copolymer. From Equation 2.19, the scattered intensity is a function of q, which is defined by Equation 2.13, and the structure factor, $S(q)$.

The small angle scattering intensity for an isotropic solution of disperse spherical micelles may be written per the decoupling approximation as shown in Equation 2.21,[152]

$$I(q) = \text{contrast}(P(q)S(q)) \tag{2.21}$$

where $P(q)$ is the block copolymer micelle form factor. For concentrated micelle solutions, where inter-micelle interactions contribute to the scattering intensity, $S(q)$ is defined by the the hard-sphere structure factor with the Percus-Yevick closure. For dilute micelle solutions, *i.e.*, concentrations below the micelle overlap concentration, $S(q)$ goes to 1, and does not contribute to the solution scattering. In this work the form factor described by Pedersen *et al.*[153] is used. In the model described by Pedersen, the scattering intensity for a BCP micelle solution is defined by Equation 2.22,

$$I(q) = \int D(R_{\text{core}})\left[P_{\text{mic}}(q) + A^2_{\text{mic}}(q)(S(q)-1)\right]\text{d}R_{\text{core}} \tag{2.22}$$

where R_{core} is the micelle core radius with distribution $D(R_{\text{core}})$, $P_{\text{mic}}(q)$ is the spherical form factor for the micelle core[153] and $A_{\text{mic}}(q)$ is the form factor amplitude. Micelle polydispersity is introduced to Equation 2.22 from the term $D(R_{\text{core}}) = \exp[-(R_{\text{core}} - \langle R_{\text{core}}\rangle)^2/\sigma_{\text{core}}{}^2]/\sqrt{2\pi\sigma_{\text{core}}}$ for $R_{\text{core}} > 0$. $P_{\text{mic}}(q)$ is defined by Equation 2.23,

$$\begin{aligned} P_{\text{mic}}(q) = {} & Q^2\beta^2_{\text{core}}P_{\text{core}}(q) + Q\beta^2_{\text{corona}}P_{\text{corona}}(q) \\ & + 2Q^2\beta_{\text{core}}\beta_{\text{corona}}S_{\text{core-corona}}(q) \\ & + Q(Q-1)\beta^2_{\text{corona}}S_{\text{corona-corona}}(q) \end{aligned} \tag{2.23}$$

where $Q = (4\pi R_{\text{core}}{}^3)/(3V_{\text{core}})$, is the aggregation number calculated assuming the core is devoid of solvent, $V_{\text{core}} = M_{\text{n,core}}/\rho N_{\text{Av}}$, and β_i is the excess scattering length density of the

core or corona chains. In Equation 2.23 the first term represents the core chain self-correlations, the second term represents the corona chain self-correlations, the third term represents the core-corona chain correlations, and the fourth term represents intra-micelle corona-corona interactions. $P_{\text{core}}(q)$ is form factor for the contribution from a spherical homogeneous core of radius R_{core}, given by Equation 2.24,

$$P_{\text{core}}(q) = \left[\frac{3(\sin(qR_{\text{core}}) - qR_{\text{core}}\cos(qR_{\text{core}})}{(qR_{\text{core}})^3} \right]^2 \exp(-q^2\sigma^2) \tag{2.24}$$

where σ describes the width of the core-corona interface. In the corona self-correlation term, $P_{\text{corona}}(q)$ is given by the Debye function for a Gaussian chain with a radius of gyration R_{g}.

$$P_{\text{corona}}(q) = \frac{2[\exp(-q^2R_{\text{g}}^2) - 1 + q^2R_{\text{g}}^2]}{(q^2R_{\text{g}}^2)^2} \tag{2.25}$$

The core-corona correlations and inter-micelle interaction terms are described by Equations 2.26 and 2.27.

$$\begin{aligned} S_{\text{core-corona}}(q) = &\left[\frac{3(\sin(qR_{\text{core}}) - qR_{\text{core}}\cos(qR_{\text{core}})}{(qR_{\text{core}})^3} \right] \left[\frac{1 - \exp(-q^2R_{\text{g}}^2)}{(q^2R_{\text{g}}^2)^2} \right] \\ &\times \exp(-q^2\sigma^2/2) \frac{\sin\left[q(d + R_{\text{core}})\right]}{\left[q(d + R_{\text{core}})\right]} \end{aligned} \tag{2.26}$$

$$S_{\text{corona-corona}}(q) = \left[\frac{1-\exp(-q^2R_g^2)}{(q^2R_g^2)^2}\right]^2 \left[\frac{\sin\left[q(d+R_{\text{core}})\right]}{\left[q(d+R_{\text{core}})\right]}\right]^2 \quad (2.27)$$

2.5.2 – *Ex-situ* SAXS

Ex-situ SAXS experiments in Chapters 3 and 6 were conducted at the 5-ID-D beamline of the Dupont-Northwestern-Dow Collaborative Access Team (DND-CAT) at the Advanced Photon Source, Argonne National Laboratory. Micelle solutions of 0.5 wt % BO(8-6) were passed through 0.45 μm PTFE syringe filters to remove any dust or large aggregates, and subsequently flame-sealed under vacuum (≤ 70 mTorr) in a glass tube to prevent degradation of the block copolymer and to avoid contact with moisture and dust. The glass tubes were submerged in an oil bath at T = 170 °C and held at this temperature for the specified amount of time. Each glass tube was quenched to room temperature in a water bath to obtain a time-point sample for *ex-situ* SAXS. At room temperature the activation barrier to fragmentation is large enough where essentially no fragmentation takes place at room temperature on a reasonable timescale (*i.e.*, no change in micelle size for the as-prepared by DD solutions was observed when samples were stored at room temperature for approximately three months). The glass tubes were opened and taken into a glove box to load the micelle solutions into 1.5 mm diameter borosilicate capillaries (Charles Supper Co.), sealed with epoxy under an argon atmosphere, and then placed into a 16-capillary ambient temperature stage. SAXS measurements were conducted at room temperature. Two-dimensional scattering patterns were obtained using a Rayonix MX170-HS CCD area

detector using a 0.5 s exposure time to 17.0 keV X-rays with a wavelength of λ = 0.729 Å and a sample-to-detector distance of 8.5 m. The 2D data were azimuthally averaged to yield 1D scattering patterns as intensity versus q. The incoherent background (*i.e.*, IL and capillary scattering) exhibits a slight upturn at higher q values for the ionic liquids [C_6mim][TFSI] and [C_8mim][TFSI], which corresponds to nanometer length scale ordering within the IL itself.[154–156] The incoherent background was fit to a power law ($I(q) = A + Bq^{-m} + Cq^2$, where $2 \leq m \leq 4$) and subtracted from the solution scattering data.[154] For the solvents [C_1mim][TFSI], [C_2mim][TFSI], and [C_4mim][TFSI] no upturn at higher q is observed, and these solvents are fit to a power law equation where the constant C is equal to zero. The background-corrected intensity traces were analyzed using the Pedersen model for block copolymer micelles with the Percus-Yevick structure factor.[153,157] SAXS fitting was conducted in Igor Pro 8 software using a fitting routine based on the Pedersen BCP micelle form factor model described in Equations 2.22 – 2.27.

Ex-situ SAXS data for BO(8-6) in [C_4mim][TFSI], [C_6mim][TFSI], and [C_8mim][TFSI] are shown in Figures 2.14 – 2.16.[91] Scattering curves for BO(8-6) in [C_1mim][TFSI] and [C_2mim][TFSI] are discussed in Chapter 3. The scattering intensity traces are shifted vertically for clarity. From the figures, the shift in the first minimum of the form factor, q_{min}, to larger values of q as a function of annealing time is indicative of a decrease in R_{core}, based on the hard sphere approximation where qR = 4.493. As evidenced by Figures 2.14 – 2.16, the micelle core radius decreases with annealing time, indicative of fragmentation.

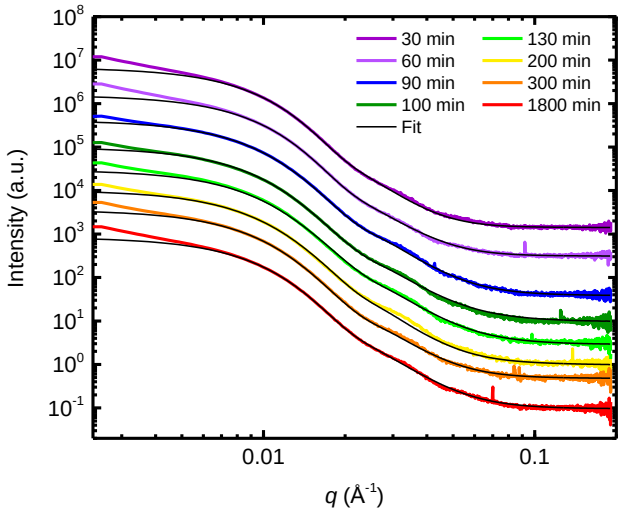

Figure 2.14: Structural evolution of 0.5 wt % BO(8-6) in [C_4mim][TFSI] during a *T*-jump to 170 °C by SAXS curves fit to the Pedersen model (solid black lines). The curves are shifted vertically for clarity. Measurements were acquired at room temperature after quenching each sample in a room temperature water bath. Reproduced from Reference 91.

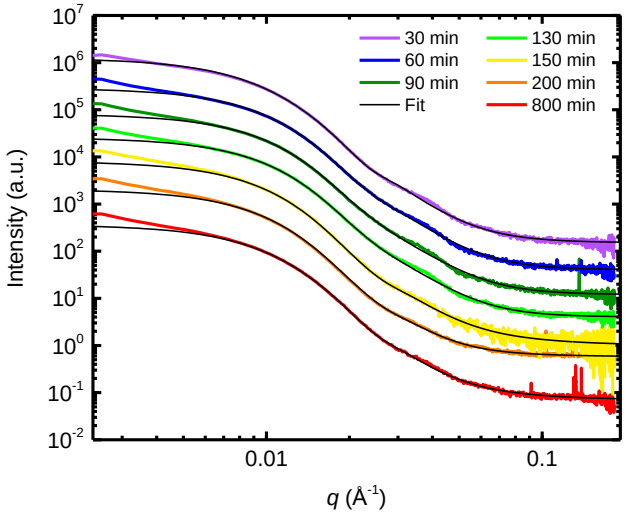

Figure 2.15: Structural evolution of 0.5 wt % BO(8-6) in [C_6mim][TFSI] during a *T*-jump to 170 °C by SAXS curves fit to the Pedersen model (solid black lines). The curves are

shifted vertically for clarity. Measurements were acquired at room temperature after quenching each sample in a room temperature water bath. Reproduced from Reference 91.

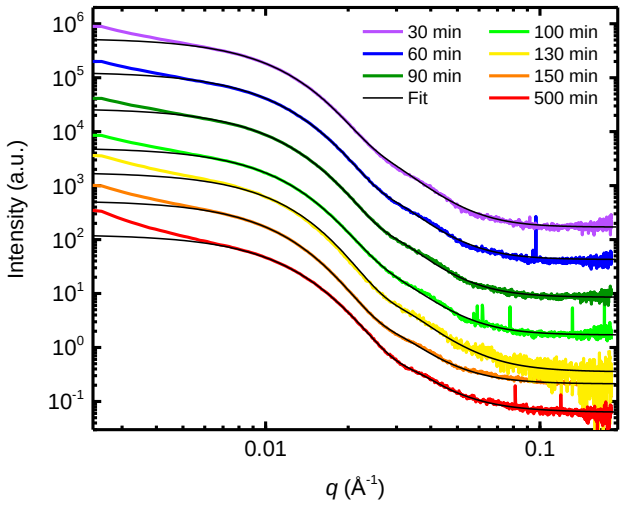

Figure 2.16: Structural evolution of 0.5 wt % BO(8-6) in [C_8mim][TFSI] during a *T*-jump to 170 °C by SAXS curves fit to the Pedersen model (solid black lines). The curves are shifted vertically for clarity. Measurements were acquired at room temperature after quenching each sample in a room temperature water bath. Reproduced from Reference 91.

2.5.3 – Time-resolved SAXS (TR-SAXS)

TR-SAXS experiments discussed in Chapters 4 and 5 were conducted at the 11-BM Complex Materials Scattering (CMS) beamline at the National Synchrotron Light Source II (NSLS-II), Brookhaven National Laboratory. Samples of 0.25 wt% PB-PEO directly dissolved in [C_2mim][TFSI] were syringe-filtered into 1.5 mm diameter borosilicate capillaries (Charles Supper Co.) and then placed into a custom 15-capillary temperature-controlled stage. SAXS measurements were conducted with samples under dynamic vacuum at room temperature and 170 °C. Two-dimensional scattering patterns were

obtained using a Dectris Pilatus 300k pixel-array detector (pixel size 172 μm × 172 μm) using a 30 s exposure time to 13.5 keV X-rays (λ = 0.918 Å) and a sample-to-detector distance of 2 m. The position where the incident beam hits the capillary was changed with each sample measurement by raising the sample stage throughout a time-resolved experiment to mitigate possible beam damage effects. The scattering vector q was calibrated using silver behenate. The 2D data were azimuthally averaged to yield 1D scattering patterns as intensity versus q. Due to the presence of higher q upturns in ionic liquid scattering, which has been observed previously in *ex-situ* SAXS, and significant capillary-to-capillary variations, the background (*i.e.*, IL and capillary scattering) was fit to a power law ($I(q) = A + Bq^{-m}$, where $2 \leq m \leq 4$) and subtracted from the solution scattering data.[154] The background-corrected intensity traces were fit using an established block copolymer micelle model.[153,157] SAXS fitting was conducted in Igor Pro 8 software using a fitting routine based on the Pedersen BCP micelle form factor model described in Equations 2.22 – 2.27.

Representative TR-SAXS curves are shown for two molar masses of 0.25 wt % BO(x-y) in [C_2mim][TFSI] in Figures 2.17b and 2.18b.[139] Additional TR-SAXS results for other BO(x-y) copolymers are discussed in Chapters 4 and 5. From the hard sphere approximation, the first minimum in the micelle form factor can be used to estimate R_{core} based on $R_{core} = 4.493/q_{min}$; this quantity was used to extract kinetic information from a TR-SAXS experiment. The scattering data before and after annealing at 170 °C were

obtained at 27 °C and fit to the Pedersen model described previously, and the curves for two BO(x-y) diblocks are shown in Figures 2.17a and 2.18a.[92]

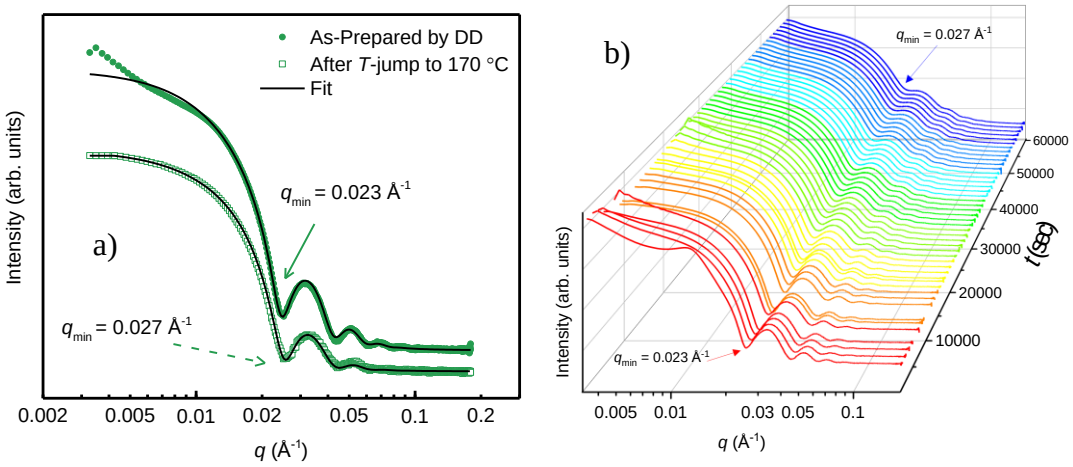

Figure 2.17: (a) SAXS of 0.25 wt % BO(8-7) in [C_2mim][TFSI] as-prepared by direct dissolution (filled green circles) and steady-state after a *T*-jump to 170 °C (open green squares). The scattering data were fit to the Pedersen model (black lines) and were vertically shifted for clarity. (b) TR-SAXS intensity (logarithmic scale) as a function of *q* for 0.25 wt % BO(8-7) in [C_2mim][TFSI] showing the evolution in the micelle core radius during annealing at 170 °C. The position of the first minimum in the form factor increases from q_{min} = 0.023 Å^{-1} for short annealing times to q_{min} = 0.027 Å^{-1} at longer annealing times. The PB core radius is estimated assuming a hard sphere ($R_{core} \cong 4.493/q_{min}$), so the radius of the micelle core decreases with increasing annealing time. Reproduced from References 92 and 139, respectively.

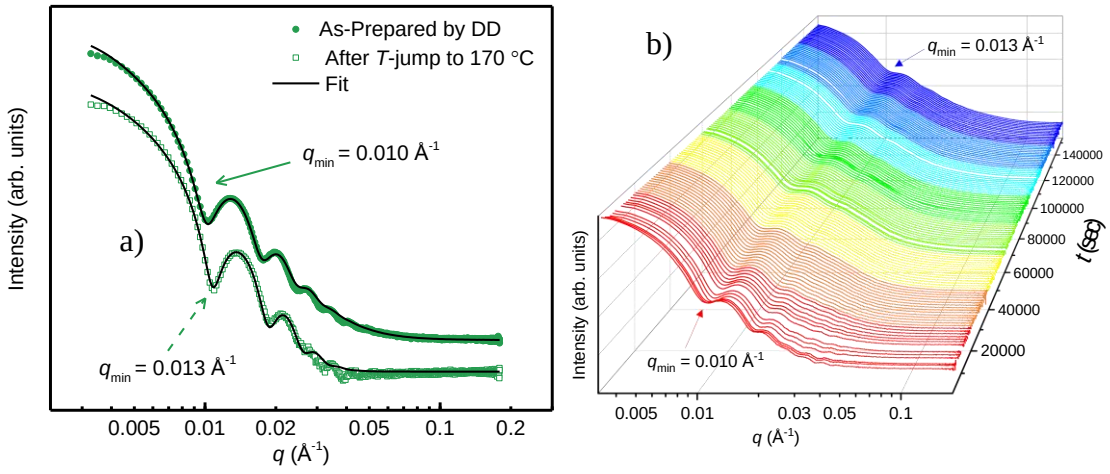

Figure 2.18: (a) SAXS of 0.25 wt % BO(25-22) in [C2mim][TFSI] as-prepared by direct dissolution (filled green circles) and steady-state after a *T*-jump to 170 °C (open green squares). The scattering data were fit to the Pedersen model (black lines) and were vertically shifted for clarity. (b) TR-SAXS intensity (logarithmic scale) as a function of q for 0.25 wt % BO(25-22) in [C2mim][TFSI] showing the evolution in the micelle core radius during annealing at 170 °C. The position of the first minimum in the form factor increases from q_{min} = 0.023 Å^{-1} for short annealing times to q_{min} = 0.027 Å^{-1} at longer annealing times. The PB core radius is estimated assuming a hard sphere ($R_{core} \cong 4.493/q_{min}$), so the radius of the micelle core decreases with increasing annealing time. Reproduced from References 92 and 139, respectively.

2.6 – Transmission electron microscopy (TEM)

In this work, we exploit the high thermal stability and non-volatility of ionic liquids to conduct high-temperature LP-TEM to observe *in-situ* fragmentation of PB-PEO micelles in [C2mim][TFSI]. Because the ionic liquid does not evaporate under the high vacuum conditions in the microscope, liquid samples can be imaged directly without the need for a

hermetically sealed sample chamber.[133,158–160] Using a temperature-controlled sample holder for LP-TEM allows *T*-jump experiments to be conducted directly in the microscope, and images of the change in the PB core morphology during fragmentation were collected.

TEM is a powerful tool used to visualize small structures at length scales on the order of 100 nm down to 1 Å. TEM is analogous to optical microscopy, but its high resolution lies in the use of electrons. Electrons have a much shorter wavelength than visible light, and the fine resolution obtained by TEM is due to the short de Broglie wavelength of electrons. In TEM, the electron source illuminates a very thin specimen (~ 100 nm thick). The transmitted beam is magnified and focused using a series of electromagnetic lenses, and then projected on a detector to observe the resulting image. In TEM imaging, there are two primary modes for sample observation, which depends on whether you are viewing the bright central spot of the direct electron beam, or whether you are using the scattered electrons to form the image. Bright-field imaging uses the direct beam to form an image, whereas dark-field imaging forms an image from electrons that are not in the direct beam, *i.e.*, the scattered electrons. In bright-field imaging, the sample will appear dark, as less electrons were transmitted through the sample, and the "field" or the electron beam itself appears bright. In dark-field imaging, the image is formed by electrons diffracted from a specimen, thus the sample appears bright, as this is what is scattering electrons, whereas the field appears dark.[161] In this work, bright-field imaging is utilized to view the micelle core in ILs.

In TEM, all images are a two-dimensional projection of a three-dimensional object. Contrast in the image is achieved by three mechanisms, namely, mass/thickness, diffraction, and phase contrast. Mass/thickness contrast arises from differences in the material the beam passes through, resulting in differences in the incoherent elastic scattering. Diffraction contrast occurs from crystalline regions of the sample that scatter electrons, and the objective aperture is used to remove scattered electrons from the image. Phase contrast occurs due to differences in the phase of the electron waves scattered through a thin specimen. Phase contrast is very sensitive to many factors including the small variations in sample thickness, orientation, and the variations in focus or astigmatism of the objective lens.[161] Phase contrast is commonly exploited for detailed imaging of the atomic structure of a thin specimen. For micelles in ionic liquids, the primary contrast mechanism is mass/thickness contrast due to the "heavier" atoms present in the ionic liquids, which results in the IL appearing dark and the micelle core appearing light.

An additional benefit of using ILs is that they have negligible vapor pressures and extremely high boiling points.[140] These properties were exploited here for imaging BO micelles in the solution state by LP-TEM, which allowed for detailed analysis of the evolution of the micelle core size following a *T*-jump to 170 °C. The core radius is not expected to change significantly by chain exchange alone, so the ability to measure the PB core size throughout the equilibration process provides more direct evidence of micelle fragmentation.

2.6.1 – *Ex-situ* liquid-phase TEM (LP-TEM)

Ex-situ LP-TEM was used in Chapters 3 and 6 to determine the average micelle core radius, $\langle R_{core} \rangle$, and the standard deviation of the core size, σ_{core}, at different time points during an annealing experiment. Each sample was passed through a 0.45 μm PTFE syringe filter to remove any dust or large aggregates, and subsequently flame-sealed under vacuum ($\leq$ 70 mTorr) in a glass tube to prevent degradation of the block copolymer and to avoid contact with moisture and dust. The glass tubes were submerged in an oil bath at T = 170 °C and held at this temperature for the specified amount of time. Each glass tube was quenched to room temperature in a water bath and opened to obtain a time-point sample for LP-TEM imaging. Prior to imaging each sample, the solutions were degassed under vacuum (< 100 mTorr) for at least 20 min to prevent the appearance of air bubbles in the sample, and then immediately imaged. Approximately 0.5 μL of solution was placed on a 200 mesh copper grid coated with lacey Formvar stabilized with carbon (Ted Pella Inc.), and the excess solution was manually blotted from below the grid with filter paper until a thin film was left spanning the holes of the lacey carbon support film. The images were obtained at ambient temperatures using a FEI Tecnai G2 Spirit BioTWIN operating at an accelerating voltage of 120 kV with an Eagle 4-megapixel CCD camera, unless noted otherwise. To minimize any effects of electron beam damage, the samples were imaged with a spot size of 5 or larger, where the spot size is inversely related to the strength of the first condenser lens. When the strength of the first condenser lens is reduced, the beam

current reaching the sample is also reduced. $\langle R_{core} \rangle$ and σ_{core} were determined from measurements of at least 400 individual micelles using ImageJ software.

Representative *ex-situ* LP-TEM micrographs of BO(8-6) in [C_2mim][TFSI] are shown in Figure 2.19,[91] where the light colored spheres are the PB micelle cores and the dark region is the IL. Additional LP-TEM micrographs of BO(8-6) in other [$C_x$mim][TFSI] ILs are discussed in Chapter 3. All images were acquired at ambient temperature. Again, due to the high activation barrier for fragmentation at room temperature, the micelle solutions are annealed at 170 °C *ex-situ*, quenched to room temperature, which suspends any further fragmentation. The quenched time-point solutions were imaged by LP-TEM, and the images were analyzed by image analysis to obtain detailed information about the decrease $\langle R_{core} \rangle$ and σ_{core} as a function of annealing time.

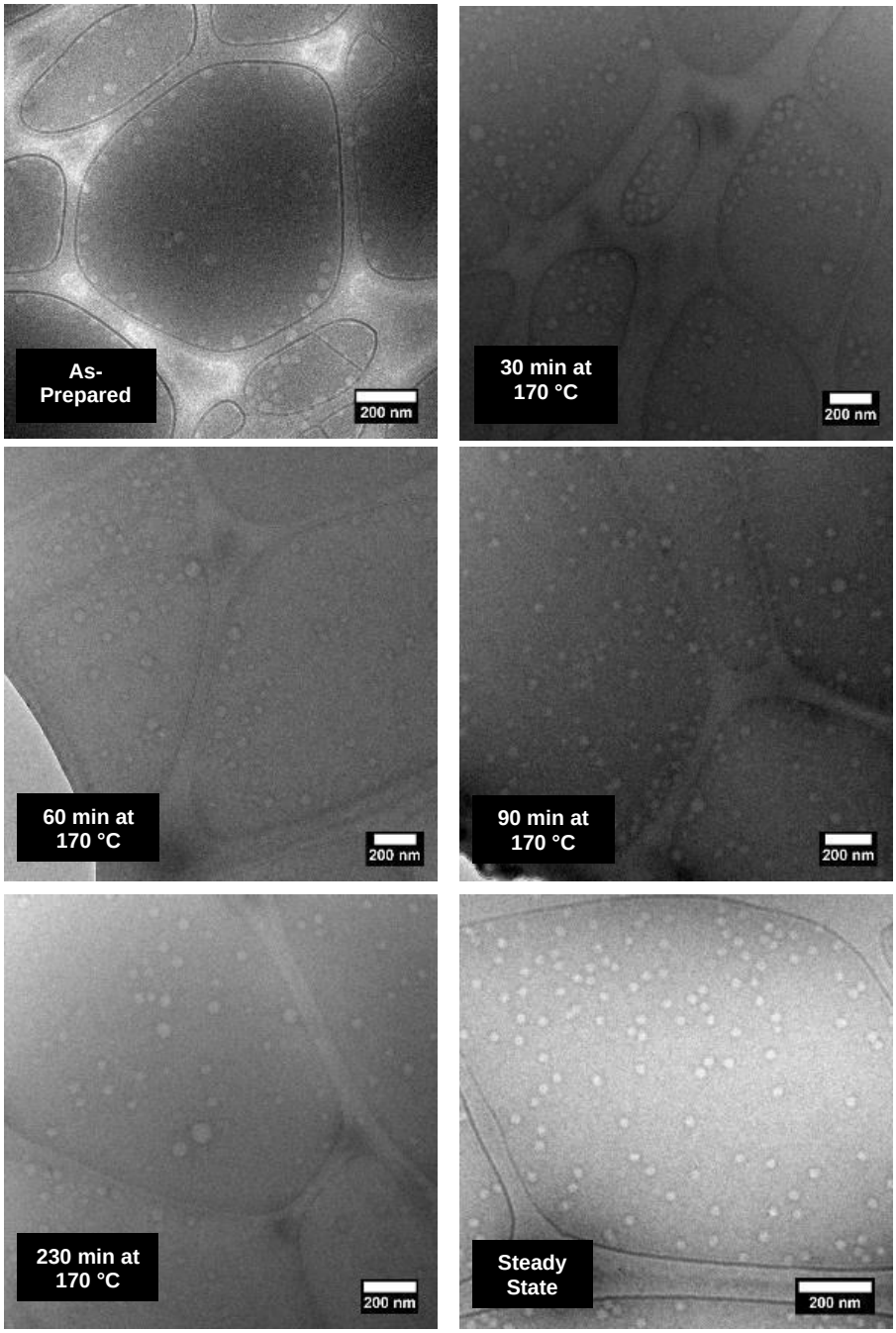

Figure 2.19: LP-TEM time points during a *T*-jump at 170 °C for 0.5 wt % BO(8-6) in [C_2mim][TFSI]. Reproduced from Reference 91.

2.6.2 – High-temperature LP-TEM

High-temperature LP-TEM was used in Chapters 4 and 5 to directly observe micelle fragmentation *in-situ*. $\langle R_{core} \rangle$ and σ_{core} at different time points during an annealing experiment (T = 170 °C) were determined *in-situ* using high-temperature LP-TEM. Approximately 0.5 μL of solution was placed on a 200 mesh copper grid coated with amorphous holey carbon (Quantifoil R1.2/1.3, Ted Pella Inc.), and the excess solution was manually blotted from below the grid with filter paper until a thin film was left spanning the holes of the holey carbon. It was found that the Formvar-coated lacey carbon support films grids used in *ex-situ* can degrade in the presence of heat, therefore, holey carbon is the preferred support film material for any high-temperature LP-TEM. The images were obtained at ambient temperatures and at 170 °C using a JEOL JEM 2100F operating at an accelerating voltage of 200 kV with a Gatan Ultrascan US1000 2k×2k CCD camera (exposure time = 0.5 sec). For high temperature imaging, samples were placed in a Gatan 652 double tilt heating holder, and the temperature was controlled with a Gatan hot stage controller. To minimize any effects of electron beam damage, the samples were imaged with a spot size of 3. The objective lens size was 100 μm and the first condenser lens size used was high contrast (HC) 30 μm. The electron dose rates were calculated using the beam current measured by the phosphorus screen of the JEOL JEM 2100F with the sample retracted and the objective lens removed, and the measured beam diameter at each magnification. $\langle R_{core} \rangle$ and σ_{core} were determined from measurements of at least 20 – 30 individual micelles using ImageJ software. Detailed image analysis to obtain the $\langle R_{core} \rangle$,

core area (A (nm^2)), eccentricity (ε) was performed using a custom open-source Python package (https://github.com/CFN-softbio/SciAnalysis). Representative high-temperature LP-TEM images of 0.25 wt % BO(8-7) in [C_2mim][TFSI] are shown in Figure 2.20.[92]

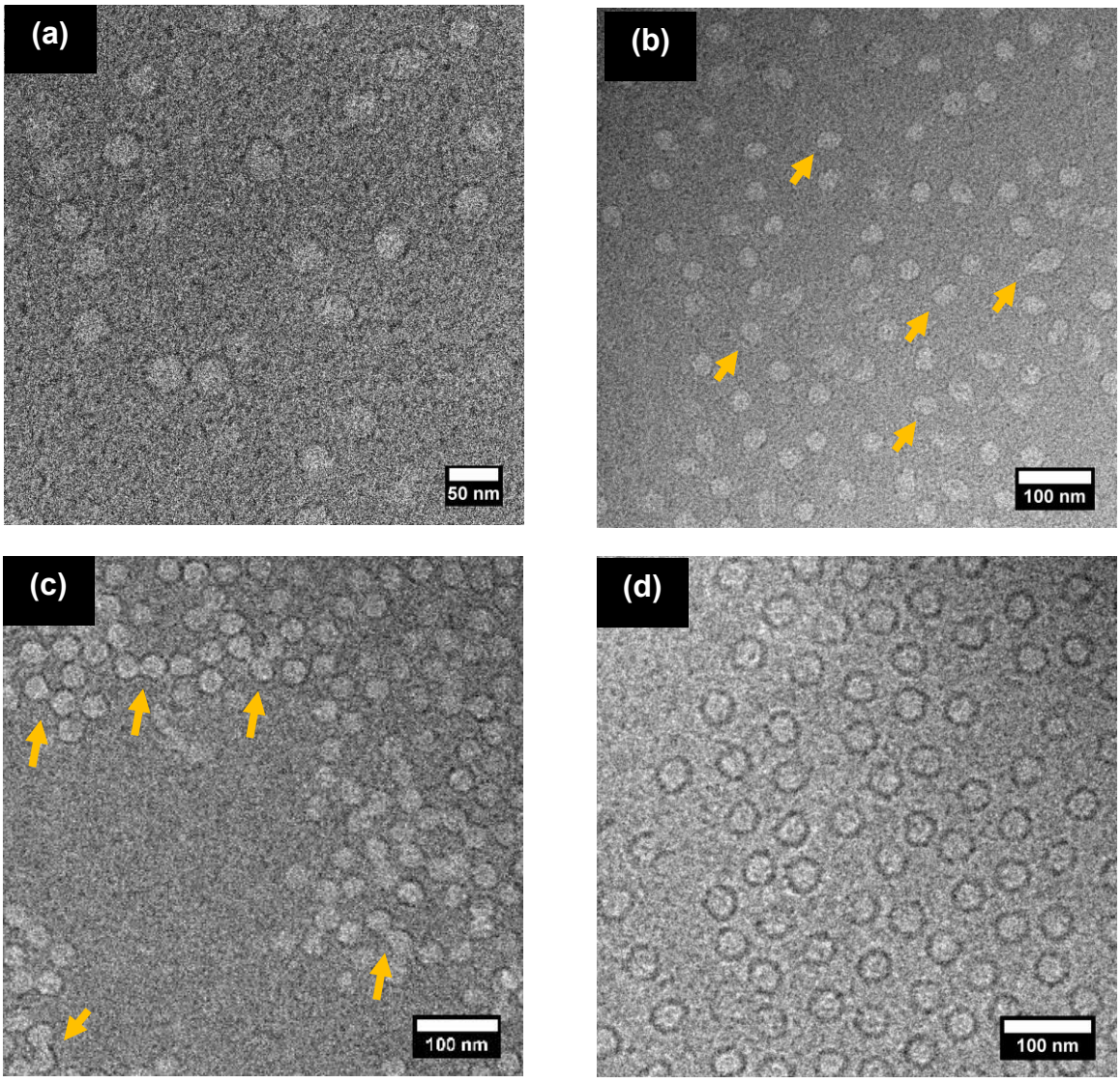

Figure 2.20: *In-situ* LP-TEM images of 0.25 wt % BO(8-7) in [C_2mim][TFSI] annealing at T = 170 °C for (a) 5 min, (b) 20 min, (c) 50 min, and (d) 100 min. Orange arrows indicate

micelles undergoing fragmentation as discussed in the text. The electron dose rate is 11.3 $e^{-}/Å^2s$ at a magnification of 20000×. Reproduced from Reference 92.

In Figure 2.20, the evolution of micelle core structure is observed directly at 170 °C during fragmentation, where (a) spherical micelle cores are observed, followed by (b) elongation of the micelles, (c) then a peanut shaped structure is observed, followed by (d) the separation of micelle cores into smaller, spherical micelles. The dose rate for Figure 2.20, obtained at a with a magnification of 20k× was 11.3 $e^{-}/Å^2s$.

2.6.3 – Bulk TEM

TEM of bulk PB-PEO copolymers was conducted in Chapter 7. This technique was used to gain a greater understanding of how the DD method yields kinetically trapped, spherical micelles, with $\langle R_{core} \rangle \approx d_{PB}$, where d_{PB} is the domain size of the PB lamellae in the bulk, swelling experiments were conducted on a PB-PEO film that was swelled with [C_2mim][TFSI] and imaged at 70 °C using LP-TEM. To obtain thin, well-ordered films of PB-PEO lamellae, the diblock copolymer was annealed in an aluminum DSC pan at 70 °C under vacuum (< 70 mTorr) for 72 h. PB-PEO was found to form a well-ordered lamellar structure in the bulk at temperatures ranging from 25 – 100 °C, however, PEO is semicrystalline ($T_{melt} \approx 60$ °C). To prevent crystallization of the PEO domains, the DSC pans containing PB-PEO were rapidly quenched in liquid nitrogen immediately after removing the samples from the vacuum oven to trap the structure of the PB-PEO lamellae. Then the samples were sectioned for TEM imaging via cryo-microtoming procedures

described here. The samples were sectioned at –80 °C with a Reichert UltraCut S Ultramicrotome system and transferred to 300 mesh Cu TEM grids. Then, ~ 6 μL of [C_2mim][TFSI] was added to the grid with the PB-PEO section, and the excess IL manually blotted from below the grid with filter paper until a thin film was left spanning the mesh of the copper TEM grid. The sample was imaged immediately after addition of IL using a FEI Tecnai T12 TEM operating at 120 kV with a double-tilt heating holder at 70 °C. A schematic illustration of this process is shown in Figure 2.21.

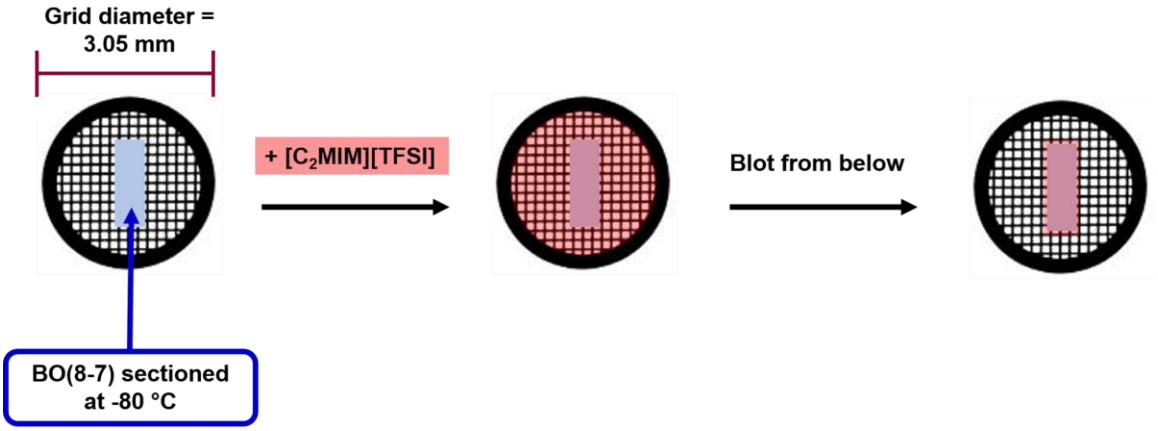

Figure 2.21: Schematic illustration of the grid preparation procedure used to image the behavior of PB-PEO lamellae swollen with [C_2mim][TFSI]. BO(8-7) was annealed in an aluminum DSC pan at 70 °C for 72 h and quenched to –170 °C in liquid nitrogen. PB-PEO was sectioned via cryo-microtoming at –80 °C and transferred to a 300-mesh copper TEM grid (diameter = 3.05 mm) to give sub-100 nm PB-PEO films. Approximately 9 μL of the IL was added to the grid via micro pipette, and excess IL was manually blotted using a piece of filter paper from below before transferring to a temperature-controlled TEM holder for imaging.

Chapter 3 – Effect of solvent selectivity on micelle fragmentation*

3.1 – Introduction

In this chapter, we exploit the approach used by Eisenberg *et al*.,[44,127,128] and later by Meli *et al.*,[89] who demonstrated that a range of micelle sizes could be obtained from a single block copolymer by changing the solution preparation method. Meli *et al*. prepared PB-PEO micelles in the ILs [C_2mim][TFSI] or [C_4mim][TFSI] by different dissolution methods. They noted that micelles formed by direct dissolution of PB-PEO into the IL formed large, polydisperse spherical aggregates, which decreased in size when subjected to annealing at elevated temperatures.[89,90] They showed that PB-PEO micelle relaxation in [C_2mim][TFSI] and [C_4mim][TFSI] was heavily dependent on temperature, but the timescale for micelle equilibration at 170 °C remained on the order of 10^3 seconds when changing the solvent from [C_2mim][TFSI] to [C_4mim][TFSI]. Analysis of this system by TR-SANS revealed that chain exchange did not occur up to at least 200 °C over the course of 24 h,[90] indicating that micelle equilibration must take place through some other

*Reprinted in part with permission from Early, J. T.; Lodge, T. P. Fragmentation of 1,2-Polybutadiene-*block*-Poly(ethylene oxide) Micelles in Imidazolium-Based Ionic Liquids. *Macromolecules* **2019**, *52*, 7089 – 7101.

mechanism(s). It was also found that the decay in PB-PEO micelle size is well described by a compressed exponential, as shown in Equation 2.18, with $n = 2$ in both ILs and at various annealing temperatures.[90] However, a physical interpretation for this compressed exponential behavior remains elusive. Although these results suggest that the primary relaxation mechanism in PB-PEO/[C_2mim][TFSI] is micelle fragmentation, there are several questions that remain unanswered, including the roles of solvent selectivity, initial micelle size, N_{core}, and N_{corona} in fragmentation kinetics.

To that end, a single PB-PEO block copolymer is studied here in five different [$C_x$mim][TFSI] ILs, where the same anion is used, but the length of the alkyl chain on the IL cation is varied. By changing the alkyl chain length, the selectivity towards the PB core block is tuned systematically, *i.e.*, the interfacial tension, which also influences the initial size of the micelles prepared by direct dissolution. Because larger micelles are formed initially in more selective solvents, the influence of micelle size, and how far the system is from the equilibrium size, was explored. As discussed in Section 1.3.3, studies on micellization kinetics use jumps in temperature,[104] pH,[108] or solvent[162] to perturb the system from equilibrium, and the time required to relax to equilibrium is determined by some detection method, such as light scattering. The method of *T*-jump DLS is used here to follow the evolution of R_h as a function of annealing time. When micelles equilibrate solely through chain exchange, the average R_h should not change much.[17] Conversely, R_h is expected to change considerably when fusion/fragmentation mechanisms dominate, so following the evolution of micelle size throughout annealing is essential.

An additional benefit of using ILs is that they have negligible vapor pressures and extremely high boiling points.[140] These properties were exploited here for imaging BO micelles in the solution state by LP-TEM, which allowed for detailed analysis of the evolution of the micelle core size following a *T*-jump to 170 °C. The core radius is not expected to change significantly by chain exchange alone, so the ability to measure the PB core size throughout the equilibration process provides more direct evidence of micelle fragmentation. To complement LP-TEM, SAXS was used to determine the micelle core radius and its distribution as a function of annealing time. From these combined techniques, the kinetics of fragmentation were determined for PB-PEO micelles in five different ILs.

3.2 – Materials and methods

Synthesis and Characterization. PB-PEO was synthesized previously by Dr. Luciana Meli using two-step sequential anionic polymerization, as described in Section 2.1.1.[136] The diblock copolymer will be referred to as BO(8-6), where the numbers in parentheses refer to the number average molar mass in kg/mol of each block, respectively. M_n, $Đ$, and f_{PEO} for BO(8-6) were determined by a combination of SEC-MALS (Wyatt Dawn Heleos II) and ^{1}H NMR spectroscopy in $CDCl_3$ (^{1}H NMR, Varian Inova 500). The d*n*/d*c* for the diblock was estimated as the weight average of the refractive index increments for PB in THF (d*n*/d*c* = 0.119 mL/g) and PEO in THF (d*n*/d*c* = 0.068 mL/g).[138] For BO(8-6) M_n is 14.6 kDa and $Đ$ = 1.10, with $M_{n,PB}$ = 8.2 kDa, $M_{n,PEO}$ = 6.4 kDa, and f_{PEO} = 0.37, as shown in Table 2.1. The SEC RI trace of BO(8-6) is shown in Figure 3.1.

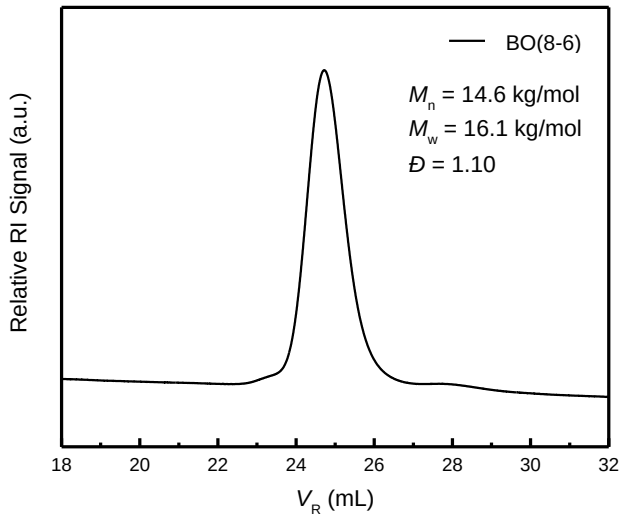

Figure 3.1: SEC RI trace of BO(8-6) in tetrahydrofuran.

The ILs [C_1mim][TFSI] 99% and [C_6mim][TFSI] 99.5% were purchased from IoLiTec. The ionic liquids [C_2mim][TFSI], [C_4mim][TFSI], and [C_8mim][TFSI] were synthesized according to Section 2.2.1.[141] All ILs were dried under vacuum (< 100 mTorr) at 60 °C for 72 h prior to use, and were characterized by ^{1}H, ^{13}C, and ^{19}F NMR spectroscopy in DMSO-d_6, as described in Section 2.2.2. The ^{1}H and ^{13}C NMR spectra for all ILs are shown in Figures 2.5 – 2.9. ^{19}F NMR spectra for all ILs is shown in Figure 2.10.

Thermal Equilibration in [C_2mim][TFSI]. The time required for thermal equilibration to reach 170 °C was determined in [C_2mim][TFSI]. An oil bath was heated to 170 °C and allowed to equilibrate for 30 min prior to placing the IL sample in the bath. Once the oil bath temperature was stabilized, 0.7 mL of [C_2mim][TFSI] was added to a glass tube, and a thermocouple was inserted into the IL tube to monitor the temperature. The initial temperature of the IL was recorded as 27.9 °C prior to submersion in the oil bath. Upon

submersion of the tube into the oil bath, the time required for the IL to reach 168 °C was measured to be ≤ 5 min.

Solution Preparation by DD. All solutions were prepared by the direct dissolution (DD) method described in Section 2.3.1, unless noted otherwise.

DLS. *T*-jump and multi-angle room temperature scattering measurements were performed according to Section 2.4.2.

***Ex-Situ* LP-TEM.** $\langle R_{core} \rangle$ and σ_{core} at different time points during an annealing experiment were determined using *ex-situ* LP-TEM, as described in Section 2.6.1.

***Ex-Situ* SAXS.** SAXS experiments were conducted according to *ex-situ* SAXS described in Section 2.5.2.

3.3 – Results and discussion

3.3.1 – Effect of micelle concentration

To determine the effect of concentration on micelle equilibration kinetics, a series of BO(8-6) solutions ranging from 0.05 wt % to 1.0 wt % in [C_2mim][TFSI] were prepared and studied by *T*-jump DLS at 170 °C. One indicator of micelle fusion is the presence of second-order kinetics with respect to micelle concentration, whereas fragmentation or chain exchange should be first-order.[97,120,163] It was found that the initial average micelle hydrodynamic radius, $\langle R_h \rangle_0$, for all concentrations prepared by the DD protocol were

relatively large ($\langle R_h \rangle_0 \approx 60 \pm 10$ nm) and disperse ($\mu_2/\overline{\Gamma}^2 \geq 0.18$). The evolution of the R_h distribution for 0.5 wt % BO(8-6) in [C_2mim][TFSI] during a *T*-jump to 170 °C is shown in Figure 3.2a, where the population is bimodal after 10 min of annealing at 170 °C with an $\langle R_h \rangle$ of 62 nm, and the distribution begins to narrow and shift to a smaller $\langle R_h \rangle$ after annealing for over 1000 min.

The $\langle R_h \rangle$ for all concentrations was determined by fitting the DLS autocorrelation functions to a second-order cumulant expansion, and these values were normalized by the initial value according to Equation 2.17 to compare the decay in $\langle R_h \rangle$ across all concentrations. In all cases $\langle R_h \rangle$ decayed more rapidly than a single exponential function, as shown in Figure 3.2b, leading to a steady-state size, $\langle R_h \rangle_f$, of 34 ± 4 nm. Note that relaxation curves for 0.5 wt %, 0.25 wt %, 0.1 wt %, and 0.05 wt % in Figure 3.2b are vertically shifted for clarity. In agreement with previous reports,[89,90] the normalized hydrodynamic radius as a function of annealing time, $R(t)$, could be well described by the Avrami equation, or compressed exponential, shown in Equation 2.18, with an exponent fixed at 2. When fits were performed with two adjustable paraments, τ_{frag} and n, the average value of the exponent was found to be equal to 2.2 ± 0.2.

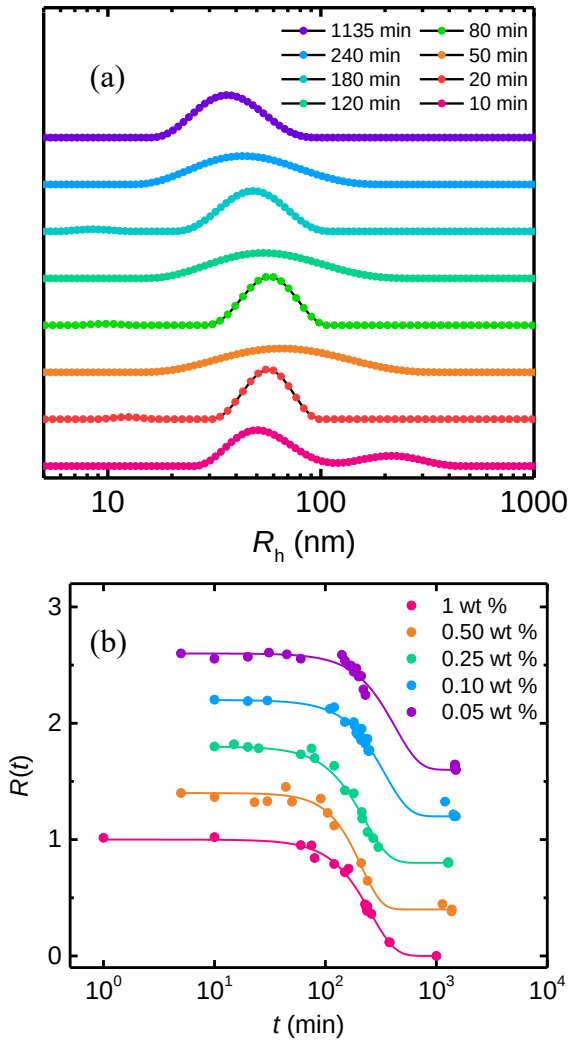

Figure 3.2: (a) REPES results for 0.5 wt % BO(8-6) in [C2mim][TFSI] after a *T*-jump to 170 °C. Light scattering measurements were performed at a scattering angle of 90°. (b) Time dependence of normalized R_h for BO(8-6) in [C2mim][TFSI] at various polymer concentrations, a scattering angle of 90°, and a relaxation temperature of 170 °C. Solid lines represent best fits to Equation 2.18, with $n = 2$.

The characteristic relaxation time τ_{frag} was obtained from fitting the *T*-jump DLS data to Equation 2.18, and the results are summarized in Table 3.1. It should be noted that the

time required for thermal equilibration (*ca*. 4 to 5 min) in [C_2mim][TFSI] is significantly shorter than the relaxation times observed here (on the order of hundreds of minutes). Therefore, we attribute these long relaxation times to the fragmentation of large, disperse spherical micelles formed by DD of BO(8-6) in ILs. The relaxation time only varies by at most a factor of two over a 20-fold variation in concentration, indicating that a first-order process is dominant. The relaxation times do increase very slightly with decreasing polymer concentration for polymer concentrations less than 1 wt %, which could indicate a minor contribution from a second-order kinetic process.[164]

Table 3.1: Concentration dependence of $\langle R_h \rangle$ and τ_{frag} determined by *T*-jump DLS at 170 °C for BO(8-6) in [C_2mim][TFSI]. Relaxation times were determined by Equation 2.18 with *n* fixed as 2.

Concentration (wt %)	$\langle R_h \rangle_0$ (nm)	$\langle \mu_2/\Gamma^2 \rangle_0$	$\langle R_h \rangle_f$ (nm)	$\langle \mu_2/\Gamma^2 \rangle_f$	τ_{frag} (min)
1	70	0.28	38	0.09	260 ± 40
0.5	85/62	bimodal	35	0.03	200 ± 20
0.25	58	0.22	35	0.09	240 ± 17
0.1	49	0.25	30	0.01	300 ± 82
0.05	58	0.18	30	0.01	440 ± 56

One process that could contribute to slightly concentration-dependent relaxation times is collisional aggregation and de-aggregation. When micelle solutions are prepared by the DD protocol, large aggregates consisting of multiple micelles could undergo some type of sticky-collisional interactions, and then disassociate upon heating. The time required for

micelle collisions would be expected to depend on polymer concentration, however, the time required for dissociation would not.[95,165] Such micelle collision and fusion events have been observed in the growth and evolution of amphiphilic block copolymers in water by TEM, and this process was reported to contribute to a concentration-dependent relaxation process.[123]

3.3.2 – Effect of solvent

To understand the influence of solvent selectivity on fragmentation kinetics, five [$C_x$mim][TFSI] ionic liquids were selected as PEO-selective solvents. In general, the longer the alkyl chain on the imidazolium cation, the less selective the IL, *i.e.*, the surface tension between the PB core block and the solvent decreases and the PB block is more solvated by the IL.[166–169] Thus, the five ionic liquids chosen here have alkyl chain lengths of one, two, four, six, and eight carbon chains. The effects of solvent selectivity on the relaxation time were investigated for 0.5 wt % BO(8-6) in these five ILs.

The time-dependent normalized hydrodynamic radii for 0.5 wt % BO(8-6) in the five ILs during a *T*-jump to 170 °C are shown in Figure 3.3. The dynamic traces obtained by DLS for 0.5 wt % BO(8-6) in four of the five ILs selected here were fit to Equation 2.18 with $n = 2$. However, relaxation in the most selective IL, [C_1mim][TFSI], was found to occur much more slowly than the other four ILs, and the relaxation in $\langle R_h \rangle$ was fit to Equation 2.18 with $n = 3.3$. To verify that $n = 2$ in [C_2mim][TFSI], [C_4mim][TFSI], [C_6mim][TFSI], and [C_8mim][TFSI], linear plots of log $R(t)$ versus t^2 are shown in Figure 3.4a. A non-linear curve is obtained for *T*-jump DLS results in [C_1mim][TFSI], shown in

Figure 3.4b. When fitting the time-dependent normalized hydrodynamic radii for 0.5 wt % BO(8-6) in [C$_2$mim][TFSI], [C$_4$mim][TFSI], [C$_6$mim][TFSI], and [C$_8$mim][TFSI] with two adjustable parameters, τ_{frag} and n, the $\langle n \rangle$ = 2.2 ± 0.1 for the four ILs, which again confirms that the exponent is essentially 2 in these solvents.

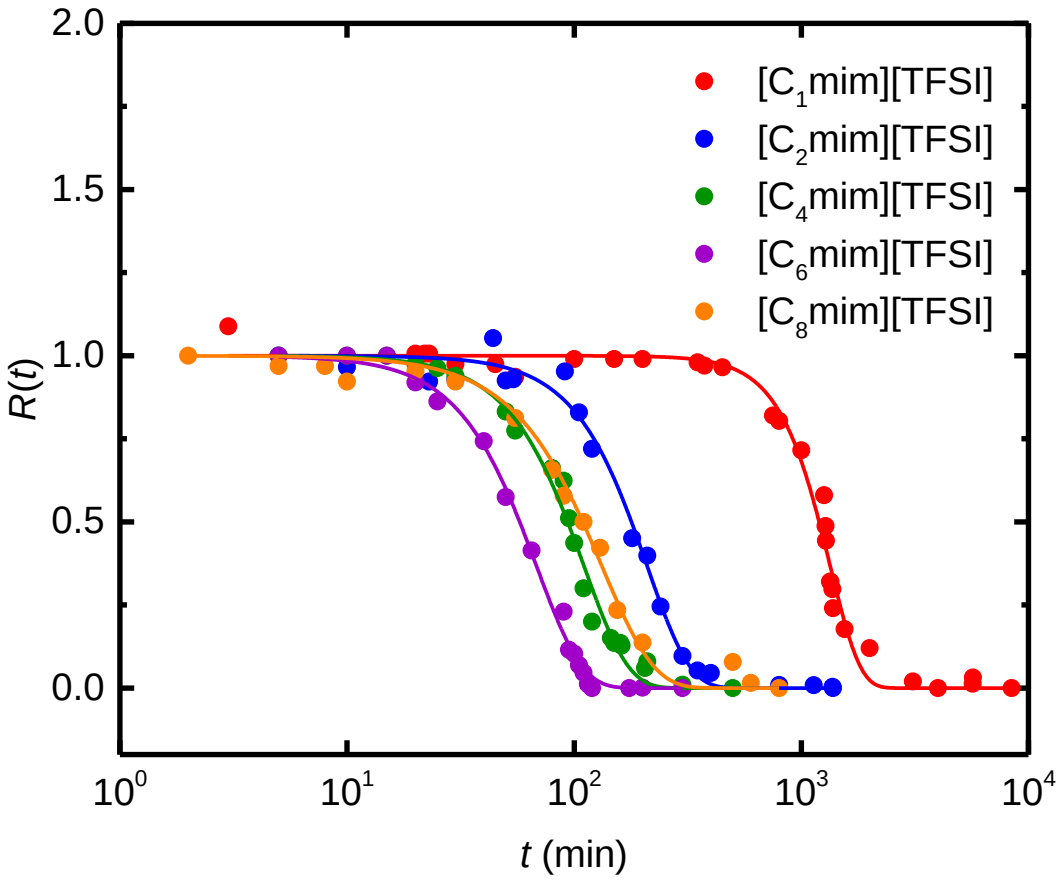

Figure 3.3: Time-dependent normalized hydrodynamic radii for 0.5 wt % BO(8-6) in [C$_x$mim][TFSI] ILs. Solid lines represent the best fits to the relaxation function shown in Equation 2.18, with n = 2 for all ILs except [C$_1$mim][TFSI], where n = 3.3. DLS measurements were performed at a temperature of 170 °C and a scattering angle of 90°.

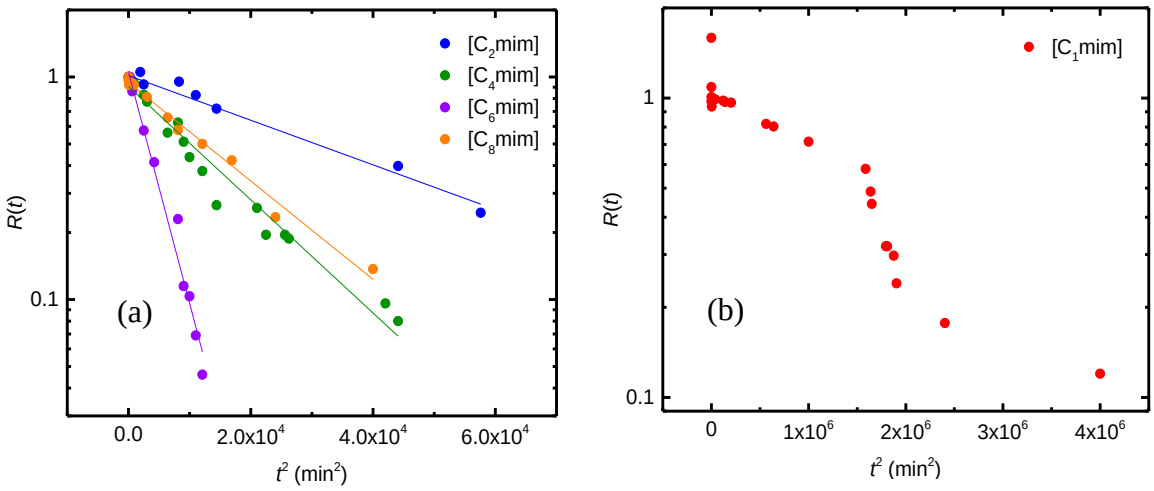

Figure 3.4: (a) Linearized *T*-jump DLS results for 0.5 wt % BO(8-6) in [C2mim][TFSI], [C4mim][TFSI], [C6mim][TFSI], and [C8mim][TFSI]. After fitting the data with two adjustable parameters, it was found that $\langle n \rangle$ = 2.17 ± 0.21. When fitting $R(t)$ with two adjustable parameters, the exponents for [C2mim][TFSI], [C4mim][TFSI], [C6mim][TFSI], and [C8mim][TFSI] were n = 2.4, 2.2, 2.1, and 1.9, respectively. (b) Non-linear $R(t)$ versus t^2 (from DLS) for 0.5 wt % BO (8-6) in [C1mim][TFSI] indicates that $R(t)$ is not well described by a compressed exponential.

Table 3.2 summarizes the fitting results of *T*-jump DLS at 170 °C, along with $\langle R_h \rangle$ and the radius dispersity before and after the *T*-jump to 170 °C. When preparing micelle solutions by DD, $\langle R_h \rangle_0$ is expected to decrease as the cation alkyl chain length is increased because the solvent becomes less selective for the PEO block. Based on the solubility parameters of the PB (δ = 17.4 MPa$^{1/2}$)[138] and PEO (δ = 20.2 MPa$^{1/2}$)[138] blocks at T = 298 K, the largest aggregates would be formed by direct dissolution in [C1mim][TFSI] or [C2mim][TFSI] (δ = 27.6 MPa$^{1/2}$)[166] and the smallest aggregates should form by direct dissolution in [C8mim][TFSI] (δ = 25.0 MPa$^{1/2}$).[166] The results in Table 3.2 are consistent

with this expectation, in that $\langle R_h \rangle_0$ = 79 nm in [C_1mim][TFSI] and $\langle R_h \rangle_0$ = 38 nm in [C_8mim][TFSI].

Table 3.2: $\langle R_h \rangle$ and τ_{frag} determined by *T*-jump DLS at 170 °C for 0.5 wt % BO(8-6) in imidazolium-based ionic liquids. The relaxation times were determined by Equation 2.18.

IL Cation	$\langle R_h \rangle_0$ (nm)	$\langle \mu_2/\Gamma^2 \rangle_0$	$\langle R_h \rangle_f$ (nm)	$\langle \mu_2/\Gamma^2 \rangle_f$	*n*	τ_{frag} (min)
[C_1mim]	79	0.24	39	0.13	3.3	1340 ± 220
[C_2mim]	85/62	bimodal	35	0.03	2.4	200 ± 20
[C_4mim]	51	0.19	34	0.13	2.2	110 ± 30
[C_6mim]	43	0.12	34	0.01	2.1	70 ± 15
[C_8mim]	38	0.17	32	0.01	1.9	130 ± 22

As expected, the initial size of the micelles, determined by multi-angle DLS at room temperature prior to a *T*-jump, decreased when the solvent quality of the IL towards the PB core becomes less poor. Surprisingly, the kinetics of fragmentation seem to be very similar for most of the ILs used here, except possibly for [C_1mim][TFSI]; we consider this to be an outlier due to the SAXS and LP-TEM data, as will be discussed in subsequent sections.

To further investigate the process of fragmentation, *ex-situ* LP-TEM and SAXS were used to follow the evolution of $\langle R_{core} \rangle$ following a *T*-jump to 170 °C. Previous works have used SAXS to study the kinetics of globule-to-cylinder transitions,[43] the ordering kinetics

of micelle-forming block copolymers,[170] and the time-dependent evolution of block copolymer micelles in THF/water mixtures.[113] This technique proves extremely useful in that specific structural details of the micelles such as the core radius, corona thickness, dispersity of the core, and the aggregation number can be obtained by fitting $I(q)$ to analytical models.[157,171,172] In addition to SAXS, TEM is an valuable technique for determining micelle morphology, including quantifying the core radius and its distribution as a function of time.

Ex-situ SAXS curves for 0.5 wt % BO(8-6) micelles prepared by DD in [C_1mim][TFSI] and [C_2mim][TFSI] are shown in Figures 3.5a and 3.5b, respectively. SAXS data for 0.5 wt % BO(8-6) in [C_4mim][TFSI], [C_6mim][TFSI], and [C_8mim][TFSI] are shown in Figures 2.14 – 2.16. In the figures, the dark purple traces indicate the first time point (30 min) obtained for these samples, *i.e.*, the sample was annealed at 170 °C for 30 min before quenching to room temperature and loaded into glass capillaries for SAXS. This process was repeated for all indicated time points. From the scattering patterns shown in Figures 3.5a and 3.5b, the average micelle core radius decreases substantially upon annealing at 170 °C. The q value of the first minimum in the SAXS curves is inversely proportional to the micelle core radius.[157,172] The first minimum in Figures 3.5a and 3.5b shift to larger q values with time, indicative of a decrease in $\langle R_{core} \rangle$.

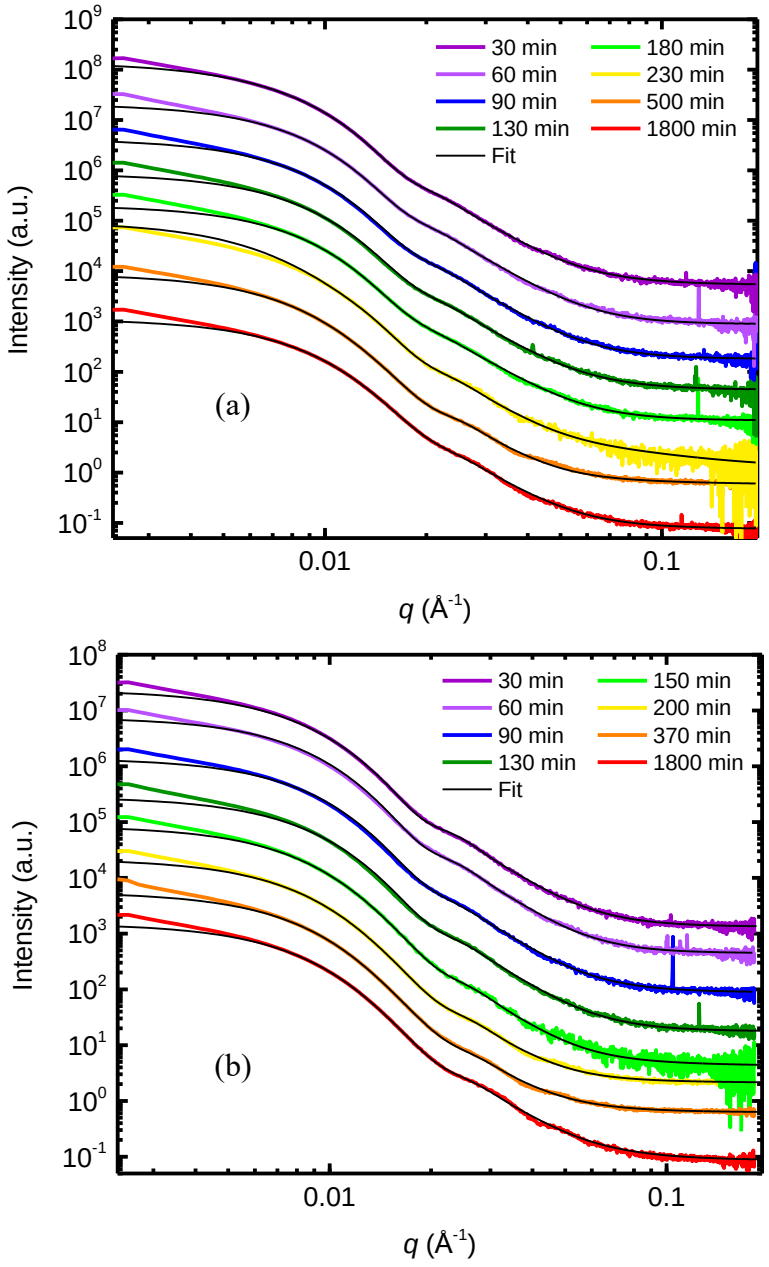

Figure 3.5: Structural evolution of 0.5 wt % BO(8-6) (a) in [C_1mim][TFSI] and (b) in [C_2mim][TFSI] upon *T*-jump to 170 °C by TR-SAXS curves fit to the Pedersen model (solid black lines). The curves are shifted vertically for clarity. Measurements were acquired at room temperature after quenching each sample in a water bath.

The time evolution of $\langle R_{core} \rangle$ from SAXS in the five ILs was also fit to the Avrami equation. Normalization of $\langle R_{core} \rangle$ was carried out as in the *T*-jump DLS data analysis, where $R(t)$ is calculated according to Equation 2.17. Figure 3.6 shows the normalized core radii from SAXS as determined by fitting the $I(q)$ data to the Pedersen model,[153,157] and the relaxation functions are well described by Equation 2.18, with fixed $n = 2$. Table 3.3 shows the results for all five ILs including the initial core size and standard deviation, the final core size and standard deviation, and the relaxation times determined by SAXS. The time required to reach steady-state is generally unaffected by the IL selectivity, in good agreement with the results from *T*-jump DLS.

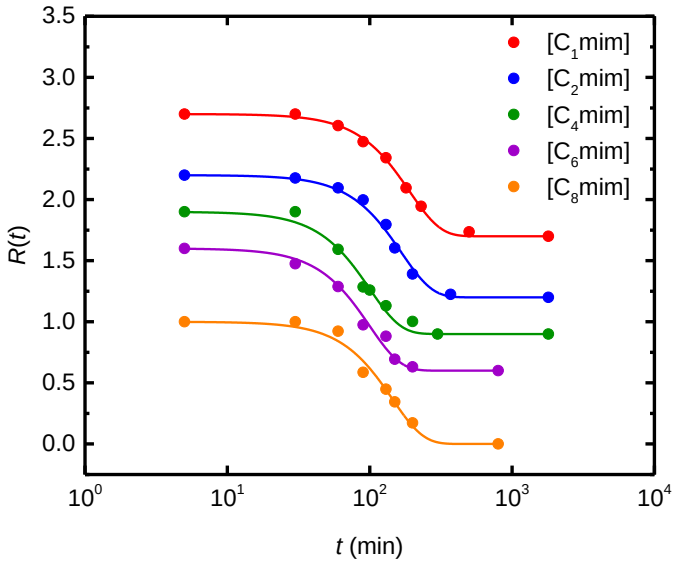

Figure 3.6: Normalized $\langle R_{core} \rangle$ from *ex-situ* SAXS during a *T*-jump to 170 °C for 0.5 wt % BO(8-6) in [C$_x$mim][TFSI]. The curves are shifted vertically for clarity. Solid lines represent the fits to the standardized relaxation function shown in Equation 2.18 with an Avrami exponent of $n = 2$.

Table 3.3: Summary of $\langle R_{core} \rangle$, σ_{core}, and τ obtained by *T*-jump SAXS at 170 °C for 0.5 wt % BO(8-6) in imidazolium-based ionic liquids. The relaxation times were determined by fitting the normalized $\langle R_{core} \rangle$ to Equation 2.18 with $n = 2$.

Ionic Liquid	$\langle R_{core} \rangle_0$ (nm)	σ_{core} (nm)	$\langle R_{core} \rangle_f$ (nm)	σ_{core} (nm)	τ_{frag} (min)
[C_1mim][TFSI]	25	5.0	19	3.6	190
[C_2mim][TFSI]	23	4.6	18	3.4	171
[C_4mim][TFSI]	20	4.5	16	3.2	100
[C_6mim][TFSI]	18	4.2	14	3.6	100
[C_8mim][TFSI]	16	3.9	13	3.1	150

To gain more insight into how the core size distribution changes with annealing time, *ex-situ* LP-TEM was used to measure the mean and standard deviation of the micelle core radius distribution at different time points following a *T*-jump to 170 °C. The change in $\langle R_{core} \rangle$ for 0.5 wt % BO(8-6) in [C_1mim][TFSI] and [C_2mim][TFSI] after a *T*-jump to 170 °C was 6 nm and 5 nm, respectively, as shown by SAXS and LP-TEM results in Figures 3.5 and 3.7. Electron micrographs of the as-prepared and steady-state micelles in [C_1mim][TFSI] and [C_2mim][TFSI] are shown in Figures 3.7a and 3.7b, and Figures 3.7c and 3.7d, respectively. In the micrographs, the densely packed PB blocks form the micelle cores, which appear lighter than the IL medium. As shown in Figures 3.7a and 3.7c, the micelles prepared by DD are all apparently spherical, but with large variations in radius.

The images in Figures 3.7b and 3.7d are representative images of the micelles in [C_1mim][TFSI] and [C_2mim][TFSI], respectively, after annealing at 170 °C for 1800 min. Qualitatively, the steady state images show that the micelle radius decreases noticeably after annealing.

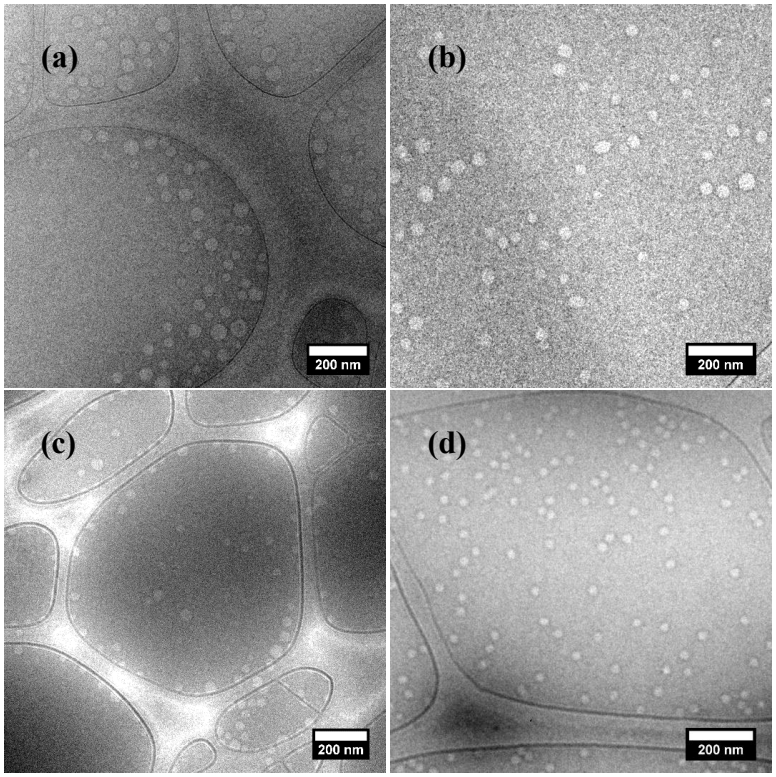

Figure 3.7: LP-TEM of 0.5 wt % BO(8-6) (a) in [C_1mim][TFSI] as-prepared by DD, and (b) after annealing at 170 °C for 1800 minutes. LP-TEM of 0.5 wt % BO(8-6) in [C_2mim][TFSI] (c) as-prepared by DD, and (d) after annealing at 170 °C for 1800 minutes.

To quantify the evolution of $\langle R_{core} \rangle$ and the standard deviation (σ_{core}), LP-TEM was employed to image the change in micelle structure throughout a *T*-jump at 170 °C for the same five ILs. Time point images for 0.5 wt % BO(8-6) in [C_1mim][TFSI], [C_4mim][TFSI], [C_6mim][TFSI], and [C_8mim][TFSI] are shown in Figures 3.8 – 3.11.

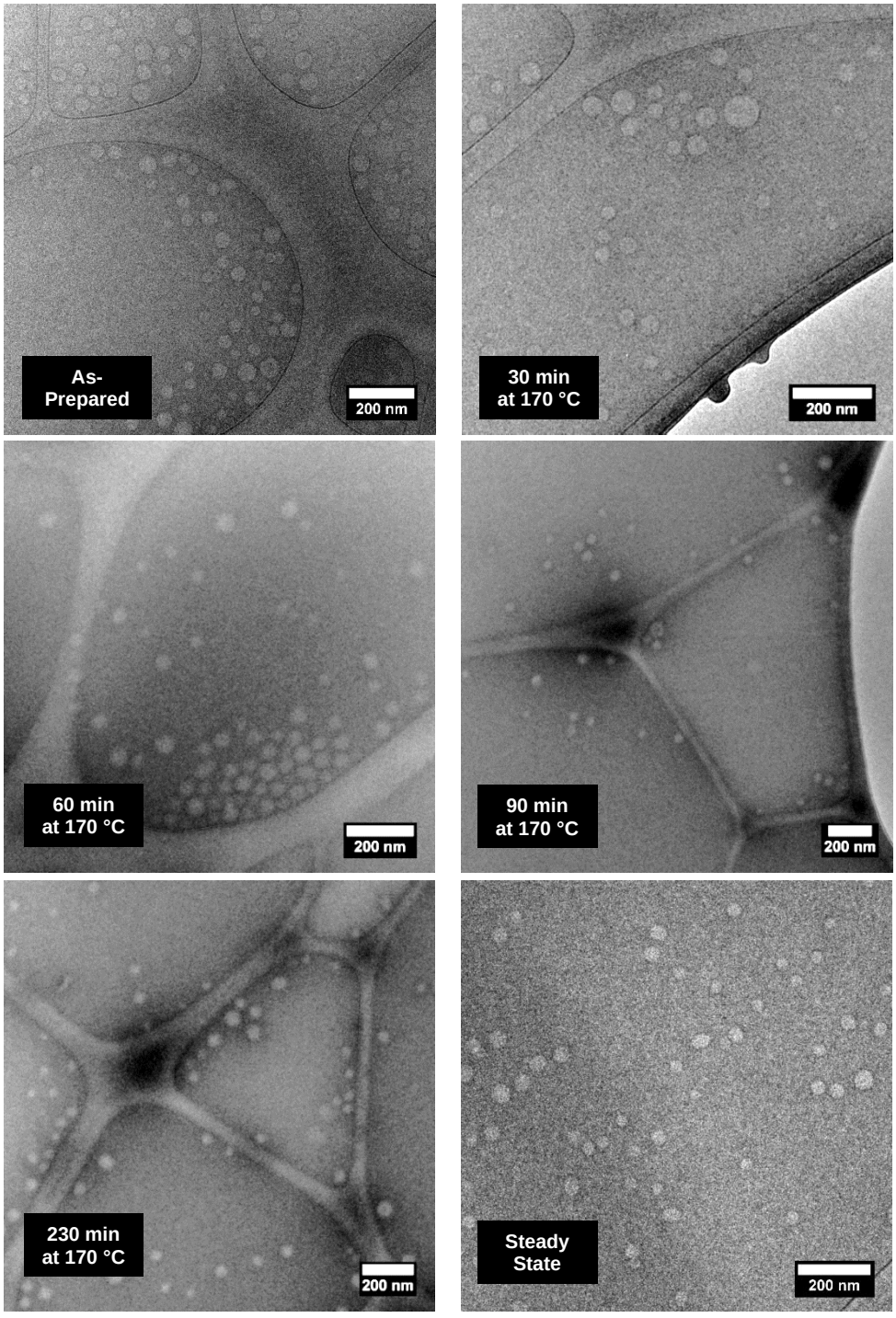

Figure 3.8: LP-TEM time points during a *T*-jump at 170 °C for 0.5 wt % BO(8-6) in [C_1mim][TFSI].

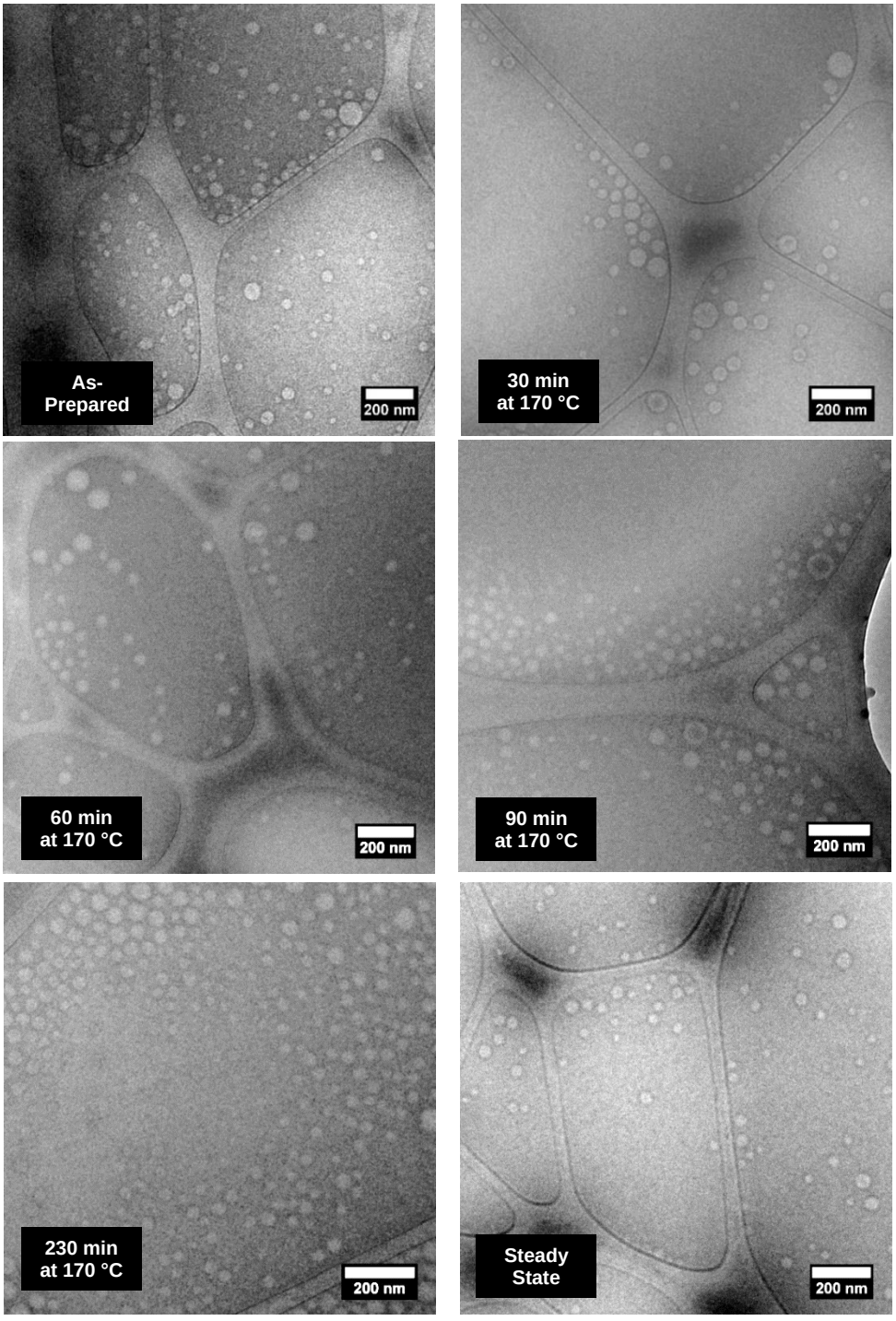

Figure 3.9: LP-TEM time points during a *T*-jump at 170 °C for 0.5 wt % BO(8-6) in [C_4mim][TFSI].

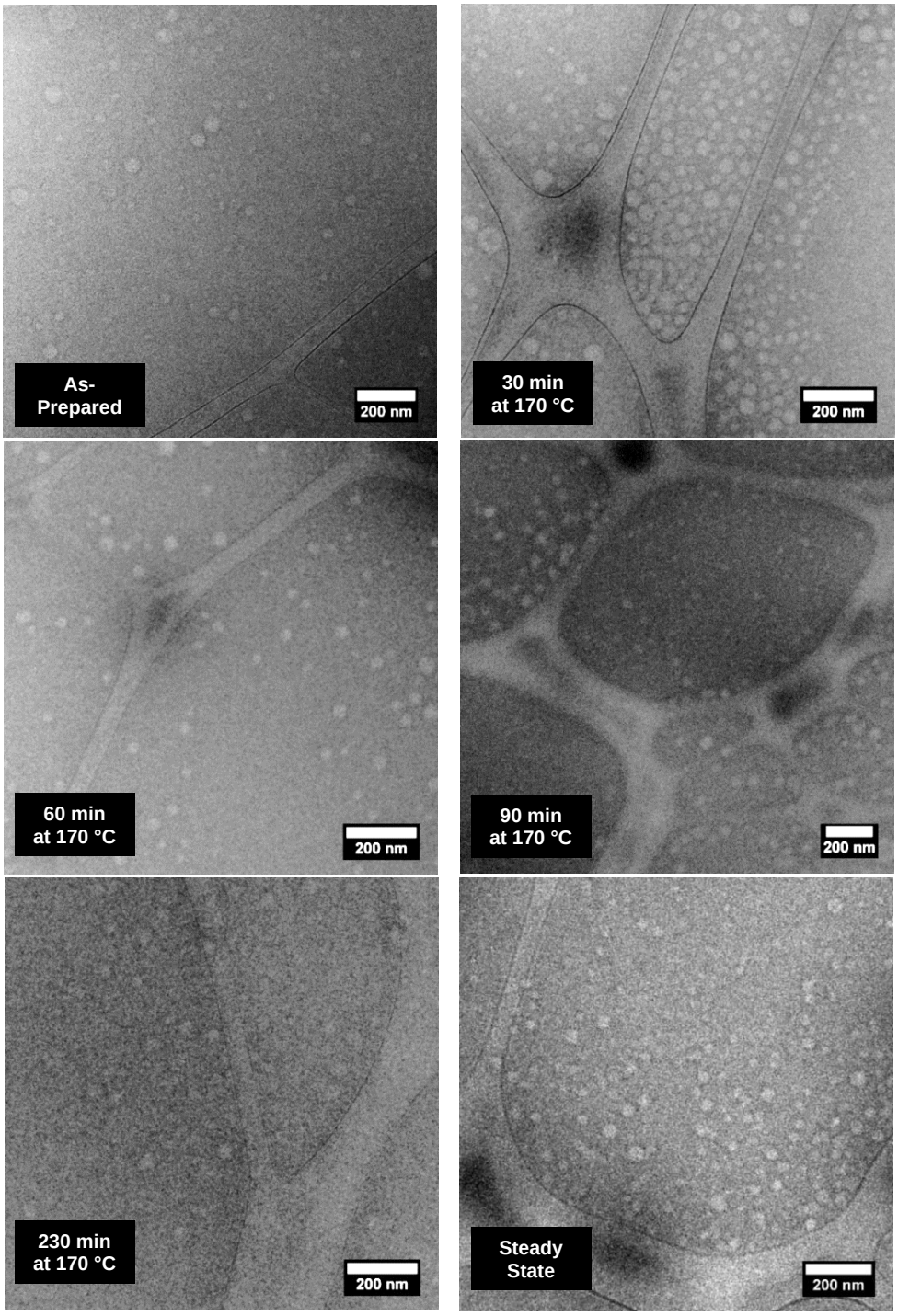

Figure 3.10: LP-TEM time points during a *T*-jump at 170 °C for 0.5 wt % BO(8-6) in [C_6mim][TFSI].

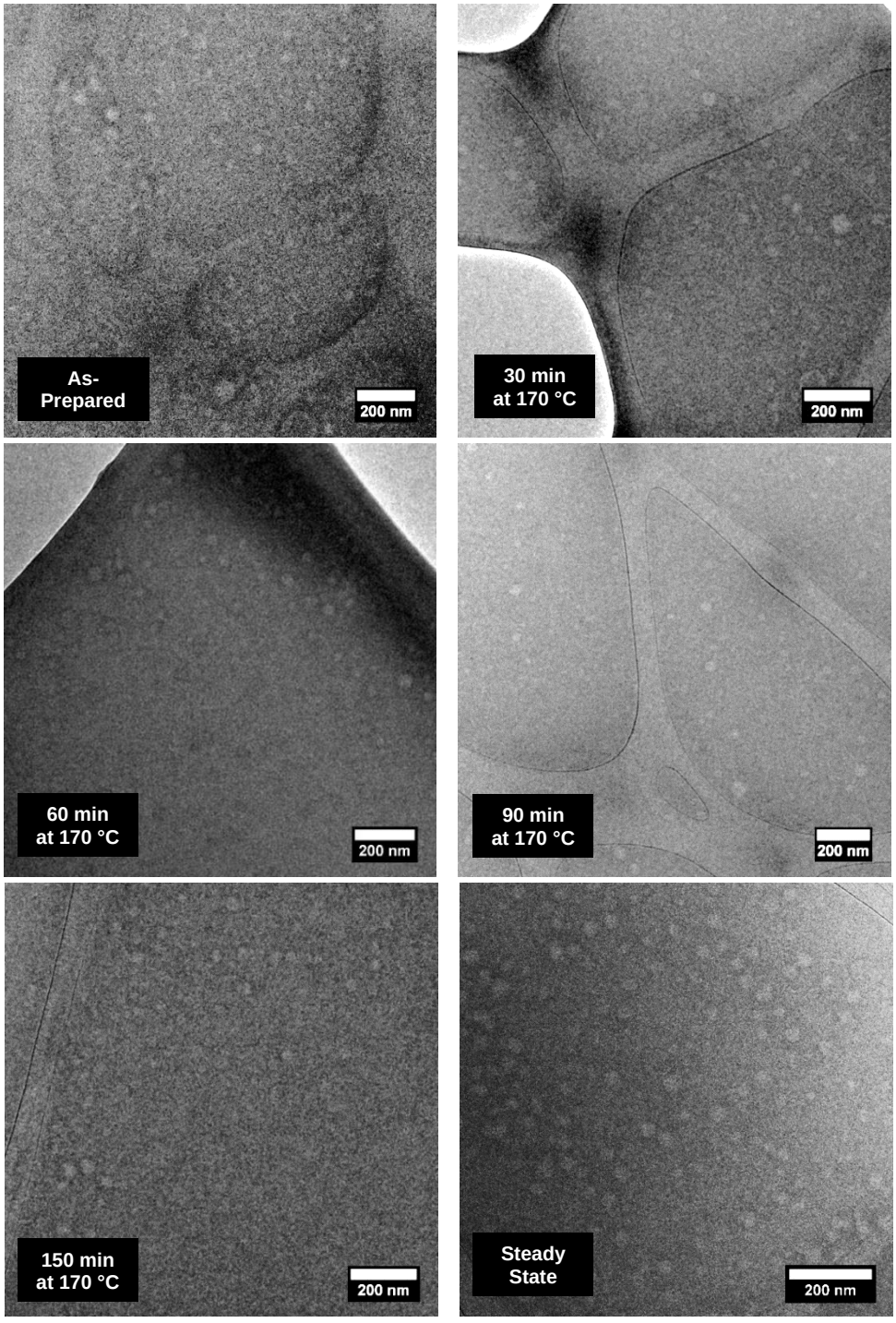

Figure 3.11: LP-TEM time points during a *T*-jump at 170 °C for 0.5 wt % BO(8-6) in [C_8mim][TFSI].

The resulting time point images are shown in Figure 2.19 for 0.5 wt % BO(8-6) in [C2mim][TFSI]. As shown in the figures, the PB core size decreases after heating at 170 °C for just 90 min. Additional structural details were obtained through image analysis of each time point. By measuring the radius of several hundred micelle cores (specifically, 600 micelles were measured for the as-prepared samples, and 400 micelles were measured for the other time points), a core radius distribution was obtained for each time point in the annealing process. From these measurements, the histograms in Figures 3.12 – 3.15 were constructed, where the bin width was set to 3 nm and the solid lines are overlays of a lognormal distribution with the mean and standard deviation denoted in each histogram. Low contrast in Figure 3.11 made detailed image analysis difficult, and histograms for micelles in [C8mim][TFSI] were not constructed.

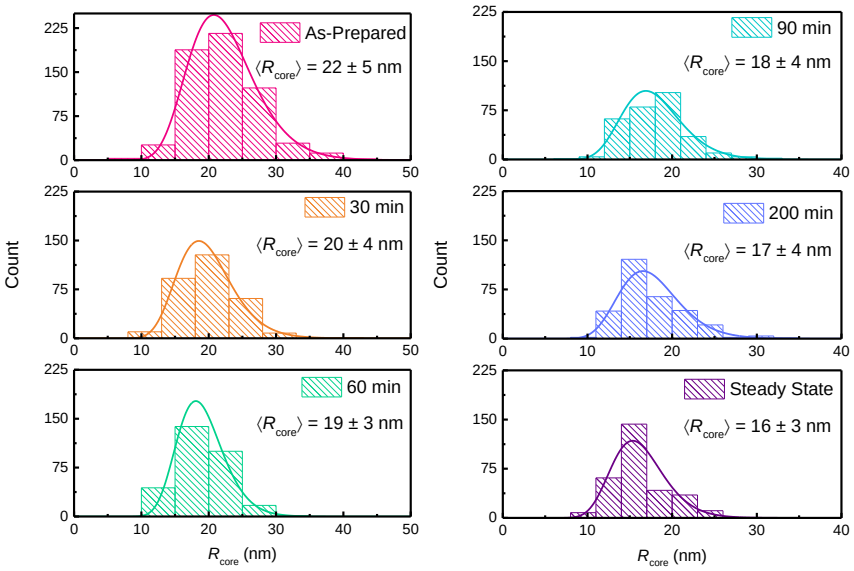

Figure 3.12: Histograms of data obtained by image analysis of Figure 3.8 from LP-TEM showing the evolution in $\langle R_{core} \rangle$ for 0.5 wt % BO(8-6) in [C1mim][TFSI] during *T*-jump at 170 °C.

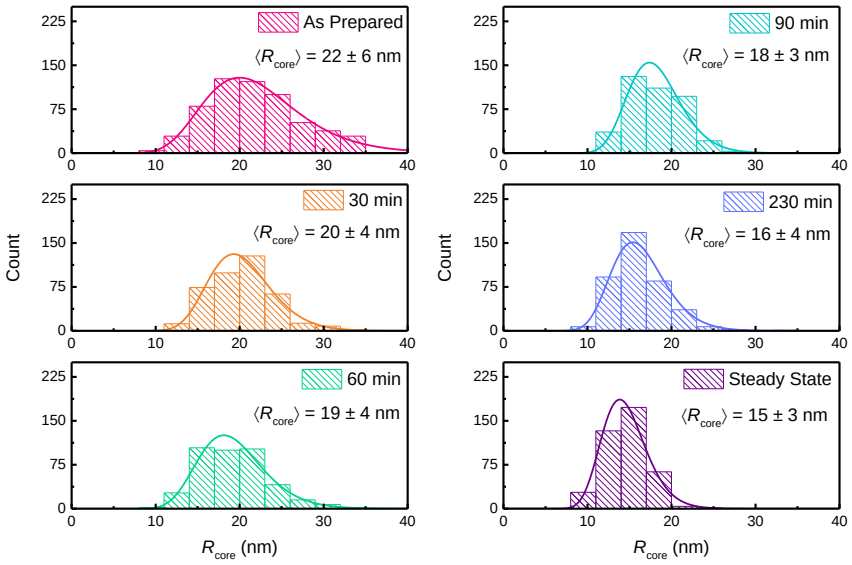

Figure 3.13: Histograms of data obtained by image analysis of Figure 2.19 from LP-TEM showing the evolution in ⟨R_{core}⟩ for 0.5 wt % BO(8-6) in [C_2mim][TFSI] during *T*-jump at 170 °C.

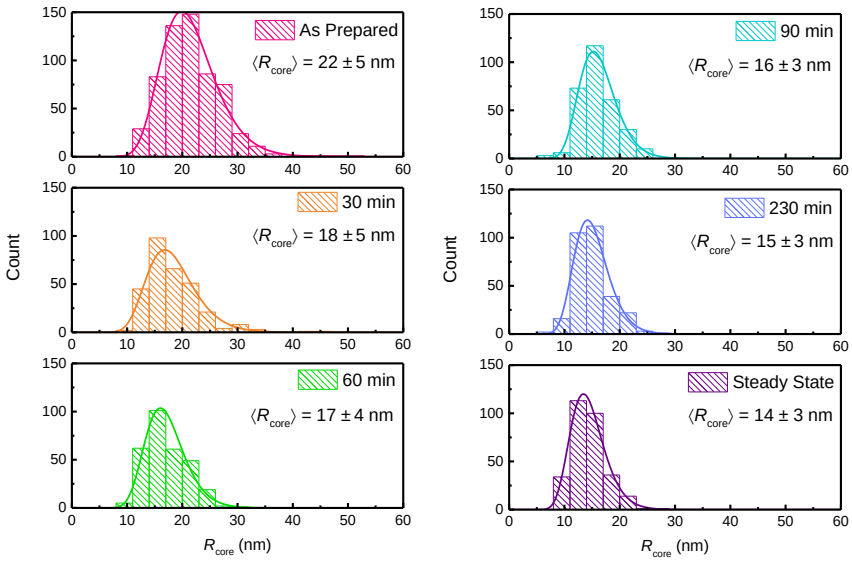

Figure 3.14: Histograms of data obtained by image analysis from LP-TEM of Figure 3.9 showing the evolution in ⟨R_{core}⟩ for 0.5 wt % BO(8-6) in [C_4mim][TFSI] during *T*-jump at 170 °C.

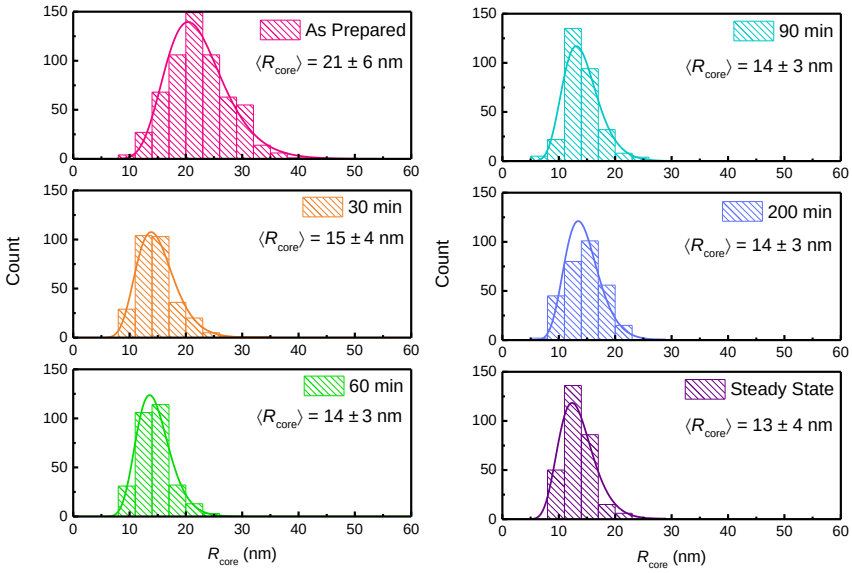

Figure 3.15: Histograms of data obtained by image analysis of Figure 3.10 from LP-TEM showing the evolution in $\langle R_{core} \rangle$ for 0.5 wt % BO(8-6) in [C_6mim][TFSI] during *T*-jump at 170 °C.

Clearly, $\langle R_{core} \rangle$ and σ_{core} decrease substantially throughout a *T*-jump to 170 °C, and the size distribution of the micelles in [C_2mim][TFSI] narrows considerably when comparing the histogram of the steady-state micelles to that of the as-prepared micelles. Furthermore, the larger size wing of the distribution changes much more significantly than the lower size wing, suggesting an increasing preference to undergo fragmentation the further from equilibrium a particular micelle is.

The difference between the final and initial $\langle R_{core} \rangle$ determined by LP-TEM agrees closely with the results from SAXS. For 0.5 wt % BO(8-6) in [C_2mim][TFSI], the initial $\langle R_{core} \rangle$ is 22 nm and 23 nm by LP-TEM and SAXS, respectively. The steady-state $\langle R_{core} \rangle$ in

[C_2mim][TFSI] is 18 nm and 15 nm as determined by LP-TEM and SAXS, respectively. The difference in the absolute values of $\langle R_{core} \rangle$ by LP-TEM and SAXS are within the standard deviation of the core radius obtained by each technique. In general, the LP-TEM results support the conclusion from SAXS, which is that the change in $\langle R_{core} \rangle$ after a *T*-jump to 170 °C occurs on the order of 100 min.

A comparison of $R(t)$ based on $\langle R_{core} \rangle$ determined by SAXS and $\langle R_h \rangle$ determined by DLS is shown in Figure 3.16. In the figure, filled circles represent the normalized $\langle R_h \rangle$ as determined by *T*-jump DLS to 170 °C, filled triangles represent the normalized $\langle R_{core} \rangle$ from SAXS, solid lines represent best fits to Equation 2.18 with $n = 2$ for all ILs except for the normalized $\langle R_h \rangle$ in [C_1mim][TFSI], where $n = 3.3$. The dashed lines in Figure 3.16 represent best fits to Equation 2.18 with n fixed at 2. The results for [C_2mim][TFSI], [C_4mim][TFSI], [C_6mim][TFSI], and [C_8mim][TFSI] agree quite well across the two techniques, but larger deviations are observed in [C_1mim][TFSI]. This discrepancy could be explained by the existence of additional relaxation mechanisms for micelles prepared by DD in [C_1mim][TFSI], including the disassociation of larger aggregates consisting of multiple micelles. The difference in the exponent determined by DLS ($n = 3.3$) and SAXS ($n = 2$) for relaxation in [C_1mim][TFSI] indicates that the change in size observed between the two techniques is likely dominated by two different mechanisms. This conclusion would also support the large differences in τ_{frag} for SAXS and DLS in [C_1mim][TFSI].[173,174] However, additional experiments on this system may be required to determine the exact

cause of the different time scales observed in *T*-jump DLS and SAXS for BO(8-6) micelles in [C$_1$mim][TFSI].

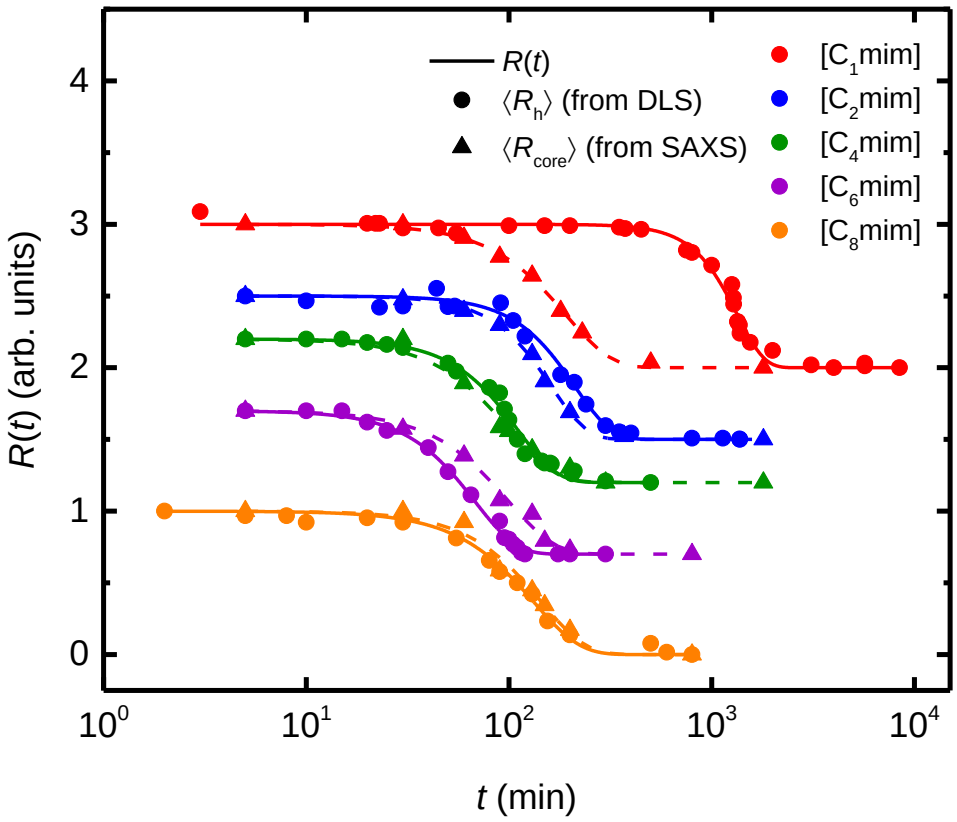

Figure 3.16: Normalized $\langle R_h \rangle$ (filled in circles) and normalized $\langle R_{core} \rangle$ (filled in triangles) for 0.5 wt % BO(8-6) at 170 ºC in [C$_1$mim][TFSI] (red points and lines), [C$_2$mim][TFSI] (blue points and lines), [C$_4$mim][TFSI] (green points and lines), [C$_6$mim][TFSI] (purple points and lines), and [C$_8$mim][TFSI] (orange points and lines). The solid and dashed lines represent the fits to Equation 2.18 where $R_i = \langle R_h \rangle$ and $R_i = \langle R_{core} \rangle$, respectively, both with *n* fixed at 2 except for *T*-jump DLS in [C$_1$mim][TFSI], where the best fit was obtained when *n* is 3.3. The plots are shifted vertically with decreasing IL cation alkyl chain length for clarity.

3.3.3 – Effect of the micelle preparation protocol

To determine the effect of solution preparation on $\langle R_h \rangle_0$ and $\langle R_h \rangle_f$ for BO(8-6) in [C_2mim][TFSI], a 0.5 wt % solution was prepared by the CS method, following the approach described previously by Meli *et al.*[90] All components were dissolved in dichloromethane (DCM), and after stirring to ensure all components are well dissolved, the DCM was slowly evaporated under a nitrogen purge over 24 h. The complete procedure for the CS method is described in Section 2.3.2. The $\langle R_h \rangle_0$ for 0.5 wt % BO(8-6) in [C_2mim][TFSI] prepared by this method was found to be 26 nm with a dispersity of 0.08. Thus the initial size of the CS micelles is less than half that of the micelles prepared by DD. Additionally, when CS micelles are annealed at 170 °C for a day $\langle R_h \rangle$ remains constant, as shown in Figure 3.17.

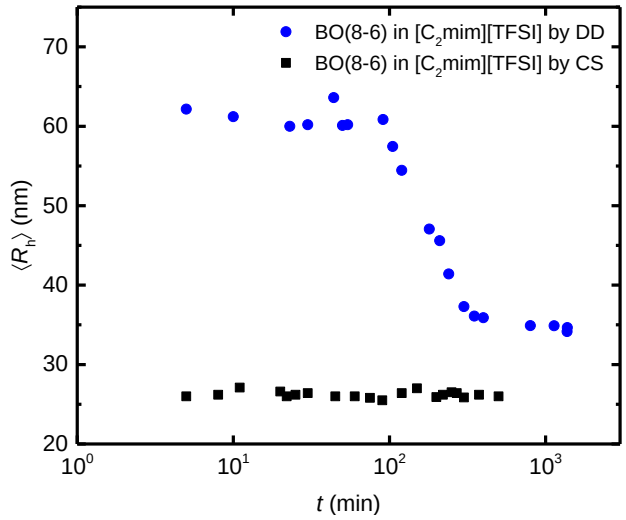

Figure 3.17: R_h versus time for 0.5 wt % BO(8-6) micelles in [C_2mim][TFSI] prepared by DD (blue circles) and CS (black squares) protocols. Scattering measurements were performed at T = 170 °C and θ = 90°.

Thus the $\langle R_h \rangle_f$ obtained for the CS micelles remain significantly smaller than the steady state size for solutions prepared by DD (35 nm). Similar results were obtained by Meli, *et al*., who conjectured that the annealed DD micelle size was closer to equilibrium than CS micelles. They argued that (a) it is clear that the CS protocol generates micelles that are at equilibrium with a much less selective, mixed solvent at the time of formation, and should therefore be much smaller than equilibrium micelles in the IL; (b) to reduce the number density of micelles is an extremely time consuming process, so it is difficult for CS micelles to coarsen with time; (c) DD micelles annealed at different temperatures relaxed to the same final size.

3.3.4 – Discussion

We now consider four general questions about these results.

1. *Is the change in micelle size due to fragmentation?*

The fact that the micelles are deliberately prepared to be significantly larger than their equilibrium size favors relaxation by fragmentation. The fact that the relaxation process is first-order in micelle concentration is consistent with fragmentation. However, it is worth noting that we have no direct proof of fragmentation, such as clear TEM evidence of an intermediate state. Direct evidence that fragmentation is occurring in this system is shown in Chapter 4 using temperature-controlled LP-TEM of PB-PEO micelles in ILs. The one aspect of the results that raises a possible doubt is the compressed exponential relaxation function, which might imply some kind of cooperative process. It is difficult to identify a

strictly first-order process that would give this functional form. Nevertheless, the presence of micelle fragmentation is consistent with the theory presented by Dormidontova, which predicts that micelles with aggregation numbers that lie very far from equilibrium are more likely to relax via fusion or fragmentation mechanisms.[97]

We assume that the steady-state aggregation number, Q_f, obtained for each sample is close to the equilibrium aggregation number, Q_{eq}. Based on the arguments posed by Dormidontova,[97] fragmentation into two equally sized micelles is favored when $Q \geq 1.5Q_{eq}$. In this work, the aggregation numbers for each sample were determined assuming a dry PB core and calculated according to $Q = (4\pi\langle R_{core}\rangle^3)/3V_{core}$, where $\langle R_{core}\rangle$ is taken from the model fits to SAXS data, and $V_{core} = M_n/\rho N_{av}$ where ρ is the amorphous density of PB ($\rho = 0.87$ g/cm^3),[138] and N_{av} is Avogadro's constant. From Table 3.4, the equilibrium aggregation number can be estimated as $Q_{eq} \approx Q_f$, and $1.5Q_{eq}$ is equal to 2960, 2500, 1770, 1185, and 945 for BO(8-6) micelles in [C_1mim], [C_2mim], [C_4mim], [C_6mim], and [C_8mim], respectively. From Q_0 in Table 3.4, all as-prepared micelles are significantly larger the 1.5 times Q_{eq}, supporting micelle fragmentation as the dominant pathway. The ratio of Q_f to Q_0 for the 5 ILs are shown in Table 3.4. Regardless of the solvent, the average aggregation number is approximately halved after heating at 170 °C. It is likely that the largest micelles (*i.e.*, those with $Q \geq 1.5Q_{eq}$) account for the observed decrease in Q, as the micelles that are at or near the equilibrium aggregation number are not expected to undergo fragmentation. Experimentally, this is consistent with the histograms shown in Figures 3.12

– 3.15, where the number of micelles with $\langle R_{core} \rangle$ greater than 18 nm decreases significantly over time, but the number of micelles with $\langle R_{core} \rangle \leq 18$ nm remain relatively constant.

Table 3.4: Effects of solvent quality on micelle size and Q for 0.5 wt % BO(8-6) in ILs before and after a T-jump to 170 °C.

IL Cation	δ^b $(MPa^{1/2})$[166]	δ^c $(MPa^{1/2})$[169]	ΔR_h (nm)	ΔR_{core} (nm)	$Q_0{}^a$	$Q_f{}^a$	Q_f/Q_0
[C_1mim]	-	21.5	40	6	4480	1970	0.44
[C_2mim]	27.6	21.1	27	5	3490	1670	0.48
[C_4mim]	26.7	19.4	17	4	2300	1180	0.51
[C_6mim]	25.6	-	9	4	1670	790	0.47
[C_8mim]	25.0	-	6	3	1180	630	0.53

[a]Aggregation number (Q_x), where x = 0, f denoting initial and final values, calculated as $4\pi\langle R_{core}\rangle_x{}^3/(3V_{PB})$ assuming the core is devoid of solvent, and V_{PB} is the volume per core chain. [b]Hildebrand solubility parameters reported for T = 298 K. [c]Hildebrand solubility parameters reported for T = 303 K. For reference, the average solubility parameters for PB and PEO are δ = 17.4 $MPa^{1/2}$ and δ = 20.2 $MPa^{1/2}$, respectively.[138]

2. *Why does the relaxation follow a compressed exponential?*

In all ILs, excluding [C_1mim][TFSI], the timescales and the exponents from fits to the data from T-jump DLS and SAXS agree well. We do not have a physical interpretation for the origin of n = 2 in the PB-PEO/[$C_x$mim][TFSI] samples studied here, but the results are consistent with previous reports on this system.[89,90] The use of compressed exponential (n

> 1) functions to describe block copolymer dynamics is documented in other reports,[173–176] and in at least one instance has been attributed to the spontaneous breakup of pre-formed structures.[174] The similarity to the Avrami form, typically used to describe a nucleation and growth kinetics, hints at a nucleation-limited or cooperative kinetic process, but the independence of the experimental rate on concentration suggests that any cooperativity is confined to processes within a single micelle.

3. *What sets the characteristic relaxation time?*

We speculate that the experimental fragmentation times follow an Arrhenius expression, shown in Equation 3.1,

$$\tau_{\text{frag}} = \tau_0 \exp(E_b / k_B T) \tag{3.1}$$

where E_b is the activation barrier and τ_0 is the characteristic attempt time to access the transition state. This attempt time is likely dependent on the viscosity of the PB core and driven by the corona crowding and core stretching (both of which are significant in this system). The corona crowding exerts a stress, σ, on the cross-sectional area of the core, given by $f/\pi\langle R_{\text{core}}\rangle_0^2$, where f is the force. This force can be estimated using the theory by Sheiko, *et al.*[177] which gives the force exerted on a linking unit by a star polymer grafted to a hard surface, and here choosing the linker length to be $\langle R_{\text{core}}\rangle_0/2$. Using this model to determine the stress from corona crowding, Equation 3.2 shows an estimate for τ_0.

$$\tau_0 \approx \frac{\eta_{\text{core}}}{\sigma} = \frac{\eta_{\text{core}} \pi \langle R_{\text{core}} \rangle_0^3}{\sqrt{2} k_B T Q_0^{3/2}} \tag{3.2}$$

Given that the viscosity of 8.2 kDa PB at 170 °C is approximately 0.6 Pa·s (see Figure A1 in the Appendix) and knowing the experimental relaxation times range from 6,000 to 11,000 s, then E_b is on the order of 25–30 k_BT per micelle. The barrier per chain is obtained by dividing E_b by Q_0 resulting in a barrier on the order of 0.01 k_BT per chain. This is very small, and makes it difficult to resolve in terms of calculating possible contributions from core stretching, corona stretching, and interfacial tension. A transition state for micelle fragmentation is not as easily identified until Chapter 4.[125,178,179] As the fragmentation process increases the net surface area of the core blocks, it is tempting to infer that the barrier involves a transition state with larger area. However, the independence of the fragmentation rate on IL selectively argues strongly against interfacial tension as rate-limiting.

A previous report on the fusion and fragmentation kinetics of ionic/nonionic mixed micelles proposed that fragmentation arises from surface instabilities, which leads to bending of the micelle surface, pinching, and finally breaking into two or more micelles.[126] The authors concluded that one of the main barriers to fragmentation would arise from the solvophobic core block, which is likely exposed to the solvent in the final stage of breaking. This is apparently inconsistent with our results. Another potential barrier to fragmentation could arise from additional corona crowding during a "pinch-off" process. Because the

total surface area of the micelle increases by only about 26% after fragmentation, the corona crowding could be quite severe in the transition state during a fragmentation event. The role of corona crowding is discussed in depth in Chapter 5. If this interpretation is correct, this could explain why the fragmentation kinetics are independent of solvent selectivity. The fragmentation process begins when separation of the micelle core occurs, which will increase the total surface free energy. Further corona separation will decrease the free energy via entropic gain of the corona chains, which allows the core chains to adopt a less-stretched conformation after fragmentation.[97]

This is likely the case for BO(8-6)/[$C_x$mim][TFSI], considering the extremely large values of Q_0 obtained for the as-prepared micelles. To accommodate such high aggregation numbers the PB blocks in the core must adopt a highly stretched conformation, which further drives the corona crowding. An estimate of the degree of core block stretching using R_{core} divided by the mean square end-to-end distance of the core block for as-prepared micelles in [C_2mim][TFSI] shows the PB chains are initially stretched to approximately 1/3 of the fully extended length. Using this same estimate for the steady-state core radius, the PB chains relax to 1/4 of the fully extended length, which is still substantial.

4. *How are the initial micelles formed?*

Table 3.4 summarizes the changes in R_h and R_{core}, the initial aggregation number (Q_0), and the final aggregation number (Q_f) for BO(8-6) micelles before and after a *T*-jump at 170 °C, along with the Hildebrand solubility parameters for each IL and the PB and PEO blocks. The χ parameter can be estimated using solubility parameters based on the

following equation, $\chi_{PB\text{-}IL} = (V/RT)(\delta_1 - \delta_2)^2$, where V is a reference volume, in this case the molar volume of the IL, R is the gas constant, and δ_i are the solubility parameters of the core block and the IL. From the difference in solubility parameters between PB and the IL, the $\chi_{PB\text{-}IL}$ parameter is expected to decrease with increasing IL cation alkyl chain length. When preparing micelles by the DD protocol, the higher $\chi_{PB\text{-}IL}$, the larger and more disperse the resulting micelles. Additionally, the relatively large χ restricts typical equilibration mechanisms observed in diblock copolymer micelles such as individual chain exchange.[17,19]

Figure 3.18a demonstrates the large dependence of ΔQ on solvent selectivity. As shown in the figure and in Table 3.4, the more selective ILs show a larger change in the as-prepared and steady-state aggregation numbers in comparison to the least selective solvent, [C_8mim][TFSI]. This trend is also observed in Figure 3.18b when comparing the as-prepared and steady-state $\langle R_h \rangle$ and $\langle R_{core} \rangle$ as a function of the IL selectivity. Specifically, the overall change in $\langle R_h \rangle$ and $\langle R_{core} \rangle$ increases with increasing solvent selectivity. In general, the effects of the solvent selectivity on the fragmentation kinetics are minimal, however, the results show that regardless of the IL selectivity, DD of BO(8-6) in these solvents lead to micelles that are not at equilibrium, and this preparation protocol results in structures that are large enough to equilibrate by fragmentation and not by chain exchange.

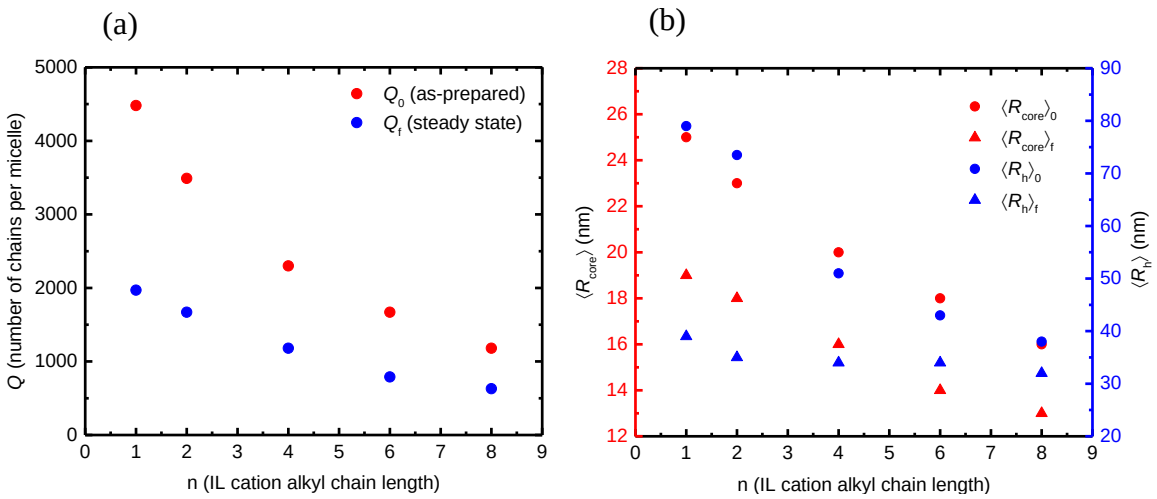

Figure 3.18: (a) Initial and final aggregation numbers versus IL cation alkyl chain length. The aggregation numbers are calculated from the $\langle R_{core}\rangle$ determined by *ex-situ* SAXS assuming a dry micelle core. (b) Dependence of $\langle R_h\rangle_0$ and $\langle R_{core}\rangle_0$ (filled circles) and $\langle R_h\rangle_f$ and $\langle R_{core}\rangle_f$ (filled triangles) on the IL cation alkyl chain length. The $\langle R_h\rangle_0$ for 0.5 wt % BO(8-6) in [C_2mim][TFSI] was calculated by taking the average of the two R_h values obtained by fitting DLS results to a double exponential.

The poor solubility of the core block is anticipated to give rise to a micellization scenario where the nucleation of micelles is overcome by the speed of micelle growth, resulting in large, polydisperse micelles. Additionally, it has been suggested that the morphology of micelles prepared by direct dissolution will depend on the morphology of the bulk polymer.[128,180] SAXS of the bulk BO(8-6) polymer was conducted. The scattering data, shown in Figure A2 of the Appendix, confirms that BO(8-6) exhibits a lamellar morphology at 70 °C, which is the temperature used for direct dissolution of BO(8-6) in ILs. The domain size of the PB lamellae was estimated to be approximately 21 nm, which is comparable to the initial micelle core size. It is possible that in direct dissolution the

solvent penetrates the PEO domains, and surface instabilities of the lamellae begin to pinch off to give large, polydisperse spherical aggregates in solution. This behavior is analogous to the Rayleigh instability, which is discussed in detail in Chapter 7, and is referenced in computations of surfactant-based micelles,[178] and experimentally in cylinder-to-sphere transitions[181] in block copolymer micelles. A schematic illustration of this process is depicted in Figure 3.19.

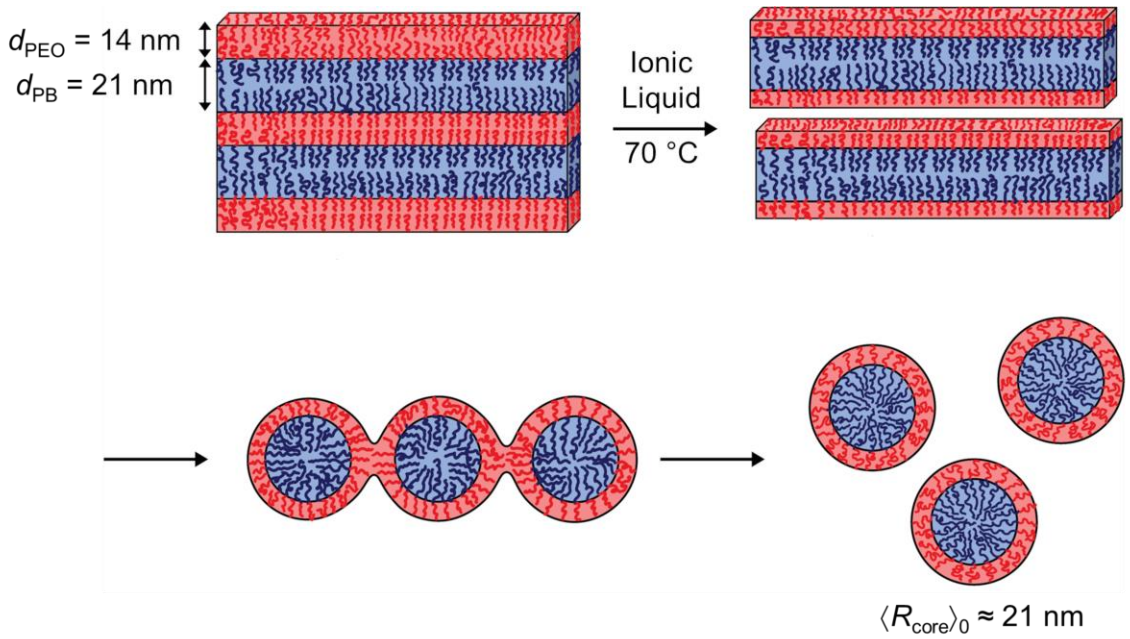

Figure 3.19: Schematic illustration of the direct dissolution process. In the bulk, BO(8-6) exhibits a lamellar morphology, with a PB domain size of 21 nm, and a PEO domain size of 14 nm. When ionic liquid, vigorous stirring, and heat are introduced to the bulk polymer, the lamella begin to tear apart into sheets, or potentially cylinders, and each lamella breaks off into either cylinders and then into spherical aggregates, or the lamella break off to form large spherical aggregates. This results in spherical micelles with $\langle R_{core} \rangle_0 \approx 21$ nm.

However, the interfacial tension between the core-forming block and the solvent also plays a role in the initial micelle size. This is shown in Table 3.3, where $\langle R_h \rangle_0$ decreases as the solvent is changed from [C_1mim][TFSI] to [C_8mim][TFSI]. Based on this view, it is reasonable that the size and polydispersity of micelles prepared by DD protocol can be tuned based on the initial domain size of the core- and corona-forming blocks in the bulk polymer in one solvent. As the solvent selectivity towards the core block is changed, the as-prepared micelle size will also be determined by the interfacial tension between the core-forming block and the solvent, but the domain size in the bulk sample can also play a role.

3.4 – Summary

In this work, the equilibration kinetics were studied for BO(8-6) micelles prepared by direct dissolution in five [$C_x$mim][TFSI] ILs using *T*-jump DLS, SAXS, and LP-TEM. From the combined techniques, it was found that the micelle size ($\langle R_h \rangle$ and $\langle R_{core} \rangle$) decreased significantly after prolonged annealing at 170 °C; the final aggregation number was about half of the original. The decay in $\langle R_h \rangle$ and $\langle R_{core} \rangle$ could be well described by a compressed exponential with an exponent of 2 in almost all cases. The origin of this functional form is not yet apparent. The characteristic relaxation times determined by fits to this equation for DLS for BO(8-6) in [C_2mim][TFSI] were essentially independent of concentration, indicating a relaxation process that is first-order with respect to polymer concentration. The effects of solvent selectivity on the equilibration kinetics were

investigated by using five different ionic liquids with varying cation alkyl chain lengths. In this case, the decay of $\langle R_h \rangle$ occurs on a similar timescale regardless of the solvent quality. To verify that micelle fragmentation was taking place, LP-TEM and SAXS were used to monitor the evolution in micelle core size after annealing at 170 °C. The large decrease in core radius indicates that fragmentation is most likely the primary equilibration mechanism observed in this system, as individual chain exchange would not be expected to change the core radius to that extent.

In general, these experiments indicate that the solvent selectivity plays a significant role in how far the as-prepared micelles are from the equilibrium size. Specifically, the more selective solvents result in micelles much larger aggregation numbers, while the least selective solvents result in as-prepared micelles that are closer to the equilibrium size. However, the solvent selectivity was found to play essentially no role in the fragmentation kinetics, as nearly all the PB-PEO micelles in imidazolium-based ILs fragmented on the order of hundreds of minutes. Because the fragmentation kinetics are independent of solvent quality, the primary barrier to micelle fragmentation is most likely not from the exposure of the micelle core to the solvent in the transition state. We speculate that the corona crowding in the transition state is quite severe, which could be the main barrier to fragmentation.

Chapter 4 – Direct observation of micelle fragmentation via *in-situ* liquid-phase transmission electron microscopy[*,†]

4.1 – Introduction

As shown in Chapter 3 and in previous work by Meli *et al*., solution preparation by the DD method of PB-PEO diblock copolymers in [C_2mim][TFSI] resulted in kinetically trapped, large micelles.[89] These micelles then became smaller, eventually reaching a steady state size, upon prolonged annealing at elevated temperatures. Similar evidence of fragmentation was reported for PB-PEO micelles prepared by DD in various [$C_x$mim][TFSI] ILs.[89–91] Although the as-prepared micelles decreased in size when subjected to annealing at 170 °C, TR-SANS experiments revealed that no individual chain exchange occurred under these conditions.[90] Additionally, the kinetics of this process were found to be independent of polymer concentration, as shown in Figure 3.2b. Because micelle fusion should be a second-order kinetic processes with respect to polymer

[*]Reprinted in part with permission from Early, J. T.; Yager, K. G.; Lodge, T. P. Direct Observation of Micelle Fragmentation via In Situ Liquid-Phase Transmission Electron Microscopy. *ACS Macro Lett.*, **2020**, *9*, 756 – 761. Copyright © 2020 American Chemical Society.
[†]This work was conducted in collaboration with Dr. Kevin G. Yager at Brookhaven National Laboratory in Upton, NY.

concentration,[95,97,117] it was concluded that PB-PEO micelles in these ionic liquids equilibrate primarily by fragmentation.[90] This strong evidence for fragmentation notwithstanding, the equilibration kinetics were determined primarily by ensemble average methods such as DLS and SAXS. Direct imaging *ex-situ* by TEM has also been employed.[91] Micelle fusion events have recently been observed for aqueous polymer solutions using *in-situ* liquid cell transmission electron microscopy.[123] To the best of our knowledge, direct observation of fragmentation has not been reported in any block copolymer/solvent system. Of particular interest is the nature of the transition state.

In this chapter, we build on the *ex-situ* LP-TEM experiments used in Chapter 3 and conduct high-temperature LP-TEM to observe *in-situ* fragmentation of PB-PEO micelles in [C_2mim][TFSI]. Because the IL does not evaporate under the high vacuum conditions in the microscope, liquid samples can be imaged directly without the need for a hermetically sealed sample chamber.[133,158–160] Using a temperature-controlled sample holder for LP-TEM allows *T*-jump experiments to be conducted directly in the microscope, and images of the change in micelle morphology during fragmentation were collected. Additionally, TR-SAXS experiments were performed to corroborate ensemble average changes in the core radius $\langle R_{core} \rangle$ during a *T*-jump to 170 °C.

4.2 – Materials and methods

Three molar masses of PB-PEO were synthesized by two-step sequential anionic polymerization, as described in Section 2.1.1,[136] with a constant volume fraction of PEO, $f_{PEO} \cong 0.40$.[136] PB-PEO diblocks and 0.1 wt % butylated hydroxytoluene as an antioxidant were dissolved in dichloromethane and dried under vacuum at 40 °C for 72 h prior to use. Each molar mass is referred to as BO(x-y), where x and y denotes M_n in kg/mol of the PB and PEO blocks, respectively. SEC-MALS from Figure 2.2 showed that the three polymers studied, BO(8-7), BO(25-22), and BO(27-27), had low dispersities ($Đ \leq 1.09$); see Sections 2.1.1 and 2.1.2 for detailed molecular characterization. Micelles were prepared by the DD method described in Section 2.3.1 to obtain 0.25 wt % solutions. The micelle core dimensions were then studied *in-situ* via high-temperature LP-TEM, described in Section 2.6.2 and TR-SAXS, as discussed in Section 2.5.3.

4.3 – Results and discussion

Prior to a *T*-jump to 170 °C, the PB core size for micelles as-prepared by DD in [C_2mim][TFSI] was characterized by room-temperature LP-TEM and SAXS. $\langle R_{core} \rangle_0$ for 0.25 wt % BO(8-7) in [C_2mim][TFSI] was found to be approximately 20 nm with a standard deviation ($\sigma_{core,0}$) of 6 nm by TEM image analysis. The 1D scattering patterns for BO(8-7), shown in Figure 2.17a, by SAXS at room temperature were fit to the Pedersen form factor for block copolymer micelles with the Percus-Yevick structure factor.[153,157]

From the fits, $\langle R_{core} \rangle_0$ = 19.5 ± 2.0 nm for BO(8-7), in excellent agreement with TEM. As shown in Figure 4.1, all micelles observed for BO(8-7) by TEM were spherical. From Figure 2.17a, the form factor scattering for BO(8-7) micelles as prepared by DD and after a *T*-jump to 170 °C are consistent with spherical cores. The initial sizes of BO(25-22) and BO(27-27) micelles in [C_2mim][TFSI] were also determined in this manner, and by TEM image analysis, $\langle R_{core} \rangle_0$ = 45 ± 5 nm for BO(25-22) and $\langle R_{core} \rangle_0$ = 50 ± 7 nm for BO(27-27). The TEM images are shown in Figures 4.2 and 4.3, respectively. SAXS data of BO(25-22), shown in Figure 2.18a, and BO(27-27) shown in Figure 4.4, confirm that the as-prepared micelles are spherical.

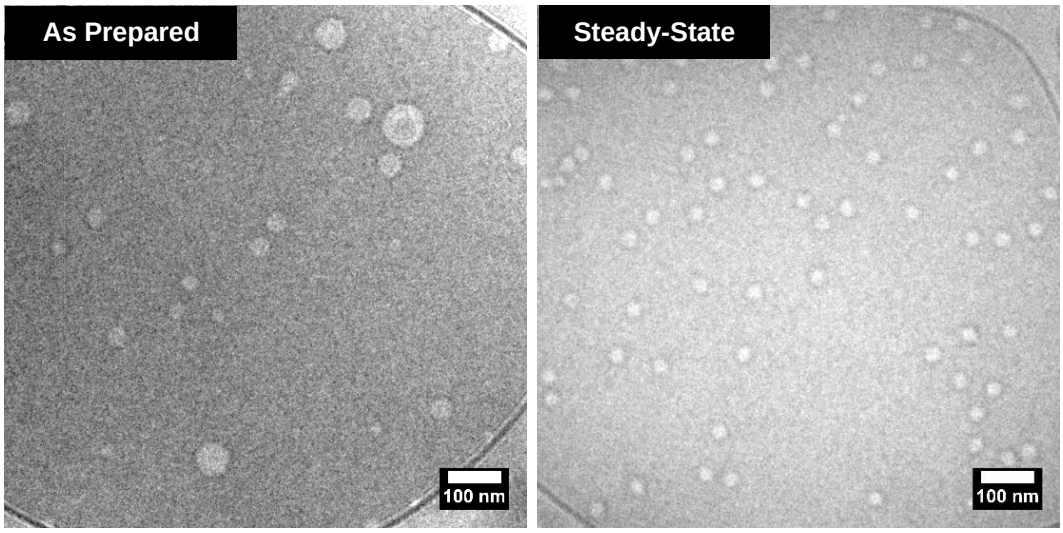

Figure 4.1: LP-TEM of 0.25 wt % BO(8-7) in [C_2mim][TFSI] as prepared by DD ($\langle R_{core} \rangle$ = 21 ± 6 nm) and steady-state ($\langle R_{core} \rangle$ = 16 ± 3 nm) after annealing at 170 °C for 200 min. In these images, the ionic liquid appears darker than the PB micelle core due to the higher electron density of [C_2mim][TFSI].

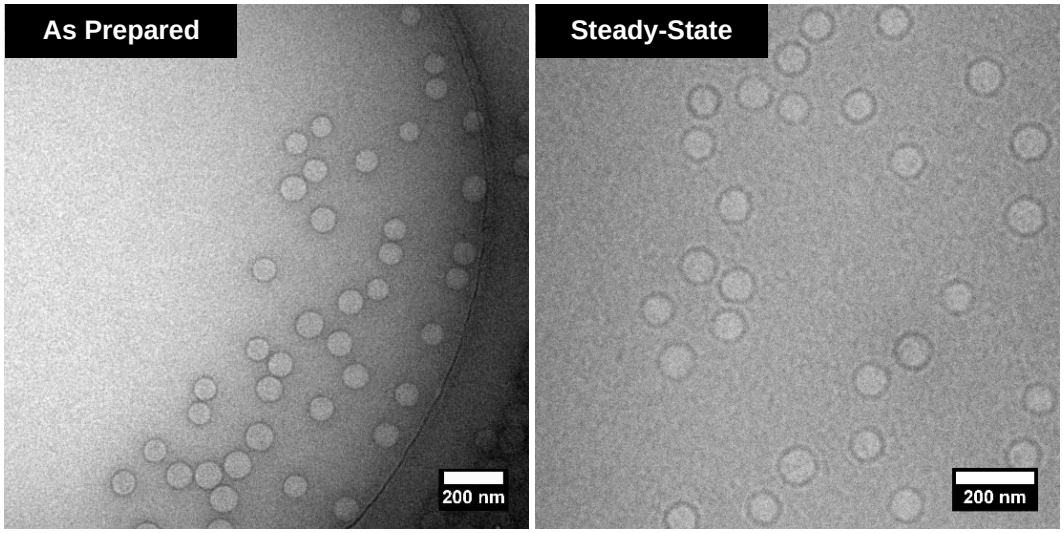

Figure 4.2: LP-TEM of 0.25 wt % BO(25-22) in [C2mim][TFSI] as prepared by DD ($\langle R_{core} \rangle$ = 45 ± 5 nm) and steady-state ($\langle R_{core} \rangle$ = 35 ± 4 nm) after annealing at 170 °C for 3000 min.

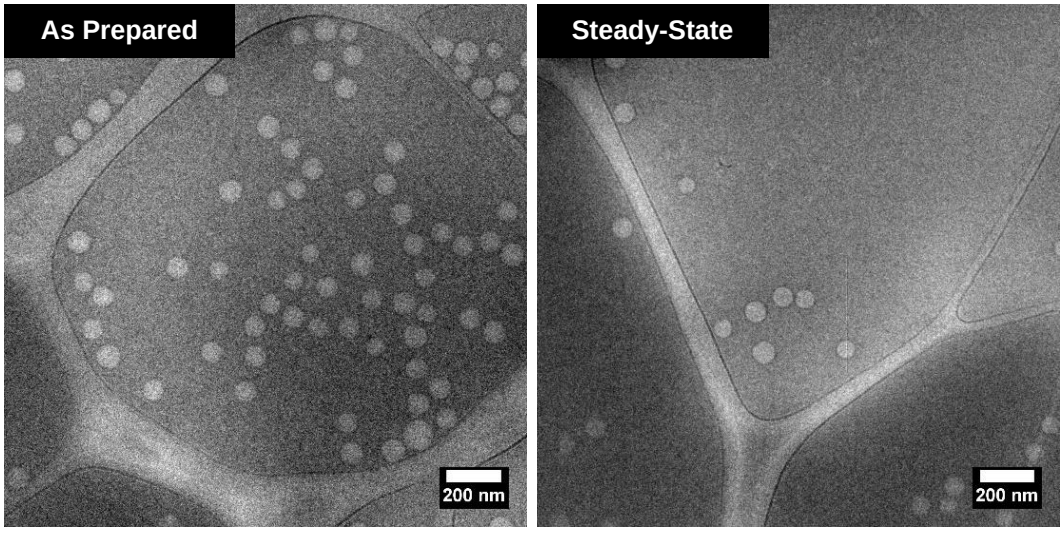

Figure 4.3: LP-TEM of 0.25 wt % BO(27-27) in [C2mim][TFSI] as prepared by DD ($\langle R_{core} \rangle$ = 50 ± 7 nm) and steady-state ($\langle R_{core} \rangle$ = 38 ± 3 nm) after annealing at 170 °C for 3000 min.

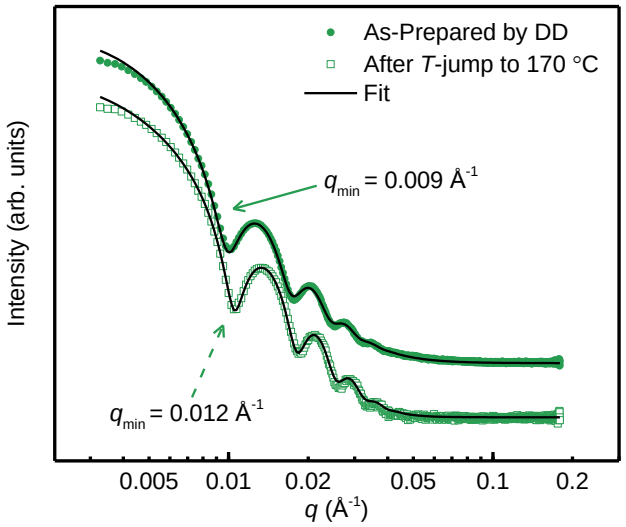

Figure 4.4: SAXS of 0.25 wt % BO(27-27) in [C2mim][TFSI] prepared by direct dissolution (filled green circles) and at steady-state after a *T*-jump to 170 °C (open green squares). The scattering data were fit to the Pedersen model (black lines) and were vertically shifted for clarity. The arrows indicate the q position of the first minimum in the form factor where $\langle R_{core} \rangle \approx 4.493/q_{min}$.

As noted above, prior work on the equilibration kinetics of PB-PEO in ILs relied on ensemble average methods, such as the work reported in Chapter 3, to determine the evolution of micelle size during a *T*-jump, and while the observed substantial decrease in the hydrodynamic radius and core radius is consistent with fragmentation, this phenomenon has yet to be observed *in-situ*.[89–91] By annealing the solutions directly in the electron microscope, a series of images were obtained throughout the micelle relaxation process, and the evolution of the core morphology was monitored during fragmentation. Representative *in-situ* high-temperature LP-TEM images are shown in Figure 4.5 and 4.6 for 0.25 wt % BO(25-22) and BO(27-27) in [C2mim][TFSI] at 170 °C, respectively.

Ideally, the time evolution of individual micelles would be recorded during annealing, but there are significant constraints on this experiment. First, the characteristic equilibration times for the polymers studied here are on the order of $10^2 – 10^3$ min, making it difficult to track a single micelle in the TEM without causing significant electron beam damage. Second, the particles observed in LP-TEM are mobile and able to diffuse out of the image frame throughout the experiment. Thus, while the time series of images shown here are obtained for the same area of the sample grid, it is difficult to establish how many micelles remained within in the field of view throughout the annealing process.

From Figure 4.5, the BO(25-22) micelle cores appear to be spherical, yet the distribution of core radii is quite significant after heating at 170 °C for 2 min (Figure 4.5a). After 20 min of annealing, some micelles become distinctly elliptical, and the core appears elongated compared to the image at 2 min; this is presumably the first stage of fragmentation (Figure 4.5b). After 180 min of annealing, the elongated cores appear more like a "peanut" with the formation of a shallow neck, which we interpret as the second major morphological change to the micelle structure during fragmentation (Figure 4.5c). After annealing for 400 min at 170 °C, a finer neck is observed in one micelle core undergoing fragmentation (Figure 4.5d). This fine neck formation was the last anisotropic morphology observed in BO(25-22) micelles during the experiment, and is therefore likely close to the final step in fragmentation, *i.e.*, the transition state, before the complete separation of the core into two smaller, spherical micelles.

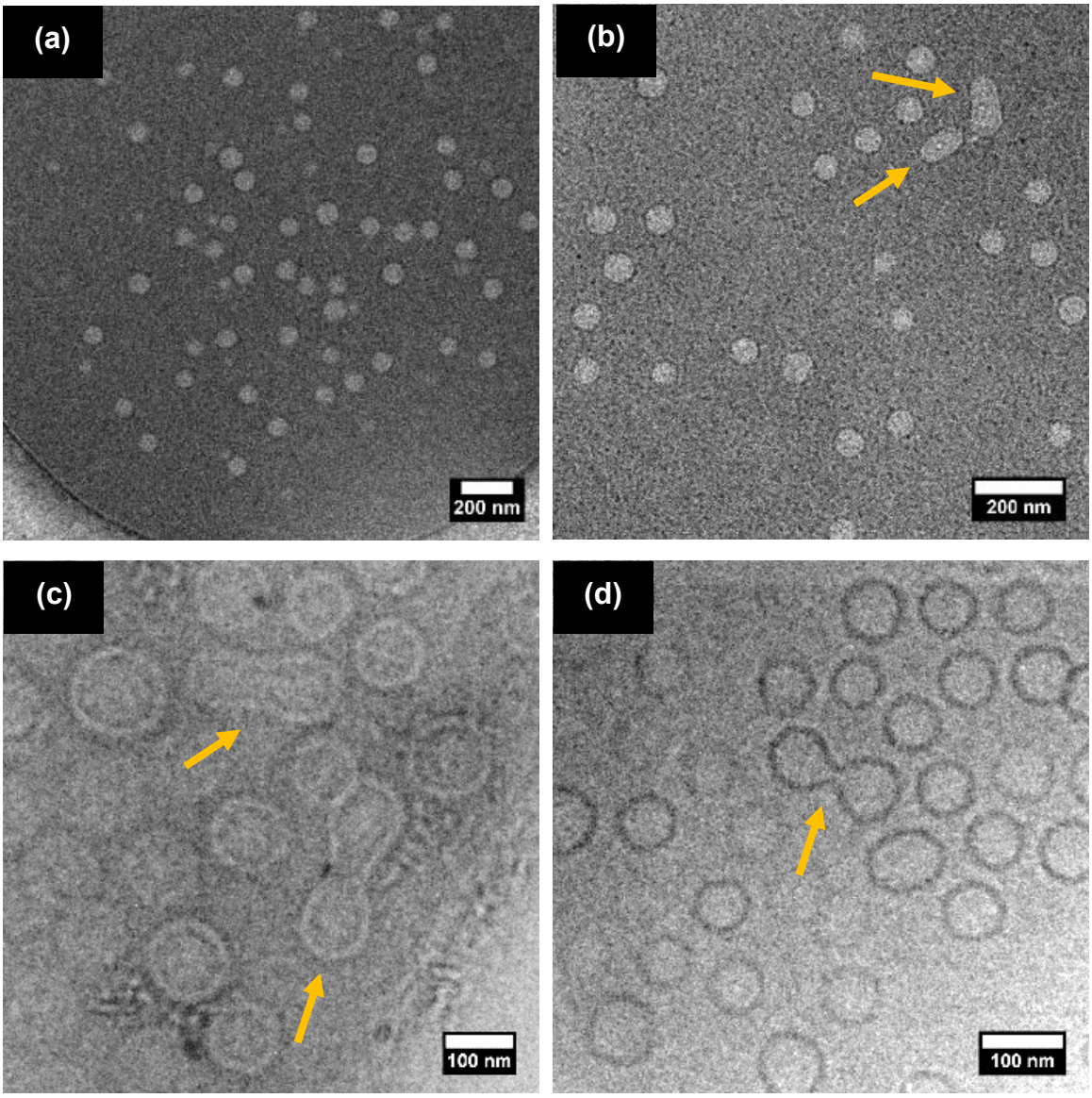

Figure 4.5: *In-situ* LP-TEM images of 0.25 wt % BO(25-22) in [C_2mim][TFSI] annealing at T = 170 °C for (a) 2 min, (b) 20 min, (c) 180 min, and (d) 400 min. Orange arrows indicate micelles referenced in the text. The electron dose rate was 9.8 $e^{-}/Å^2s$ at a magnification of 15k×.

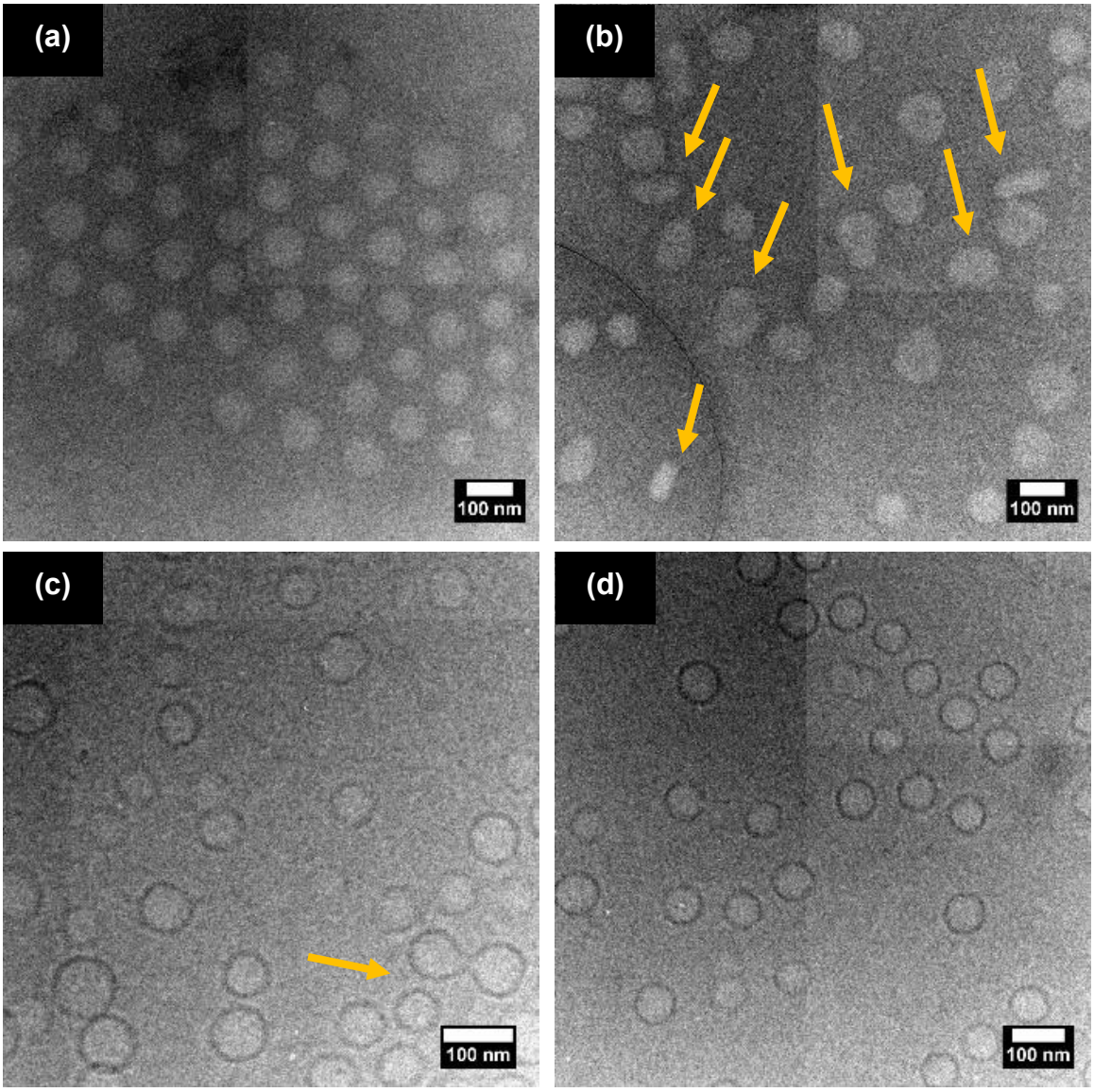

Figure 4.6: *In-situ* LP-TEM images of 0.25 wt % BO(27-27) in [C_2mim][TFSI] annealing at T = 170 °C for (a) 5 min, (b) 45 min, (c) 320 min, and (d) 450 min. Orange arrows indicate micelles referenced in the text. The electron dose rate was 9.8 $e^{-}/Å^2s$ at a magnification of 15k×.

As shown in Figure 4.6, a similar evolution of the core morphology was observed for 0.25 wt % BO(27-27) in [C_2mim][TFSI]. Note that the equilibration kinetics for this sample

are slightly slower than for BO(25-22) micelles at 170 °C, and about an order of magnitude slower than for BO(8-7) micelles. A more quantitative study of the effect of molar mass on fragmentation kinetics is presented in Chapter 5. The PB cores remain spherical after annealing at 170 °C for 5 min (Figure 4.6a), but a variety of more elongated micelles emerge after annealing for 45 min (Figure 4.6b). It is interesting to note the variety of anisotropic core morphologies observed in the 45 min image, and some particles appear to have formed a slight necking point. The fine-neck formation in one micelle was also observed for this sample after 320 min of annealing (Figure 4.6c), and after 450 min of annealing the PB core morphology again appears spherical, but distinctly smaller (Figure 4.6d). The evolution of BO(8-7) micelles in [C_2mim][TFSI] during annealing at 170 °C proceeds by the same general mechanism observed for BO(25-22) and BO(27-27) micelles, and *in-situ* LP-TEM images for this polymer are shown in Figure 2.20.

It is important to address the contrast variation observed in the *in-situ* LP-TEM images. At short annealing times, the micelle cores appear bright, with minimal appearance of Fresnel fringes. During high temperature annealing the changes in sample height causes a variation of focus, which is likely the cause for the appearance of darker Fresnel fringes at longer times. This change in sample thickness is relatively common in the LP-TEM literature, particularly for the open environmental chamber used here.[133,182–184] Due to the transient nature of the fragmenting micellar structures, such as the one highlighted in Figure 4.6c, focus adjustments were difficult to perform. In this experiment, the beam was blanked (*i.e.*, turned off) between each time point image; this approach mitigates additional

beam damage to the specimen, but makes it difficult to perform focus adjustments in a timely manner. However, we conclude that this change in focus and the appearance of dark Fresnel fringes in some of the images is due to the experimental setup, and not due to changes in the mass distribution of the micelle core.

Additionally, the influence of beam damage on the micelle structure is anticipated to be negligible compared to the effect of the electron beam on the stability of the free-standing ionic liquid films.[91,133] This is because the time required to observe beam damage effects to the sample (on the order of 10 min) is longer than the time required to rupture an IL film, which was found to be almost instantaneous when film rupture did occur. We observed that the ionic liquid films become less stable at higher magnifications (> 20k×) and at elevated temperatures, where the formation of holes in the liquid films becomes common. At higher temperatures, the liquid layers can burst and adhere to the holey carbon support. This phenomenon has been reported previously for ionic liquids in open environment LP-TEM,[133] and some examples of beam-damaged ionic liquid films are shown in Figure 4.7.

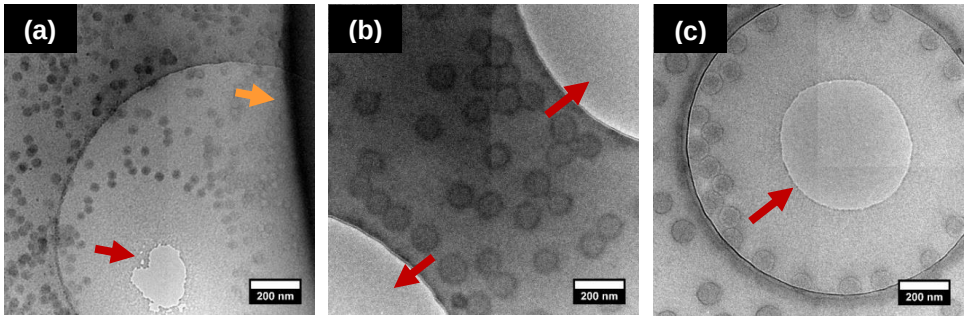

Figure 4.7: Examples of beam damage observed in LP-TEM experiments at T = 170 ºC. Beam damage to the ionic liquid was indicated by either a dark ionic liquid region, a hole

in the liquid film, or complete rupture of the film. Examples of beam damage to the PB cores are shown by the inverted contrast (*i.e.* micelle core appears darker than the ionic liquid) present in all three images. (a) 0.25 wt % BO(8-7) in [C_2mim][TFSI] where the red arrow point to the ruptured ionic liquid layer and the orange arrow points to dark region that is due to beam damage of the ionic liquid. (b) 0.25 wt % BO(25-22) in [C_2mim][TFSI] where the red arrows point to the ruptured ionic liquid layer. (c) 0.25 wt % BO(27-27) in [C_2mim][TFSI] where the red arrows point to the ruptured ionic liquid layer.

To quantify the change in the core dimensions during fragmentation, an automated image analysis routine was applied to the images in Figures 4.5, 4.6, and 2.20 (details in Section 2.6.2). The count histograms generated by the automated image analysis routine for the change in core radius and area are shown in Figures 4.8, 4.9, and 4.10.

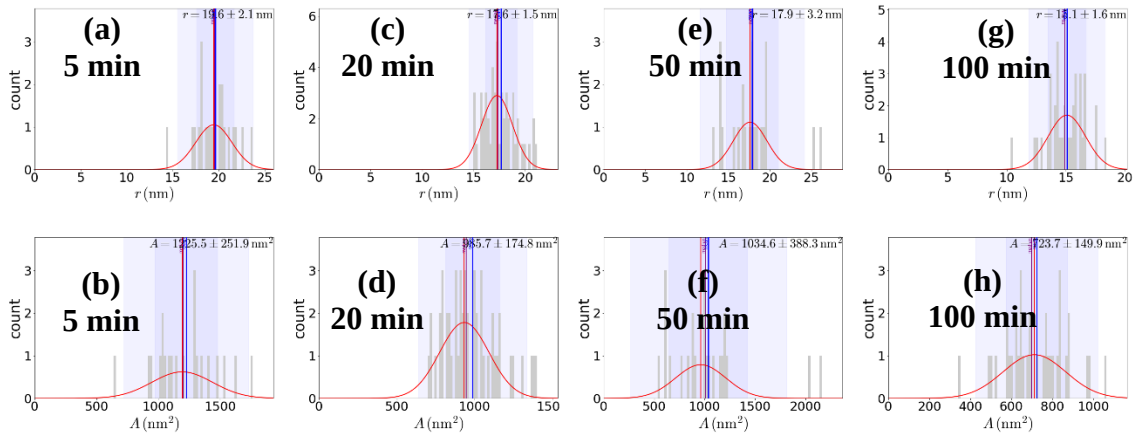

Figure 4.8: Automated image analysis histograms of micelle core radius (a, c, e, g) and area (b, d, f, h) from *in-situ* LP-TEM images of 0.25 wt % BO(8-7) in [C_2mim][TFSI] annealing at T = 170 °C.

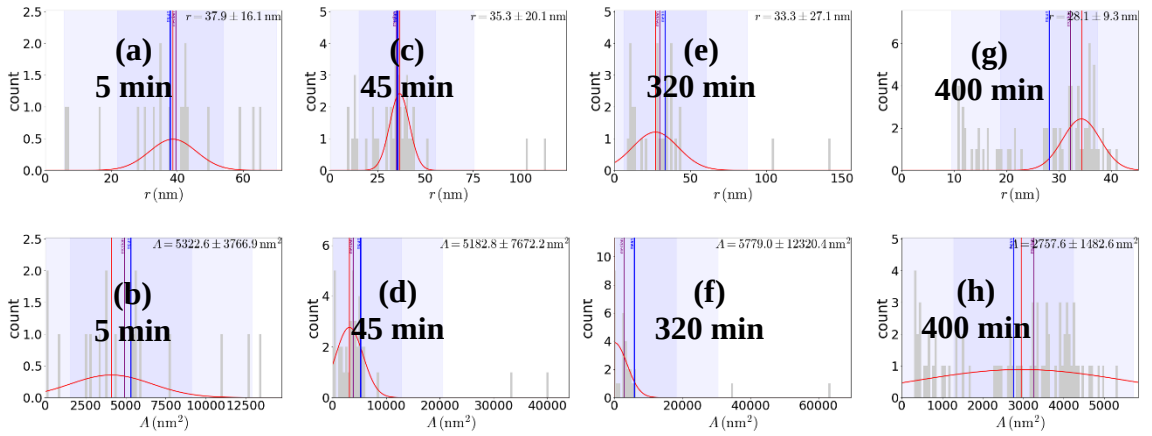

Figure 4.9: Automated image analysis histograms of micelle core radius (a, c, e, g) and area (b, d, f, h) from *in-situ* LP-TEM images of 0.25 wt % BO(25-22) in [C_2mim][TFSI] annealing at T = 170 °C.

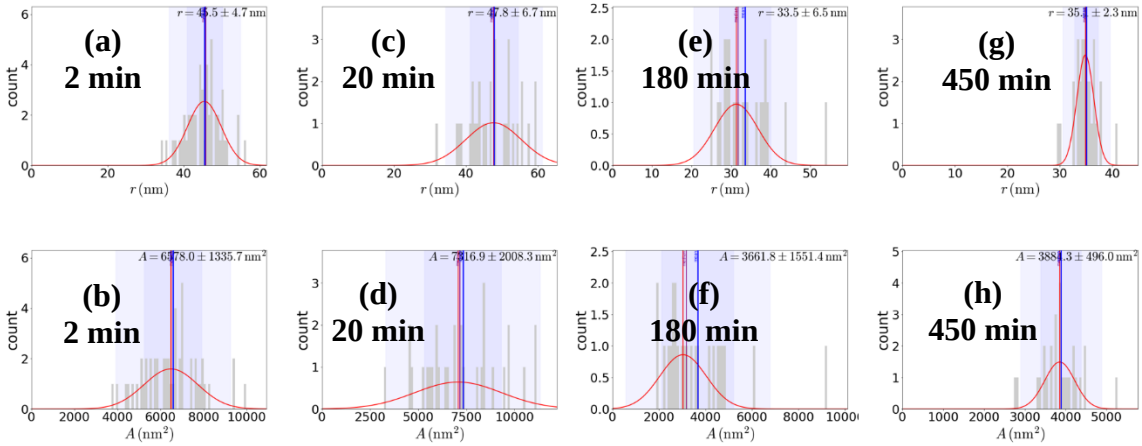

Figure 4.10: Automated image analysis histograms of micelle core radius (a, c, e, g) and area (b, d, f, h) from *in-situ* LP-TEM images of 0.25 wt % BO(27-27) in [C_2mim][TFSI] annealing at T = 170 °C.

The average values obtained from image analysis are summarized in Table 4.1. For each time point $\langle R_{core} \rangle$ (nm), σ_{core} (nm), mean aggregation number Q, core area A (nm^2),

average eccentricity ε (where $\varepsilon = 0$ for a perfectly spherical object and ε approaches 1 for elongated, high aspect-ratio objects), and $P \times R_{core}/A$ were determined.

Table 4.1: Automated image analysis of *in-situ* LP-TEM images for 0.25 wt % PB-PEO in [C_2mim][TFSI] while annealing at T = 170 °C.

t (min)	$\langle R_{core} \rangle$[a] (nm)	σ_{core} (nm)[b]	Q[c]	A (nm^2)[d]	ε[e]	$P \times R_{core}/A$[f]	s_{core}[g]
BO(8-7)							
5	20	2	1750	1230	0.5	2.1	2.2
20	18	2	1270	986	0.6	2.1	1.9
50	18	3	1340	1040	0.5	2.2	2.0
100	16	2	972	814	0.3	2.1	1.8
BO(25-22)							
2	38	9	6840	5322	0.4	2.1	2.9
20	35	11	3890	5180	0.6	2.5	2.4
180	33	8	3270	5780	0.5	2.7	2.3
400	28	5	2440	2758	0.1	2.1	2.0
BO(27-27)							
5	46	5	7520	6580	0.4	2.1	3.0
45	48	7	8720	7320	0.5	2.2	3.1
320	34	7	3000	3660	0.4	2.2	2.2
450	35	2	3450	3880	0.3	2.1	2.3

[a]$\langle R_{core} \rangle = (A/\pi)^{1/2}$. [b]One standard deviation from $\langle R_{core} \rangle$. [c]Aggregation number (Q) calculated as $4\pi\langle R_{core} \rangle^3/(3V_{PB})$ assuming the core is devoid of solvent, and V_{PB} is the volume per core chain. [d]Surface area measured by automated image analysis. [e]Eccentricity calculated by fitting an ellipse to the object, determined as $\varepsilon = (1 - b^2/a^2)^{1/2}$; for a perfect circle, $\varepsilon = 0$, and for an infinitely long object $\varepsilon = 1$. [f]Perimeter × average radius/area is equal to 2 for a perfectly spherical boundary, and the boundary is less spherical if this value is greater than 2. [g]s_{core} is the degree of core block stretching calculated as $\langle R_{core} \rangle$ divided by the root-mean-square end-to-end distance of the core block.

In Table 4.1 $P \times R_{core}/A$ is the perimeter of the micelle core multiplied by the radius divided by the area, which describes how circular the boundary of the particle is; if $P \times R_{core}/A = 2$ the boundary is perfectly circular and if $P \times R_{core}/A > 2$ the particle boundary has more undulations. From Table 4.1, $\langle R_{core} \rangle$ for all samples decreases with time, as expected for micelle fragmentation. Interestingly, the ratio of the aggregation numbers from the final to the initial time points are 0.55 for BO(8-7), 0.36 for BO(25-22), and 0.46 for BO(27-27). This indicates that the BO(8-7) micelles after 100 min of annealing are approximately half of the size of the micelles after only 5 min of annealing. Similarly, BO(27-27) micelles contain approximately half of the number of polymer chains after 450 min of annealing compared to at only 5 min of annealing. The decrease in Q for BO(25-22) is slightly more substantial, as the average number of chains per micelle decrease by almost 70% after 400 min of annealing compared to 2 min of annealing at 170 °C. This decrease in Q for all samples further confirms that the micelles are equilibrating primarily by fragmentation. It also suggests that most, if not all, micelles undergo only a single

fragmentation event during these experiments. This would be expected if the initial average aggregation were approximately a factor of two larger than the equilibrium value. Another interesting trend is the change in the micelle eccentricity ε throughout fragmentation. This was calculated by fitting micelle images using the typical definition of anisotropy for an ellipse. From Table 4.1, the average ε for all micelles at the shortest annealing times is ~ 0.4 – 0.5, which could imply shape fluctuations at short timescales related to τ_0 from Equation 3.2, and the eccentricity increases for intermediate annealing times, consistent with the elongation of micelles during the early stages of fragmentation. For the longest annealing times, the eccentricity decreases to $\varepsilon \leq 0.3$, which indicates the micelle core achieves an even more spherical morphology after fragmentation.

TR-SAXS at 170 °C was used to corroborate the change in $\langle R_{core} \rangle$ with annealing time, where the background-subtracted 1D scattering intensity was fit to the Pedersen form factor model for block copolymer micelles with the Percus-Yevick hard sphere structure factor to directly obtain $\langle R_{core} \rangle$ and σ_{core}, with superior temporal resolution and counting statistics than LP-TEM.[153,157] The $\langle R_{core} \rangle$ versus time from TR-SAXS for 0.25 wt % BO(8-7) in [C_2mim][TFSI] and 0.25 wt % BO(27-27) in [C_2mim][TFSI] are shown in Figure 4.11, superposed with $\langle R_{core} \rangle$ determined by *in-situ* LP-TEM from Table 4.1. Longer annealing times are readily obtained with TR-SAXS, and a steady-state $\langle R_{core} \rangle$ is reached, indicated by the second plateau at longer *t* in Figure 4.11.

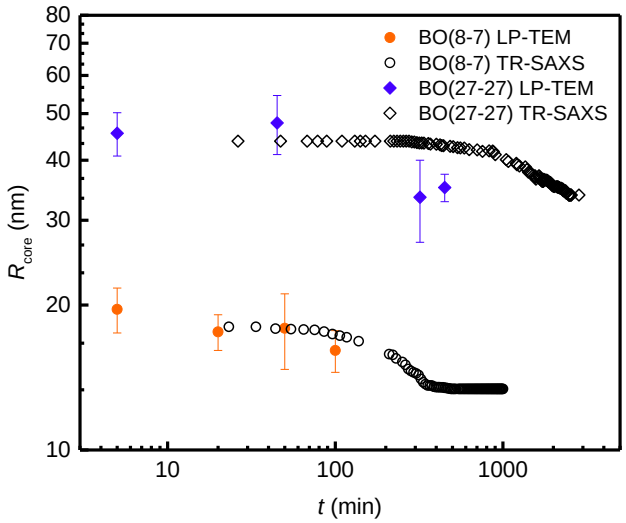

Figure 4.11: Image analysis of *in-situ* LP-TEM of 0.25 wt % BO(8-7) (orange circles) and BO(27-27) (blue diamonds) in [C_2mim][TFSI] at 170 °C. The change in $\langle R_{core} \rangle$ determined using an automated image analysis program, where several micelles were measured for each time point. The error bars represent one standard deviation from the average value. Data points in black were determined by fitting 1D scattering intensity obtained by TR-SAXS to the Pedersen model with the Percus-Yevick hard sphere structure factor.

For BO(8-7) micelles, $\langle R_{core} \rangle$ values from TR-SAXS and LP-TEM agree remarkably well as a function of time, which indicates that $\langle R_{core} \rangle$ from the automated TEM image analysis is consistent with the ensemble average. This agreement is expected because the fragmentation time for BO(8-7) micelles is approximately 200 min, which is a reasonable interval over which to conduct the LP-TEM experiment. The $\langle R_{core} \rangle$ obtained by each experiment for BO(27-27) micelles agrees within the errors of the two techniques at early times, but the $\langle R_{core} \rangle$ values from LP-TEM at 320 min and 450 min are slightly smaller than the averages obtained by TR-SAXS. As the number of micelles measured in Figure 4.6 to obtain this average is relatively small (~ 20 – 30 micelles), this is presumably not an

adequate representation of the ensemble $\langle R_{core} \rangle$. Nevertheless, the kinetic information from TR-SAXS supports the statistics obtained through analysis of the LP-TEM images.

To rationalize the fragmentation kinetics reported previously for BO(8-7) in ionic liquids,[89–91] and to understand the morphological evolution of the PB micelle core during fragmentation observed here, we consider the degree of chain stretching in the core (s_{core}) and the corona (s_{corona}), along with the extent of corona crowding in the transition state for fragmentation. The proposed transition state of a "two-spherical-compartment" micelle is illustrated in Figure 4.12 as structure **IV**. The equilibrium size and morphology of a micelle is governed by the free energy balance among the core, corona, and the interface.[36] The as-prepared micelles and those imaged at the shortest annealing times exhibit a relatively high degree of stretching in the core chains as shown in Table 4.1, where s_{core} was calculated as $\langle R_{core} \rangle$ divided by the root-mean-square end-to-end distance of the PB block.

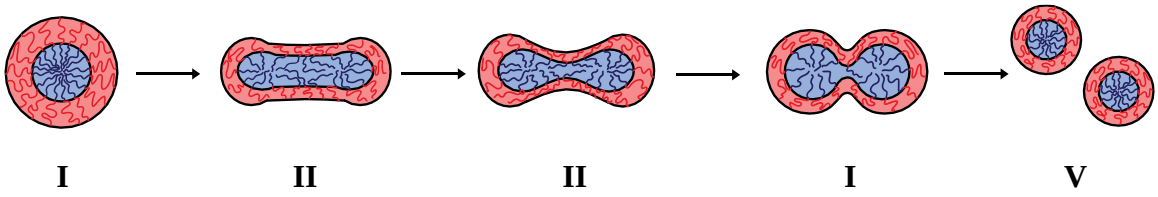

Figure 4.12: Schematic illustration of block copolymer micelle fragmentation where the as-prepared micelles begin to elongate at short annealing times to relieve chain stretching in the larger, as-prepared micelles, followed by necking at longer annealing times, and the thinning of the neck, which is believed to be the rate-limiting step to this process, and finally separation of the micelle core and corona into two smaller micelles.

The relative instability of the intermediates shown in Figure 4.12 likely explains the observation of a small number of anisotropic micelles with a neck for BO(25-22) and BO(27-27). It is likely that the stability of the shapes illustrated in Figure 4.12 decreases as **I** > **II** > **III** > **IV**. Therefore, the number of micelles observed in the experiment decreases in that order. Previous reports on the fragmentation kinetics of BO(8-6) in [C_2mim][TFSI], such as those in Chapter 3, found that the change in $\langle R_{core} \rangle$ with annealing time is well-described by a compressed exponential with a compression exponent of 2.[90,91]

Although the mechanism of fragmentation was observed here, the origin of the compressed exponential behavior remains to be determined. The first stage of fragmentation proceeds via the elongation of spherical micelles into a roughly cylindrical morphology. This change in core area is entropically favorable due to the relief of both core and corona chain stretching in the as-prepared micelles, but opposed by the increased surface area. From Chapter 3, measurements of fragmentation in five different ionic liquids revealed that the kinetics were largely independent of surface tension, indicating that the transition state does not involve exposing the core to the solvent.[91] Rather, the kinetic barrier most likely results from increased corona crowding during the neck formation in "two-compartment" micelles. In this scenario the thinning of the neck, represented as the fourth structure in Figure 4.12, causes increased corona crowding for the polymer chains near the necking point, and is presumably close to the transition state.

4.4 – Summary

In summary, we report the direct observation of block copolymer micelle fragmentation for PB-PEO in [C_2mim][TFSI]. Due to the nonvolatility of ionic liquids, high-temperature LP-TEM allows imaging of dynamic processes of soft matter in solution. From this chapter, we identified four distinct changes in micelle core morphology during fragmentation. Initially, the micelles prepared by direct dissolution are spherical, and upon heating to 170 °C the micelles begin to elongate. The elliptical micelles then begin to form a slight neck, or peanut shape, and then the neck thins out to connect two nearly spherical core compartments, which we hypothesize is the rate limiting step in micelle fragmentation; further annealing results in the necked micelles to fragment into two smaller micelles.

Chapter 5 – Effect of molar mass on micelle fragmentation kinetics[*,§]

5.1 – Introduction

The molar mass (M) of diblock copolymers not only affects the equilibrium structure of micelles, but also the dynamics and equilibration kinetics in solution.[18,23,116] The aggregation number Q of a given micelle can vary depending on history, and micelle equilibration occurs by some combination of the exchange of individual chains,[17,19,22–24,26–28,114] fusion, or fragmentation.[90,117,120,126] Halperin and Alexander proposed that the chain exchange kinetics depends on a characteristic relaxation time, τ_{ex}, that depends on the core and corona block lengths as $\tau_{ex} \sim N_{core}^{2/25} N_{corona}^{9/5} \exp(E_a/k_B T)$, where E_a is the activation barrier given by $\gamma N_{core}^{2/3} b^2$, where γ is the interfacial tension between the core block and the solvent and b is the monomer size of the core block.[95] Experimentally, the effect of M on micelle chain exchange kinetics has been found to be very strong, with the barrier to exchange increasing linearly with N_{core} in contrast to the Halperin-Alexander model.[18,21,24,26,27,185] Interestingly, it has also been reported that increasing N_{corona} of PS-

[*]Reprinted in part with permission from Early, J. T.; Block, A.; Yager, K. G.; Lodge, T. P. Molecular Weight Dependence of Block Copolymer Micelle Fragmentation Kinetics. *J. Am. Chem. Soc.*, **2021**, *143*, 7748 – 7758. Copyright © 2021 American Chemical Society.
[§]This work was conducted in collaboration with Alison Block and Dr. Kevin G. Yager.

PEP micelles in squalane could increase the rate of chain exchange by up to two orders of magnitude,[23] whereas studies of C_{27}-PEO$_n$ in water showed that increasing N_{corona} had the opposite effect.[18]

Despite the dramatic effect of M on chain exchange, essentially nothing is known experimentally about the influence of M on the kinetics of fragmentation.[90] In general, fragmentation is much slower than chain exchange for micelles that are not too far from equilibrium, thus increasing M should lead to longer fragmentation timescales.[90,120,126] As demonstrated in Chapters 3 and 4, techniques including DLS and TR-SAXS are useful for monitoring changes in micelle size over a wide range of timescales.[44,89,104,109,113] This is primarily due to the relatively short acquisition times required for DLS (*i.e.*, minutes), and particularly for synchrotron SAXS (seconds). Previous work by Kelley *et al*. showed that micellization of PB-PEO in mixtures of tetrahydrofuran and water occurs via a distinct bimodal pathway, and the increase of $\langle R_h \rangle$ was monitored using DLS for as long as 90 days.[113] They concluded that the initial growth of micelles occurs via micelle fusion.[113] Additionally, the combination of DLS and TR-SAXS proves invaluable for determining micelle fragmentation kinetics, as $\langle R_h \rangle$ and $\langle R_{core} \rangle$ are readily determined. Again, chain exchange by itself is not expected to change $\langle R_{core} \rangle$ to a significant extent.[90,91,123]

As discussed in Section 1.3.2, a theoretical model of the M dependence, specifically the dependence on N_{corona}, of micelle fusion and fragmentation has been reported.[97] Dormidontova proposed a scaling model to account for micellization in systems far from equilibrium, and assumed that micelle fragmentation proceeds by the reverse mechanism

as micelle fusion.[97] The relaxation time (τ_{fus}) for fusion of two micelles with similar aggregation numbers ($Q_1 \leq Q_2$) scales with aggregation number and the degree of polymerization of the corona block as $\tau_{fus} \sim N_{corona}^{17/5} Q_1^{4/5} Q_2$.[97] The strong N_{corona} dependence on the characteristic time for fusion is attributed to the corona chain deformation during the merging process, where the corona chains of a smaller micelle penetrate into the corona region of a larger micelle. Based on this observation for micelle fusion, the fragmentation times for micelles with small Q were estimated to scale with $N_{corona}^{17/5}$ as well. The fragmentation time was predicted to scale as $\tau_{frag} \sim N_{corona}^{9/5} Q^{13/5}$ for micelles with very large aggregation numbers $Q > (cV_{corona})^{5/2} N_{corona}^2$, where c is the micelle concentration and V_{corona} is the molar volume of a corona-forming chain.

Previous work on the micellization of PB-PEO in [C_2mim][TFSI] showed that the solution preparation method influences $\langle R_h \rangle$. For micelles prepared by DD of the bulk copolymer in the IL, the $\langle R_h \rangle$ of the as-prepared micelles is quite large compared to micelles prepared by the co-solvent method, in which a good solvent is introduced to the solution and slowly evaporated away.[89] For micelles prepared by DD, $\langle R_h \rangle$ decreased to approximately half of the original size when annealed at 170 ºC.[89] Further work on this system showed that the time-dependent decrease in $\langle R_h \rangle$ was consistently well-described by a compressed exponential function $\exp(-(t/\tau)^n)$ with an exponent $n \approx 2$, even at lower annealing temperatures (T = 120 ºC).[90] As discussed in Chapter 3, to further understand the mechanism, the fragmentation kinetics for one molar mass of PB-PEO was studied in [$C_x$mim][TFSI] based ILs, where x = 1, 2, 4, 6, and 8.[91] The solvent quality with respect to

the PB core-forming block was improved by increasing the length of the alkyl chain on the IL cation, but it was found that the improvement in solvent quality did not affect the fragmentation kinetics of PB-PEO micelles to any significant extent.[91] In Chapter 4, we reported the direct observation of micelle fragmentation for three molar masses of PB-PEO in [C_2mim][TFSI] using high-temperature LP-TEM, and intermediate structures close to an apparent transition state for micelle fragmentation were observed *in situ*.[92]

The absence of experimental results on the M dependence of fragmentation kinetics motivates the work in this chapter. Here we monitor the fragmentation of PB-PEO in the IL [C_2mim][TFSI] where the total molar mass of the diblock is varied from 11 to 100 kg mol^{-1} while maintaining a constant volume composition $f_{PEO} \approx 0.4$. The thermal stability and nonvolatility of ILs is once again advantageous here as the solutions can be heated to much higher temperatures than organic solvents, allowing the kinetics of fragmentation to be studied over more accessible time scales.[140]

5.2 – Materials and methods

Synthesis and Characterization. Six molar masses of PB-PEO were synthesized by two-step sequential anionic polymerization, as described in Section 2.1.1.[136] M_n, $Đ$, and f_{PEO} for BO(x-y) were determined by a combination of SEC-MALS (Wyatt Dawn Heleos II) and ^{1}H NMR in $CDCl_3$ (^{1}H NMR, Varian Inova 500). The dn/dc for the diblocks were estimated as the weight average of the refractive index increments for PB in THF (dn/dc = 0.119

mL/g) and PEO in THF (d*n*/d*c* = 0.068 mL/g).[138] Detailed molecular characterization is provided in Figure 2.2 and Table 2.1.

Solution Preparation by DD. All solutions were prepared by the direct dissolution (DD) method described in Section 2.3.1, unless noted otherwise.

DLS. *T*-jump and multi-angle room temperature scattering measurements were performed according to Section 2.4.2.

Liquid-Phase Transmission Electron Microscopy (LP-TEM). High-temperature LP-TEM of BO(53-46) in [C_2mim][TFSI] was conducted as described in Section 2.6.2.

TR-SAXS. Time-resolved SAXS experiments were conducted according to the *in-situ* SAXS procedure described in Section 2.5.3.

5.3 – Results and discussion

Initial and final micelle dimensions

SAXS and DLS were used to determine the effect of molar mass on the size of micelles, both as prepared by direct dissolution and also at steady-state after annealing at 170 °C. The initial size of micelles prepared by DD and after a *T*-jump to 170 °C were determined by multi-angle DLS and SAXS, in terms of the overall micelle radius R_h and the micelle core radius R_{core}, respectively. The overall radii were determined by fitting the intensity autocorrelation function from DLS to a 2nd order cumulant expansion shown in Equation

2.15. The radii increased monotonically with increasing *M*, as seen in Figures 2.12 and 5.1. REPES analysis of DLS data, shown in Figure 2.12, for the as-prepared and steady-state $\langle R_h \rangle$ of 0.25 wt % PB-PEO in [C_2mim][TFSI] corroborates the fitting results in that the $\langle R_h \rangle$ decreases after annealing at 170 °C for all values of *M*. The percent decrease in $\langle R_h \rangle$ after long-time annealing at 170 °C was 31%, 36%, 33%, 17%, 25%, and 29% for BO(6-5), BO(8-7), BO(10-9), BO(25-22), BO(27-27), and BO(53-46), respectively.

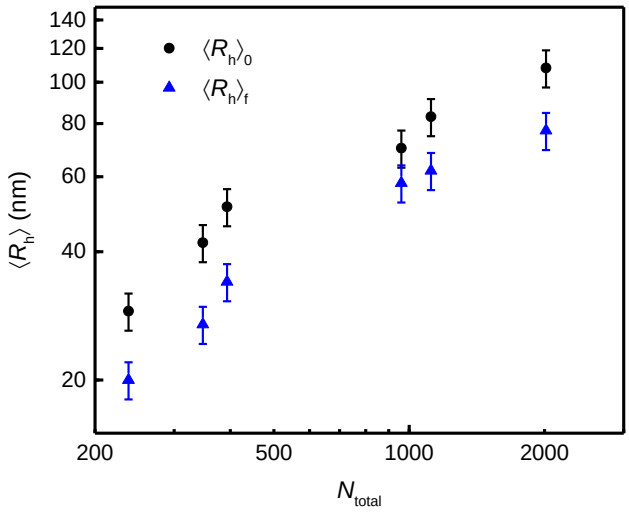

Figure 5.1: Dependence of $\langle R_h \rangle$ on the total degree of polymerization N_{total} for 0.25 wt % PB-PEO in [C_2mim][TFSI] as-prepared by DD (black circles) and at steady-state after annealing at 170 °C (blue triangles). The error bars represent estimated 10% measurement uncertainty.

To determine the effect of *M* on R_{core}, SAXS was performed at room temperature before and after annealing at 170 °C. The background corrected scattering intensity traces versus *q* for the as-prepared and steady-state micelles are shown in Figures 5.2a and 5.2b, respectively. The as-prepared micelles for all polymers, except for BO(53-46), are well-

defined spheres. This is confirmed by the distinct first minimum in the form factor and oscillations at higher q values, which generally reflect a narrow size distribution and a modest interfacial width at the core-corona interface.[153,171] The increased size dispersity of BO(53-46) micelles may be due to the fixed time used to prepare the solutions, and longer dissolution times may be required to obtain more narrowly distributed initial micelles. Similarly, well-defined smaller spherical micelles are obtained after annealing at 170 °C, as shown in Figure 5.2b, for all but the largest polymer.

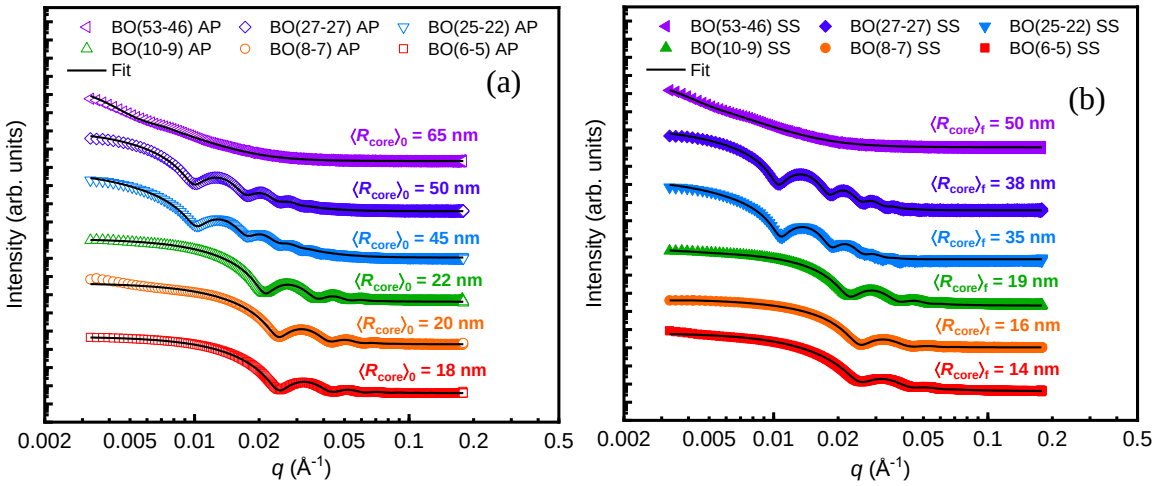

Figure 5.2: SAXS intensity versus q, on logarithmic scales, for 0.25 wt % PB-PEO in [C2mim][TFSI] (T = 27 °C) (a) as prepared by DD and (b) steady-state after annealing at 170 °C. The black lines represent the best fits of the scattering data to the Pedersen model for block copolymer micelles described in Section 2.5.1. The data sets are shifted vertically for clarity.

As with the total micelle radius, $\langle R_{core} \rangle$ from SAXS was found to increase monotonically with M for the as-prepared and steady-state micelles, as shown in Figure 5.3. The changes in micelle size before and after annealing at 170 °C are summarized in

Table 5.1. The percent decrease in $\langle R_{core} \rangle$ exhibits a similar trend to that observed in $\langle R_h \rangle$; the percent decrease in $\langle R_{core} \rangle$ with increasing M was 22%, 20%, 14%, 22%, 24%, and 23%. From $\langle R_{core} \rangle$, the average aggregation number Q was calculated assuming that the micelle core is devoid of solvent (i.e., $Q = (4\pi \langle R_{core} \rangle^3)/3V_{core}$, where $V_{core} = M_{n,PB}/\rho_{PB}N_{Av}$ is the molar volume of one core block). This is a reasonable approximation for such a strongly segregated system. From these values, the fragmentation process results in a population of micelles with an average aggregation number that is approximately half that of the initial aggregation number. The core size of strongly segregated block copolymer micelles should scale as $R_{core} \sim N_{core}^{3/5}$.[35,37,79]

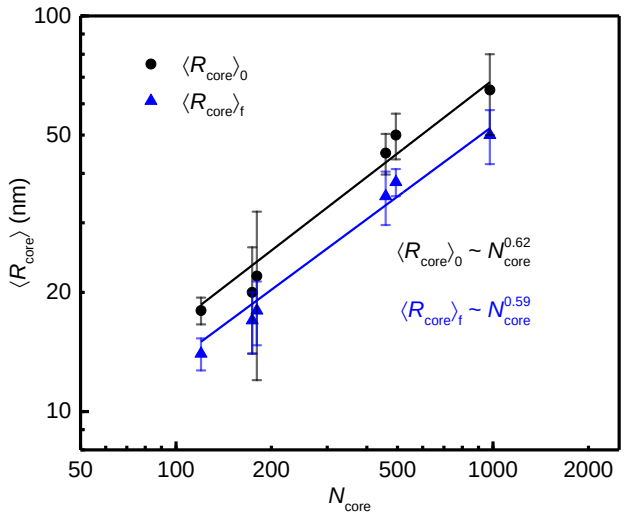

Figure 5.3: Scaling of $\langle R_{core} \rangle$ versus N_{core} for 0.25 wt % PB-PEO in [C$_2$mim][TFSI] as prepared by DD (black circles) and steady-state after annealing at 170 °C (blue triangles). The solid lines for the as prepared and steady-state values represent the scaling obtained for $\langle R_{core} \rangle_0 \sim N_{core}^{0.62}$ (black line) and $\langle R_{core} \rangle_f \sim N_{core}^{0.59}$ (blue line). The error bars represent $\pm\sigma_{core}$ shown in Table 5.1.

Table 5.1: Micelle Dimensions for 0.25 wt % Solutions in [C_2mim][TFSI] at T = 27 °C, Before and After Annealing at 170 °C.

As Prepared by Direct Dissolution							
Sample	$\langle R_h \rangle_0$ (nm)	$\langle \mu_2/\Gamma^2 \rangle_0$	$\langle R_{core} \rangle_0$ (nm)	$\sigma_{core,0}$ (nm)	Q_0[a]	$s_{core,0}$[b]	$s_{corona,0}$[c]
BO(6-5)	29	0.08	18	1.4	1260	2.1	2.2
BO(8-7)	42	0.25	20	6.0	1900	2.5	2.5
BO(10-9)	51	0.23	22	10.0	2400	2.4	3.3
BO(25-22)	70	0.09	45	5.3	8060	2.9	1.9
BO(27-27)	83	0.17	50	6.6	11000	3.4	2.2
BO(53-46)	108	0.18	65	15.0	11400	3.2	2.1
Steady-state After Annealing at 170 °C							
Sample	$\langle R_h \rangle_f$ (nm)	$\langle \mu_2/\Gamma^2 \rangle_f$	$\langle R_{core} \rangle_f$ (nm)	$\sigma_{core,f}$ (nm)	Q_f[a]	$s_{core,f}$[b]	$s_{corona,f}$[c]
BO(6-5)	20	0.05	14	1.3	930	2.0	0.8
BO(8-7)	27	0.05	16	3.0	950	1.6	1.5
BO(10-9)	34	0.04	19	3.3	1500	2.1	1.7
BO(25-22)	58	0.07	35	5.4	3800	2.3	1.7
BO(27-27)	62	0.09	38	3.0	4900	2.6	1.6
BO(53-46)	77	0.09	50	7.8	5200	2.0	1.8

[a]The aggregation number (Q), where the subscripts 0 and f denote initial and final values, respectively, was calculated as $4\pi\langle R_{core}\rangle^3/(3V_{PB})$ assuming the core is devoid of solvent,

and $V_{PB} = M_{n,PB}/\rho_{PB}N_{Av}$ is the volume per core chain, $\rho_{PB} = 0.89$ g/cm^3, N_{Av} is Avogadro's number, and $M_{n,PB}$ is the molar mass of PB, as reported in Table 2.1.

[b]The degree of core chain stretching (s_{core}), was calculated as $\langle R_{core} \rangle$ divided by the root mean square end-to-end distance of the core block using the statistical segment length of PB, $b = 5.9$ Å.[186]

[c]The degree of corona chain stretching (s_{corona}) calculated as the corona thickness ($L_{corona} = \langle R_h \rangle - \langle R_{core} \rangle$) divided by the root mean square end-to-end distance of the corona block using the statistical segment length of PEO, $b = 6.0$ Å.[135]

As shown in Figure 5.3, $\langle R_{core} \rangle$ increases with N_{core} essentially as predicted for both the as-prepared and steady-state samples. This former result is somewhat unexpected, in that micelles prepared by DD apparently adhere to an equilibrium scaling relationship of $\langle R_{core} \rangle$ with N_{core}, even though they are clearly far from equilibrium. This result highlights another difficulty in assessing the true equilibrium state in block copolymer micelles – apparent adherence to an equilibrium scaling law is far from a sufficient criterion.

Fragmentation Kinetics

The substantial decrease in micelle size after annealing has previously been established as being due to micelle fragmentation.[90,91] Thus, the fragmentation kinetics were studied for six molar masses of PB-PEO in [C$_2$mim][TFSI] using *T*-jump DLS and TR-SAXS to determine the dependence of τ_{frag} on the total degree of polymerization of the copolymer N_{total}. The change in $\langle R_{core} \rangle$ was monitored with high temporal resolution by heating micelle solutions directly on the beamline to 170 °C under vacuum, and the scattering was

measured during annealing for 48 h. Representative TR-SAXS data for 0.25 wt % BO(6-5), BO(10-9), and BO(27-27) in [C2mim][TFSI] are shown in Figure 5.4, 5.5, and 5.6, respectively, where the background-subtracted intensity traces versus *q* are plotted as a function of annealing time. Analogous TR-SAXS data for BO(8-7) and BO(25-22) are shown in Figures 2.17b and 2.18b, respectively.

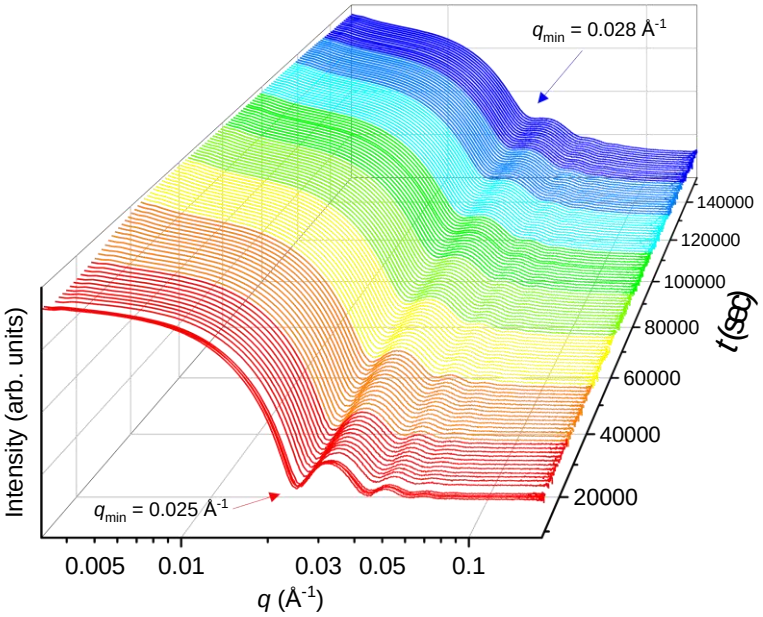

Figure 5.4: TR-SAXS intensity (logarithmic scale) as a function of *q* showing the evolution in the micelle core radius while annealing at 170 °C for 0.25 wt% BO(6-5) in [C2mim][TFSI]. The position of the first minimum in the form factor increases from q_{min} = 0.025 Å^{-1} for short annealing times to q_{min} = 0.028 Å^{-1} at longer annealing times.

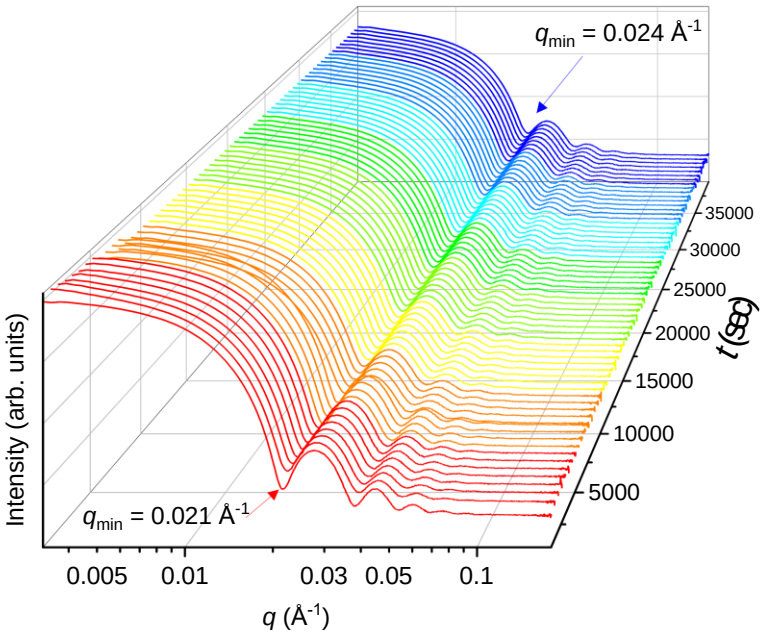

Figure 5.5: TR-SAXS intensity (logarithmic scale) as a function of *q* showing the evolution in the micelle core radius at 170 °C for 0.25 wt % BO(10-9) in [C$_2$mim][TFSI].

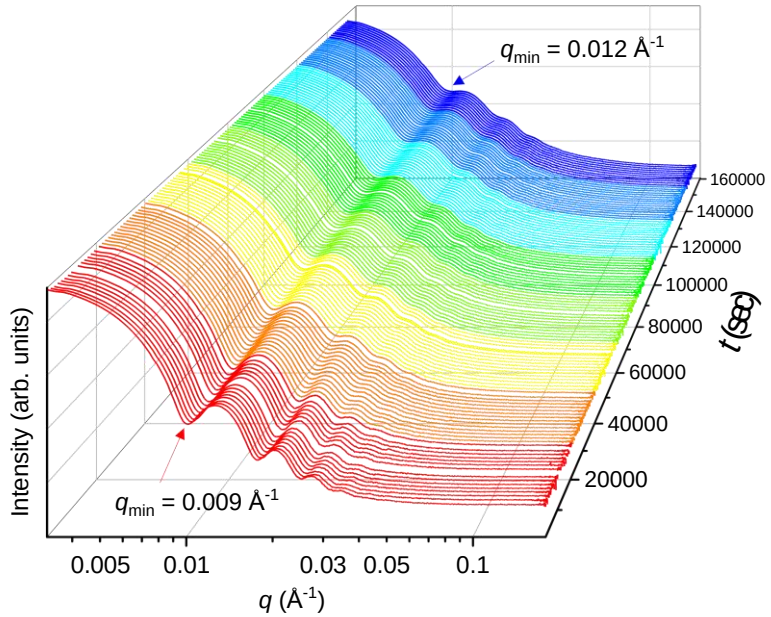

Figure 5.6: TR-SAXS intensity (logarithmic scale) as a function of *q* showing the evolution in the micelle core radius at 170 °C for 0.25 wt% BO(27-27) in [C$_2$mim][TFSI].

As shown in Figure 5.6, the form factor for BO(27-27) shows a first minimum at q_{min} = 0.009 Å^{-1} after annealing at 170 °C for approximately 26 min, which corresponds to $\langle R_{core} \rangle$ = 50 nm from the hard sphere approximation where qR_{core} = 4.493. Throughout the course of an annealing experiment, the q-position of the first minimum shifts progressively to higher values of q, indicative of a smaller $\langle R_{core} \rangle$. After annealing at 170 °C for approximately 2500 min, q_{min} shifts to 0.012 Å^{-1} and $\langle R_{core} \rangle$ = 37.4 nm. Fitting the scattering data to the block copolymer micelle model before and after annealing at 170 °C shows good agreement with the hard sphere approach used to determine $\langle R_{core} \rangle$ from TR-SAXS.

To quantify the fragmentation kinetics, the change in micelle size, either $\langle R_h \rangle$ or $\langle R_{core} \rangle$, is normalized according to Equation 2.17, and i = h or core denotes either the average hydrodynamic radius from DLS or the average micelle core radius from SAXS. The normalized change in size was fit to the Avrami equation or "compressed" exponential, shown in Equation 2.18, where τ_{frag} is the fragmentation time constant and n is the Avrami exponent. The normalized change in $\langle R_h \rangle$ from DLS is shown in Figure 5.7, and that for $\langle R_{core} \rangle$ in Figure 5.8.

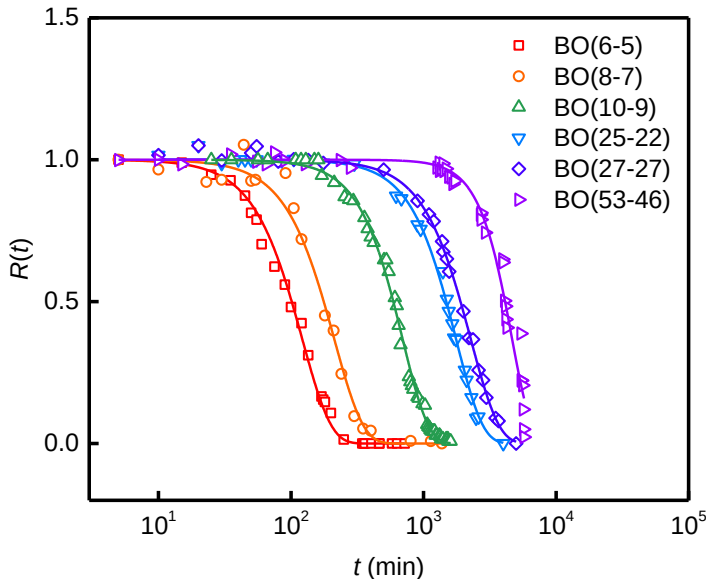

Figure 5.7: Time dependence of normalized $\langle R_h \rangle$ for 0.25 wt % solutions of PB-PEO *M* series in [C_2mim][TFSI]. DLS measurements were performed at a scattering angle of 90° and a relaxation temperature of 170 °C. Solid lines represent best fits to Equation 2.18 with $\langle n \rangle = 2.2 \pm 0.3$.

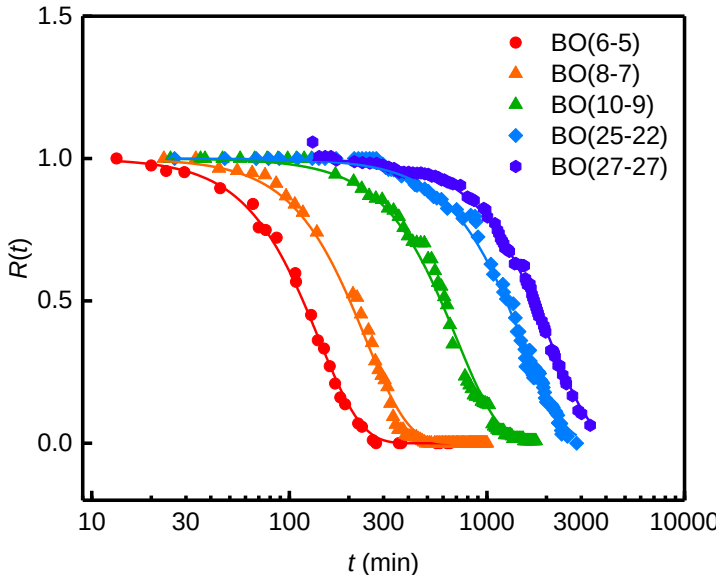

Figure 5.8: Time dependence of normalized $\langle R_{core} \rangle$ for 0.25 wt % solutions of PB-PEO in [C_2mim][TFSI]. TR-SAXS measurements were performed at a relaxation temperature of 170 °C. Solid lines represent best fits to Equation 2.18 with $\langle n \rangle = 2.0 \pm 0.1$.

From DLS, the change in $\langle R_h \rangle$ while annealing at 170 °C is well-described by Equation 2.18, with an exponent of 2.0–2.3, as shown in Table 5.2. The fitting was performed using n as an adjustable parameter, resulting in an average value of $n = 2.2 \pm 0.3$. Refitting the data with a fixed exponent of $n = 2.0$ resulted in fits of similar quality with only modest variations in τ_{frag}, as shown in Table 5.3. Attempts to fit the change in normalized $\langle R_h \rangle$ to a single or a double exponential resulted in poor fit quality for the former, and physically unreasonable values of τ_{frag} for the latter. This is consistent with previous reports on a single, low molar mass of PB-PEO in various ionic liquids.[89–91]

Table 5.2: M dependence of τ_{frag} determined by T-jump DLS and TR-SAXS at 170 °C for 0.25 wt % BO(x-y) in [C_2mim][TFSI].

	T-jump DLS		TR-SAXS	
Sample	τ_{frag} (min)	n	τ_{frag} (min)	n
BO(6-5)	120 ± 10	2.0	140	2.1
BO(8-7)	200 ± 75	2.0	250	2.2
BO(10-9)	690 ± 90	2.2	710	2.2
BO(25-22)	1750 ± 170	2.2	1500	2.1
BO(27-27)	2300 ± 250	2.1	2070	2.3
BO(53-46)	5000 ± 360	2.7	-	-

Table 5.3: M dependence of τ_{frag} determined by T-jump DLS and TR-SAXS at 170 °C for 0.25 wt % BO(x-y) in [C_2mim][TFSI] when n is fixed at 2.0.

	T-jump DLS	TR-SAXS
Sample	τ_{frag} (min)	τ_{frag} (min)
BO(6-5)	120 ± 10	142
BO(8-7)	200 ± 75	243
BO(10-9)	695 ± 90	702
BO(25-22)	1760 ± 170	1489
BO(27-27)	2270 ± 250	2093
BO(53-46)	4780 ± 360	-

From Figure 5.8, the fragmentation time τ_{frag} increases strongly with M; the 11 kg mol^{-1} diblock has a τ_{frag} on the order of 100 min, whereas the 100 kg mol^{-1} diblock has $\tau_{frag} \approx$ 5000 min. To corroborate the results from T-jump DLS, the time-dependent change in R_{core} from SAXS at 170 °C was normalized according to Equation 2.18. The results for all polymers except BO(53-46) are shown in Figure 5.8. The dispersity in R_{core} for BO(53-46) made estimating the radius using the hard sphere approximation based on the first minimum of the form factor unreliable. Although the intensity traces for BO(53-46) could be fit to the Pedersen model, the error in $\langle R_{core} \rangle$ was quite large. The large micelle size

dispersity and exponent by DLS shown in Table 5.2 for BO(53-46) are likely due to the fact that this sample is prepared using the same dissolution time as the lower *M* samples, whereas the micellization process might be much slower for the highest *M*. Due to this uncertainty, the fragmentation kinetics were determined only for the other five *M*. In general, values of τ_{frag} obtained from DLS and SAXS agree remarkably well.

M dependence of fragmentation time.

Comparing theory and experiment

As noted above, the fragmentation kinetics for PB-PEO in [C$_2$mim][TFSI] depend strongly on *M*. Figure 5.9 shows the values of τ_{frag} obtained from fitting the normalized change in micelle size to Equation 2.18 as a function of the total degree of polymerization; the results from DLS and SAXS are very consistent. The fit to a power law gives the scaling $\tau_{frag} \sim N_{total}^{1.8 \pm 0.1}$. As discussed in Section 1.3.2, Dormidontova proposed a scaling model for micelle fusion kinetics, and further assumed that fragmentation would proceed as the reverse of micelle fusion, and thus the *N* scaling would be the same for both processes.[97] For micelles with large aggregation numbers (*Q*) with respect to their equilibrium size, Dormidontova defined a characteristic time for corona deformation (τ_{def}) as the inverse translational diffusion constant for chains, where V_B is the molar volume per monomer unit in the corona.[97]

$$\tau_{frag} \approx \tau_{def} \cong \frac{\eta_s V_B}{k_B T} N_{corona}^{9/5} Q^{13/5} \tag{5.1}$$

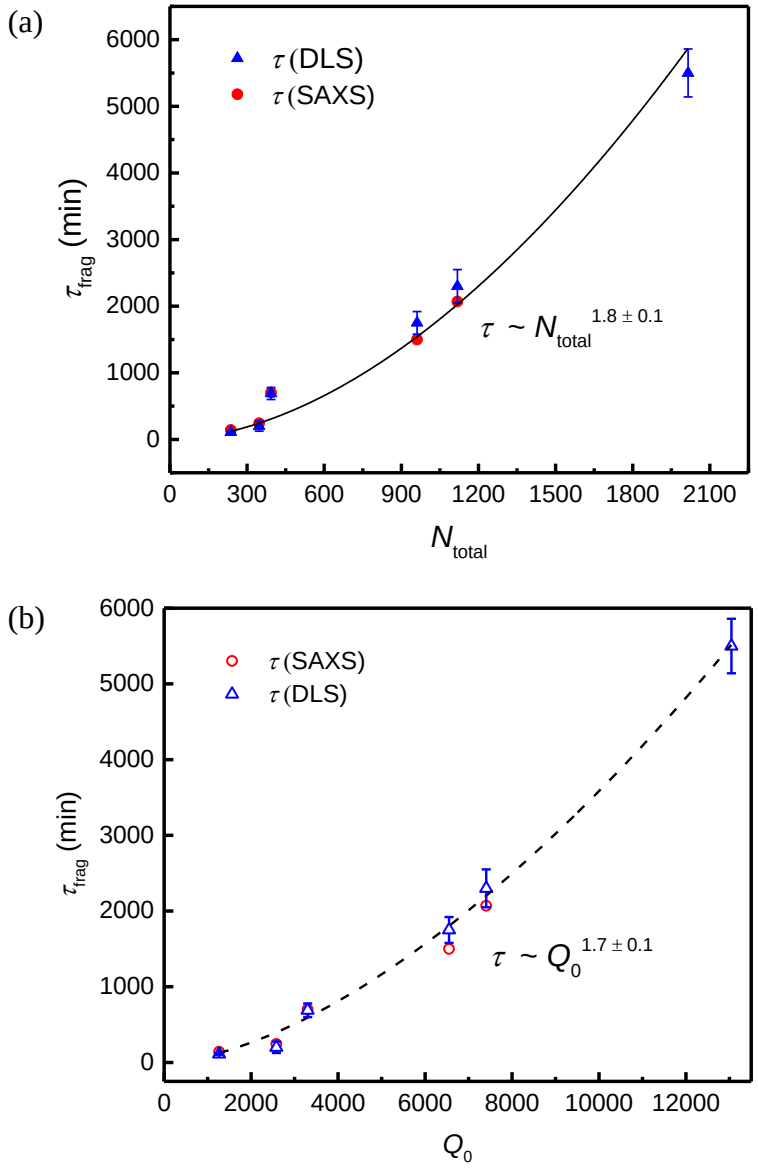

Figure 5.9: Dependence of the fragmentation time constants (τ_{frag}) determined by *T*-jump DLS (red circles) and TR-SAXS (blue triangles) on (a) N_{total} and (b) Q_0. From this plot, the scaling of τ_{frag} with Q_0 is nearly identical to the N_{total} dependence.

Assuming the fragmenting micelle is large, Dormidontova's theory proposes that $\tau_{frag} \sim N_{corona}^{1.8}$ at constant Q, as shown in Equation 5.1. It should be noted that for very large aggregation numbers, such as the ones obtained for the as-prepared micelles, there is at most a small M dependence to Q. The Q dependence of τ_{frag} is shown in the Figure 5.9b, where $\tau_{frag} \sim Q_0^{1.7 \pm 0.1}$. The agreement between the scaling of τ_{frag} with N_{corona} and Q_0 implies that the strong Q dependence from Equation 5.1 does not reflect our experimental results, and this is consistent with the assumption that Q does not depend strongly on N_{total} for very large Q.

The results are apparently in excellent agreement with the theory. However, some caution is warranted. First, the theory does not anticipate the compressed exponential form in Equation 2.18, so there is clearly an aspect of the fragmentation mechanism that is not yet fully appreciated. Second, the separate effects of N_{core} and N_{corona} on the experimental fragmentation times cannot be assessed individually because the volume fraction of PEO in this work has been constant. Thus, the experimental scaling represents the dependence of the fragmentation time on the total degree of polymerization, which may not coincide with the dependence on N_{corona}. However, it does seem physically reasonable that the corona blocks play a much larger role in the process than the core blocks.

Further comparison of this model to the experimental results requires discussion of the time constants from the model and from estimates of corona dynamics. Here, we use Dormidontova's theory for fragmentation to estimate the corona deformation time. We then compare these values to rough estimates based on reptation theory; the two answers

differ by many orders of magnitude. In Dormidontova's model, following micelle core extension and necking, corona chains must reptate a certain distance R_0 to form two distinct micelles. The corona separation involves the reorganization of the "inner" corona regions for the fragmenting micelle, which constitutes a decrease in solvent concentration and a redistribution of corona block monomers among the blobs, as well as an increase in blob size.

The corona chain deformation was estimated using the analogy between the motion of the chain of blobs inside a sphere of radius R_0 and the rotational motion of rod-like polymer chains in semidilute solutions.[187] The process is described by two parts: 1) the rotation inside of the original tube of blobs where the corona chain conformation is described as a radially oriented chain of blobs increasing in size as the distance from the core increases,[42] as shown in Figure 1.2, and 2) the tube relaxation. The angle which the polymer chains can rotate (φ) is given by

$$\varphi \cong \frac{\xi}{L_{\text{corona}}} = N_{\text{corona}}^{3/5} Q^{-3/10} V_{\text{corona}}^{1/3} \tag{5.2}$$

where ξ is the blob size at a distance R_0 from the core and L_{corona} is the corona thickness. The blob size is calculated according to $\xi = (cV)^{-3/4} V^{1/3}$. The characteristic time for corona chain disentanglement τ_B plays a role in the tube relaxation time, which is defined by Equation 5.3.

$$\tau_B = \frac{\eta_s V_B}{k_B T} N_{corona}^{9/5} Q^{8/5} \tag{5.3}$$

The characteristic time for corona separation, given by Equation 5.1, for large is estimated by τ_B/φ^2 as shown in Equation 5.4.

$$\tau_{def} \cong \frac{\tau_B}{\varphi^2} \cong \frac{\eta_s V_B}{k_B T} N_{corona}^{9/5} Q^{13/5} \tag{5.4}$$

Resulting values of τ_{def} are collected in Table 5.4. Cleary these estimates are unrealistically large, and orders of magnitude greater than the experimental times

Table 5.4: Estimates at T = 170 ºC of the corona chain disentanglement time (τ_{def}) calculated according to Equation 5.4 where τ_e = 10 ns and the longest relaxation time by reptation (τ_{rep}) for PEO.

Sample	N_{corona}	L_{corona} (nm)	τ_{def} (s)	τ_{rep} (s)	τ_{arm} (s)	$\tau_{rep,3Me}$ (s)	$\tau_{arm,3Me}$ (s)
BO(6-5)	118	11	7.1×10^{6}	3.4×10^{-7}	8.9×10^{-6}	1.3×10^{-8}	3.8×10^{-8}
BO(8-7)	173	22	1.5×10^{7}	1.1×10^{-6}	1.3×10^{-4}	4.0×10^{-8}	2.0×10^{-7}
BO(10-9)	213	29	7.8×10^{7}	2.0×10^{-6}	7.2×10^{-4}	7.5×10^{-8}	5.3×10^{-7}
BO(25-22)	502	25	3.7×10^{9}	2.7×10^{-5}	2.7×10^{1}	9.8×10^{-7}	9.9×10^{-5}
BO(27-27)	624	33	1.1×10^{10}	5.1×10^{-5}	1.5×10^{3}	1.9×10^{-6}	5.8×10^{-4}
BO(53-46)	1038	43	3.1×10^{10}	2.3×10^{-4}	6.2×10^{8}	8.7×10^{-6}	1.2×10^{-1}

The longest relaxation time for a linear chain can be estimated according to the reptation model by Equation 5.5,

$$\tau_{\text{rep}} \cong \frac{N_{\text{corona}}^3}{N_{\text{e}}} \tau_{\text{seg}} \cong \frac{N_{\text{corona}}^3}{N_{\text{e}}^3} \tau_{\text{e}} \tag{5.5}$$

where $N_{\text{e}} = M_{\text{e}}/M_0$ is the number of monomers per entanglement, the entanglement molar mass (M_{e}) for PEO is 1.6 kg mol^{-1}, and the statistical segment length of PEO is b = 6.0 Å.[135] The entanglement time for PEO at 25 ºC in the melt, τ_{e}, was reported previously by Niedzwiedz *et al*. as 10 ns.[188] Values of τ_{rep} from Equation 5.5 are also presented in Table 5.4. In reality, the corona chains are solvated, which might change the friction compared to the melt, and are relaxing at elevated temperature, but these factors will not alter the conclusion. More importantly, corona chains are tethered at one end, making the situation more analogous to a star polymer. In such a case, the relaxation time would be increased by a factor of approximately exp(M/M_{e}). This gives the quantity τ_{arm} in Table 5.4. However, because of dilution, M_{e} would be increased with respect to the melt. If we simply assume the concentration is about 33% in a compressed corona, then M_{e} would be increased by a factor of 3. These leads to the two final estimates in the table. The robust conclusion from this crude analysis is that the PEO corona chain dynamics alone cannot account for the magnitude of the fragmentation times we observe.

Dependence of fragmentation time on N

To rationalize the dependence of the fragmentation kinetics on *N*, one must consider the transition state and activation barrier of this process. Previous work from Chapter 3 on this system revealed that the fragmentation kinetics were unaffected by changes in the solvent selectivity towards the core-forming block,[91] thus indicating independence of interfacial tension. In Chapter 4, the presumed "peanut" shaped transition state was imaged by high-temperature LP-TEM. Accordingly, we propose that severe corona crowding in the transition state is the primary barrier to fragmentation. When considering the free energy of polymer chains in a block copolymer micelle at equilibrium, the interfacial free energy and the free energy of chains in the corona contribute more to the total free energy of the micelle compared to the free energy of chains in the core, but in this case the core blocks are very stretched meaning the core block likely contributes somewhat to the overall free energy.[36,37,189] We calculate the free energy of PB-PEO micelles as prepared by DD, after annealing at 170 ºC, and for the proposed "peanut-shaped" transition state, shown in Figure 5.10 for BO(53-46) micelles, and which was observed in Chapter 4 for PB-PEO in [C_2mim][TFSI] by high-temperature liquid phase transmission electron microscopy.[92]

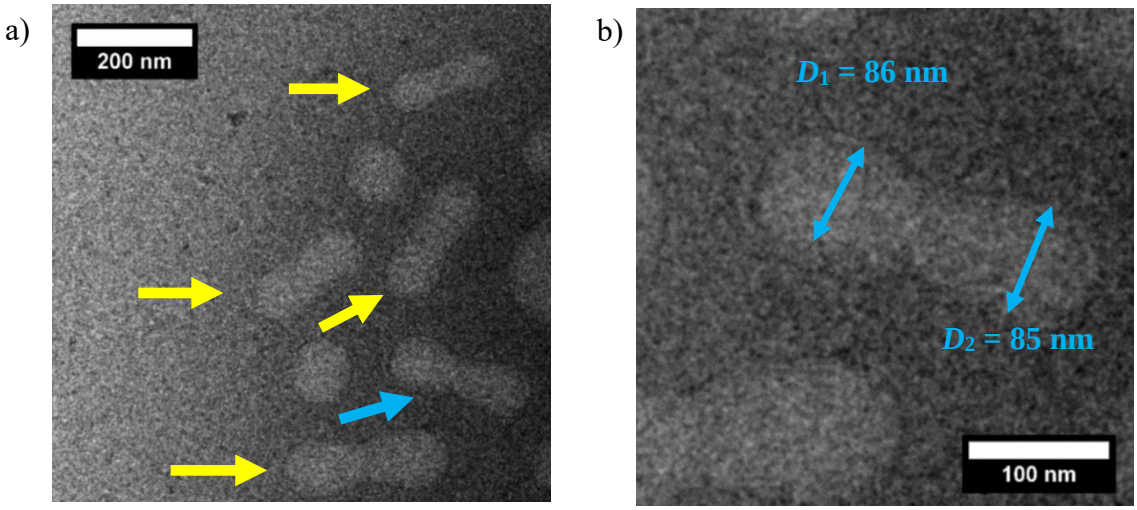

Figure 5.10: High-temperature liquid-phase transmission electron micrograph obtained at 170 °C (t_{anneal} = 500 min) of 0.25 wt % BO(53-46) in [C2mim][TFSI]. a) The proposed near-transition state (yellow and blue arrows) observed is consistent with the "peanut" shaped micelle cores observed in Chapter 4 for BO(8-7), BO(25-22), and BO(27-27) in [C2mim][TFSI].[92] b) Dimensions of "peanut" shaped micelle (blue arrow in Figure 5.10a) where the core radius of each spherical cap is $\langle R_{core} \rangle_f \approx 50$ nm.

A schematic illustration of the transition state is shown in Figure 5.11. The total free energy of a spherical block copolymer micelle in solution (F_{mic}) was well described by Zhulina *et al.*,[36] and is given by the sum of the free energy contribution from the core chains (F_{core}), the free energy of the corona chains (F_{corona}), and the interfacial energy (F_{int}). Therefore, the free energy can be estimated for the as-prepared and steady state micelles. More details on this calculation are provided in the Appendix, and were previously reported by Zhulina *et al.*[36] Because the transition state morphology is "peanut-shaped" the transition state free energy cannot be treated in the same manner as the spherical micelles before and after fragmentation.

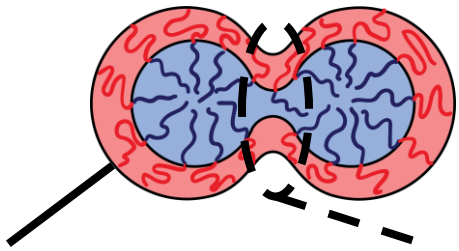

Spherical corona region: $n_{blob,sphere} \approx n_{blob,0} = F_{corona,0}/k_BT$

"Neck" region: $n_{blob,neck} \approx 2n_{blob,0} = 2F_{coron,0}/k_BT$

Figure 5.11: Schematic illustration of the "peanut" shaped transition state based on previous direct observation via high-temperature liquid-phase TEM and Figure 5.10.[92] The dashed circle indicates the location of the neck region in the transition state where ~1/6 of corona chains overlap. The outer ends of each sphere in the micelle are the spherical region of the corona. Because 1/6 of the chains are overlapped in the neck region where $n_{blob,neck} = 2n_{blob,0}$ the total number of blobs in the transition state is $n_{blob,TS} = 5n_{blob,0}/6 + n_{blob,0}/3$ and the free energy of the corona in the transition state is given by $F_{corona,TS}/kT = (5/6) F_{corona,0}/kT + (1/3)F_{corona,0}/kT$. This calculation is described in more detail in the text.

To calculate the corona free energy in the transition state, the fraction of corona chains overlapped in the neck region indicated in Figure 5.11 must be estimated. The transition state is represented schematically in Figure 5.11, and the regions of the peanut-shaped transition state used in discussion of this calculation are labeled in the figure. We propose that the increase in the local concentration of corona chains near the neck point, *i.e.*, the increase in the number of blobs per corona chain n_{blob}, in the formation of the transition state is the primary barrier to fragmentation. To estimate the degree of corona crowding in the transition state first, we estimate the fraction of corona overlap in the transition state, and then relate the overlap fraction to the concentration of blobs per PEO chain in the neck

region using the theory from Zhulina, *et al*.[36] To estimate the fraction of corona chain overlap ($f_{overlap}$) in the transition state (the neck region of Figure 5.11) we simplify the geometry of the transition state by using two steady state micelles that are overlapping to the point where the cores are touching, as shown in Figure 5.12, and calculate the area of corona overlap within the triangle of the figure.

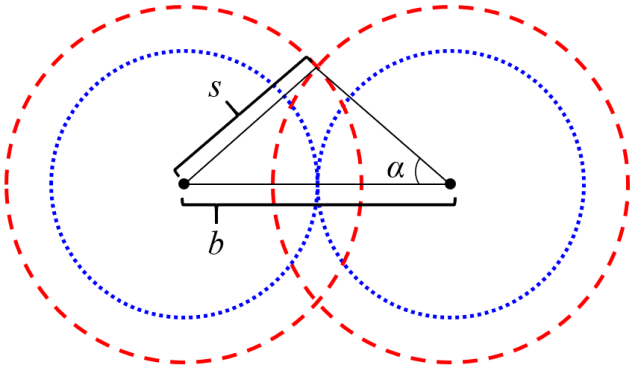

$$b = 2\,\langle R_{core}\rangle_f$$

$$s = \langle R_{core}\rangle_f \left(1 + \frac{L_{corona}}{\langle R_{core}\rangle_f}\right)$$

Figure 5.12: Illustration of two spherical steady state micelles used to estimate the fraction of overlapping chains in the "peanut" shaped transition state.

In this case, the base of the triangle $b = 2\langle R_{core}\rangle_f$, the sides of the triangle are both described as $s = \langle R_{core}\rangle_f(1 + L_{corona}/\langle R_{core}\rangle_f)$, the two angles opposite of the triangle sides are α, and the angle opposite to the base of the triangle is β. The area of the entire triangle, A_{tri} is defined by:

$$A_{tri} = 2\langle R_{core}\rangle_f \tan\alpha \tag{5.6}$$

where α is determined from the law of cosines.

$$\alpha = \cos^{-1}\left[\frac{\langle R_{\text{core}}\rangle_f^2}{\left[\langle R_{\text{core}}\rangle_f\left(1+\frac{L_{\text{corona}}}{\langle R_{\text{core}}\rangle_f}\right)\right]\langle R_{\text{core}}\rangle_f}\right] \tag{5.7}$$

The area of the core regions (A_{sec}) within A_{tri} are subtracted from A_{tri}. These are determined by estimating the area of the sector within the circle according to Equation 5.8.

$$A_{\text{sec}} = \pi\langle R_{\text{core}}\rangle_f^2 \frac{\alpha}{360} \tag{5.8}$$

Then, the overlap area is given by $A_{overlap} = A_{tri} - 2A_{sec}$. To estimate the fraction of corona chain overlap the total area of the corona is calculated as $A_{corona} = \pi\langle R_h\rangle_f^2$, and the overlap fraction is given by Equation 5.9.

$$f_{\text{overlap}} = 2\left(\frac{A_{\text{overlap}}}{A_{\text{corona}} - A_{\text{sec}}}\right) = 0.16 \tag{5.9}$$

Using this simplified model for the transition state, illustrated in Figure 5.12, to determine the area of corona overlap in the transition state results in $f_{overlap}$ = 1/6 for all molar masses. The simplified model from Figure 5.12 was also adapted to calculate the overlap fraction of spherical micelles in three dimensions, which also gave an overlap fraction of 1/6 for all molar masses. Then, the concentration of PEO chains in the neck region of the transition state is determined by estimating the number of blobs per corona chain. In the neck region, the number of blobs per chain is expected to be approximately twice the number of blobs per chain in the as-prepared micelles ($n_{blob,neck} = 2n_{blob,sphere}$ =

$2F_{corona,0}/k_BT$), whereas the outer spherical regions would have $n_{blob,sphere} = F_{corona,0}/k_BT$, where the free energy is calculated using the as-prepared size of the micelle as discussed in the Appendix.

It is not immediately clear whether the number of blobs per chain is approximately two, three, or more times larger than the number of blobs per chain in the as-prepared micelles. Therefore, the values of $n_{blob,neck}$ were also approximated as exactly equal to, two times, and three times larger than $n_{blob,sphere}$ as shown in Table 5.5.

Table 5.5: Estimates of the free energies of the corona in the transition state, using $n_{blob,neck} = n_{blob,sphere}$ ($F_{corona,TS}(1)/k_BT$), $n_{blob,neck} = 2n_{blob,sphere}$ ($F_{corona,TS}(2)/k_BT$), and $n_{blob,neck} = 3n_{blob,sphere}$ ($F_{corona,TS}(3)/k_BT$). F_{corona}/k_BT in the transition state was calculated using the dimensions for as-prepared micelles.

BO(x-y)	(6-5)	(8-7)	(10-9)	(25-22)	(27-27)	(53-46)
$F_{corona,TS}(1)/k_BT$	3.8	4.2	4.7	11	12	16
$F_{corona,TS}(2)/k_BT$	4.4	5.0	5.5	13	14	19
$F_{corona,TS}(3)/k_BT$	5.0	5.7	6.3	14	16	21

The values in Table 5.5 were calculated using $n_{blob,neck} = n_{blob,sphere}$, the total corona free energy in the transition state is calculated as $F_{corona,TS}/k_BT = F_{corona,0}/k_BT$, these values are denoted as $F_{corona,TS}(1)/k_BT$. Using $n_{blob,neck} = 2n_{blob,sphere}$, the total corona free energy in the

transition state is calculated as $F_{corona,TS}/k_BT = (5/6)F_{corona,0}/k_BT + (1/3)F_{corona,0}/k_BT$, and is denoted as $F_{corona,TS}(2)/k_BT$ in Table 5.5. Finally, $F_{corona,TS}(3)/k_BT$ in Table 5.5 is calculated using $n_{blob,neck} = 3n_{blob,sphere}$. In this case, the total corona free energy in the transition state is calculated as $F_{corona,TS}/k_BT = (5/6)F_{corona,0}/k_BT + (1/2)F_{corona,0}/k_BT$.

The transition state free energy for the core and the interface was calculated using the steady state micelle dimensions. For the remainder of this discussion, the transition state corona free energy was calculated as $F_{corona,TS}(2)/k_BT$ from Table 5.5, where $n_{blob,neck} = 2n_{blob,sphere} = 2F_{corona,0}/k_BT$. These values, along with F_{core} and F_{int}, are summarized in Table 5.6 for micelles prepared by DD, the transition state, and the steady state. From Table 5.6, the average n_{blob} is 16 for BO(53-46) before a T-jump to 170 °C. Assuming that the number of blobs in the neck point is double the calculated $n_{blob,0}$ shown in Table 5.6, approximately 1/6 of the corona chains experience corona crowding where there are approximately 32 blobs per chain near the neck, whereas n_{blob} is 16 for chains in the spherical region of the micelle indicated in Figure 5.11. The fraction of corona chain overlap was determined to be 1/6 for all molar masses by Equation 5.9, and thus assuming n_{blob} at the neck point is twice that of the spherical regions gives n_{blob} of 8, 9, 10, 21, 24, and 32 for BO(6-5), BO (8-7), BO(10-9), BO(25-22), BO(27-27), and BO(53-46). If the local concentration of corona chains at the neck point was three times that of $n_{blob,sphere}$, as shown in Table 5.5, then this free energy is even larger.

Table 5.6: Estimates of the F_{core}, F_{corona}, F_{int}, and F_{tot} before and after fragmentation, and the transition state, using normalized interfacial energy $\gamma = 0.1$. F_{corona}/k_BT in the transition state was calculated using the dimensions for as-prepared micelles.

As Prepared by DD (F_0/kT)						
BO(x-y)	(6-5)	(8-7)	(10-9)	(25-22)	(27-27)	(53-46)
F_{core}/k_BT	2.1	1.8	2.1	3.4	4.0	3.4
F_{int}/k_BT	1.0	1.2	1.2	1.4	1.4	2.1
F_{corona}/k_BT	3.8	4.2	4.7	11	12	16
F_{tot}/k_BT	6.8	7.3	8.0	16	17	22
Transition State (F_{TS}/kT)						
F_{core}/k_BT	1.3	1.1	1.6	2.1	2.3	2.0
F_{int}/k_BT	1.2	1.5	1.3	1.8	1.8	2.8
F_{corona}/k_BT	4.4	5.0	5.5	13	14	19
F_{tot}/k_BT	6.9	7.6	8.4	17	18	24
Steady-state (F_f/kT)						
F_{core}/k_BT	1.3	1.1	1.6	2.1	2.3	2.0
F_{int}/k_BT	1.2	1.5	1.3	1.8	1.8	2.8
F_{corona}/k_BT	2.8	3.1	4.3	7.1	8.4	9.2
F_{tot}/k_BT	5.3	5.8	7.2	11	13	14

This large increase in the local concentration of PEO chains in the neck region of the transition state supports the strong M dependence of micelle fragmentation kinetics. Because the confinement free energy of corona chains is directly proportional to n_{blob}, the chains near the neck point become much more confined and the entropic penalty associated with this chain confinement contributes to this being the primary activation barrier to fragmentation. Although these estimates are encouraging, we emphasize that the uncertainties in estimating the transition state free energy are quite large, and the differences in the calculated free energies for the spherical and "peanut" shaped micelles are only ~5 – 10k_BT. Given that the aggregation numbers are huge and the barrier is known to be of order 30-40 k_BT,[90,91] the estimated barriers per chain are small fractions of k_BT, and therefore beyond the resolution of this calculation.

M dependence of initial micelle size by direct dissolution.

To understand the N dependence of the initial core size for micelles prepared by DD, SAXS measurements on the pure PB-PEO diblock copolymers were conducted. The 1D scattering intensity traces for these samples are shown in Figure 5.13. It has been suggested that the morphology of micelles prepared by direct dissolution depends on the morphology of the bulk diblock copolymer.[90,128] The scattering data confirms that BO(6-5), BO(8-7), BO(10-9), BO(25-22), and BO(27-27) exhibit a lamellar morphology at 70 °C, which is the temperature used for preparing micelle solutions by direct dissolution. The domain size of the PB lamellae was estimated from the q-position of the primary scattering peak (d =

$2\pi/q^*$) and the known volume fraction of PB. The domain sizes were found to be approximately 16, 17, 19, 47, and 54 nm for BO(6-5), BO(8-7), BO(10-9), BO(25-22), and BO(27-27), respectively.

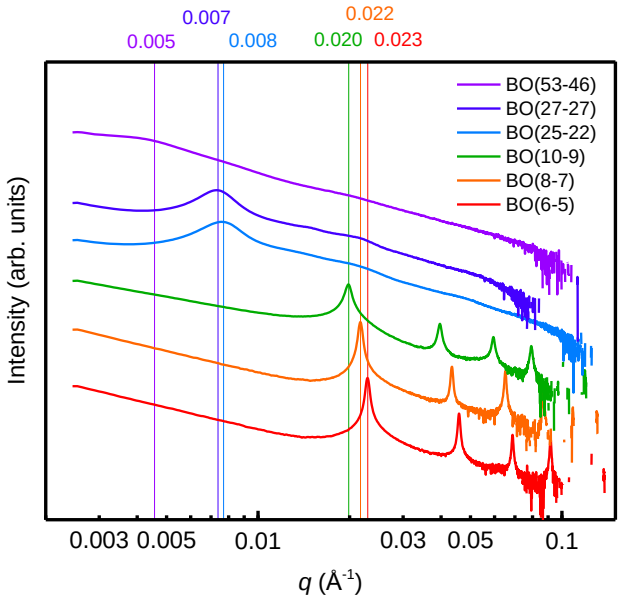

Figure 5.13: SAXS intensity (logarithmic scale) versus q of bulk PB-PEO diblocks after annealing at 70 °C for 15 min. The vertical lines indicate the center of each primary scattering peak and the q values of each line are indicated above. From the peak indexing, BO(6-5), BO(8-7), BO(10-9), BO(25-22), and BO(27-27) diblocks exhibit a lamellar morphology at the temperature used for direct dissolution. For BO(53-46), the broad nature of the peaks makes identifying a morphology difficult, but an approximate domain size is estimated by the primary scattering peak position.

Interestingly, the domain sizes obtained from SAXS of the bulk polymers are comparable to the initial micelle core size. This dependence is represented in Figure 5.14 as a plot of $\langle R_{core} \rangle_0$ vs. d_{PB}. From this figure, the direct relationship between the domain size of the bulk copolymer and the initial micelle core radius is apparent. This result is also

consistent with that of Chapter 3 for BO(8-6) in [$C_x$mim][TFSI] ILs.[90,91] It should be noted that a linear dependence should not necessarily be expected. The dependence begins to weaken slightly at higher M, as evidenced by the slight downward curvature of $\langle R_{core} \rangle$ for the two largest polymers. The dependence of $\langle R_{core} \rangle_0$ on d_{PB} follows the strong segregation limit scaling of 2/3,[39] as shown in Figure 5.14, while the apparent equilibrium scaling of $\langle R_{core} \rangle$ with N_{core} for the initial micelles has an exponent closer to 3/5, as shown in Figure 5.3. These slightly different dependences could account for the curvature evident in Figure 5.14.

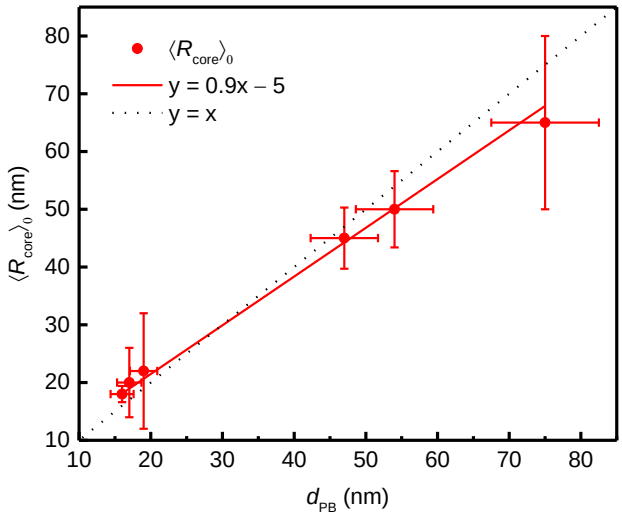

Figure 5.14: Dependence of $\langle R_{core} \rangle_0$ (nm) on the PB domain size (d_{PB}) indicating a direct relationship between $\langle R_{core} \rangle_0$ for micelles prepared by DD and the PB domain size of the bulk diblock copolymer. The solid red line represents the best linear fit to $\langle R_{core} \rangle_0$ as a function of d_{PB}, and the dotted black line represents y = x. The error bars in $\langle R_{core} \rangle_0$ represent $\pm \sigma_{core}$ from Table 5.1, and 10% error in d_{PB} is assumed.

Figure 5.15 shows the relationship of d_{PB} as a function of N_{core} for the domain size determined experimentally by SAXS, and the estimated domain spacing calculated from self-consistent field theory (SCFT); the experimental domain size of the PB lamellae agrees well with SCFT. We therefore speculate that during direct dissolution the solvent penetrates the PEO domains, peeling apart layers of PEO-decorated PB layers. Some surface instabilities in these separate layers drive a pinching-off process to give large, disperse spherical aggregates in solution. This behavior is broadly analogous to a Rayleigh instability, and has been referenced in computations of surfactant-based micelles,[178] and experimentally in cylinder-to-sphere transitions[110,181,190–193] in block copolymer micelles.

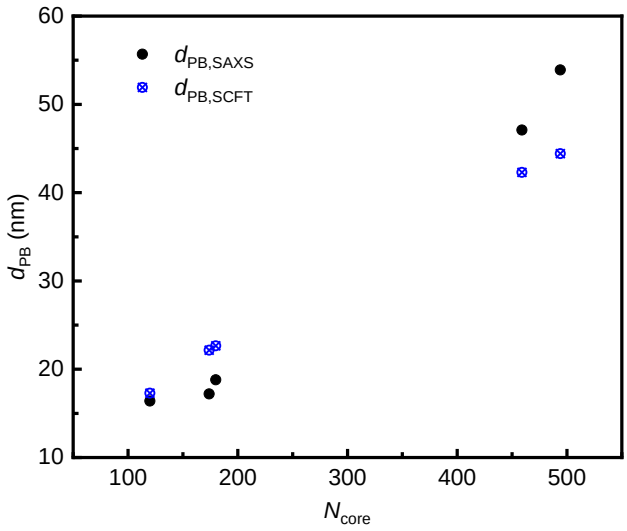

Figure 5.15: Comparison of the domain size of PB determined by SAXS ($d_{PB,SAXS}$) and the estimated domain size for a lamellar diblock copolymer using self-consistent field theory ($d_{PB,SCFT}$).

In experimental works on the cylinder-to-sphere transitions in block copolymer micelles, it is concluded that the surface-instability-mediated transitions induce pinching

of immature spherical micelles, followed by rapid chain exchange.[110] Based on the lack of chain exchange in PB-PEO/[C_2mim][TFSI] systems reported previously,[90] the direct dissolution mechanism is related to this process, but not identical. Furthermore, even accounting for the molar mass difference, our system undergoes fragmentation about three orders of magnitude more slowly than the PEP-PEO cylindrical micelles, implying a very small barrier in the latter case.

Another possibly surprising result of the dependence of $\langle R_{core}\rangle_0$ on d_{PB} is that the micelles prepared by direct dissolution have a core radius that is approximately equal to the full PB domain size, rather than $d_{PB}/2$. The interfacial tension in the swollen state is clearly greater than in the dry copolymer, so an increase in core chain stretching is certainly expected. Moreover, the degree of interdigitation of the PB chains in the dry lamellae can affect this picture of the dissolution mechanism. In the dry state, the degree of stretching of PB (s_{PB}) can be estimated from two limits: the first assumes no interdigitation of chains, where $s_{PB,1} = d_{PB}/\langle h^2\rangle_0^{1/2}$; the second method assumes full interdigitation of chains, where $s_{PB,2} = d_{PB}/2\langle h^2\rangle_0^{1/2}$. Calculating the degree of stretching for BO(8-7) by these two methods gives $s_{PB,1}$ = 1.1 and $s_{PB,2}$ = 2.2, respectively. These may be compared to the degree of stretching of chains in the micelle core from Table 5.1, s_{core} = 2.5. This result implies some significant degree of interdigitation in the bulk state. It is worth noting that the degree of chain stretching, and therefore interdigitation in the bulk state, is highly dependent on the solvent selectivity. As shown previously in Table 3.3, changing the length of the IL alkyl

chain changes results in some variation in micelle size prepared by DD, and therefore the degree of chain stretching is expected to decrease as the IL alkyl chain length increases.

5.4 – Summary

In this chapter, the effect of polymer molar mass on micelle fragmentation kinetics was studied for the first time, using six molar masses of PB-PEO with a near constant volume fraction of PEO ($f_{PEO} \approx 0.40$) in the ionic liquid [C_2mim][TFSI]. Disperse micelles prepared by direct dissolution in [C_2mim][TFSI] were found to be larger than the equilibrium size, and all micelles decreased in size, in terms of both $\langle R_h \rangle$ and $\langle R_{core} \rangle$, when subjected to high temperature annealing. The decrease in micelle size while annealing at 170 ºC was monitored by *T*-jump DLS and TR-SAXS, and it was concluded that PB-PEO micelles equilibrate by fragmentation. The final aggregation number was approximately half of the original aggregation number prior to a *T*-jump. The decay in $\langle R_h \rangle$ and $\langle R_{core} \rangle$ was consistently well described by a compressed exponential with an exponent of 2; the origin of this functional form remains to be elucidated. The characteristic fragmentation times determined by fitting the normalized change in micelle size to this equation was found to depend strongly on the molar mass of the block copolymer, where $\tau_{frag} \sim N_{total}^{1.8 \pm 0.1}$. A previous model of micelle fragmentation by Dormidontova predicts a similar scaling, albeit in terms of N_{corona}. Future measurements on a series of polymers with constant N_{core} will be required to assess whether this apparent agreement is robust. The core size of the initial

micelles was shown to correlate closely with the PB domain dimensions in the precursor dry, lamellar copolymer, suggesting a formation mechanism involving peeling apart of layers, followed by pinching off into spherical domains.

Chapter 6 – Fragmentation of hybrid micelles

6.1 – Introduction

Micelle hybridization experiments, where mixtures of different micelles are prepared and their formation/relaxation is monitored, have been of interest for some time.[22,194–198] In many applications, the formulation of BCP micelles rarely involves the use of well-controlled polymerization techniques to give narrow dispersity block copolymers, so the relaxation of hybrid micelles is of interest from an applications perspective. Early micelle hybridization experiments were reported by Cantu and co-workers,[198] who monitored the change in light scattering intensity upon mixing two different populations of micelles, and found that the equilibration time could be related to the CMC of the individual micelles. It was concluded that the formation time of mixed micelles is related to the chain exchange rates of individual micelles.

Tian *et al*.[196] studied the rate of micelle hybridization via sedimentation velocity, and determined that the rate of hybridization depends on the architecture of BCPs used and the thermodynamic properties of the solvent mixture. They found that hybridization of micelles did not occur if the solvent selectivity towards the corona-forming block was very

strong, *i.e.*, chain exchange was suppressed in high χ systems. Cai *et al*.[195] investigated the hybridization of coil-rod copolymer micelles by SLS and DLS, and found that upon mixing, larger hybrid micelles formed at the expense of "pure" micelles of a single copolymer. They argued that the driving force for hybridization arises from the entropic gain in the relief of chain stretching, as well as the space-filling nature of the rod-like core-forming block.

Previous work by Lu, Bates, and Lodge used the copolymer blending approach to study chain exchange of hybrid PS-PEP micelles in squalane to gain insights into the mechanism of chain expulsion.[22] In their work, PS-PEP diblocks with constant corona block lengths but different PS core block lengths were used. In this system, one molar mass of PS-PEP was contrast matched with the solvent, so as to specifically monitor the exchange of the deuterated copolymer by TR-SANS. They found that regardless of the molar mass of the PS block, the chain exchange time in these hybrid micelles was identical to that of the pure diblock copolymer micelles. This confirmed that the exchange time is dictated by the independent exchange of chains between micelles, and not a cooperative process such as micelle fragmentation/fusion.[22]

Zhao *et al*. used a similar approach to prepare hybrid micelles of PMMA-PnBMA in [C_2mim][TFSI] with fixed N_{corona} but different lengths of N_{core}.[142,194] The chain exchange kinetics of pure PMMA-PnBMA micelles in these IL mixtures was well characterized in previous work, as discussed in Section 1.3.3.[17,19] It was found that mixtures of micelles prepared from PMMA-PnBMA micelles with constant core block lengths, but different

corona block lengths, occurs through the chain exchange between mixed micelles, as well as some evidence for micelle fusion/fragmentation evidenced by changes in micelle size with prolonged annealing times above the LCMT.[194] Fragmentation and fusion of PMMA-PnBMA micelles in IL mixtures was not previously observed for the "pure" diblock case.

In this work, hybrid micelles are prepared by blending different molar masses of PB-PEO prior to DD preparation in [C_2mim][TFSI]. Because there is no chain exchange in this system, it was anticipated that hybridization would not occur if mixtures of pure micelles were combined after formation, which is consistent with the conclusions of Tian *et al*.[196] Because chain exchange is restricted in this system, the influence of molar mass dispersity on fragmentation kinetics of hybrid PB-PEO micelles was explored. First, the fragmentation kinetics of hybrid micelles comprising 50:50 blends (by weight) of PB-PEO were studied using *T*-jump DLS, *ex-situ* SAXS, and TEM. Then, the effect of composition was studied for one PB-PEO blend, namely, BO(8-7)/(10-9), using *T*-jump DLS to gain a deeper understanding of the effect of molar mass dispersity on micelle fragmentation kinetics.

6.2 – Materials and methods

Synthesis and Characterization. Five molar masses of PB-PEO were synthesized by two-step sequential anionic polymerization, as described in Section 2.1.1.[136] The fragmentation kinetics of each molar mass of PB-PEO in [C_2mim][TFSI] were investigated in depth, as

discussed in Chapter 5. M_n, $Đ$, and f_{PEO} for BO(x-y) were determined by a combination of SEC-MALS (Wyatt Dawn Heleos II) and ^{1}H NMR spectroscopy in $CDCl_3$ (^{1}H NMR, Varian Inova 500) shown in Figures 2.2 and 2.3, respectively. The d*n*/d*c* for the diblocks were estimated as the weight average of the refractive index increments for PB in THF (d*n*/d*c* = 0.119 mL/g) and PEO in THF (d*n*/d*c* = 0.068 mL/g).[138]

PB-PEO blending method. Blends of PB-PEO diblocks were prepared by freeze-drying two distinct molar masses of PB-PEO with a composition of 50:50 (wt:wt). This procedure is described in Section 2.3.3. The molecular characteristics of the 50:50 blends are summarized in Table 6.1, where $x_{L,i}$ is the mole fraction of the long block defined by Equation 2.7 and $\langle N_L \rangle$ is defined by Equation 2.8. The same freeze-drying process was used to make varying compositions of BO(8-7)/(10-9) blends, where the desired amount of each diblock was combined by weight and freeze-dried in benzene.

Table 6.1: Average mole-fraction of long PB block ($x_{L,PB}$), average mole-fraction of long PEO block ($x_{L,PEO}$), number average degree of polymerization of long PB block $\langle N_{PB,L} \rangle$, and number average degree of polymerization of long PEO block $\langle N_{PEO,L} \rangle$ in PB-PEO 50:50 blends. For all blends, the weight fraction of the longer block is $w_L = 0.5$.

PB-PEO 50:50 Blend	$x_{L,PB}$	$x_{L,PEO}$	$\langle N_{PB,L} \rangle$	$\langle N_{PEO,L} \rangle$
(6-5)/(8-7)	0.41	0.40	142	140
(8-7)/(10-9)	0.50	0.44	174	194
(10-9)/(25-22)	0.27	0.31	252	306
(25-22)/(27-27)	0.48	0.45	476	556

Solution Preparation by DD. All solutions were prepared by the direct dissolution (DD) method described in Section 2.3.1, unless noted otherwise.

DLS. *T*-jump and multi-angle room temperature scattering measurements were performed according to Section 2.4.2.

***Ex-situ* LP-TEM.** $\langle R_{core} \rangle$ and σ_{core} at different time points during an annealing experiment were determined using LP-TEM, as described in Section 2.6.1.

***Ex-situ* SAXS.** SAXS experiments were conducted according to *ex-situ* SAXS described in Section 2.5.2.

6.3 – Results and discussion

REPES results from Figure 6.1a show that the 50:50 blends form well-defined hybrid micelles with an $\langle R_h \rangle_0$ that is intermediate between the average values in the pure micelle case. This result suggests that the freeze-drying process gives well-mixed PB-PEO chains, which are distributed randomly throughout micelles prepared by DD in [C_2mim][TFSI]. From Figure 6.1a, $\langle R_h \rangle_0$ increases with increasing $\langle N \rangle$, which is consistent with the observed N dependence of $\langle R_h \rangle_0$ reported in Chapter 5 for pure PB-PEO micelles. After annealing at 170 °C, $\langle R_h \rangle_f$ decreases, indicative of micelle fragmentation. BO(8-7)/(10-9) micelles give results that are distinct from other PB-PEO blends, where $\langle R_h \rangle_f$ does not increase monotonically with increasing $\langle N \rangle$. However, there is a clear decrease in $\langle R_h \rangle$ after

annealing at 170 °C for all hybrid micelles, as shown in Table 6.2, which strongly implies that fragmentation occurs in the hybrid micelle system. Again, the monomodal $\langle R_h \rangle$ distribution obtained before and after annealing at 170 °C indicates that the micelles formed by PB-PEO blends contain both molar masses of PB-PEO used to prepare hybrid micelles, and not individual populations of each molar mass.

Table 6.2: $\langle R_h \rangle$ by multi-angle DLS at 27 °C before and after annealing at 170 °C, for 0.25 wt % PB-PEO pure and hybrid micelles in [C_2mim][TFSI]. $\langle R_h \rangle$ is reported from fitting multi-angle DLS data to the second cumulant expansion, as described in Section 2.4.2.

BO(x-y)	$\langle R_h \rangle_0$ (nm)	$\langle \mu_2/\Gamma^2 \rangle_0$	$\langle R_h \rangle_f$ (nm)	$\langle \mu_2/\Gamma^2 \rangle_f$
(6-5)	29	0.08	20	0.05
(8-7)	42	0.25	27	0.05
(10-9)	51	0.23	34	0.04
(25-22)	70	0.09	58	0.07
(27-27)	83	0.17	62	0.09
PB-PEO (50:50) blend	$\langle R_h \rangle_0$ (nm)	$\langle \mu_2/\Gamma^2 \rangle_0$	$\langle R_h \rangle_f$ (nm)	$\langle \mu_2/\Gamma^2 \rangle_f$
(6-5)/(8-7)	37.1	0.14	29.4	0.01
(8-7)/(10-9)	52.4	0.19	27.5	0.10
(10-9)/(25-22)	59.7	0.23	45.4	0.12
(25-22)/(27-27)	81.1	0.18	71.1	0.01

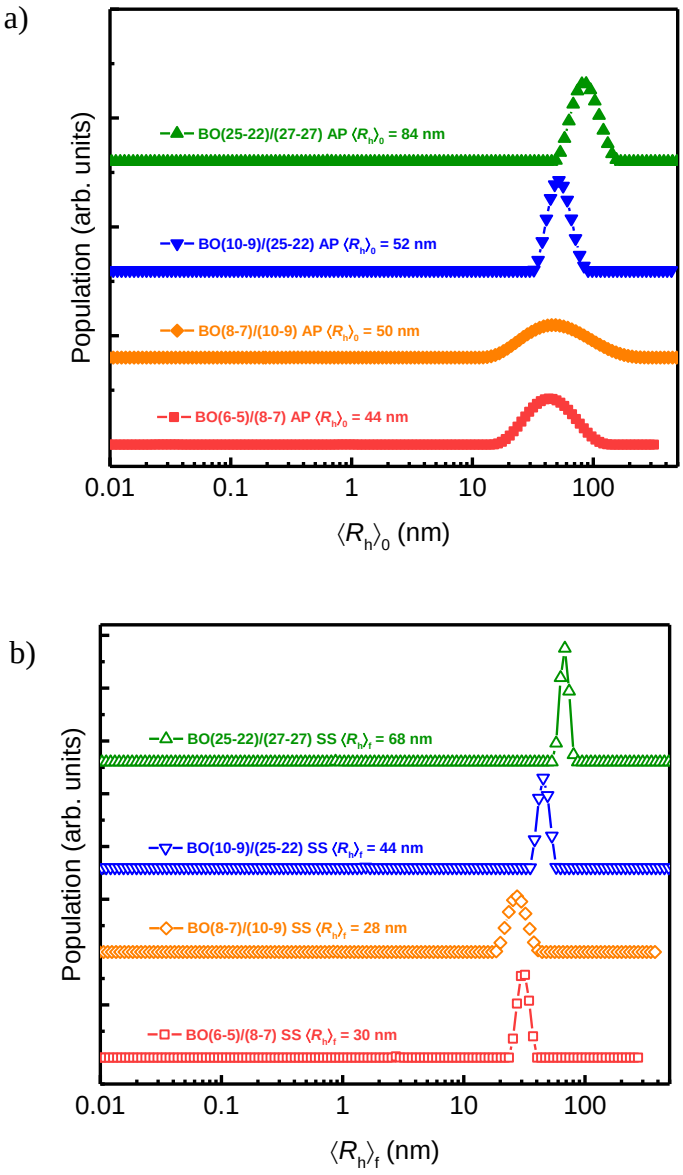

Figure 6.1: REPES results for 0.25 wt % PB-PEO hybrid micelles in [C_2mim][TFSI] (a) as prepared by DD and (b) steady-state after annealing at 170 °C. Measurements were conducted at T = 27 °C and θ = 90°. All blends had a composition of 50:50 (wt:wt) for each molar mass of PB-PEO.

Further confirmation that blends of PB-PEO resulted in well-distributed chains was obtained by SAXS of the bulk PB-PEO molar mass blends. A single domain size is observed for 50:50 PB-PEO blends, as shown in Figure 6.2. From the scattering data, all 50:50 blends exhibit one primary scattering peak with higher order reflections consistent with a lamellar morphology. This is expected as the molar mass blends were prepared via freeze-drying, which commonly results in well mixed samples.[199] The domain spacings for PB-PEO diblocks and PB-PEO blends are summarized in Table 6.3.

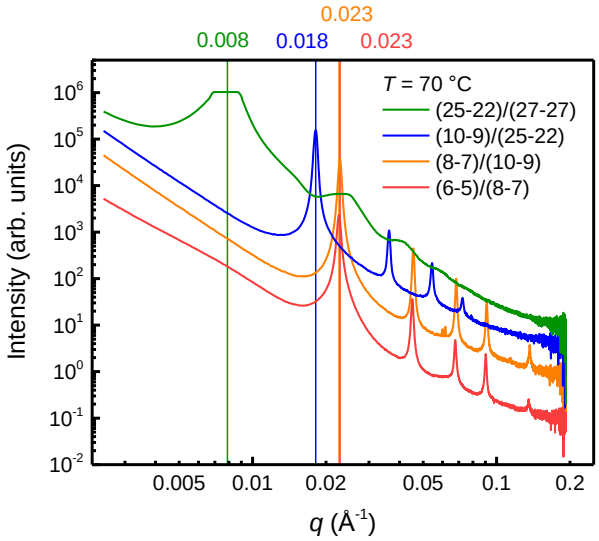

Figure 6.2: SAXS intensity (logarithmic scale) versus *q* of bulk PB-PEO molar mass blends after annealing at 70 °C for 15 min. The vertical lines indicate the center of each primary scattering peak and the *q* values of each line are indicated above. From the peak indexing, BO(6-5)/(8-7), BO(8-7)/(10-9), BO(10-9)/(25-22), and BO(25-22)/(27-27) diblocks exhibit a single lamellar morphology at the temperature used for DD solution preparation. For BO(25-22)/(27-27), the maximum of the primary scattering peak saturated the X-ray detector, which is the cause for the truncated primary scattering peak.

Table 6.3: Domain spacing from SAXS of BO(x-y) diblock copolymers and PB-PEO 50:50 blends. The domain size was calculated from the primary scattering peak as $d = 2\pi/q^*$.

BO(x-y)	q^* (Å^{-1})	d (nm)	d_{PB} (nm)	d_{PEO} (nm)
(6-5)	0.023	27.3	16.4	10.9
(8-7)	0.022	28.6	17.2	11.4
(10-9)	0.020	31.4	18.8	12.6
(25-22)	0.008	78.5	47.1	31.4
(27-27)	0.007	89.8	53.9	35.9
PB-PEO (50:50) blend	q^* (Å^{-1})	d (nm)	d_{PB} (nm)	d_{PEO} (nm)
(6-5)/(8-7)	0.023	27.3	16.4	10.9
(8-7)/(10-9)	0.023	27.3	16.4	10.9
(10-9)/(25-22)	0.018	34.9	20.9	14.0
(25-22)/(27-27)	0.008	78.5	47.1	31.4

The change in $\langle R_{core} \rangle$ before and after annealing at 170 °C was investigated by *ex-situ* LP-TEM and SAXS. LP-TEM images of 50:50 hybrid micelles are shown in Figures 6.3 – 6.6. From image analysis, a decrease in $\langle R_{core} \rangle$ for hybrid micelles of 3.6, 2.3, 8.2, and 8.1 nm for BO(6-5)/(8-7), BO(8-7)/(10-9), BO(10-9)/(25-22), and BO(25-22)/(27-27), respectively, was observed. From the aggregation numbers in Table 6.4, the ratio of Q_f/Q_0 is 0.46, 0.59, 0.62, and 0.76 for BO(6-5)/(8-7), BO(8-7)/(10-9), BO(10-9)/(25-22), and

BO(25-22)/(27-27), respectively. The decrease in $\langle R_{core} \rangle$ and the ratio of Q_f/Q_0 is consistent with the conclusions from Chapter 3 that *ex-situ* LP-TEM imaging provides evidence that fragmentation occurs in the hybrid PB-PEO micelles.

a) 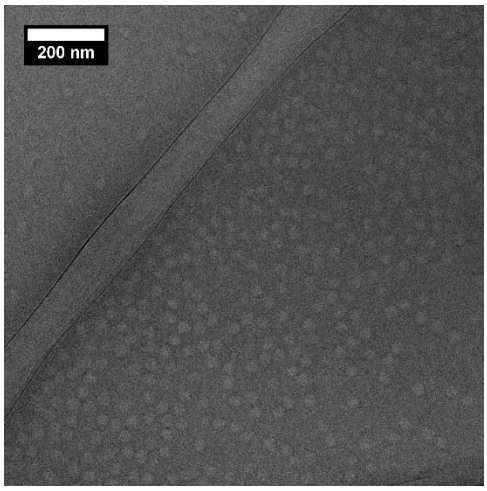

b) 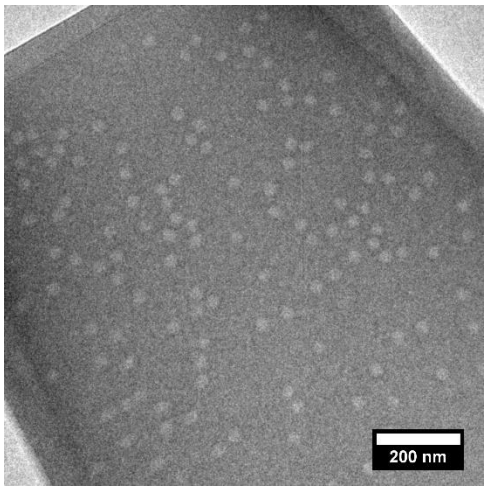

Figure 6.3: LP-TEM images of 0.25 wt % BO(6-5)/(8-7) hybrid micelles in [C_2mim][TFSI] a) before and b) after annealing at 170 °C. From image analysis, $\langle R_{core} \rangle_0$ = 17.8 ± 3.8 nm and $\langle R_{core} \rangle_f$ = 14.2 ± 1.6 nm.

a) 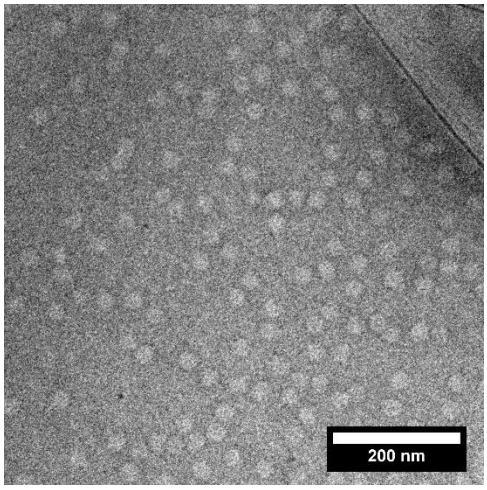

b) 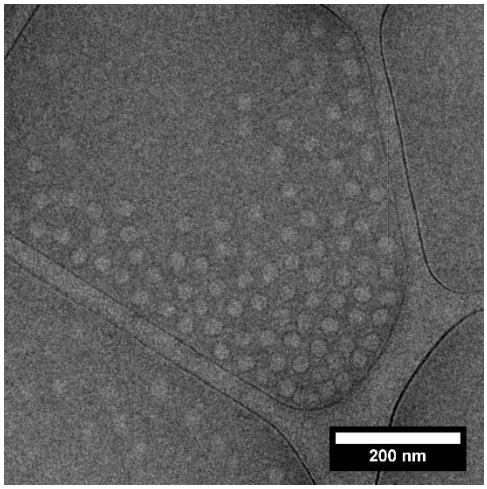

Figure 6.4: LP-TEM images of 0.25 wt % BO(8-7)/(10-9) hybrid micelles in [C_2mim][TFSI] a) before and b) after annealing at 170 °C. From image analysis, $\langle R_{core} \rangle_0$ = 15.8 ± 2.0 nm and $\langle R_{core} \rangle_f$ = 13.5 ± 0.9 nm.

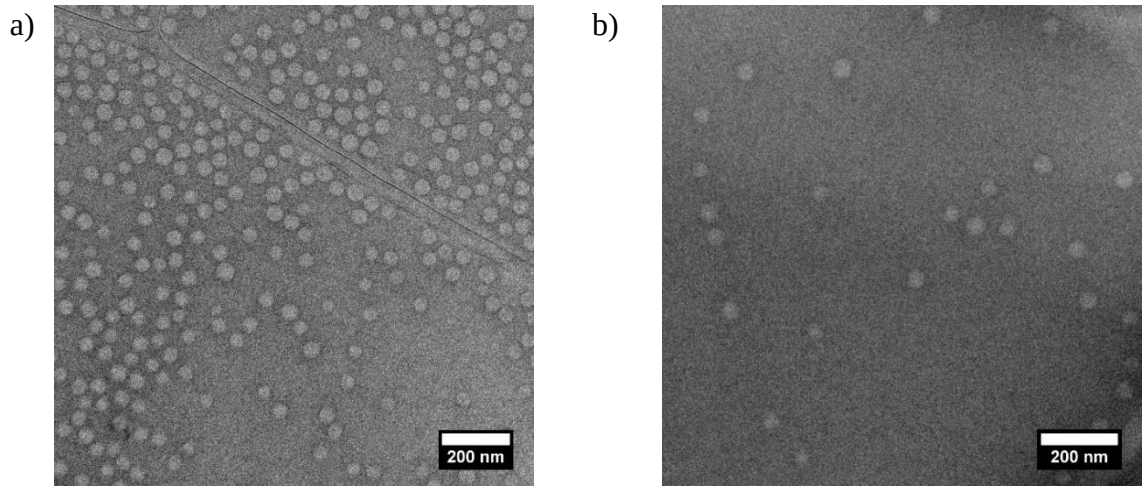

Figure 6.5: LP-TEM images of 0.25 wt % BO(10-9)/(25-22) hybrid micelles in [C_2mim][TFSI] a) before and b) after annealing at 170 °C. From image analysis, $\langle R_{core} \rangle_0$ = 27.3 ± 3.1 nm and $\langle R_{core} \rangle_f$ = 19.1 ± 2.8 nm.

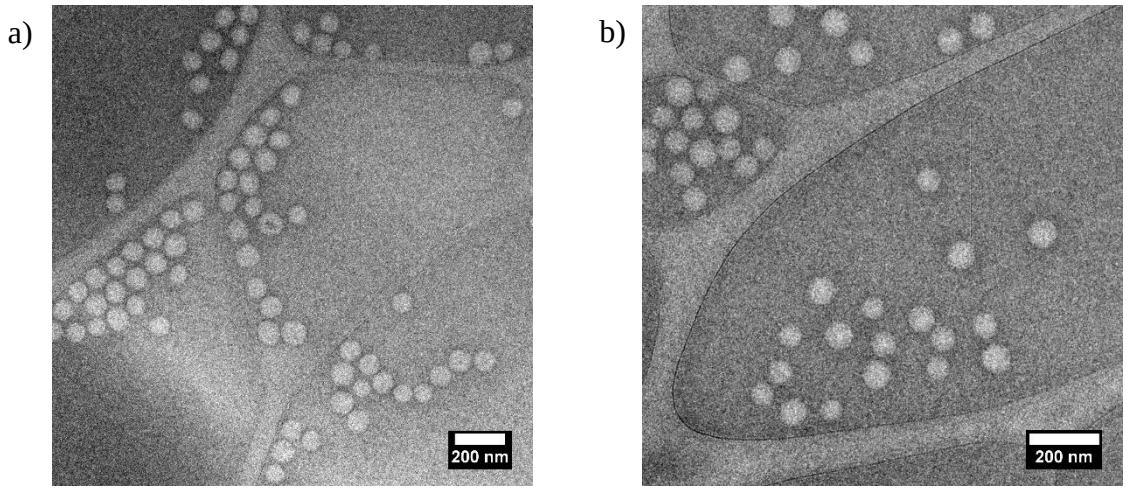

Figure 6.6: LP-TEM images of 0.25 wt % BO(25-22)/(27-27) hybrid micelles in [C_2mim][TFSI] a) before and b) after annealing at 170 °C. From image analysis, $\langle R_{core} \rangle_0$ = 40.4 ± 4.5 nm and $\langle R_{core} \rangle_f$ = 32.3 ± 4.6 nm.

Ex-situ SAXS shows a similar decrease in $\langle R_{core} \rangle$ as a function of annealing time that is consistent with LP-TEM image analysis. The scattering intensities as a function of q for 0.25 wt % 50:50 hybrid micelles of BO(6-5)/(8-7), BO(8-7)/(10-9), BO(10-9)/(25-22), and BO(25-22)/(27-27) in [C$_2$mim][TFSI] are shown in Figure 6.7.

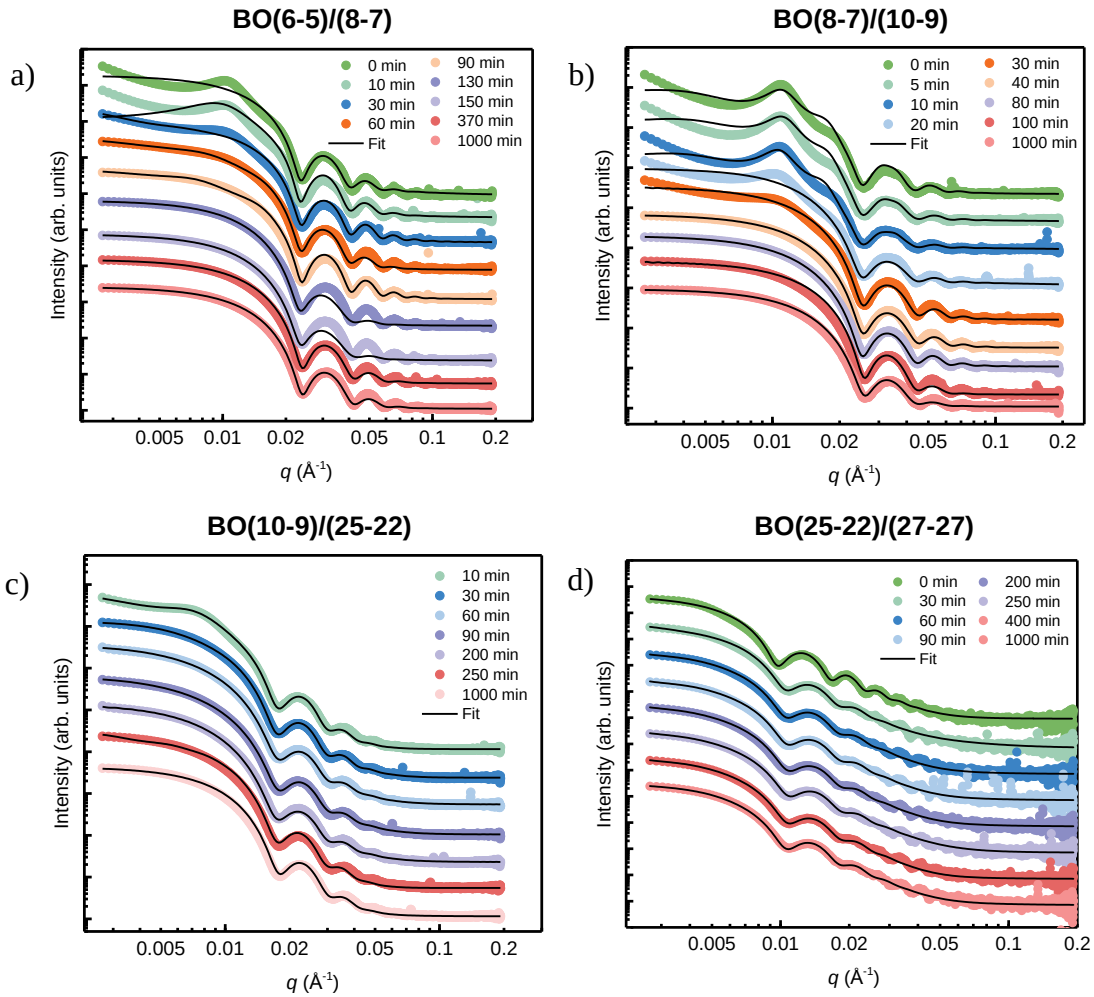

Figure 6.7: Structural evolution of 0.25 wt % PB-PEO hybrid micelles of (a) BO(6-5)/(8-7), (b) BO(8-7)/(10-9), (c) BO(10-9)/(25-22), and (d) BO(25-22)/(27-27) in [C$_2$mim][TFSI] for while annealing at 170 °C by *ex-situ* SAXS. Scattering curves were fit to the Pedersen model (solid black lines). The curves are shifted vertically for clarity.

Measurements were acquired at room temperature after quenching each sample in a water bath.

The spherical micelle form factor is observed for all annealing time points, and $\langle R_{core} \rangle$ decreases while annealing at 170 °C, as evidenced by the increase in the *q*-position of the first minimum in the form factor. The scattering curves are well-described by the block copolymer micelle form factor,[153] as described in Section 2.5.1, and from the fit detailed structural information about the micelles is obtained at each time point.

Micelle core dimensions and aggregation numbers before and after annealing at 170 °C are summarized in Table 6.4. From *ex-situ* SAXS, hybrid micelles prepared by DD in [C_2mim][TFSI] were found to have an average core radii of $\langle R_{core} \rangle_0$ = 19.1, 18.0, 26.5, and 48.1 nm for BO(6-5)/(8-7), BO(8-7)/(10-9), BO(10-9)/(25-22), and BO(25-22)/(27-27) hybrid micelles, respectively. After fragmentation at 170 °C, *ex-situ* SAXS was used to determine the steady-state core radii of $\langle R_{core} \rangle_f$ = 14.7, 15.0, 22.5, and 42.0 nm for BO(6-5)/(8-7), BO(8-7)/(10-9), BO(10-9)/(25-22), and BO(25-22)/(27-27) hybrid micelles, respectively.

Table 6.4: $\langle R_{core} \rangle$ and τ_{frag} determined by *ex-situ* SAXS during an annealing experiment at 170 °C for 0.25 wt % PB-PEO hybrid micelles in [C_2mim][TFSI]. The relaxation times were determined by Equation 2.18. $\langle R_{core} \rangle$ and σ_{core} were determined from fitting the scattering data shown in Figure 6.7 to the Pedersen model described in Section 2.5.2.

(50:50) blend	(6-5)/(8-7)	(8-7)/(10-9)	(10-9)/(25-22)	(25-22)/(27-27)
$\langle R_{core} \rangle_0$ (nm)	19.1	18.0	26.5	48.1
$\sigma_{core,0}$ (nm)	0.7	0.8	2.2	4.2
$L_{corona,0}$ (nm)	18.0	34.5	33.2	34.0
Q_0	1920	1310	2360	8800
$\langle R_{core} \rangle_f$ (nm)	14.7	15.0	22.5	42.0
$\sigma_{core,f}$ (nm)	0.5	0.4	2.0	3.0
$L_{corona,f}$ (nm)	14.7	18.3	22.8	28.1
Q_f	880	770	1470	6700
τ_{frag} (min)	79	90	193	230
n	1.5	2.7	2.5	2.2

The fragmentation kinetics for 0.25 wt % PB-PEO hybrid micelles in [C_2mim][TFSI] were monitored by high-temperature DLS and *ex-situ* SAXS, as shown in Figures 6.8a and 6.8b, respectively. The time-dependent normalized $\langle R_h \rangle$ at 170 °C for 50:50 PB-PEO hybrid

micelles are shown in Figure 6.8a, where $\langle R_h \rangle$ from DLS was normalized according to Equation 2.17, and the relaxation was well described by the compressed exponential shown in Equation 2.18 where n was used as a fitting parameter in addition to τ_{frag}. The fitting results are summarized in Table 6.4 and 6.5 for *ex-situ* SAXS and high temperature DLS, respectively. A comparison of the values of τ_{frag} between the two techniques shows that the fragmentation times agree reasonably between SAXS and DLS; however, the compression exponent n differs between the two techniques. Fitting the normalized change in $\langle R_{core} \rangle$ from *ex-situ* SAXS to Equation 2.18 gives $\langle n \rangle = 2.2 \pm 0.5$, whereas $\langle n \rangle = 1.4 \pm 0.5$ when fitting the normalized change in $\langle R_h \rangle$ to Equation 2.18. The higher temporal resolution in DLS when compared to *ex-situ* SAXS may be the cause for the discrepancies in $\langle n \rangle$.

Table 6.5: τ_{frag} determined by *T*-jump DLS at 170 °C for 0.25 wt % PB-PEO hybrid micelles in [C_2mim][TFSI]. The relaxation times were determined by Equation 2.18.

PB-PEO (50:50) blend	(6-5)/(8-7)	(8-7)/(10-9)	(10-9)/(25-22)	(25-22)/(27-27)
τ_{frag} (min)	100 ± 23	37 ± 11	190 ± 33	240 ± 83
n	1.5	2.0	1.0	1.0

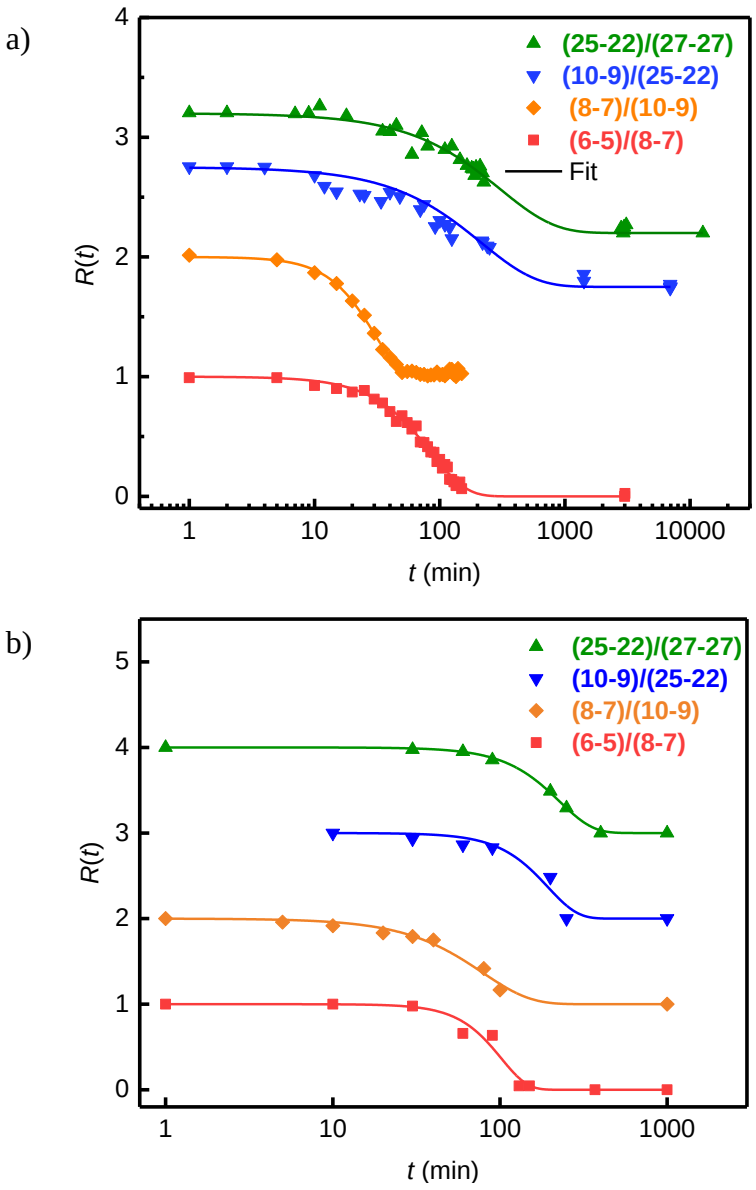

Figure 6.8: a) Time-dependent normalized $\langle R_h \rangle$ for 0.25 wt % solutions of PB-PEO hybrid micelles in [C_2mim][TFSI]. DLS measurements were performed at a scattering angle of 90° and a relaxation temperature of 170 °C. b) Time-dependent normalized $\langle R_{core} \rangle$ for 0.25 wt % solutions of PB-PEO hybrid micelles in [C_2mim][TFSI]. Solid lines represent best fits to Equation 2.18 with *n* as an adjustable parameter.

From Table 6.5, it is worth noting that all blends, expect for BO(8-7)/(10-9), exhibit nearly single exponential relaxation ($n \approx 1$), and not the compressed exponential behavior observed consistently in pure PB-PEO micelles with narrow molar mass distributions. While the exponents from Table 6.4 seem closer to the compressed exponential relaxation, there are fewer time points obtained in an *ex-situ* experiment, and these values of n may not be as reliable as the ones obtained by high temperature DLS, which has higher temporal resolution. The change in n from high temperature DLS implies that the blending approach may be altering the molecular mechanism of micelle fragmentation. Additionally, it is apparent that the values of τ_{frag} obtained by fitting normalized $\langle R_h \rangle$ to Equation 2.18 give fragmentation times that are significantly faster than those of pure PB-PEO micelles (Table 5.2). Figure 6.9 demonstrates the increased rate of fragmentation for a 50:50 blend of BO(8-7)/(10-9) in comparison to the pure BO(8-7) and BO(10-9). For the hybrid micelle case, the decrease in $R(t)$ occurs on a much faster time scale than the pure micelle case. Specifically, τ_{frag} = 200, 690, and 37 min for BO(8-7), BO(10-9), and BO(8-7)/(10-9) micelles, respectively.

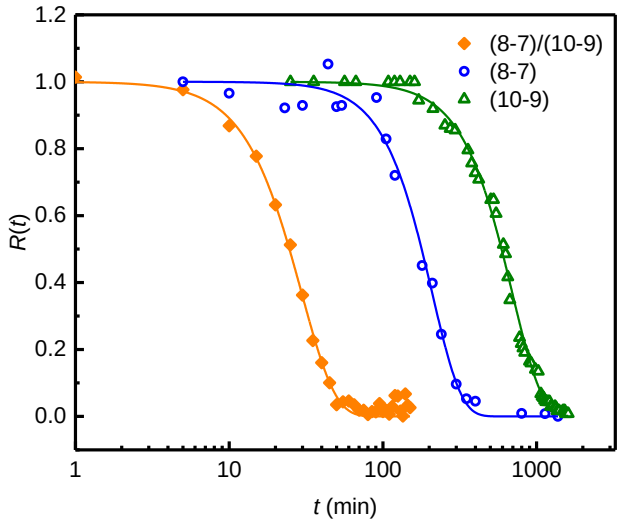

Figure 6.9: Comparison of the time dependent normalized $\langle R_h \rangle$ for 0.25 wt % solutions of pure BO(8-7) and BO(10-9) micelles, and BO(8-7)/(10-9) hybrid micelles in [C_2mim][TFSI]. DLS measurements were performed at a scattering angle of 90° and a relaxation temperature of 170 °C. Solid lines represent best fits to Equation 2.18.

Figure 6.10 compares the values of τ_{frag} determined by DLS for neat PB-PEO micelles, where these values are summarized in Table 5.2, and those of the hybrid micelles. The blending approach significantly decreases the fragmentation times of PB-PEO micelles in [C_2mim][TFSI]. As shown previously in Table 5.2 for 0.25 wt % PB-PEO micelles in [C_2mim][TFSI], τ_{frag} = 120, 200, 690, 1750, and 2300 min for BO(6-5), BO(8-7), BO(10-9), BO(25-22), and BO(27-27) micelles, respectively, where $\langle n \rangle$ = 2.1 ± 0.1 from fitting *T*-jump DLS data to Equation 2.18. From *T*-jump DLS experiments, 0.25 wt % PB-PEO hybrid micelles, made from 50:50 mixtures of two molar masses, give τ_{frag} = 100, 37, 190, and 240 min for BO(6-5)/(8-7), BO(8-7)/(10-9), BO(10-9)/(25-22), and BO(25-22)/(27-27) hybrid micelles, respectively, where $\langle n \rangle$ = 1.4 ± 0.5. Additionally, the fragmentation

times were found to increase with increasing $\langle N \rangle$, apart from the BO(8-7)/(10-9) hybrid micelles. In general, the increase in τ_{frag} with increasing $\langle N \rangle$ is consistent with the molar mass dependence observed in Chapter 5. To further examine the exception obtained for BO(8-7)/(10-9) hybrid micelles, the dependence of blend composition was explored by *T*-jump DLS.

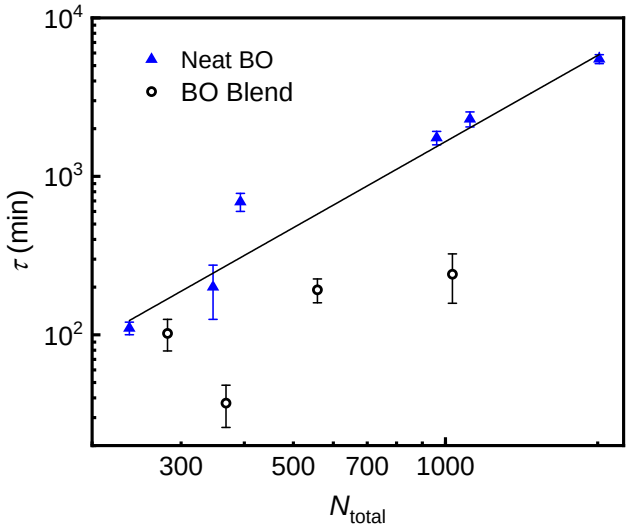

Figure 6.10: Comparison of τ_{frag} for pure PB-PEO micelles and hybrid PB-PEO micelles in [C_2mim][TFSI].

Five compositions of BO(8-7)/(10-9) blends were prepared by freeze-drying BO(8-7) and BO(10-9) at varying weight percentages. Specifically, the compositions of BO(8-7)/(10-9) studied by DLS were 20:80, 40:60, 50:50, 60:40, and 80:20 (wt:wt). Figure 6.11 shows the REPES results for BO(8-7)/(10-9) hybrid micelles with varying composition, before and after annealing at 170 °C. From Figure 6.11a, there is a slight composition dependence to $\langle R_h \rangle_0$ where increasing the weight fraction of BO(10-9) increases the

average micelle radius for hybrid micelles prepared by direct dissolution. The composition dependence of $\langle R_h \rangle_f$ is much weaker, where all BO(8-7)/(10-9) micelles fragment to give micelles with $\langle R_h \rangle_f \approx 33.8 \pm 1.1$ nm.

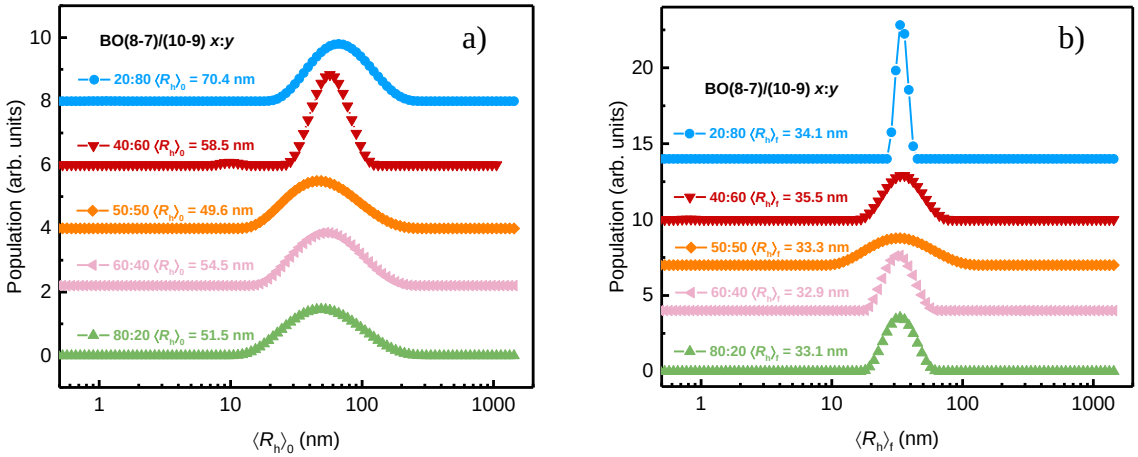

Figure 6.11: REPES results for 0.25 wt % BO(8-7)/(10-9) hybrid micelles in [C2mim][TFSI] with varying composition of BO(8-7) and BO(10-9): (a) as-prepared by DD and (b) steady-state after annealing at 170 °C. Light scattering measurements were conducted at T = 27 °C and θ = 90°.

Again, *T*-jump DLS was used to explore the composition dependence of PB-PEO hybrid micelle fragmentation kinetics for 0.25 wt % BO(8-7)/(10-9) in [C2mim][TFSI] at T = 170 °C. Figure 6.12a shows the normalized change in $\langle R_h \rangle$ at 170 °C for five compositions of BO(8-7)/(10-9). The fragmentation kinetics were well-described by Equation 2.18, with n as an adjustable parameter. All compositions resulted in best fits with $n \approx 2$, apart from 80:20 (8-7)/(10-9), where n = 4.4. Due to the increased fragmentation rate for this sample, where τ_{frag} = 9 min, it is likely that the time between light scattering

measurements must be reduced to reproduce the compression exponent of 2, thereby increasing the temporal resolution of the experiment.

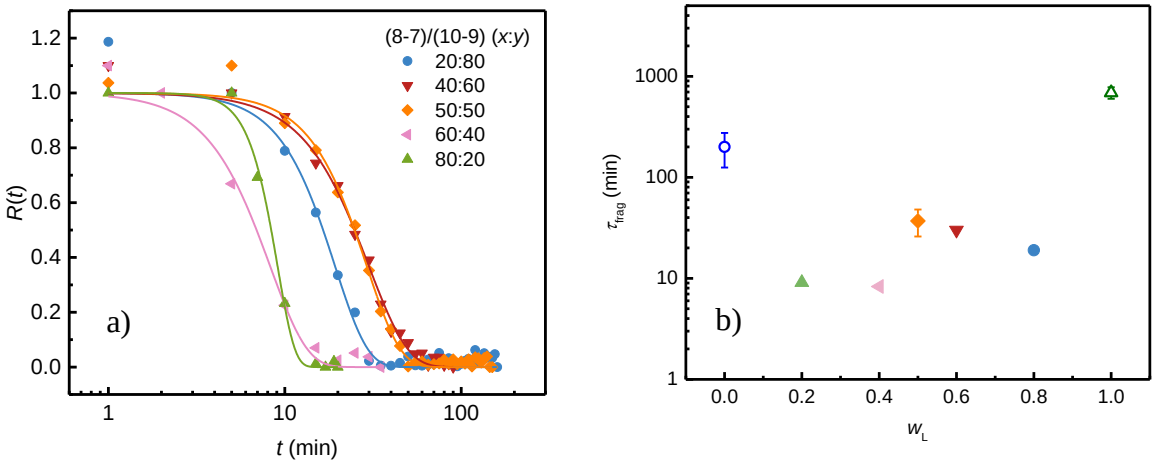

Figure 6.12: Composition dependence of fragmentation kinetics for 0.25 wt % BO(8-7)/(10-9) hybrid micelles in [C2mim][TFSI]. a) Time-dependent normalized $\langle R_h \rangle$ fit to Equation 2.18 for 0.25 wt % BO(8-7)/(10-9) hybrid micelles in [C2mim][TFSI] with varied compositions of BO(8-7) and BO(10-9). b) τ_{frag} as a function of the weight fraction of the longer PB-PEO diblock for BO(8-7)/(10-9) hybrid micelles. DLS measurements were performed at T = 170 °C and θ = 90°.

The fitting results for the composition dependence of $\langle R_h \rangle$ and τ_{frag} determined by T-jump DLS at 170 °C for 0.25 wt % BO(8-7)/(10-9) (x:y) hybrid micelles in [C2mim][TFSI] are summarized in Table 6.6, where T-jump DLS data from Figure 6.12a was fit to Equation 2.18 using n as an adjustable parameter. The composition dependence of τ_{frag} determined by DLS for BO(8-7)/(10-9) hybrid micelles in [C2mim][TFSI] is summarized in Figure 6.12b, where the values of τ_{frag} for pure BO(8-7) and BO(10-9) micelles are shown for comparison.

Table 6.6: Composition dependence of $\langle R_h \rangle$ and τ_{frag} determined by *T*-jump DLS at 170 °C for 0.25 wt % BO(8-7)/(10-9) (*x*:*y*) hybrid micelles in [C_2mim][TFSI], where *x* and *y* are the weight percentages of BO(8-7) and BO(10-9), respectively. The relaxation times were determined by Equation 2.18.

BO(8-7)/(10-9) (*x*:*y*) blend	$\langle R_h \rangle_0$ (nm)	$\langle \mu_2/\Gamma^2 \rangle_0$	$\langle R_h \rangle_f$ (nm)	$\langle \mu_2/\Gamma^2 \rangle_f$	τ_{frag} (min)	*n*
20:80	70.4	0.16	34.1	0.01	19	2.3
40:60	58.5	0.17	35.5	0.04	30	2.0
50:50	49.6	0.19	33.3	0.11	37 ± 11	2.0
60:40	54.5	0.21	32.9	0.02	8.3	2.0
80:20	51.5	0.25	33.1	0.05	9.1	4.4

From Figure 6.12b, it is apparent that the hybrid micelles fragment significantly more rapidly than the corresponding pure micelles. Additionally, τ_{frag} is minimized when the weight fraction of the longer block is approximately 0.4 and begins to increase when w_L > 0.4. This result emphasizes that many details about the fragmentation process remain unknown, as our current understanding would not necessarily anticipate that the blending of two molar masses of PB-PEO would result in fragmentation times that are an order of magnitude faster than either of the pure, single component micelles.

However, there is a precedent for hybrid micelles exhibiting unique relaxation kinetics when compared to the equivalent pure micelles. Zhao *et al.*[142,194] showed that the hybridization of a binary mixture of PMMA-PnBMA in ILs with constant corona block lengths, but different core block lengths results in dramatic changes in relaxation behavior, where a system that primarily undergoes chain exchange for pure micelles exhibits some combination of chain exchange, fusion, and fragmentation in the hybrid micelle case.[194] In the case of PMMA-PnBMA blends, the disparity in the core block length was not large, which favors well-mixed micelles, similar to what is observed for PB-PEO blends studied here, as the molar mass of each diblock in these binary blends are relatively similar. In Zhao and co-workers hybridization experiments, they argued that chain exchange is the dominant mechanism at short time scales, where the shorter chains will exchange to make smaller micelles even smaller, and further increase the size of larger micelles at early time scales in the micellization process. At longer times, the relaxation behavior was posited to occur by some combination of chain exchange and fragmentation/fusion, in agreement with predictions by Nyrkova and Semenov.[194,200]

For PB-PEO hybrid micelles studied here, it is expected that the small variation in molar mass between the two diblocks favors well-mixed micelles as opposed to a binary mixture of micelles of different sizes. However, the resulting scaling of $\langle R_h \rangle$ and $\langle R_{core} \rangle$ with degree of polymerization, shown in Figures 6.13a and 6.13b, is skewed from the equilibrium scaling of $\langle R_{core} \rangle \sim N_{core}^{3/5}$.[35,37,79] Deviations from equilibrium were reported by Zhao *et al*. for hybrid micelles of PMMA-PnBMA in [C_2mim][TFSI] as well, which

was attributed to the high degree of chain stretching for shorter core blocks.[142] While the scaling of $\langle R_h \rangle$ with the total degree of polymerization of the longer diblock, $\langle N_L \rangle$, is relatively close to the equilibrium scaling for the as-prepared and steady-state micelles, it seems the core dimensions are more affected in this hybrid micelle system.

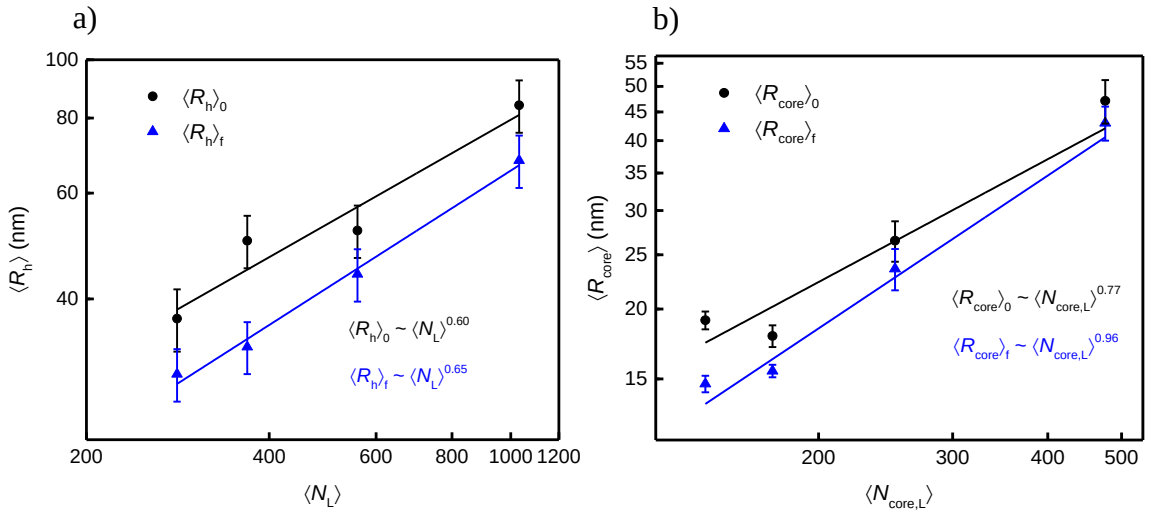

Figure 6.13: a) Dependence of $\langle R_h \rangle$ on $\langle N_L \rangle$ for 0.25 wt % PB-PEO hybrid micelles in [C_2mim][TFSI], as-prepared by DD (black circles) and at steady-state after annealing at 170 °C (blue triangles). The error bars represent estimated 10% measurement uncertainty. b) Scaling of $\langle R_{core} \rangle$ versus $\langle N_{core,L} \rangle$ for 0.25 wt % PB-PEO hybrid micelles in [C_2mim][TFSI] as prepared by DD (black circles) and steady-state after annealing at 170 °C (blue triangles). The solid lines for the as prepared and steady-state values represent the scaling obtained for $\langle R_{core} \rangle_0 \sim \langle N_{core,L} \rangle^{0.77}$ (black line) and $\langle R_{core} \rangle_f \sim \langle N_{core,L} \rangle^{0.96}$ (blue line).

From Figure 5.3, the pure PB-PEO micelles conform to equilibrium scaling behavior as discussed in Chapter 5. However, it is clear from Figure 6.13b that the core size of hybrid micelles deviates strongly from the predicted scaling for equilibrium micelles. This is likely

due to an increase in the core stretching of shorter chains within the core. The degree of chain stretching in the core, s_{core}, and corona, s_{corona}, are calculated according to equations 6.1 and 6.2, respectively,

$$s_{\text{core}} = \frac{\langle R_{\text{core}} \rangle}{\langle h^2 \rangle_0^{1/2}} = \frac{\langle R_{\text{core}} \rangle}{\sqrt{N_{\text{core},i} b_{\text{PB}}^2}} \tag{6.1}$$

$$s_{\text{corona}} = \frac{L_{\text{corona}}}{\langle h^2 \rangle_0^{1/2}} = \frac{\langle R_{\text{h}} \rangle - \langle R_{\text{core}} \rangle}{\sqrt{N_{\text{corona},i} b_{\text{PEO}}^2}} \tag{6.2}$$

where $\langle h^2 \rangle_0^{1/2}$ is the unperturbed root-mean-square end-to-end distance of the polymer chain, and b is the statistical segment length where b_{PB} = 5.9 Å and b_{PEO} = 6.0 Å. The degree of chain stretching in the core and corona before and after fragmentation for 50:50 hybrid micelles is summarized in Table 6.7. In Table 6.7, the degree of chain stretching in is calculated using Equations 6.1 and 6.2, where N_{core} and N_{corona} are either the degrees of polymerization of the longer (i = L) or shorter (i = S) diblock copolymer in the blend. For example, in the BO(6-5)/(8-7) hybrid micelles, the degree of chain stretching in the long diblock is calculated where N_{core} = 174 and N_{corona} =172 , as those are the degrees of polymerization of the longer diblocks used in that particular blend. The degree of chain stretching for pure PB-PEO micelles was shown previously in Table 5.1.

Table 6.7: Degree of chain stretching in the core and corona for the long and short diblock of 50:50 PB-PEO hybrid micelles in [C_2mim][TFSI]. Degree of chain stretching is estimated according to Equations 6.1 and 6.2, where N_L is used for the long diblock calculations and N_s is used for the short diblock calculations.

(50:50) blend	(6-5)/(8-7)	(8-7)/(10-9)	(10-9)/(25-22)	(25-22)/(27-27)
Degree of chain stretching in long diblock				
$s_{core,0}$	2.5	2.3	2.1	3.6
$s_{corona,0}$	2.3	3.9	2.5	2.3
$s_{core,f}$	1.9	1.9	1.8	3.3
$s_{corona,f}$	1.9	2.1	1.7	1.9
Degree of chain stretching in short diblock				
$s_{core,0}$	3.0	2.3	3.3	3.7
$s_{corona,0}$	2.8	4.4	3.8	2.5
$s_{core,f}$	2.3	1.9	2.9	3.4
$s_{corona,f}$	2.3	2.3	2.6	2.1

From the estimates in Table 6.7, not only is there an entropic drive to fragmentation in the form of relief in core chain stretching, but there is also a significant relief in the degree of corona stretching after fragmentation. Due to the lack of chain exchange for PB-PEO micelles in [C_2mim][TFSI], it is not expected that blending two molar masses of PB-PEO would alter the relaxation mechanism. Additionally, the small variations in micelle

dimensions and comparable chain stretching in the hybrid micelles in comparison to the pure PB-PEO micelles does not account for the strong decrease in τ_{frag} for hybrid micelles. The chain stretching in micelles studied in Chapter 5 is also quite high, so this does not truly explain why the observed fragmentation kinetics are much faster for hybrid micelles when compared to the pure micelle case.

It would be of interest to explore the composition dependence for other molar masses of PB-PEO hybrid micelles in the future to determine whether the composition dependence obtained in the case of BO(8-7)/(10-9) blends is applicable to a larger range of $\langle N \rangle$. Initially, it was anticipated that the low molar mass chains may localize towards the interface in a fragmenting micelle to relieve the corona crowding penalty of fragmentation discussed previously. If this were the case, the fragmentation kinetics would be limited by the fragmentation times of the single component micelles used to prepare the hybrid micelles, *i.e.*, τ_{frag} would be approximately 200 ± 75 min for BO(8-7)/(10-9) hybrid micelles, as this is the fragmentation time determined for pure BO(8-7) micelles in [C_2mim][TFSI]. As evidenced by the values of τ_{frag} in Table 6.3, this is not the case. Further consideration of the structure of the micelles prepared by DD of PB-PEO blends can rationalize this result. Assuming the chains in PB-PEO blends are well mixed, which is reasonable based on Figures 6.1 and 6.2, the shorter PB-PEO chains are randomly distributed throughout the hybrid micelles. Because the chains are distributed throughout a given micelle, this picture where short chains are localized to the interface and long chains are concentrated in the spherical caps of a "peanut" shaped micelle undergoing fragmentation seems unreasonable.

It is more reasonable that the relief of chain stretching and increase in configurational entropy slightly lowers the barrier to fragmentation in molar mass blends of PB-PEO micelles. However, this does not fully explain the decrease in τ_{frag} for the hybrid micelles, as the low dispersity PB-PEO diblocks studied in Chapter 5 are also quite stretched.

6.4 – Summary

Blending different molar masses of diblock copolymers to make micelles is known to affect the size and equilibration kinetics in comparison to micelles prepared from a relatively monodisperse diblock copolymer.[22,194,197] Molar mass blends of PB-PEO diblocks were prepared using the polymers studied in Chapter 5, and micelles were prepared by DD of PB-PEO blends in [C_2mim][TFSI]. The influence of blending and molar mass dispersity on fragmentation kinetics was explored using *T*-jump DLS, SAXS, and TEM. It was found that the hybrid micelles of PB-PEO exhibit significantly faster fragmentation kinetics when compared to the fragmentation times obtained for the analogous pure micelles in [C_2mim][TFSI]. One hybrid micelle system, BO(8-7)/(10-9), exhibited very fast fragmentation kinetics, where τ_{frag} = 37 min for a 50:50 (wt:wt) mixture of the two molar masses was used. The composition dependence was explored using *T*-jump DLS which showed that different ratios of BO(8-7) and BO(10-9) did, in fact, influence the rate of fragmentation, where fragmentation times as fast as 8.3 min were obtained when the blend contained 60% BO(8-7) by weight. Because the fragmentation times of these hybrid micelles were faster than either of the single component micelles, it

is proposed that the increase in fragmentation rates can be attributed to the highly stretched low molar mass polymers in micelles prepared by DD, but this does not fully describe the kinetics obtained here, as the chain stretching in the pure micelle case is also quite high. Furthermore, the relief in chain stretching is the primary drive for micelle fragmentation in general, but does not fully explain the increased fragmentation rates obtained here. This work highlights how limited the current understanding of micelle fragmentation and fusion is, and further exploration of this phenomenon is warranted.

Chapter 7 – Imaging the swelling behavior of PB-PEO in [C_2mim][TFSI]

7.1 – Introduction

The direct dissolution (DD) method to prepare nonequilibrium, kinetically trapped micelles has proved to be an enabling process in studying micelle fragmentation. An open question of interest in this regard is why does the DD protocol lead to micelles with aggregation numbers at least twice the equilibrium aggregation number, and how does the ordered morphology of the bulk copolymer influence the size of micelles prepared by DD? Understanding the relationship between the bulk copolymer domain size and the as-prepared micelle radius could allow for more precise control over the size of micelles prepared by DD. In Chapters 3 and 5, it was found that PB-PEO diblocks self-assemble into a lamellar morphology in the bulk, and it was hypothesized that the DD protocol gives rise to a Rayleigh-type instability along the length of the alternating lamellae, which could explain the relationship between d_{PB} and $\langle R_{core} \rangle_0$ observed in Chapter 5.[91,139] Specifically, it was proposed that in the DD method the ionic liquid swells the PEO lamellae, which begin to peel apart into sheets, and instabilities in the form of periodic undulations along the surfaces of the lamellae lead to the pinch-off and formation of kinetically trapped micelles. This process is illustrated schematically in Figure 3.19.[91]

Instabilities involving peristaltic undulations, such as the Rayleigh instability, have been reported as the underlying mechanism in some thermotropic order-order transitions (OOTs) between BCP microphases in the bulk.[201] For example, experimental reports on the thermoreversible cylinder-to-sphere transition attributed the mechanism of this phase change to a Rayleigh-type instability.[190,191,202,203] Theoretical frameworks on the stability of ordered BCP microphases often predict the occurrences of these types of instabilities in BCP OOTs.[204–209] Ryu and Lodge studied the thermoreversible cylinder-to-sphere transition in PS-PI-PS triblock copolymers, where the cylindrical domains were preferentially oriented using large amplitude reciprocating shear. From small amplitude oscillatory shear along the cylinder axis, T_{OOT} was identified as 198 °C.[190,191] The mechanism of the cylinder-to-sphere transition was studied using a combination of SAXS and TEM, which was anticipated by Laradji *et al*.[204,206] and Qi and Wang[207] to proceed via anisotropic fluctuations with cubic symmetry. Ryu and Lodge confirmed this mechanism was involved in the cylinder-to-sphere transition of PS-PI-PS triblocks using SAXS and TEM, where clear evidence of these fluctuations were observed directly by TEM, and SAXS confirmed the bcc symmetry of these fluctuations as predicted by theory.[190,191] In addition to the mechanism of morphological transitions, the kinetics of these processes are of interest as well. There are several experimental reports on the kinetics of morphological transitions for BCPs in solution and in the bulk, such as disorder-to-order,[210] lamella-to-cylinder,[201] cylinder-to-sphere,[211] and cylinder-to-gyroid[212] transitions.

The Rayleigh instability is thought to be the primary mechanism of the cylinder-to-sphere transition in BCP micelles as well.[110,181,192,213–216] Lund *et al.* studied this transition for PEP-PEO micelles in mixtures of D_2O and DMF-d_7 using TR-SAXS and TR-SANS, where increased DMF content above 50% DMF/D_2O induces the transition from cylindrical to spherical micelles.[110] From TR-SANS experiments, they found that the time-dependent fraction of cylindrical micelles in solution follows a single exponential decay, with a rate constant of 328 ms. The authors concluded that the decomposition of cylindrical micelles directly to spheres occurs without any intermediate structures, where surface instabilities along the length of the cylindrical axis leads to rapid break-up into spherical micelles, which further equilibrate in size via chain exchange.[110]

Preliminary insights into the DD mechanism using high-temperature LP-TEM for one molar mass of PB-PEO films swollen with [C_2mim][TFSI] are discussed herein. Specifically, thin sections of BO(8-7) prepared by cryo-microtoming are swollen with [C_2mim][TFSI] and imaged at 70 °C in the TEM to mimic the conditions of the DD solution preparation method. Due to the high *Z*-contrast of ILs and large value of $\chi_{PB\text{-}IL}$, contrast between the PB and PEO domains is induced by preferential swelling of PEO lamellae with [C_2mim][TFSI], and further annealing in the microscope provides some hints on the presence of surface instabilities in the DD of PB-PEO in [C_2mim][TFSI].

7.2 – Materials and methods

Preparation of PB-PEO films. BO(8-7) was annealed in a vacuum oven (< 100 mTorr) at T = 70 °C for 48 h, followed by rapid quenching in liquid nitrogen ($T \approx$ –196 °C). Thin films of BO(8-7) were prepared via cryo-microtoming at T = –80 °C, as described in Section 2.6.3. BO(25-22) films shown in Figure 7.2b were prepared in this manner.

TEM and staining of BO(8-7). TEM of BO(8-7) stained with OsO_4 was conducted according to Section 2.6.3. 300 mesh copper TEM grids (Ted Pella Inc.) with sections of BO(8-7) were stained with aq. OsO_4 (Sigma Aldrich) vapor at 40 °C for 1 h.

High-temperature TEM of BO(8-7) swollen with [C_2mim][TFSI]. Unstained BO(8-7) sections on 300 mesh copper TEM grids (Ted Pella Inc.) were swollen with 9 μL of [C_2mim][TFSI]. The excess IL was manually blotted with filter paper from below to give thin specimens for TEM imaging. Immediately after blotting, the sample was transferred to a temperature-controlled TEM sample holder for imaging. High-temperature TEM (T = 70 °C) of BO(8-7) films swollen with [C_2mim][TFSI] was conducted according to Section 2.6.3.

Image corrections. Some minor image corrections were applied using ImageJ software to enhance the brightness and/or contrast of some LP-TEM micrographs obtained in the swelling experiment. Images where contrast or brightness corrections were applied are indicated as such in the associated captions.

7.3 – Results and discussion

The ordered morphology of BO(8-7) at 70 °C in the bulk was found to be lamellar, as determined by SAXS in Figure 5.11. TEM of the bulk copolymer was used to confirm this assignment, and to ensure that the thermal treatment prior to microtoming resulted in samples with minimal structural defects and suppressed crystallization of the PEO domains. As shown in Figure 7.1, BO(8-7) undergoes microphase separation into alternating lamellae of PB and PEO domains after annealing at 70 °C for 48 h.

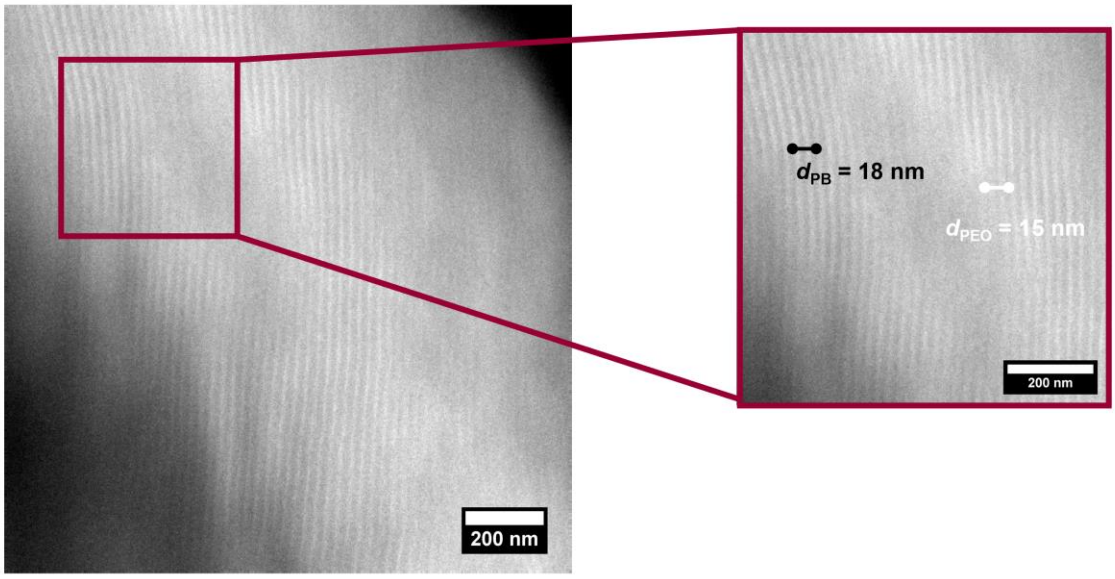

Figure 7.1: TEM micrograph of BO(8-7) stained with OsO_4. In the left image the long-range ordering of the PB-PEO lamellae is evident, and the inset to the right shows the domain spacings measured by taking the average size of ten domains, where $d_{PB} \approx 18$ nm and $d_{PEO} \approx 16$ nm.

Note that this temperature is of interest here as this is the temperature used in the DD of PB-PEO in [C_2mim][TFSI]. Due to the osmium stain used to image the bulk copolymer, the PEO domains appear light and the PB domains appear dark in Figure 7.1. Image analysis of Figure 7.1 gives domain sizes for the PB and PEO domains, where d_{PB} = 18 nm and d_{PEO} = 15 nm, which is in reasonable agreement with estimates by SAXS, where d_{PB} = 17 nm and d_{PEO} = 11 nm. Note that TEM often gives a larger domain spacing than SAXS due to domain tilting.

Initially, it was thought that a higher molar mass such as BO(25-22) would be better suited for swelling experiments, due to the larger domain spacing. With larger features, the sample could be imaged at a lower magnification, which minimizes the potential for electron beam damage. However, it was found that the thermal treatment described in Section 7.2 did not eliminate local defects, such as grain boundaries, in BO(25-22). TEM micrographs of BO(25-22) stained with OsO_4 are shown in Figure 7.2 using two methods of sample preparation. The first sample was prepared without annealing prior to cryo-microtoming (Figure 7.2a), while the other sample was annealed at 70 °C, quenched in liquid nitrogen, and sectioned (Figure 7.2b). As shown in Figure 7.2a, without thermal annealing at 70 °C prior to microtoming, defects due to the crystallization of PEO were observed. From Figure 7.2b, thermal annealing and quenching in liquid nitrogen suppressed crystallization of PEO, but microstructural defects remained. From Figure 7.1, BO(8-7) orders into well-defined, alternating lamellae with fewer defects compared to BO(25-22). While it is not possible to eliminate the presence of grain boundaries, it is ideal

to minimize them as the presence of defects could cause difficulties in the identification of evolving surface instabilities during swelling. Thus, experiments were conducted using BO(8-7). The films were swollen in [C_2mim][TFSI] and annealed in the microscope directly at 70 °C to mimic the conditions of the DD protocol.

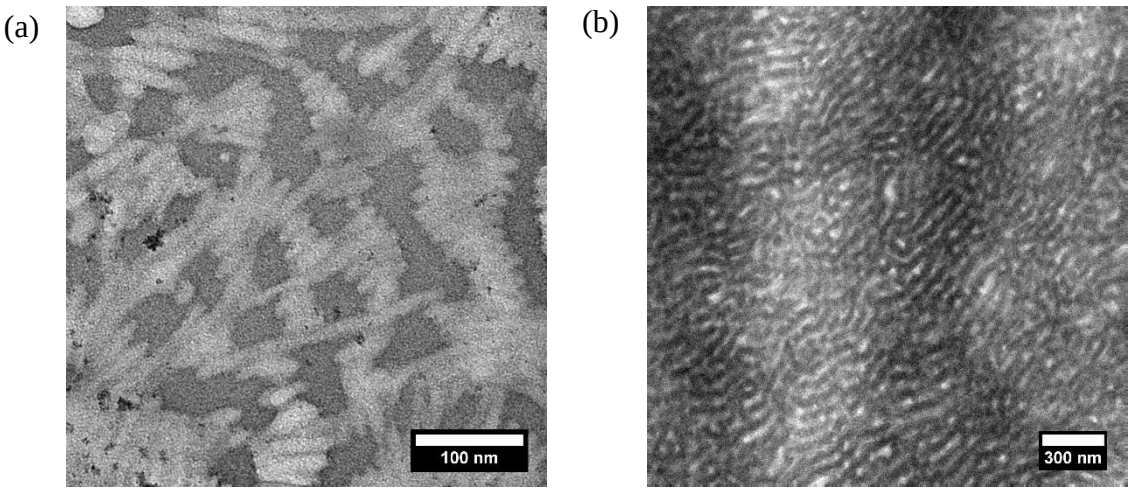

Figure 7.2: TEM micrographs of BO(25-22) stained with aq. OsO_4 vapors with: (a) no prior thermal treatment, and (b) when annealed at 70 °C for 48 h and immediately quenched in liquid nitrogen prior to microtoming.

Once the bulk morphology of PB-PEO was confirmed, and the sample preparation method was optimized, the swelling behavior of PB-PEO films with [C_2mim][TFSI] was explored at 70 °C via LP-TEM. The difference between the images obtained in the swelling experiment and those shown in Figures 7.1 and 7.2 is that the IL itself acts as a type of stain, eliminating the need for OsO_4 staining of BO(8-7). Therefore, the images shown for the swelling experiment exhibit an inversion of contrast, consistent with images obtained in Chapters 3 – 5,[91,92] where the PB domains appear light and the PEO domains appear

dark due to the preferential dissolution of PEO in the IL. After the addition of [C2mim][TFSI] to the TEM grid containing sections of BO(8-7), excess IL was manually blotted away, and the grid was then immediately placed in the TEM for imaging while annealing at 70 °C. Figure 7.3 shows the early time points obtained at room temperature (left) and after annealing at 70 °C for approximately 10 min (inset, right). Image analysis of the inset in Figure 7.3 was used to confirm that the IL causes enhanced TEM contrast, where the domain spacings were $d_{PEO} \approx 20$ nm and $d_{PB} \approx 19$ nm.

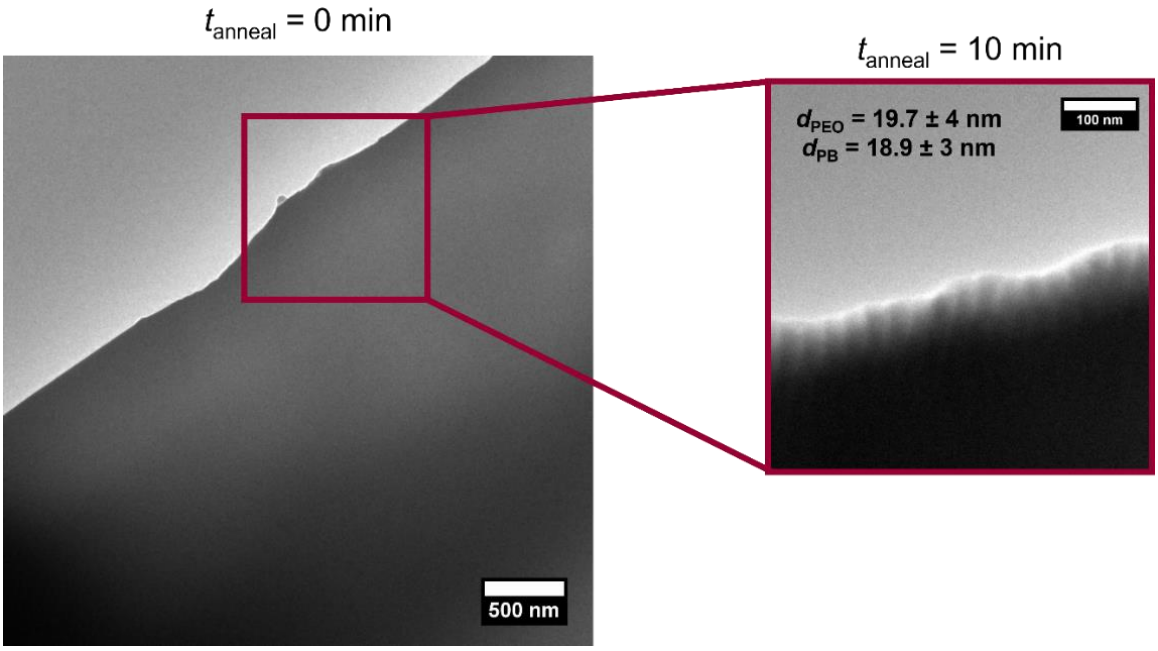

Figure 7.3: LP-TEM micrographs of BO(8-7) swollen with [C2mim][TFSI] at room temperature (left, t_{anneal} = 0 min). The inset (right) shows a higher-magnification image of the area indicated in the left image after annealing at 70 °C for 10 min. In the inset, the onset of contrast appears as [C2mim][TFSI] begins preferential swelling of the PEO domains (dark) and is assumed to be excluded from the PB domains (light).

Further annealing of the IL-swollen BO(8-7) film results in a slight improvement in contrast, as shown in Figure 7.4. After approximately 1 h of annealing at 70 °C, undulations along the length of the PB lamellae become visible, and after 65 min of annealing the undulations become even more apparent. Analysis of the 65 min image in Figure 7.4 gives d_{PB} = 21 nm and d_{PEO} = 24 nm. The increase in d_{PEO} with annealing times could be attributed to further swelling of PEO domains in [C_2mim][TFSI]. The undulations likely arise due to the change in surface tension between the PB and [C_2mim][TFSI]-swollen PEO domains. The undulations observed in Figure 7.4 are consistent with the first step in a Rayleigh-instability-triggered morphological transformation.[181,215]

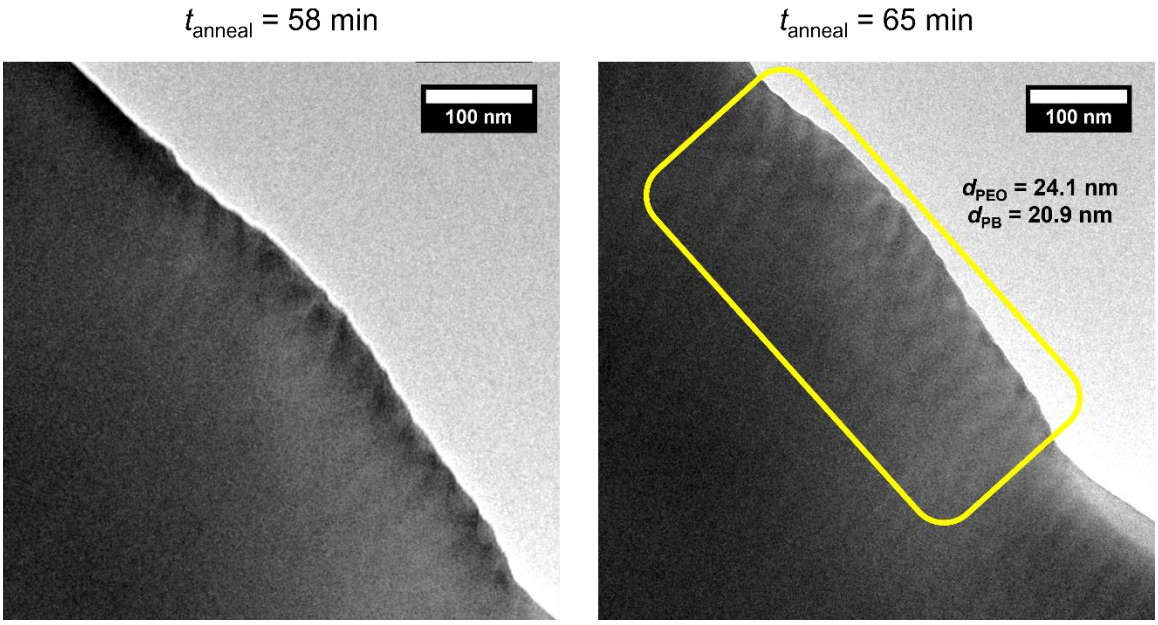

Figure 7.4: LP-TEM micrographs of BO(8-7) swollen with [C_2mim][TFSI] at 70 °C after 58 min of annealing (left) and 65 min of annealing (right). After t_{anneal} = 65 min, undulations of the PB lamellae are observed (right, yellow box) where d_{PB} = 21 nm and d_{PEO} = 24 nm.

Figure 7.5 shows LP-TEM micrographs after 72 min of annealing, where the undulations along the length of the PB lamellae become more distinct, and adequate contrast is achieved to conduct image analysis. From Figure 7.5, d_{PEO} increases again to approximately 23.7 nm, whereas d_{PB} = 16.3 nm. The absolute values of the domain spacings after annealing may have some inherent error due to the relatively low contrast achieved throughout the swelling experiment.

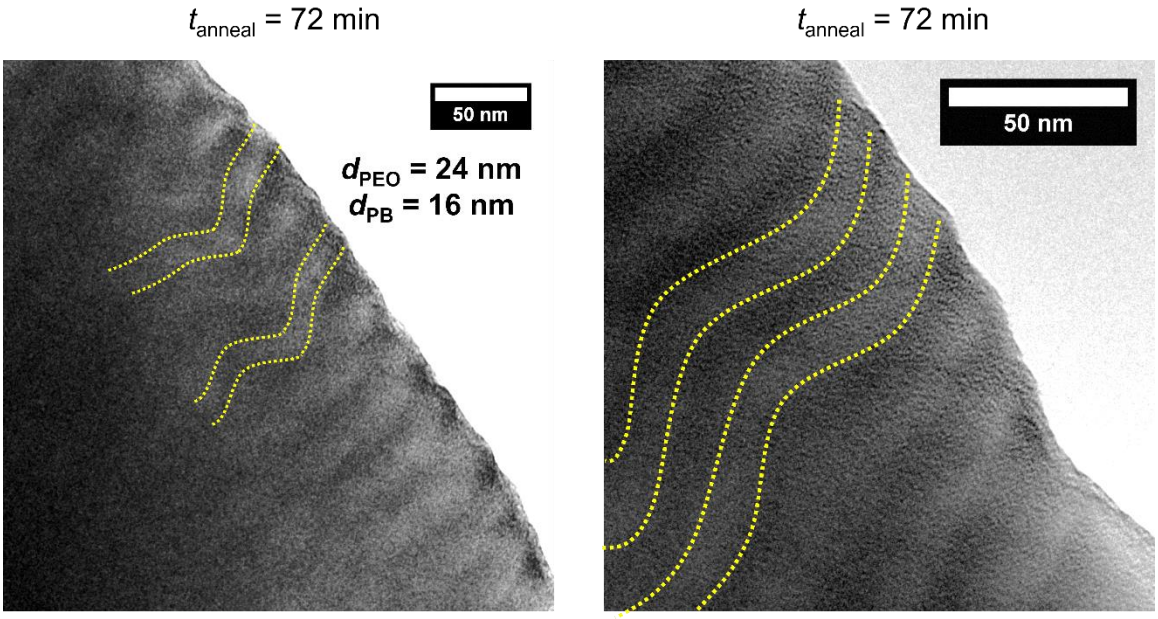

Figure 7.5: LP-TEM micrographs of BO(8-7) swollen with [C2mim][TFSI] at 70 °C after 72 min of annealing. After t_{anneal} = 72 min, undulations of the PB lamellae remain, and the the wavelength of the undulation is estimated by image analysis to be $\lambda/2 = 50 \pm 8$ nm, d_{PB} = 16.3 nm and d_{PEO} = 23.7 nm. Brightness and contrast corrections were applied to the left image, and contrast corrections were applied to the right image. Some undulations are outlined in yellow dashes to guide the eye.

However, comparisons of the change in domain spacing and structure throughout one swelling experiment were conducted. As is expected for a Rayleigh-like instability, the transition from cylinders to spheres will occur for some minimal perturbation wavelength, $\lambda_{min} = 2\pi R_0$, where R_0 is the radius of the initial cylinder. From Figure 7.5, the wavelength of the undulation is estimated as $\lambda/2 = 50 \pm 8$ nm, where $\lambda/2$ is measured as the length, in nm, from the peak to valley of an undulating PB lamella.

A significant change in the morphology of the PB domains is observed after 80 min of annealing, as shown in Figure 7.6, where a transition from undulating lamellae to a pearl-necklace-like structure is observed. This, again, is another characteristic of a Rayleigh-type instability, where the perturbations first result in undulations along the length of the lamellae followed by the formation of connected spherical domains, which eventually pinch off into single-compartment spheres.[181] Due to the relatively low contrast in Figure 7.6, image analysis of the sphere diameter was difficult to perform at this annealing time; however, further annealing at 70 °C for 90 min results in improvements in contrast between the PB and PEO/IL domains, and this last intermediate structure in a Rayleigh-type transition persisted for at least 10 min, as shown in Figure 7.7. From Figure 7.7, the formation of distinct, spherical PB domains connected in the lamellar plane are observed after annealing the BO(8-7) films swollen with [C_2mim][TFSI] at 70 °C for 90 min. The inset in Figure 7.7 shows a magnified portion of this structure.

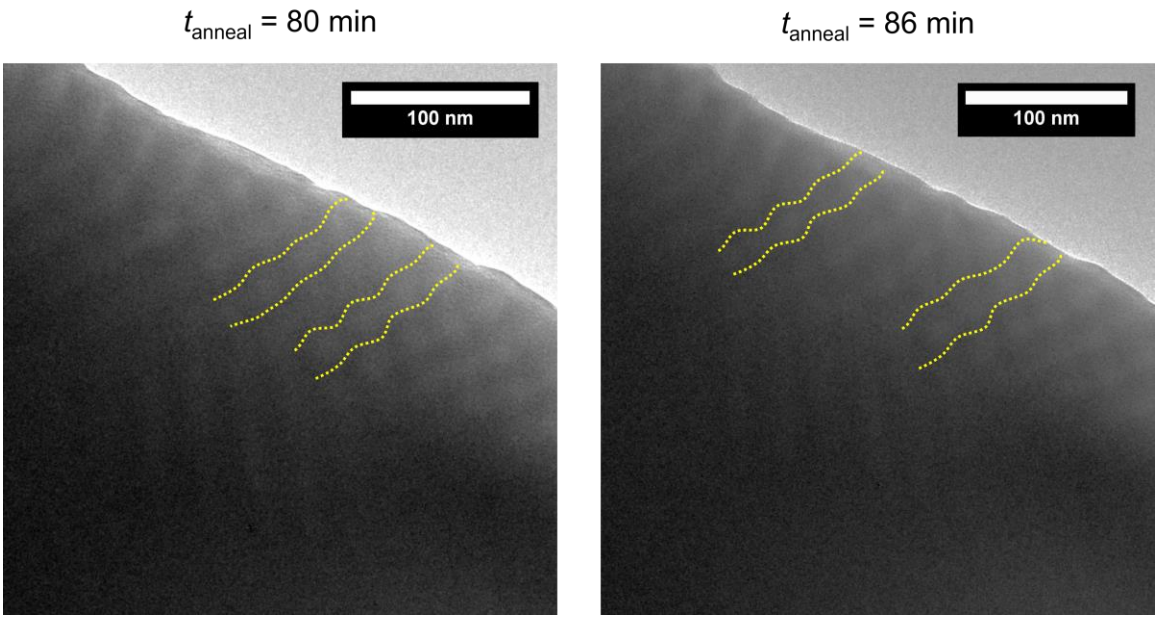

Figure 7.6: LP-TEM micrographs of BO(8-7) swollen with [C_2mim][TFSI] at 70 °C after 80 min of annealing. At t_{anneal} = 80 min, the undulations of the PB lamellae begin to appear as interconnected, spheres. Brightness corrections applied to both images. Some undulations are outlined in yellow dashes to guide the eye.

While it may appear that the PB domains are forming a type of network structure, this could be due to the presence of additional layers of PB-PEO. The films prepared by cryo-microtoming have a thickness on the order of 100 nm, so the presence of additional layers of PB-PEO below the surface is possible. Further experiments of this phenomenon by techniques which give information on the overall sample morphology, such as grazing-incidence SAXS (GI-SAXS), could give more insights into the symmetry of this perturbation and the overall sample structure. Nevertheless, it is clear from Figures 7.3 – 7.7 that swelling a lamellar sample of PB-PEO with IL causes a change in interfacial tension significant enough to induce instabilities along the length of the lamellae. The

mechanism of the instabilities observed here are qualitatively similar to the previously hypothesized Rayleigh instability discussed in Chapters 3 and 5.

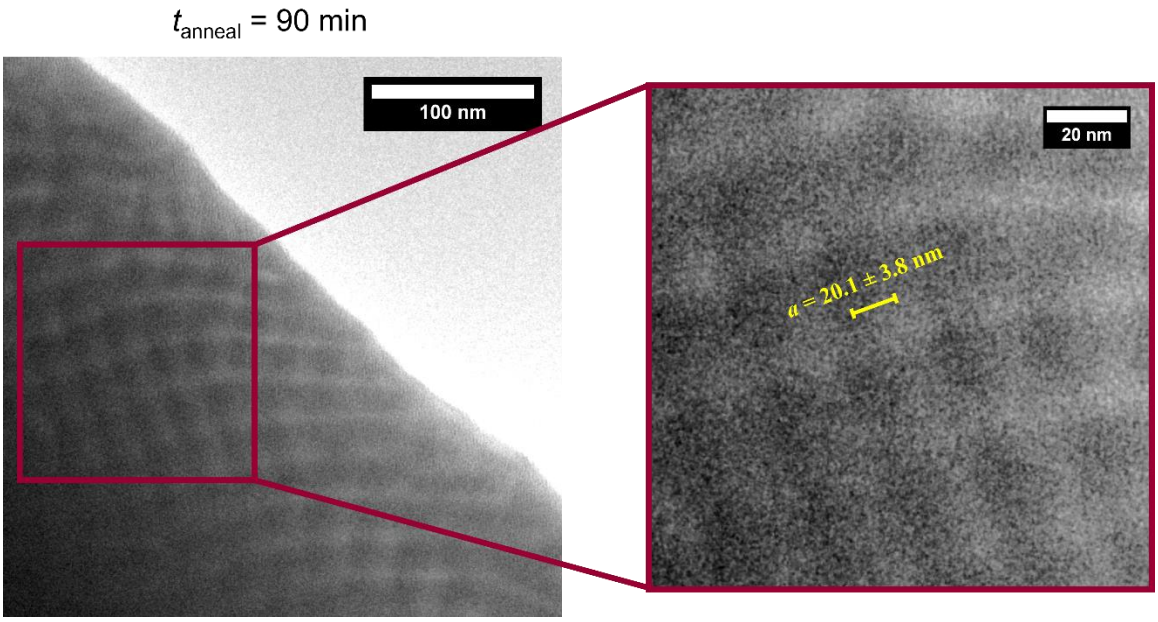

Figure 7.7: LP-TEM micrographs of BO(8-7) swollen with [C_2mim][TFSI] at 70 °C after 90 min of annealing. At t_{anneal} = 90 min, the interconnected sphere PB domains become more apparent throughout the film, and the amplitude of the perturbation a = 20.1 ± 3.8 nm. Brightness corrections applied to left image and inset (right).

While the swelling experiment was used to mimic the conditions of a DD experiment, there are notable differences including polymer concentration and the absence of stirring. Stirring may decrease the time required for lamellae to pinch off into spherical micelles, and could increase the maximum wavelength of the instability within the sample. Additionally, because a majority of the 9 μL of [C_2mim][TFSI] was manually blotted away to give samples that are thin enough for imaging (~ 200 nm or less), it was not anticipated

that the full dissolution of the copolymer would be achieved. The main objective in this swelling experiment was to establish what is determining the as-prepared micelle radius when making solutions by DD of PB-PEO in [C_2mim][TFSI], and to uncover the mechanism of this transformation. From Figure 7.8, the formation of connected spherical domains in the PB domain is maintained after 95 min of annealing, which is expected to be close to the transition from a swollen, bulk polymer to single-compartment micelles, as shown previously in Figure 3.19. While these results are promising, they are preliminary. More details on the bulk sample morphology from scattering experiments should be conducted to confirm whether the fluctuations in the PB microstructure occur throughout the entirety of the sample, and not just the small sample area imaged by TEM.

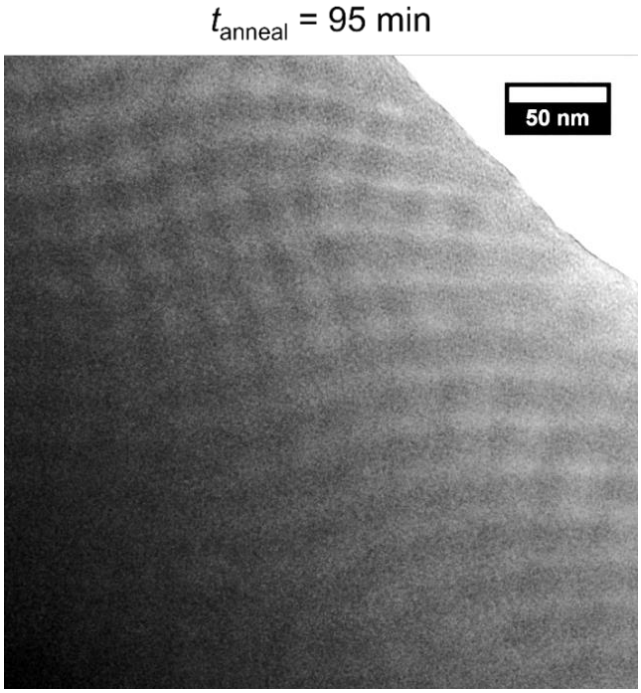

Figure 7.8: LP-TEM micrographs of BO(8-7) swollen with [C_2mim][TFSI] at 70 °C after 95 min of annealing. The interconnected sphere PB domains persist throughout the film at

t_{anneal} = 95 min, and the amplitude of the perturbation a = 20.1 ± 3.8 nm. Brightness corrections applied.

A cylinder-to-sphere transition driven by the Rayleigh instability is illustrated schematically in Figure 7.9. Nichols and Mullins applied the Rayleigh instability analysis to transitions of solid cylinders to spheres.[217]

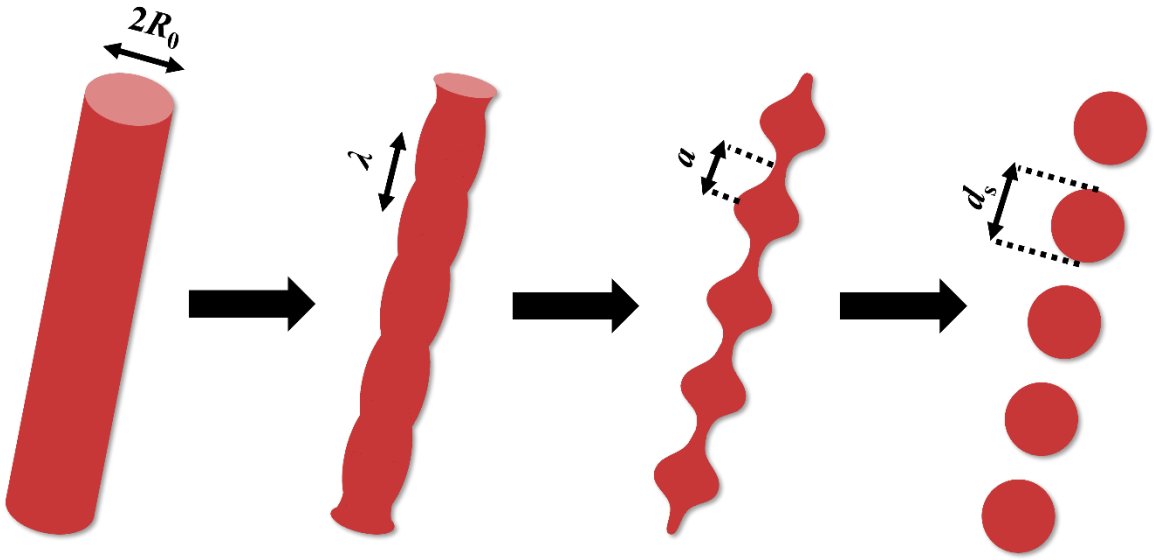

Figure 7.9: Schematic illustration of the Rayleigh instability driven cylinder-to-sphere transition.

According to the theory, a cylinder with isotropic surface energy is analyzed with respect to variations of the cylinder radius r by surface undulations described by Equation 7.1,

$$r = R_0 + a \sin \frac{2\pi}{\lambda} x \tag{7.1}$$

where R_0 is the radius of the initial smooth cylinder, a is the amplitude of the perturbation, λ is the wavelength of the perturbation, and x is the coordinate along the cylindrical axis.[181] In the case of a lamellar-to-sphere transition, the initial cylinder radius is substituted by one half of the initial domain spacing of the PB lamellae.

The classical Rayleigh-Plateua criterion for stability states that a cylinder of radius R_0 is unstable to sufficiently long, sinusoidal disturbances with wavelengths larger than the circumference of the cylinder (*i.e.*, $\lambda > \lambda_{min}$),[218] where the Rayleigh criterion in defined in Equation 7.2.[219]

$$\lambda > \lambda_{min} = 2\pi R_0 \tag{7.2}$$

If the perturbations are resolved into sinusoidal components, perturbations with $\lambda > \lambda_{min}$ will continue to grow with time (*i.e.*, unstable perturbations), while others with $\lambda < \lambda_{min}$ decay in time (*i.e.*, stable perturbations). For sinusoidal perturbations, the rate of growth is given by the wavenumber (*i.e.*, wavelength) of the perturbation. Rayleigh showed through linear stability analysis that the fastest growing mode, or maximum disturbance wavelength, λ_{max}, leads to a cylinder-to-sphere transition, and is given by Equation 7.3. This critical disturbance is expressed in terms of the maximum wavenumber k_{max} shown in Equation 7.4.

$$\lambda_{max} = 9.01R_0 \tag{7.3}$$

$$k_{max} = 0.697 / R_0 \tag{7.4}$$

In other words, λ_{min} is the minimum instability wavelength required for perturbations to grow, the perturbations will continue to grow in wavelength until reaching a critical maximum wavelength λ_{max} which causes breakup into spheres. It is well recognized that k_{max}, and therefore λ_{max}, can be used as a first approximation of the drop sized formed after breakup.[181,215] Then, knowing λ_{max}, the droplet radius, d_s, is estimated according to Equation 7.5. Based on this theory, estimates of the features observed in Figures 7.5 – 7.8 were obtained to determine whether the undulations observed in Figure 7.5 have a wavelength long enough to induce a transition, and what the resulting sphere diameter should be, given the initial domain spacing of PB-PEO.

$$d_s = 3.78R_0 \tag{7.5}$$

As the ordered morphology of BO(8-7) is lamellar and not cylindrical, the wavelength is approximated as $\lambda_{min} = \pi d_{PB,0}$, where $2R_0 = d_{PB,0}$ is the unperturbed domain size of PB measured in Figure 7.1. For BO(8-7) in [C_2mim][TFSI], $\lambda_{min} = \pi(19\text{ nm}) = 60$ nm, and the wavelength of the undulations measured in Figure 7.5 is significantly longer than λ_{min}, where $\lambda = 100 \pm 16$ nm. Therefore, these perturbations cause the lamellar morphology to become unstable. From Equation 7.3, the required wavelength for breakup of BO(8-7) into

spheres is λ_{max} = 9.01/(8 nm) = 72 nm. Again, the wavelength of undulations observed in Figure 7.5 exceeds the stability criterion, which leads to the observed pearl-necklace-like structures in Figures 7.7 – 7.8. The values measured by image analysis for BO(8-7) swollen in [C_2mim][TFSI] are summarized in Table 7.1.

Table 7.1: Parameters measured via image analysis of Figures 7.4 – 7.7 and estimates of the theoretical maximum ($d_{s,max}$) and minimum ($d_{s,max}$) as-prepared micelle diameter for BO(8-7) in [C_2mim][TFSI].

	$2R_0 = d_{PB}$ (nm)	$\lambda/2$ (nm)	a (nm)	$d_{BO(8\text{-}7),C2mim}$ (nm)	$d_{s,max}$ (nm)*	$d_{s,min}$ (nm)*
	19 ± 3	50 ± 8	20 ± 4	42 ± 12	41	30
counts	30	30	80	500	-	-

*Theoretical minimum and maximum micelle diameters calculated using $d_s = 3.78(d_{PB,0} \pm 6)/2$

In Table 7.1 image analysis of Figures 7.7 and 7.5 was used to obtain the values of a and $\lambda/2$, respectively. Image analysis of Figure 4.1 was used to report the as-prepared micelle diameter of BO(8-7) in [C_2mim][TFSI], where $d_{BO(8\text{-}7),C2mim} = 2\langle R_{core}\rangle_0 = 42 \pm 12$ nm. Assuming the DD process proceeds via a Rayleigh-type instability, the theoretical maximum ($d_{s,max}$) and minimum ($d_{s,min}$) diameters of BO(8-7) micelles in [C_2mim][TFSI] were determined, as shown in Table 7.1. Using one standard deviation in d_{PB}, ± 3 nm, as the upper and lower limits of $d_{PB,0}$, the minimum and maximum micelle core diameters are estimated from Equation 7.5 as $d_{s,min} = 3.78R_0 = 3.78(16\text{ nm})/2 = 30$ nm and $d_{s,max} = 3.78R_0$

= 3.78(21 nm)/2 = 41 nm, respectively. The average as-prepared micelle diameter for BO(8-7) in [C_2mim][TFSI] is 42 ± 12 nm, which agrees relatively well with the estimated micelle diameters shown in Table 7.1.

Although, the as-prepared micelle diameter lies much closer to the anticipated value of $d_{s,max}$. This is likely because the maximum perturbation wavelength measured in the swelling experiment is in the absence of stirring. In the DD process, prolonged stirring over a period of 48 h is used to prepared micelle solutions, and the presence of stirring likely increases the average perturbation wavelength in the DD protocol leading to a larger λ_{max} and faster breakup into larger, kinetically trapped micelles. Given the instabilities imaged in the swelling experiment, and the rough agreements between the theory and measured micelle size, the hypothesis presented in Chapters 3 and 5, that the DD of PB-PEO in ILs proceeds through a Rayleigh-type instability, is reasonable.

7.4 – Summary

In this chapter, the underlying mechanism involved in the direct dissolution of PB-PEO in ILs was explored using LP-TEM. A thin film of one molar mass of PB-PEO was swollen with [C_2mim][TFSI] and annealed at 70 °C in the microscope to mimic conditions of the DD protocol. After annealing for 10 min, the IL began to penetrate the PEO domains, inducing TEM contrast in the swollen film. Undulations along the lamellar surface were observed for longer annealing times (~ 60 min), with wavelengths estimated to be $\lambda/2$ = 50

± 8 nm. Based on the initial domain spacing of the PB lamellae, the minimum wavelength required for sphere formation is 60 nm. Additionally, the as-prepared micelle diameters are consistent with the distribution of sphere sizes anticipated for a Rayleigh instability driven transition from cylinders to spheres. The perturbations observed in the swelling experiment are consistent with that of a Rayleigh-type instability, which may then be responsible for the dependence of d_{PB} on $\langle R_{core} \rangle_0$.

Chapter 8 – Summary and outlook

8.1 – Thesis summary

The goal of this thesis was to expand the current understanding of block copolymer micelle fragmentation kinetics in ILs. Specifically, the fragmentation of kinetically trapped PB-PEO micelles in the [C$_x$mim][TFSI] solvent family was explored using a combination of scattering and TEM techniques. The nonvolatility of ILs allowed for the direct imaging of micelle dynamics in solution, and the use of a temperature-controlled TEM sample holder allowed for annealing of micelle solutions directly in the microscope.

Prior to this work, the barrier to micelle fragmentation was proposed to arise from the exposure of the core block to the solvent during micelle breakup.[126] If this were the case, the solvent quality should influence the rate of fragmentation. In Chapter 3, the fragmentation kinetics were studied for BO(8-6) micelles prepared by direct dissolution in five [C$_x$mim][TFSI] ionic liquids, where x = 1, 2, 4, 6, and 8. This was achieved using *T*-jump DLS, SAXS, and *ex-situ* LP-TEM. It was found that the micelle size decreased significantly after prolonged annealing at 170 °C. After annealing, the final aggregation number was about half of the original. The decay in $\langle R_h \rangle$ and $\langle R_{core} \rangle$ could be well described by a compressed exponential with an exponent of 2 in almost all cases.[91] The origin of this functional form is not yet apparent. The characteristic relaxation times determined by fits

to this equation for DLS for BO(8-6) in [C_2mim][TFSI] were essentially independent of concentration, indicating a relaxation process that is first-order with respect to polymer concentration. The effects of solvent selectivity on the equilibration kinetics were investigated by using five different ionic liquids with varying cation alkyl chain lengths. In this case, the decay of $\langle R_h \rangle$ occurs on a similar timescale regardless of the solvent quality. Indirect evidence of micelle fragmentation was obtained by *ex-situ* LP-TEM and SAXS. The large decrease in core radius indicates that fragmentation is most likely the primary equilibration mechanism observed in this system, as individual chain exchange would not be expected to change the core radius to that extent.

These experiments indicate that the solvent selectivity plays a significant role in how far the as-prepared micelles are from the equilibrium size. Specifically, the more selective solvents result in micelles much larger aggregation numbers, while the least selective solvents result in as-prepared micelles that are closer to the equilibrium size. However, the solvent selectivity was found to play essentially no role in the fragmentation kinetics, as nearly all PB-PEO micelles in imidazolium-based ILs fragmented on the order of hundreds of minutes. Because the fragmentation kinetics are independent of solvent quality, the primary barrier to micelle fragmentation is most likely not from the exposure of the micelle core to the solvent in the transition state.[91]

Next, the direct observation of micelle fragmentation was conducted using high-temperature LP-TEM.[92] The previous studies on BCP micelle fragmentation were limited by ensemble averaging techniques such as SAXS and DLS; individual particles were

imaged by *ex-situ* LP-TEM. Chapter 4 demonstrated the direct observation of fragmentation for three molar masses of PB-PEO micelles in [C_2mim][TFSI] using high-temperature LP-TEM at 170 °C, which provided unique insights into the evolution of BCP micelles during fragmentation. Upon heating to 170 ºC a sequence of morphological transitions were observed, from a spherical micelle, to a prolate ellipsoid, then a "peanut" shape, followed by a two-spherical-compartment aggregate, where the last shape is presumed to be closest to the transition state. To the best of our knowledge, this iss the first direct evidence of BCP micelle fragmentation reported in the literature.[92]

In Chapter 5, the effect of molar mass on the fragmentation kinetics of micelles formed by PB-PEO copolymers was studied in [C_2mim][TFSI]. A series of six samples, with total M ranging from 10^4 to 10^5 g mol^{-1} and nearly constant composition ($f_{PEO} \approx 0.4$), were examined; all six formed spherical micelles with PEO coronas. Non-equilibrium PB-PEO micelles were prepared by direct dissolution. When subjected to high temperature annealing at 170 °C, the average micelle radius was found to decrease substantially, as determined by *T*-jump DLS and TR-SAXS. The characteristic fragmentation times were found to increase strongly with degree of polymerization as $\tau_{frag} \sim N^{1.8}$.[139] A previous model of micelle fragmentation by Dormidontova predicts a similar scaling, albeit in terms of N_{corona}.[97] Future measurements on a series of polymers with constant N_{core} will be required to assess whether this apparent agreement is robust. Again, the core size of the initial micelles was shown to correlate closely with the PB domain dimensions in the precursor

dry, lamellar copolymer, suggesting a formation mechanism involving peeling apart of layers, followed by pinching off into spherical domains.

In Chapter 6, molar mass blends of PB-PEO diblocks were prepared using the polymers studied in Chapter 5, and "hybrid" micelles were prepared by DD of PB-PEO blends in [C_2mim][TFSI]. The influence of blending and molar mass dispersity on fragmentation kinetics was explored using *T*-jump DLS, SAXS, and *ex-situ* LP-TEM. It was found that the hybrid micelles of PB-PEO exhibit significantly faster fragmentation kinetics when compared to the analogous pure micelles in [C_2mim][TFSI]. One hybrid micelle system, BO(8-7)/(10-9), exhibited notably faster fragmentation kinetics than the pure micelles of either diblock, where τ_{frag} = 37 ± 11 min for a 50:50 (wt:wt) mixture of the two molar masses was used. The pure BO(8-7) and BO(10-9) micelles had fragmentation times of τ_{frag} = 200 ± 75 min and τ_{frag} = 695 ± 90 min, respectively.

The composition dependence was explored using *T*-jump DLS which showed that different ratios of BO(8-7) and BO(10-9) did, in fact, influence the rate of fragmentation, where fragmentation times as fast as 8 min were obtained when the blend contained 60% BO(8-7) by weight. Because the fragmentation times of these hybrid micelles were shorter than either of the single component micelles, it is unclear why the hybrid micelles fragment so quickly. Despite the advances made in understanding micelle fragmentation, this work on hybrid PB-PEO micelles highlights the limitations in current understanding of micelle fragmentation and fusion. Further exploration of this phenomenon is warranted.

Finally, Chapter 7 explored the underlying mechanism involved in the direct dissolution of PB-PEO in IL using LP-TEM. A thin film of BO(8-7) was swollen with [C_2mim][TFSI] and annealed at 70 °C in the microscope to mimic conditions of the DD protocol. After annealing for 10 min, the IL began to penetrate the PEO domains, inducing TEM contrast in the swollen film. Undulations along the lamellar surface were observed for longer annealing times (~ 60 min), with wavelengths estimated to be $\lambda/2 = 50 \pm 8$ nm. Based on the initial domain spacing of the PB lamellae, the minimum wavelength required for sphere formation is 60 nm. Additionally, the as-prepared micelle diameters are consistent with the distribution of sphere sizes anticipated for a Rayleigh-instability-driven transition from cylinders to spheres. The perturbations observed in the swelling experiment are consistent with that of a Rayleigh-type instability, which may then be responsible for the dependence of d_{PB} on $\langle R_{core} \rangle_0$. However, additional experiments using small-angle scattering and TEM conditions that more closely mimic those in the DD protocol are necessary to confirm these results.

8.2 – Outlook

While significant advances in understanding BCP micelle fragmentation were made, studies related to micelle fragmentation and fusion are in their early stages. There are many aspects regarding the fragmentation of PB-PEO micelles in ILs that remain unexplained, and reports on micelle fusion are relatively limited. Additionally, while the PB-PEO/IL

system is very well characterized, it would be of interest to attempt to confirm micelle fragmentation occurs in other BCP/solvent systems. Therefore, many future directions exist in this field, with a few suggestions listed below.

1. To date, a detailed explanation of the compressed exponential relaxation behavior reported for the fragmentation of PB-PEO in ILs remains elusive.[89–91,139]
2. Currently, there is one report in the literature of the direct observation of micelle fusion.[123] Dormidontova's model for micelle equilibration kinetics assumes that fusion and fragmentation proceed through the same mechanism, in reverse. Detailed explorations into the kinetics of BCP micelle fusion must be conducted to verify this and could prove valuable in answering many open questions about micelle fragmentation.
3. Further details on the dependence of τ_{frag} and $\tau_{frag,0}$ on molecular parameters such as N_{core}, N_{corona}, γ, and Q/Q_{eq} would be informative.
4. Effect of copolymer architecture on fragmentation kinetics, and specifically, the fragmentation of triblock copolymers in ILs could elucidate more details about this equilibration mechanism.

To determine why micelle fragmentation consistently follows compressed exponential relaxation behavior, the universality of this process should be explored, and answers to questions 2 – 4 could provide additional insights. If micelle fusion proceeds via the same mechanism as fragmentation, but in reverse, it may be that fusion is well described by a compressed exponential growth in micelle size as a function of time. From Dormidontova's

theory,[97] micelle fusion is likely to contribute during the micelle formation process. One method to study micelle formation experimentally is through the cosolvent dissolution technique described in Section 2.3.2. By slowly increasing χ between the core block and the solvent through slow evaporation of the cosolvent, controlled micelle growth occurs from unimers in solution. This solution preparation method could be studied in more detail to gain insights into micelle fusion. The kinetics during formation may be difficult to determine by sample average techniques, such as small angle scattering, if multiple processes are contributing to micelle creation such as chain exchange, fusion, or a combination of the two processes. This is where single-particle imaging techniques can be incredibly useful in micelle equilibration studies. Parent, *et al*.[123] demonstrated that liquid-cell TEM can be used to observe micelle-micelle fusion events, but rigorous details on the kinetics of this process, and how it depends on N_{core}, N_{corona}, γ, and Q/Q_{eq} remain largely unexplored. Leveraging the capabilities of a flow-cell LC-TEM experiment to conduct cosolvent evaporation *in-situ* could provide further details on micelle fusion kinetics and confirm whether fusion proceeds via the same mechanism as fragmentation.

It is also of interest to explore the reproducibility of the scaling of $\tau_{frag} \sim N^{1.8}$ in other BCP/solvent systems, and to determine whether the N dependence is stronger in N_{corona} or N_{core}. In exploring other BCP/solvent systems with high $\chi_{core\text{-}solvent}$, it would be of interest to understand how the glass transition temperature of the core and corona blocks affects the fragmentation kinetics. Additionally, how does the temperature used for DD, and the distance this temperature is from the glass transition temperature, influence the relaxation

behavior of kinetically trapped micelles? Some BCPs in [$C_x$mim][TFSI] ILs that could be promising for further fragmentation studies include PS-PEO, PS-PMMA, PEP-PDMS, PEP-PEO, or PEE-PEO.

In addition to other copolymer systems, varying the corona block composition of PB-PEO within the sphere-forming window to resolve the exact scaling of τ_{frag} with N_{core} and N_{corona} is of interest. Part of the difficulty in varying f_{PEO} lies in the preparation of kinetically trapped, large micelles by DD. Previous work by Meli *et al.*[90] used the DD protocol to prepare micelles of PB-PEO in [C_2mim][TFSI] using three volume fractions where f_{PEO} = 0.39, 0.60, and 0.66. For $f_{PEO} \geq 0.6$, the authors found little change in $\langle R_h \rangle$ upon high temperature annealing at 170 °C, which could be because the overall solubility of the copolymer is much higher with increasing f_{PEO}. The volume fractions of PEO that are accessible for exploring the N_{corona} dependence of τ_{frag} may be limited, but small variations in N_{corona} can be explored, and an ideal range may lie somewhere between $0.38 \leq f_{PEO} < 0.60$. Answering these remaining questions should allow for a more complete understanding of BCP micelle fusion and fragmentation, and the development of a quantitative model of these processes remains to be elucidated. In general, there are many open questions in the field of micelle relaxation kinetics, with much yet to be determined about the fragmentation and fusion of BCP micelles in solution.

Bibliography

(1) Halperin, A.; Tirrell, M.; Lodge, T. P. Tethered Chains in Polymer Microstructures. *Adv. Polym. Sci.* **1992**, *100*, 31–71.

(2) Gohy, J. F. Block Copolymers II. In *Advances in Polymer Science*; Abetz, V., Ed.; Springer Berlin: Heidelberg, 2005; pp 65–136.

(3) Tyrrell, Z. L.; Shen, Y.; Radosz, M. Fabrication of Micellar Nanoparticles for Drug Delivery through the Self-Assembly of Block Copolymers. *Prog. Polym. Sci.* **2010**, *35*, 1128–1143.

(4) Hubbell, J. A. Enhancing Drug Function. *Science* **2003**, *300*, 595–596.

(5) Meier, W. Polymer Nanocapsules. *Chem. Soc. Rev.* **2000**, *29*, 295–303.

(6) Park, T. G.; Jeong, J. H.; Kim, S. W. Current Status of Polymeric Gene Delivery Systems. *Adv. Drug Deliv. Rev.* **2006**, *58*, 467–486.

(7) Cotanda, P.; Lu, A.; Patterson, J. P.; Petzetakis, N.; O'Reilly, R. K. Functionalized Organocatalytic Nanoreactors: Hydrophobic Pockets for Acylation Reactions in Water. *Macromolecules* **2012**, *45*, 2377–2384.

(8) Krishnamoorthy, S.; Pugin, R.; Brugger, J.; Heinzelmann, H.; Hinderling, C. Nanopatterned Self-Assembled Monolayers by Using Diblock Copolymer Micelles as Nanometer-Scale Adsorption and Etch Masks. *Adv. Mater.* **2008**, *20*,

1962–1965.

(9) Anderson, W. Block Copolymers as Viscosity Index Improvers for Lubrication Oils. U.S. Patent 3763044, 1973.

(10) Riess, G. Micellization of Block Copolymers. *Prog. Polym. Sci.* **2003**, *28*, 1107–1170.

(11) Cho, H. K.; Cheong, I. W.; Lee, J. M.; Kim, J. H. Polymeric Nanoparticles, Micelles and Polymersomes from Amphiphilic Block Copolymer. *Korean J. Chem. Eng.* **2010**, *27*, 731 – 740.

(12) Letchford, K.; Burt, H. A Review of the Formation and Classification of Amphiphilic Block Copolymer Nanoparticulate Structures: Micelles, Nanospheres, Nanocapsules and Polymersomes. *Eur J Pharm Biopharm*. **2007**, *65*, 259–269.

(13) Linse, P. Modelling of the Self-Assembly of Block Copolymers in Selective Solvent. In *Amphiphilic Block Copolymers*; Elsevier, 2000; pp 13–40.

(14) Liu, T.; Liu, L.-Z.; Chu, B. Formation of Amphiphilic Block Copolymer Micelles in Nonaqueous Solution. In *Amphiphilic Block Copolymers*; Elsevier, 2000; pp 115–149.

(15) Alexandridis, P.; Olsson, U.; Linse, P.; Lindman, B. Structural Polymorphism of Amphiphilic Block Copolymers in Mixtures with Water and Oil: Comparison with Solvent-Free Block Copolymers and Surfactant Systems. In *Amphiphilic Block Copolymers*; Elsevier, 2000; pp 169–190.

(16) Goldraich, M.; Talmon, Y. Direct-Imaging Cryo-Transmission Electron Microscopy in the Study of Colloids and Polymer Solutions. In *Amphiphilic Block Copolymers*; Elsevier, 2000; pp 253–280.

(17) Zhao, D.; Ma, Y.; Lodge, T. P. Exchange Kinetics for a Single Block Copolymer in Micelles of Two Different Sizes. *Macromolecules* **2018**, *51*, 2312–2320.

(18) Zinn, T.; Willner, L.; Pipich, V.; Richter, D.; Lund, R. Molecular Exchange Kinetics of Micelles: Corona Chain Length Dependence. *ACS Macro Lett.* **2016**, *5*, 884–888.

(19) Ma, Y.; Lodge, T. P. Chain Exchange Kinetics in Diblock Copolymer Micelles in Ionic Liquids: The Role of χ. *Macromolecules* **2016**, *49*, 9542–9552.

(20) Aniansson, E. A. G. G.; Wall, S. N.; Almgren, M.; Hoffmann, H.; Kielmann, I.; Ulbricht, W.; Zana, R.; Lang, J.; Tondre, C. Theory of the Kinetics of Micellar Equilibria and Quantitative Interpretation of Chemical Relaxation Studies of Micellar Solutions of Ionic Surfactants. *J. Phys. Chem.* **1976**, *80*, 905–922.

(21) Choi, S. H.; Lodge, T. P.; Bates, F. S. Mechanism of Molecular Exchange in Diblock Copolymer Micelles: Hypersensitivity to Core Chain Length. *Phys. Rev. Lett.* **2010**, *104*, 047802(1–4).

(22) Lu, J.; Bates, F. S.; Lodge, T. P. Chain Exchange in Binary Copolymer Micelles at Equilibrium: Confirmation of the Independent Chain Hypothesis. *ACS Macro Lett.* **2013**, *2*, 451–455.

(23) Wang, E.; Lu, J.; Bates, F. S.; Lodge, T. P. Effect of Corona Block Length on the Structure and Chain Exchange Kinetics of Block Copolymer Micelles. *Macromolecules* **2018**, *51*, 3563–3571.

(24) Willner, L.; Poppe, A.; Allgaier, J.; Monkenbusch, M.; Richter, D. Time-Resolved SANS for the Determination of Unimer Exchange Kinetics in Block Copolymer Micelles. *Europhys. Lett.* **2001**, *55*, 667–673.

(25) Lund, R.; Willner, L.; Stellbrink, J.; Radulescu, A.; Richter, D. Tuning of Structure and Kinetics of Chain Exchange in Star-like PEP-PEO Block Copolymer Micelles. *Phys. B Condens. Matter* **2004**, *350*, 909–912.

(26) Lund, R.; Willner, L.; Stellbrink, J.; Lindner, P.; Richter, D. Logarithmic Chain-Exchange Kinetics of Diblock Copolymer Micelles. *Phys. Rev. Lett.* **2006**, *96*, 1–4.

(27) Lund, R.; Willner, L.; Richter, D.; Dormidontova, E. E. Equilibrium Chain Exchange Kinetics of Diblock Copolymer Micelles: Tuning and Logarithmic Relaxation. *Macromolecules* **2006**, *39*, 4566–4575.

(28) Lund, R.; Willner, L.; Stellbrink, J.; Richter, D. Equilibrium Exchange Kinetics in PEP-PEO Block Copolymer Micelles. A Time Resolved SANS Study. *Phys. B Condens. Matter* **2006**, *385–386*, 735–737.

(29) Lund, R.; Willner, L.; Richter, D.; Iatrou, H.; Hadjichristidis, N.; Lindner, P. Unraveling the Equilibrium Chain Exchange Kinetics of Polymeric Micelles Using Small-Angle Neutron Scattering - Architectural and Topological Effects. *J. Appl.*

Crystallogr. **2007**, *40*, 327–331.

(30) Lund, R.; Willner, L.; Pipich, V.; Grillo, I.; Lindner, P.; Colmenero, J.; Richter, D. Equilibrium Chain Exchange Kinetics of Diblock Copolymer Micelles: Effect of Morphology. *Macromolecules* **2011**, *44*, 6145–6154.

(31) Zhulina, E. B.; Birshtein, T. M. Equilibrium Parameters of Block-Copolymer Superstructures. *Polym. Sci. U.S.S.R* **1986**, *28*, 2880–2886.

(32) de Gennes, P. G. Macromolecules and Liquid Crystals : Reflections on Certain Lines of Research. In *Advances in Polymer Science*; Academic Press, Inc., 1978; Vol. 3, pp 1–18.

(33) Leibler, L.; Orland, H.; Wheeler, J. C. Theory of Critical Micelle Concentration for Solutions of Block Copolymers. *J. Chem. Phys.* **1983**, *79*, 3550–3557.

(34) Noolandi, J.; Hong, K. M. Theory of Block Copolymer Micelles in Solution. *Macromolecules* **1983**, *16*, 1443–1448.

(35) Nagarajan, R.; Ganesh, K. Block Copolymer Self-Assembly in Selective Solvents: Spherical Micelles with Segregated Cores. *J. Chem. Phys.* **1989**, *90*, 5843–5856.

(36) Zhulina, E. B.; Adam, M.; Larue, I.; Sheiko, S. S.; Rubinstein, M. Diblock Copolymer Micelles in a Dilute Solution. *Macromolecules* **2005**, *38*, 5330–5351.

(37) Halperin, A. Polymeric Micelles: A Star Model. *Macromolecules* **1987**, *20*, 2943–2946.

(38) Meier, D. J. Theory of Block Copolymers. I. Domain Formation in A-B Block

Copolymers. *J. Polym. Sci. Part B Polym. Phys.* **1996**, *34*, 1821–1838.

(39) Helfand, E.; Wasserman, Z. R. Block Copolymer Theory. 4. Narrow Interphase Approximation. *Macromolecules* **1976**, *9*, 879–888.

(40) Helfand, E.; Wasserman, Z. R. Block Copolymer Theory. 5. Spherical Domains. *Macromolecules* **1978**, *11*, 960–966.

(41) Helfand, E.; Wasserman, Z. R. Block Copolymer Theory. 6. Cylindrical Domains. *Macromolecules* **1980**, *13*, 994–998.

(42) Daoud, M.; Cotton, J. P. Star Shaped Polymers: A Model for the Conformation and Its Concentration Dependence. *J. Phys.* **1982**, *43*, 531–538.

(43) Jensen, G. V.; Lund, R.; Narayanan, T.; Pedersen, J. S. Transformation from Globular to Cylindrical Mixed Micelles through Molecular Exchange That Induces Micelle Fusion. *J. Phys. Chem. Lett.* **2016**, *7*, 2039–2043.

(44) Zhang, L.; Eisenberg, A. Thermodynamic vs Kinetic Aspects in the Formation and Morphological Transitions of Crew-Cut Aggregates Produced by Self-Assembly of Polystyrene-b-Poly(Acrylic Acid) Block Copolymers in Dilute Solution. *Macromolecules* **1999**, *32*, 2239–2249.

(45) Gao, Z.; Varshney, S. K.; Wong, S.; Eisenberg, A. Block Copolymer "Crew-Cut" Micelles in Water. *Macromolecules* **1994**, *27*, 7923–7927.

(46) Won, Y. Y.; Ted Davis, H.; Bates, F. S. Giant Wormlike Rubber Micelles. *Science* **1999**, *283*, 960–963.

(47) Zheng, Y.; Won, Y. Y.; Bates, F. S.; Davis, H. T.; Seriven, L. E.; Talmon, Y. Directly Resolved Core-Corona Structure of Block Copolymer Micelles by Cryo-Transmission Electron Microscopy. *J. Phys. Chem. B* **1999**, *103*, 10333–10334.

(48) Yu, K.; Zhang, L.; Eisenberg, A. Novel Morphologies of "Crew-Cut" Aggregates of Amphiphilic Diblock Copolymers in Dilute Solution. *Langmuir* **1996**, *12*, 5980–5984.

(49) Zhang, L.; Shen, H.; Eisenberg, A. Phase Separation Behavior and Crew-Cut Micelle Formation of Polystyrene-6-Poly(Acrylic Acid) Copolymers in Solutions. *Macromolecules* **1997**, *30*, 1001–1011.

(50) Bang, J.; Jain, S.; Li, Z.; Lodge, T. P.; Pedersen, J. S.; Kesselman, E.; Talmon, Y. Sphere, Cylinder, and Vesicle Nanoaggregates in Poly(Styrene-b-Isoprene) Diblock Copolymer Solutions. *Macromolecules* **2006**, *39*, 1199–1208.

(51) He, Y.; Li, Z.; Simone, P.; Lodge, T. P. Self-Assembly of Block Copolymer Micelles in an Ionic Liquid. *J. Am. Chem. Soc.* **2006**, *128*, 2745–2750.

(52) Zhang, L.; Barlow, R. J.; Eisenberg, A. Scaling Relations and Coronal Dimensions in Aqueous Block Polyelectrolyte Micelles. *Macromolecules* **1995**, *28*, 6055–6066.

(53) Shen, H.; Eisenberg, A. Block Length Dependence of Morphological Phase Diagrams of the Ternary System of PS-b-PAA/Dioxane/H2O. *Macromolecules* **2000**, *33*, 2561–2572.

(54) Won, Y. Y.; Brannan, A. K.; Davis, H. T.; Bates, F. S. Cryogenic Transmission Electron Microscopy (Cryo-TEM) of Micelles and Vesicles Formed in Water by Poly(Ethylene Oxide)-Based Block Copolymers. *J. Phys. Chem. B* **2002**, *106*, 3354–3364.

(55) Stellbrink, J.; Rother, G.; Laurati, M.; Lund, R.; Willner, L.; Richter, D. Poly(Ethylene-Alt-Propylene)-Poly(Ethylene Oxide) Diblock Copolymer Micelles: A Colloidal Model System with Tunable Softness. *J. Phys. Condens. Matter* **2004**.

(56) Hall, C. C.; Zhou, C.; Danielsen, S. P. O.; Lodge, T. P. Formation of Multicompartment Ion Gels by Stepwise Self-Assembly of a Thermoresponsive ABC Triblock Terpolymer in an Ionic Liquid. *Macromolecules* **2016**, *49*, 2298–2306.

(57) Moon, H. C.; Lodge, T. P.; Frisbie, C. D. Solution Processable, Electrochromic Ion Gels for Sub - 1 V, Flexible Displays on Plastic. *Chem. Mater.* **2015**, *27*, 1420–1425.

(58) Kitazawa, Y.; Ueki, T.; McIntosh, L. D.; Tamura, S.; Niitsuma, K.; Imaizumi, S.; Lodge, T. P.; Watanabe, M. Hierarchical Sol-Gel Transition Induced by Thermosensitive Self-Assembly of an ABC Triblock Polymer in an Ionic Liquid. *Macromolecules* **2016**, *49*, 1414–1423.

(59) Xie, Y.; Xie, R.; Yang, H. C.; Chen, Z.; Hou, J.; López-Barrón, C. R.; Wagner, N. J.; Gao, K. Z. Iono-Elastomer-Based Wearable Strain Sensor with Real-Time

Thermomechanical Dual Response. *ACS Appl. Mater. Interfaces* **2018**, *10*, 32435–32443.

(60) López-Barrón, C. R.; Chen, R.; Wagner, N. J. Ultrastretchable Iono-Elastomers with Mechanoelectrical Response. *ACS Macro Lett.* **2016**, *5*, 1332–1338.

(61) Mehnert, C. P. Supported Ionic Liquid Catalysis. *Chem. Eur. J.* **2005**, *11*, 50–56.

(62) Riisager, A.; Fehrmann, R.; Haumann, M.; Wasserscheid, P. Supported Ionic Liquid Phase (SILP) Catalysis: An Innovative Concept for Homogeneous Catalysis in Continuous Fixed-Bed Reactors. *Eur. J. Inorg. Chem.* **2006**, *4*, 695–706.

(63) Fukushima, T.; Kosaka, A.; Ishimura, Y.; Yamamoto, T.; Takigawa, T.; Ishii, N.; Aida, T. Molecular Ordering of Organic Molten Salts Triggered by Single-Walled Carbon Nanotubes. *Science* **2003**, *300*, 2072–2074.

(64) Phillips, D. M.; Drummy, L. F.; Conrady, D. G.; Fox, D. M.; Naik, R. R.; Stone, M. O.; Trulove, P. C.; De Long, H. C.; Mantz, R. A. Dissolution and Regeneration of Bombyx Mori Silk Fibroin Using Ionic Liquids. *J. Am. Chem. Soc.* **2004**, *126*, 14350–14351.

(65) Forsyth, S. A.; MacFarlane, D. R.; Thomson, R. J.; von Itzstein, M. Rapid, Clean, and Mild O-Acetylation of Alcohols and Carbohydrates in an Ionic Liquid. *Chem. Commun.* **2002**, *2*, 714–715.

(66) Xie, H.; Li, S.; Zhang, S. Ionic Liquids as Novel Solvents for the Dissolution and

Blending of Wool Keratin Fibers. *Green Chem.* **2005**, *7*, 606–608.

(67) Ueki, T.; Watanabe, M. Lower Critical Solution Temperature Behavior of Linear Polymers in Ionic Liquids and the Corresponding Volume Phase Transition of Polymer Gels. *Langmuir* **2007**, *25*, 988–990.

(68) Ueki, T.; Watanabe, M. Macromolecules in Ionic Liquids: Progress, Challenges, and Opportunities. *Macromolecules* **2008**, *41*, 3739–3749.

(69) Asai, H.; Fujii, K.; Ueki, T.; Sawamura, S.; Nakamura, Y.; Kitazawa, Y.; Watanabe, M.; Han, Y.; Kim, T.; Shibayama, M. Structural Study on the UCST-Type Phase Separation of Poly (N-Isopropylacrylamide) in Ionic Liquid. *Macromolecules* **2013**, *46*, 1101–1106.

(70) Hirosawa, K.; Fujii, K.; Ueki, T.; Kitazawa, Y.; Littrell, K. C.; Watanabe, M.; Shibayama, M. SANS Study on the Solvated Structure and Molecular Interactions of a Thermo-Responsive Polymer in a Room Temperature Ionic Liquid. *Phys. Chem. Chem. Phys.* **2016**, *18*, 17881–17889.

(71) Lee, H. N.; Bai, Z.; Newell, N.; Lodge, T. P. Micelle/Inverse Micelle Self-Assembly of a PEO-PNIPAm Block Copolymer in Ionic Liquids with Double Thermoresponsivity. *Macromolecules* **2010**, *43*, 9522–9528.

(72) Mok, M. M.; Thiagarajan, R.; Flores, M.; Morse, D. C.; Lodge, T. P. Apparent Critical Micelle Concentrations in Block Copolymer/Ionic Liquid Solutions: Remarkably Weak Dependence on Solvophobic Block Molecular Weight.

Macromolecules **2012**, *45*, 4818–4829.

(73) López-Barrón, C. R.; Li, D.; Derita, L.; Basavaraj, M. G.; Wagner, N. J. Spontaneous Thermoreversible Formation of Cationic Vesicles in a Protic Ionic Liquid. *J. Am. Chem. Soc.* **2012**, *134*, 20728–20732.

(74) López-Barrón, C. R.; Chen, R.; Wagner, N. J.; Beltramo, P. J. Self-Assembly of Pluronic F127 Diacrylate in Ethylammonium Nitrate: Structure, Rheology, and Ionic Conductivity before and after Photo-Cross-Linking. *Macromolecules* **2016**, *49*, 5179–5189.

(75) Chen, Z.; Fitzgerald, P. A.; Kobayashi, Y.; Ueno, K.; Watanabe, M.; Warr, G. G.; Atkin, R. Micelle Structure of Novel Diblock Polyethers in Water and Two Protic Ionic Liquids (EAN and PAN). *Macromolecules* **2015**, *48*, 1843–1851.

(76) Patrascu, C.; Gauffre, F.; Nallet, F.; Bordes, R.; Oberdisse, J.; De Lauth-Viguerie, N.; Mingotaud, C. Micelles in Ionic Liquids: Aggregation Behavior of Alkyl Poly(Ethyleneglycol)-Ethers in 1-Butyl-3-Methyl-Imidazolium Type Ionic Liquids. *ChemPhysChem* **2006**, *7*, 99–101.

(77) Hoarfrost, M. L.; He, Y.; Lodge, T. P. Lower Critical Solution Temperature Phase Behavior of Poly(n -Butyl Methacrylate) in Ionic Liquid Mixtures. *Macromolecules* **2013**, *46*, 9464–9472.

(78) Mok, M. M.; Lodge, T. P. Temperature-Based Fluorescence Measurements of Pyrene in Block Copolymer Micelles: Probing Micelle Core Glass Transition

Breadths. *J. Polym. Sci. Part B Polym. Phys.* **2012**, *50*, 500–515.

(79) Ma, Y.; Lodge, T. P. Poly(Methyl Methacrylate)-Block-Poly(n-Butyl Methacrylate) Diblock Copolymer Micelles in an Ionic Liquid: Scaling of Core and Corona Size with Core Block Length. *Macromolecules* **2016**, *49*, 3639–3646.

(80) Xie, R.; López-Barrón, C. R.; Wagner, N. J. Self-Assembly of Block Copolymers in Ionic Liquids. In *ACS Symposium Series*; American Chemical Society, 2017; Vol. 1250, pp 83–142.

(81) Xie, R.; López-Barrón, C. R.; Greene, D. G.; Wagner, N. J. Comicellization of Binary PEO-PPO-PEO Triblock Copolymer Mixtures in Ethylammonium Nitrate. *Macromolecules* **2018**, *51*, 1453–1461.

(82) Simone, P. M.; Lodge, T. P. Lyotropic Phase Behavior of Polybutadiene-Poly (Ethylene Oxide) Diblock Copolymers in Ionic Liquids. *Macromolecules* **2008**, *41*, 1753–1759.

(83) Hoarfrost, M.; Lodge, T. Effects of Solvent Quality and Degree of Polymerization on the Critical Micelle Temperature of Poly(Ethylene Oxide-b-n-Butyl Methacrylate) in Ionic Liquids. *Macromolecules* **2014**, *47*, 1455–1461.

(84) Simone, P. M.; Lodge, T. P. Micellization of PS-PMMA Diblock Copolymers in an Ionic Liquid. *Macromol. Chem. Phys.* **2007**, *208*, 339–348.

(85) López-Barrón, C. R.; Li, D.; Wagner, N. J.; Caplan, J. L. Triblock Copolymer Self-Assembly in Ionic Liquids: Effect of PEO Block Length on the Self-

Assembly of PEO-PPO-PEO in Ethylammonium Nitrate. *Macromolecules* **2014**, *47*, 7484–7495.

(86) Nagarajan, R.; Ganesh, K. Solubilization in Spherical Block Copolymer Micelles: Scaling Analysis Based on Star Model. *J. Chem. Phys.* **1993**, *98*, 7440–7450.

(87) Bai, Z.; He, Y.; Lodge, T. P. Block Copolymer Micelle Shuttles with Tunable Transfer Temperatures between Ionic Liquids and Aqueous Solutions. *Langmuir* **2008**, *24*, 5284–5290.

(88) So, S.; Lodge, T. P. Size Control and Fractionation of Ionic Liquid Filled Polymersomes with Glassy and Rubbery Bilayer Membranes. *Langmuir* **2016**, *32*, 4959–4968.

(89) Meli, L.; Lodge, T. P. Equilibrium vs Metastability: High-Temperature Annealing of Spherical Block Copolymer Micelles in an Ionic Liquid. *Macromolecules* **2009**, *42*, 580–583.

(90) Meli, L.; Santiago, J. M.; Lodge, T. P. Path-Dependent Morphology and Relaxation Kinetics of Highly Amphiphilic Diblock Copolymer Micelles in Ionic Liquids. *Macromolecules* **2010**, *43*, 2018–2027.

(91) Early, J. T.; Lodge, T. P. Fragmentation of 1,2-Polybutadiene-Block-Poly(Ethylene Oxide) Micelles in Imidazolium-Based Ionic Liquids. *Macromolecules* **2019**, *52*, 7089–7101.

(92) Early, J. T.; Yager, K. G.; Lodge, T. P. Direct Observation of Micelle

Fragmentation via In Situ Liquid- Phase Transmission Electron Microscopy. *ACS Macro Lett.* **2020**, *9*, 756–761.

(93) Aniansson, E. A. G.; Wall, S. N. On the Kinetics of Step-Wise Micelle Association. *J. Phys. Chem.* **1974**, *78*, 1024–1030.

(94) Aniansson, E. A. G.; Wall, S. N. Kinetics of Step-Wise Micelle Association. Correction and Improvement. *J. Phys. Chem.* **1975**, *79*, 857–858.

(95) Halperin, A.; Alexander, S. Polymeric Micelles: Their Relaxation Kinetics. *Macromolecules* **1989**, *22*, 2403–2412.

(96) Kahlweit, M. Kinetics of Formation of Association Colloids. *J. Colloid Interface Sci.* **1982**, *90*, 92–99.

(97) Dormidontova, E. E. Micellization Kinetics in Block Copolymer Solutions: Scaling Model. *Macromolecules* **1999**, *32*, 7630–7644.

(98) Kositza, M. J.; Rees, G. D.; Holzwarth, A.; Holzwarth, J. F. Aggregation Dynamics of the Block Copolymer L64 in Aqueous Solution: Copolymer-Sodium Dodecyl Sulfate Interactions Studied by Laser T-Jump. *Langmuir* **2000**, *16*, 9035–9041.

(99) Waton, G.; Michels, B.; Zana, R. Dynamics of Block Copolymer Micelles in Aqueous Solution. *Macromolecules* **2001**, *34*, 907–910.

(100) Grubić, M.; Strey, R.; Teubner, M. On the Application of a Laser T-Jump Apparatus for Perturbation of Ionic Micellar Solutions. *J. Colloid Interface Sci.*

1981, *80*, 453–458.

(101) Strey, R.; Pakusch, A. On Relaxation Amplitudes in T-Jump Experiments in Micellar Solutions. *Ber. Bunsenges. Phys. Chem.* **1980**, *84*, 1163–1168.

(102) Candau, S. J.; Merikhi, F.; Waton, G.; Lemarechal, P. Temperature-Jump Study of Elongated Micelles of Cetyltrimethylammonium Bromide. *J. Phys.* **1990**, *51*, 977–989.

(103) Stejskal, J.; Hlavata, D.; Sikora, A.; Konak, C.; Plestil, J.; Kratochvil, P. Equilibrium and Non-Equilibrium Copolymer Micelles: Polystyrene-Block-Poly(Ethylene-Co-Propylene) in Decane and in Diisopropylether. *Polymer* **1992**, *33*, 3675–3685.

(104) Honda, C.; Abe, Y.; Nose, T. Relaxation Kinetics of Micellization in Micelle-Forming Block Copolymer in Selective Solvent. *Macromolecules* **1996**, *29*, 6778–6785.

(105) Michels, B.; Waton, G.; Zana, R.; Pasteur, L.; Pascal, B.; Zana, R. Dynamics of Micelles of Poly (Ethylene Oxide)-Poly(Propylene Oxide)-Poly(Ethylene Oxide) Block Copolymers in Aqueous Solutions. *Langmuir* **1997**, *13*, 3111–3118.

(106) Zhu, Z.; Armes, S. P.; Liu, S. pH-Induced Micellization Kinetics of ABC Triblock Copolymers Measured by Stopped-Flow Light Scattering. *Macromolecules* **2005**, *38*, 9803–9812.

(107) Zhang, J.; Li, Y.; Armes, S. P.; Liu, S. Probing the Micellization Kinetics of

Pyrene End-Labeled Diblock Copolymer via a Combination of Stopped-Flow Light-Scattering and Fluorescence Techniques. *J. Phys. Chem. B* **2007**, *111*, 12111–12118.

(108) Zhang, J.; Xu, J.; Liu, S. Chain-Length Dependence of Diblock Copolymer Micellization Kinetics Studied by Stopped-Flow PH-Jump. *J. Phys. Chem. B* **2008**, *112*, 11284–11291.

(109) Honda, C.; Hasegawa, Y.; Hirunuma, R.; Nose, T. Micellization Kinetics of Block Copolymers in Selective Solvent. *Macromolecules* **1994**, *27*, 7660–7668.

(110) Lund, R.; Willner, L.; Richter, D.; Lindner, P.; Narayanan, T. Kinetic Pathway of the Cylinder-to-Sphere Transition in Block Copolymer Micelles Observed in Situ by Time-Resolved Neutron and Synchrotron Scattering. *ACS Macro Lett.* **2013**, *2*, 1082–1087.

(111) Jensen, G. V.; Lund, R.; Gummel, J.; Narayanan, T.; Pedersen, J. S. Monitoring the Transition from Spherical to Polymer-like Surfactant Micelles Using Small-Angle X-Ray Scattering. *Angew. Chemie - Int. Ed.* **2014**, *53*, 11524–11528.

(112) Wu, H.; Ting, J. M.; Yu, B.; Jackson, N. E.; Meng, S.; de Pablo, J. J.; Tirrell, M. V. Spatiotemporal Formation and Growth Kinetics of Polyelectrolyte Complex Micelles with Millisecond Resolution. *ACS Macro Lett.* **2020**, *9*, 1674–1680.

(113) Kelley, E. G.; Murphy, R. P.; Seppala, J. E.; Smart, T. P.; Hann, S. D.; Sullivan, M. O.; Epps, T. H. Size Evolution of Highly Amphiphilic Macromolecular

Solution Assemblies via a Distinct Bimodal Pathway. *Nat. Commun.* **2014**, *5*, 3599.

(114) Lu, J.; Bates, F. S.; Lodge, T. P. Remarkable Effect of Molecular Architecture on Chain Exchange in Triblock Copolymer Micelles. *Macromolecules* **2015**, *48*, 2667–2676.

(115) Zinn, T.; Willner, L.; Pipich, V.; Richter, D.; Lund, R. Effect of Core Crystallization and Conformational Entropy on the Molecular Exchange Kinetics of Polymeric Micelles. *ACS Macro Lett.* **2015**, *4*, 651–655.

(116) Lu, J.; Bates, F. S.; Lodge, T. P. Addition of Corona Block Homopolymer Retards Chain Exchange in Solutions of Block Copolymer Micelles. *Macromolecules* **2016**, *49*, 1405–1413.

(117) Rharbi, Y.; Winnik, M. A. Kinetics of Fusion and Fragmentation Nonionic Micelles: Triton X-100. *Langmuir* **1999**, *15*, 4697–4700.

(118) Rharbi, Y.; Winnik, M. A. Solute Exchange between Surfactant Micelles by Micelle Fragmentation and Fusion. *Adv. Colloid Interface Sci.* **2001**, *89*, 25–46.

(119) Rharbi, Y.; Winnik, M. A. Salt Effects on Solute Exchange and Micelle Fission in Sodium Dodecyl Sulfate Micelles below the Micelle-to-Rod Transition. *J. Phys. Chem. B* **2003**, *107*, 1491–1501.

(120) Rharbi, Y. Fusion and Fragmentation Dynamics at Equilibrium in Triblock Copolymer Micelles. *Macromolecules* **2012**, *45*, 9823–9826.

(121) Esselink, F. J.; Dormidontova, E.; Hadziioannou, G. Evolution of Block Copolymer Micellar Size and Structure Evidenced with Cryo Electron Microscopy. *Macromolecules* **1998**, *31*, 2925–2932.

(122) Esselink, F. J.; Dormidontova, E. E.; Hadziioannou, G. Redistribution of Block Copolymer Chains between Mixed Micelles in Solution. *Macromolecules* **1998**, *31*, 4873–4878.

(123) Parent, L. R.; Bakalis, E.; Ramírez-Hernández, A.; Kammeyer, J. K.; Park, C.; De Pablo, J.; Zerbetto, F.; Patterson, J. P.; Gianneschi, N. C. Directly Observing Micelle Fusion and Growth in Solution by Liquid-Cell Transmission Electron Microscopy. *J. Am. Chem. Soc.* **2017**, *139*, 17140–17151.

(124) Choi, S. H.; Bates, F. S.; Lodge, T. P. Molecular Exchange in Ordered Diblock Copolymer Micelles. *Macromolecules* **2011**, *44*, 3594–3604.

(125) Rharbi, Y.; Li, M.; Winnik, M. A.; Hahn, K. G. Temperature Dependence of Fusion and Fragmentation Kinetics of Triton X-100 Micelles. *J. Am. Chem. Soc.* **2000**, *122*, 6242–6251.

(126) Rharbi, Y.; Karrouch, M.; Richardson, P. Fusion and Fission Inhibited by the Same Mechanism in Electrostatically Charged Surfactant Micelles. *Langmuir* **2014**, *30*, 7947–7952.

(127) Desbaumes, L.; Eisenberg, A. Single-Solvent Preparation of Crew-Cut Aggregates of Various Morphologies from an Amphiphilic Diblock Copolymer. *Langmuir*

1999, *15*, 36–38.

(128) Cameron, N. S.; Corbierre, M. K.; Eisenberg, A. 1998 E.W.R. Steacie Award Lecture Asymmetric Amphiphilic Block Copolymers in Solution: A Morphological Wonderland. *Can. J. Chem.* **1999**, *77*, 1311–1326.

(129) Rehn, S. M.; Jones, M. R. New Strategies for Probing Energy Systems with in Situ Liquid-Phase Transmission Electron Microscopy. *ACS Energy Lett.* **2018**, *3*, 1269–1278.

(130) Tan, S. F.; Chee, S. W.; Lin, G.; Mirsaidov, U. Direct Observation of Interactions between Nanoparticles and Nanoparticle Self-Assembly in Solution. *Acc. Chem. Res.* **2017**, *50*, 1303–1312.

(131) Parent, L. R.; Bakalis, E.; Proetto, M.; Li, Y.; Park, C.; Zerbetto, F.; Gianneschi, N. C. Tackling the Challenges of Dynamic Experiments Using Liquid-Cell Transmission Electron Microscopy. *Acc. Chem. Res.* **2018**, *51*, 3–11.

(132) Touve, M. A.; Figg, C. A.; Wright, D. B.; Park, C.; Cantlon, J.; Sumerlin, B. S.; Gianneschi, N. C. Polymerization-Induced Self-Assembly of Micelles Observed by Liquid Cell Transmission Electron Microscopy. *ACS Cent. Sci.* **2018**, *4*, 543–547.

(133) Mansfeld, U.; Hoeppener, S.; Schubert, U. S. Investigating the Motion of Diblock Copolymer Assemblies in Ionic Liquids by in Situ Electron Microscopy. *Adv. Mater.* **2013**, *25*, 761–765.

(134) Szwarc, M. *Living Polymers and Mechanisms of Anionic Polymerization*, 1st ed.; Springer-Verlag Berlin Heidelberg, 1983.

(135) Hiemenz, P. C.; Lodge, T. P. *Polymer Chemistry*, 2nd ed.; Taylor & Francis Group/CRC Press: Boca Raton, 2007.

(136) Hillmyer, M. A.; Bates, F. S. Synthesis and Characterization of Model Polyalkane-Poly(Ethylene Oxide) Block Copolymers. *Macromolecules* **1996**, *29*, 6994–7002.

(137) Ndoni, S.; Papadakis, C. M.; Bates, F. S.; Almdal, K. Laboratory Scale Setup for Anionic Polymerization under Inert Atmosphere. *Rev. Sci. Instrum.* **1995**, *66*, 1090–1095.

(138) Brandrup, J.; Immergut, E. H.; Grulke, E. A. *Polymer Handbook*; Wiley-Interscience: New York, 1999.

(139) Early, J. T.; Block, A.; Yager, K. G.; Lodge, T. P. Molecular Weight Dependence of Block Copolymer Micelle Fragmentation Kinetics. *J. Am. Chem. Soc.* **2021**, *143*, 7748–7758.

(140) Zaitsau, D. H.; Kabo, G. J.; Strechan, A. A.; Paulechka, Y. U.; Tschersich, A.; Verevkin, S. P.; Heintz, A. Experimental Vapor Pressures of 1-Alkyl-3-Methylimidazolium Bis(Trifluoromethylsulfonyl)Imides and a Correlation Scheme for Estimation of Vaporization Enthalpies of Ionic Liquids. *J. Phys. Chem. A* **2006**, *110*, 7303–7306.

(141) Bonhôte, P.; Dias, A. P.; Papageorgiou, N.; Kalyanasundaram, K.; Grätzel, M.

Hydrophobic, Highly Conductive Ambient-Temperature Molten Salts. *Inorg. Chem.* **1996**, *35*, 1168–1178.

(142) Zhao, D.; Ma, Y.; Wang, E.; Lodge, T. P. Micellization of Binary Diblock Co-Polymer Mixtures in an Ionic Liquid. *Macromolecules* **2019**, *52*, 4729–4738.

(143) Brown, W. *Dynamic Light Scattering: The Method and Some Applications (Monographs on the Physics and Chemistry of Materials)*; Clarendon Press; Oxford University Press: Oxford (England); New York, 1993.

(144) Tokuda, H.; Hayamizu, K.; Ishii, K.; Susan, M. A. B. H.; Watanabe, M. Physicochemical Properties and Structures of Room Temperature Ionic Liquids. 1. Variation of Anionic Species. *J. Phys. Chem.* **2004**, *108*, 16593–16600.

(145) Nazet, A.; Sokolov, S.; Sonnleitner, T.; Makino, T.; Kanakubo, M.; Buchner, R. Densities, Viscosities, and Conductivities of the Imidazolium Ionic Liquids [Emim][Ac], [Emim][FAP], [Bmim][BETI], [Bmim][FSI], [Hmim][TFSI], and [Omim][TFSI]. *J. Chem. Eng. Data* **2015**, *60*, 2400–2411.

(146) Zhao, N.; Jacquemin, J.; Oozeerally, R.; Degirmenci, V. New Method for the Estimation of Viscosity of Pure and Mixtures of Ionic Liquids Based on the UNIFAC − VISCO Model. *J. Chem. Eng. Data* **2016**, *61*, 2160–2169.

(147) Wang, X.; Wang, M.; Chen, Z.; Tao, X.; Shen, W. Critical Phenomena of {1-Butanol + 1-Ethyl-3-Methylimidazolium Bis(Trifluoromethylsulfonyl)Imide} Binary Solution. *J. Mol. Liq.* **2016**, *224*, 284–289.

(148) Muhammad, A.; Abdul Mutalib, M. I.; Wilfred, C. D.; Murugesan, T.; Shafeeq, A. Thermophysical Properties of 1-Hexyl-3-Methyl Imidazolium Based Ionic Liquids with Tetrafluoroborate, Hexafluorophosphate and Bis(Trifluoromethylsulfonyl)Imide Anions. *J. Chem. Thermodyn.* **2008**, *40*, 1433–1438.

(149) Rodrigues, A. S. M. C.; Almeida, H. F. D.; Freire, M. G.; Lopes-da-Silva, J. A.; Coutinho, J. A. P.; Santos, L. M. N. B. F. The Effect of n vs. Iso Isomerization on the Thermophysical Properties of Aromatic and Non-Aromatic Ionic Liquids. *Fluid Phase Equilib.* **2016**, *423*, 190–202.

(150) Tariq, M.; Forte, P. A. S.; Gomes, M. F. C.; Lopes, J. N. C.; Rebelo, L. P. N. Densities and Refractive Indices of Imidazolium- and Phosphonium-Based Ionic Liquids: Effect of Temperature, Alkyl Chain Length, and Anion. *J. Chem. Thermodyn.* **2009**, *41*, 790–798.

(151) Jakes, J. Testing of the Constrained Regularization Method of Inverting Laplace Transform on Simulated Very Wide Quasielastic Light Scattering Autocorrelation Functions. *Czechoslov. J. Phys. B* **1988**, *38*, 1305–1316.

(152) Kotlarchyk, M.; Chen, S. H. Analysis of Small Angle Neutron Scattering Spectra from Polydisperse Interacting Colloids. *J. Chem. Phys.* **1983**, *79*, 2461–2469.

(153) Pedersen, J. S.; Svaneborg, C.; Almdal, K.; Hamley, I. W.; Young, R. N. A Small-Angle Neutron and x-Ray Contrast Variation Scattering Study of the Structure of

Block Copolymer Micelles: Corona Shape and Excluded Volume Interactions. *Macromolecules* **2003**, *36*, 416–433.

(154) Kharel, A.; Lodge, T. P. Coil Dimensions of Poly(Ethylene Oxide) in an Ionic Liquid by Small-Angle Neutron Scattering. *Macromolecules* **2017**, *50*, 8739–8744.

(155) Araque, J. C.; Hettige, J. J.; Margulis, C. J. Modern Room Temperature Ionic Liquids, a Simple Guide to Understanding Their Structure and How It May Relate to Dynamics. *J. Phys. Chem. B* **2015**, *119*, 12727–12740.

(156) Kharel, A.; Lodge, T. P. Effect of Ionic Liquid Components on the Coil Dimensions of PEO. *Macromolecules* **2019**, *52*, 3123–3130.

(157) Pedersen, J. S. Determination of Size Distributions from Small-Angle Scattering Data for Systems with Effective Hard-Sphere Interactions. *J. Appl. Crystallogr.* **1994**, *27*, 595–608.

(158) Kim, P. Y.; Ribbe, A. E.; Russell, T. P.; Hoagland, D. A. Visualizing the Dynamics of Nanoparticles in Liquids by Scanning Electron Microscopy. *ACS Nano* **2016**, *10*, 6257–6264.

(159) Kuwabata, S.; Tsuda, T.; Torimoto, T. Room-Temperature Ionic Liquid. A New Medium for Material Production and Analyses under Vacuum Conditions. *J. Phys. Chem. Lett.* **2010**, *1*, 3177–3188.

(160) Uematsu, T.; Baba, M.; Oshima, Y.; Tsuda, T.; Torimoto, T.; Kuwabata, S. Atomic Resolution Imaging of Gold Nanoparticle Generation and Growth in Ionic

Liquids. *J. Am. Chem. Soc.* **2014**, *136*, 13789–13797.

(161) Carter, C. B.; Williams, D. B. *Transmission Electron Microscopy: A Textbook for Materials Science*, 2nd ed.; Springer Science & Business Media, 2009.

(162) Patist, A.; Kanicky, J. R.; Shukla, P. K.; Shah, D. O. Importance of Micellar Kinetics in Relation to Technological Processes. *J. Colloid Interface Sci.* **2002**, *245*, 1–15.

(163) Rharbi, Y.; Kitaev, V.; Winnik, M. A.; Hahn, K. G. Characterizing Aqueous Micellar Triton X-100 Solutions of a Fluorescent Model Triglyceride. *Langmuir* **1999**, *15*, 2259–2266.

(164) Zana, R. Dynamics in Micellar Solutions of Amphiphilic Block Copolymers. In *Dynamics of Surfactant Self-Assemblies: Micelles, Microemulsions, Vesicles, and Lyotropic Phases*; Hubbard, A. T., Ed.; Taylor & Francis Group/CRC Press: Boca Raton, 2005; pp 161–231.

(165) Li, Z.; Dormidontova, E. E. Kinetics of Diblock Copolymer Micellization by Dissipative Particle Dynamics. *Macromolecules* **2010**, *43*, 3521–3531.

(166) Marciniak, A. The Solubility Parameters of Ionic Liquids. *Int. J. Mol. Sci.* **2010**, *11*, 1973–1990.

(167) Lee, S. H.; Lee, S. B. The Hildebrand Solubility Parameters, Cohesive Energy Densities and Internal Energies of 1-Alkyl-3-Methylimidazolium-Based Room Temperature Ionic Liquids. *Chem. Commun.* **2005**, No. 27, 3469–3471.

(168) Marciniak, A. The Hildebrand Solubility Parameters of Ionic Liquids-Part 2. *Int. J. Mol. Sci.* **2011**, *12*, 3553–3575.

(169) Yoo, B.; Afzal, W.; Prausnitz, J. M. Solubility Parameters for Nine Ionic Liquids. *Ind. Eng. Chem. Res.* **2012**, *51*, 9913–9917.

(170) Liu, Y.; Spring, J. D.; Steinhart, M.; Bansil, R. Pressure Jump Kinetics of Disorder to BCC Ordering in Diblock Copolymer Micelles in a Selective Solvent. *Macromolecules* **2012**, *45*, 9147–9154.

(171) Pedersen, J. S.; Svaneborg, C. Scattering from Block Copolymer Micelles. *Curr. Opin. Colloid Interface Sci.* **2002**, *7*, 158–166.

(172) Pedersen, J. S. Analysis of Small-Angle Scattering Data from Micelles and Microemulsions: Free-Form Approaches and Model Fitting. *Curr. Opin. Colloid Interface Sci.* **1999**, *4*, 190–196.

(173) Falus, P.; Borthwick, M. A.; Narayanan, S.; Sandy, A. R.; Mochrie, S. G. J. Crossover from Stretched to Compressed Exponential Relaxations in a Polymer-Based Sponge Phase. *Phys. Rev. Lett.* **2006**, *97*, 1–4.

(174) Ruegg, M. L.; Patel, A. J.; Narayanan, S.; Sandy, A. R.; Mochrie, S. G. J.; Watanabe, H.; Balsara, N. P. Condensed Exponential Correlation Functions in Multicomponent Polymer Blends Measured by X-Ray Photon Correlation Spectroscopy. *Macromolecules* **2006**, *39*, 8822–8831.

(175) Lewis, R. M.; Arora, A.; Beech, H. K.; Lee, B.; Lindsay, A. P.; Lodge, T. P.;

Dorfman, K. D.; Bates, F. S. Role of Chain Length in the Formation of Frank-Kasper Phases in Diblock Copolymers. *Phys. Rev. Lett.* **2018**, *121*, 208002.

(176) Oparaji, O.; Narayanan, S.; Sandy, A.; Ramakrishnan, S.; Hallinan, D. Structural Dynamics of Strongly Segregated Block Copolymer Electrolytes. *Macromolecules* **2018**, *51*, 2591–2603.

(177) Sheiko, S. S.; Panyukov, S.; Rubinstein, M. Bond Tension in Tethered Macromolecules. *Macromolecules* **2011**, *44*, 4520–4529.

(178) Sammalkorpi, M.; Karttunen, M.; Haataja, M. Micelle Fission through Surface Instability and Formation of an Interdigitating Stalk. *J. Am. Chem. Soc.* **2008**, *130*, 17977–17980.

(179) Pool, R.; Bolhuis, P. G. Prediction of an Autocatalytic Replication Mechanism for Micelle Formation. *Phys. Rev. Lett.* **2006**, *97*, 5–8.

(180) Webber, S. E.; Munk, P.; Tuzar, Z. Solvents and Self-Organization of Polymers. In *NATO Science Series E*; 1996; Vol. 327, pp 1–81.

(181) Wang, L.; Huang, H.; He, T. Rayleigh Instability Induced Cylinder-to-Sphere Transition in Block Copolymer Micelles: Direct Visualization of the Kinetic Pathway. *ACS Macro Lett.* **2014**, *3*, 433–438.

(182) De Jonge, N.; Ross, F. M. Electron Microscopy of Specimens in Liquid. *Nat. Nanotechnol.* **2011**, *6*, 695–704.

(183) Helveg, S.; López-Cartes, C.; Sehested, J.; Hansen, P. L.; Clausen, B. S.; Rostrup-

Nielsen, J. R.; Abild-Pedersen, F.; Nørskov, J. K. Atomic-Scale Imaging of Carbon Nanofibre Growth. *Nature* **2004**, *427*, 426–429.

(184) Dai, L. L.; Sharma, R.; Wu, C. Y. Self-Assembled Structure of Nanoparticles at a Liquid-Liquid Interface. *Langmuir* **2005**, *21*, 2641–2643.

(185) Zinn, T.; Willner, L.; Lund, R.; Pipich, V.; Richter, D. Equilibrium Exchange Kinetics in N-Alkyl-PEO Polymeric Micelles: Single Exponential Relaxation and Chain Length Dependence. *Soft Matter* **2012**, *8*, 623–626.

(186) Bates, F. S. Measurement of the Correlation Hole in Homogeneous Block Copolymer Melts. *Macromolecules* **1985**, *18*, 525–528.

(187) Doi, M.; Edwards, S. F. *The Theory of Polymer Dynamics*; Oxford University Press: New York, 1988.

(188) Niedzwiedz, K.; Wischnewski, A.; Pyckhout-Hintzen, W.; Allgaier, J.; Richter, D.; Faraone, A. Chain Dynamics and Viscoelastic Properties of Poly(Ethylene Oxide). *Macromolecules* **2008**, *41*, 4866–4872.

(189) Zhulina, E. B.; Borisov, O. V. Theory of Block Polymer Micelles: Recent Advances and Current Challenges. *Macromolecules* **2012**, *45*, 4429–4440.

(190) Ryu, C. Y.; Vigild, M. E.; Lodge, T. P. Fluctuations with Cubic Symmetry in a Hexagonal Copolymer Microstructure. *Phys. Rev. Lett.* **1998**, *81*, 5354–5357.

(191) Ryu, C. Y.; Lodge, T. P. Thermodynamic Stability and Anisotropie Fluctuations in the Cylinder-to-Sphere Transition of a Block Copolymer. *Macromolecules* **1999**,

32, 7190–7201.

(192) Burke, S. E.; Eisenberg, A. Kinetics and Mechanisms of the Sphere-to-Rod and Rod-to-Sphere Transitions in the Ternary System PS310-b-PAA52/Dioxane/Water. *Langmuir* **2001**, *17*, 6705–6714.

(193) Abbas, S.; Li, Z.; Hassan, H.; Lodge, T. P. Thermoreversible Morphology Transitions of Poly(Styrene-b-Dimethylsiloxane) Diblock Copolymer Micelles in Dilute Solution. *Macromolecules* **2007**, *40*, 4048–4052.

(194) Zhao, D.; Wang, E.; Lodge, T. P. Hybridization of a Bimodal Distribution of Copolymer Micelles. *Macromolecules* **2020**, *53*, 7705–7716.

(195) Cai, P.; Wang, C.; Ye, J.; Xie, Z.; Wu, C. Hybridization of Polymeric Micelles in a Dispersion Mixture. *Macromolecules* **2004**, *37*, 3438–3443.

(196) Tian, M.; Qin, A.; Ramireddy, C.; Webber, S. E.; Munk, P.; Tuzar, Z.; Procházka, K. Hybridization of Block Copolymer Micelles. *Langmuir* **1993**, *9*, 1741–1748.

(197) Wright, D. B.; Patterson, J. P.; Pitto-Barry, A.; Lu, A.; Kirby, N.; Gianneschi, N. C.; Chassenieux, C.; Colombani, O.; OReilly, R. K. The Copolymer Blending Method: A New Approach for Targeted Assembly of Micellar Nanoparticles. *Macromolecules* **2015**, *48*, 6516–6522.

(198) Cantú, L.; Corti, M.; Salina, P. Direct Measurement of the Formation Time of Mixed Micelles. *J. Phys. Chem.* **1991**, *95*, 5981–5983.

(199) Jachowicz, J.; Morawetz, H. Characterization of Polymer Chain Interpenetration in

Solution by Fluorescence after Freeze-Drying. *Macromolecules* **1982**, *15*, 828–831.

(200) Nyrkova, I. A.; Semenov, A. N. On the Theory of Micellization Kinetics. *Macromol. Theory Simulations* **2005**, *14*, 569–585.

(201) Jeong, U.; Lee, H. H.; Yang, H.; Kim, J. K.; Okamoto, S.; Aida, S.; Sakurai, S. Kinetics and Mechanism of Morphological Transition from Lamella to Cylinder Microdomain in Polystyrene-Block-Poly(Ethylene-Co-but-1-Ene)-Block-Polystyrene Triblock Copolymer. *Macromolecules* **2003**, *36*, 1685–1693.

(202) Koppi, K. A.; Tirrell, M.; Bates, F. S.; Almdal, K.; Mortensen, K. Epitaxial Growth and Shearing of the Body Centered Cubic Phase in Diblock Copolymer Melts. *J. Rheol.* **1994**, *38*, 999–1027.

(203) Ryu, C. Y.; Lee, M. S.; Hajduk, D. A.; Lodge, T. P. Structure and Viscoelasticity of Matched Asymmetric Diblock and Triblock Copolymers in the Cylinder and Sphere Microstructures. *J Polym Sci B Polym Phys* **1997**, *35*, 2811–2823.

(204) Laradji, M.; Shi, A. C.; Noolandi, J.; Desai, R. C. Stability of Ordered Phases in Diblock Copolymer Melts. *Macromolecules* **1997**, *30*, 3242–3255.

(205) Shi, A. C.; Noolandi, J.; Desai, R. C. Theory of Anisotropic Fluctuations in Ordered Block Copolymer Phases. *Macromolecules* **1996**, *29*, 6487–6504.

(206) Laradji, M.; Shi, A. C.; Desai, R. C.; Noolandi, J. Stability of Ordered Phases in Weakly Segregated Diblock Copolymer Systems. *Phys. Rev. Lett.* **1997**, *78*, 2577–

2580.

(207) Qi, S.; Wang, Z. G. Weakly Segregated Block Copolymers: Anisotropic Fluctuations and Kinetics of Order-Order and Order-Disorder Transitions. *Polymer* **1998**, *39*, 4639–4648.

(208) Qi, S.; Wang, Z. G. Kinetic Pathways of Order-Disorder and Order-Order Transitions in Weakly Segregated Microstructured Systems. *Phys. Rev. Lett.* **1996**, *76*, 1679–1682.

(209) Qi, S.; Wang, Z. G. Kinetics of Phase Transitions in Weakly Segregated Block Copolymers: Pseudostable and Transient States. *Phys. Rev. E* **1997**, *55*, 1682–1697.

(210) Nie, H.; Bansil, R.; Ludwig, K.; Steinhart, M.; Estmír, K.; Bang, J. Time-Resolved Small-Angle X-Ray Scattering Study of the Kinetics of Disorder-Order Transition in a Triblock Copolymer in a Selective Solvent for the Middle Block. *Macromolecules* **2003**, *36*, 8097–8106.

(211) Krishnamoorti, R.; Modi, M. A.; Tse, M. F.; Wang, H. C. Pathway and Kinetics of Cylinder-to-Sphere Order-Order Transition in Block Copolymers. *Macromolecules* **2000**, *33*, 3810–3817.

(212) Wang, C. Y.; Lodge, T. P. Kinetics and Mechanisms for the Cylinder-to-Gyroid Transition in a Block Copolymer Solution. *Macromolecules* **2002**, *35*, 6997–7006.

(213) Sakurai, S.; Hashimoto, T.; Fetters, L. J. Thermoreversible Cylinder-Sphere

Transition of Polystyrene-Block-Polyisoprene Diblock Copolymers in Dioctyl Phthalate Solutions. *Macromolecules* **1996**, *29*, 740–747.

(214) Ruokolainen, J.; Brinke, G.; Ikkala, O. Mesomorphic Structures in Flexible Polymer-Surfactant Systems Due to Hydrogen Bonding : Poly(4-Vinylpyridine)-Pentadecylphenol. **1996**, *9297*, 3409–3415.

(215) Yan, N.; Sheng, Y.; Liu, H.; Zhu, Y.; Jiang, W. Templated Self-Assembly of Block Copolymers and Morphology Transformation Driven by the Rayleigh Instability. *Langmuir* **2015**, *31*, 1660–1669.

(216) Takahashi, R.; Narayanan, T.; Yusa, S. I.; Sato, T. Kinetics of Morphological Transition between Cylindrical and Spherical Micelles in a Mixture of Anionic-Neutral and Cationic-Neutral Block Copolymers Studied by Time-Resolved SAXS and USAXS. *Macromolecules* **2018**, *51*, 3654–3662.

(217) Nichols, F. A.; Mullins, W. W. Surface-(Interface-) and Volume-Diffusion Contributions to Morphological Changes Driven by Capillarity. *Trans. Met. Soc. AIME* **1965**, *233*, 1840–1848.

(218) Plateua, J. A. F. *Statique Expérimentale et Théorique Des Liquides Soumis Aux Seules Forces Moléculaires.* Gauthier, Paris, 1873.

(219) Rayleigh, L. On the Instability of Jets. *Proc. Lond. Math. Soc.* **1878**, *1*, 4–13.

Appendix

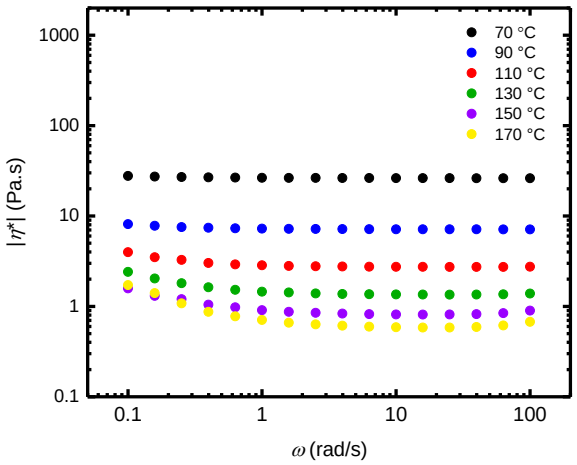

Figure A1: Complex viscosity versus frequency of 8.2 kDa 1,2-polybutadiene-OH with 0.1 wt% BHT inhibitor. Measurements were obtained under nitrogen atmosphere using a parallel plate rheometer (gap = 300 μm and γ = 5%). The sample was held at each temperature for 10 min before each measurement.

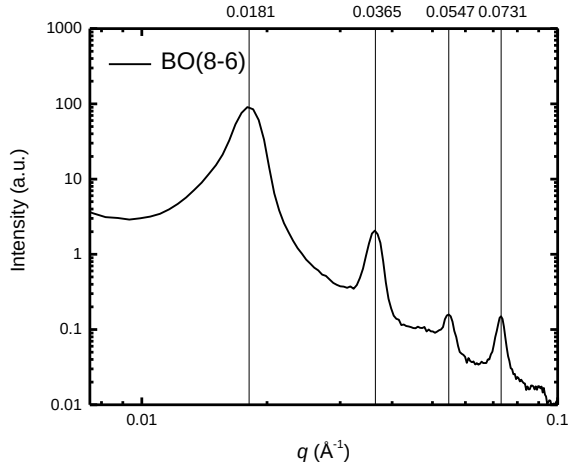

Figure A2: SAXS of bulk BO(8-6) after annealing at 70 °C for 15 min. The vertical black lines indicate the center of each peak and the q values of each line are indicated above. From the peak indexing, the block copolymer exhibits a lamellar morphology at the temperature used for direct dissolution. The domain sizes for BO(8-6) from the primary

scattering peak ($q^* = 0.0181$ Å^{-1}) are $d_{PEO} = 14$ nm and $d_{PB} = 21$ nm. The PB domain size is close to the as-prepared micelle core radius obtained for solutions prepared by direct dissolution.

Estimating the free energy of a micelle[36]

From Zhulina *et al.*,[36] the total micelle free energy is determined by the sum of the free energy contributions from the core chains (F_{core}), the corona chains (F_{corona}), and the interface (F_{int}). For a spherical micelle, these free energy contributions are shown below.

$$\frac{F_{core}}{k_B T} = \frac{3\pi^2 R_{core}^2}{80 N_{core} p_{core} a_{core}^2} \tag{A1}$$

In Equation A1, a_{core} is the volumetric size of one repeat unit in the core and p_{core} is the chain stiffness parameter of the core chains, given by Equations A5 and A6, respectively. The interfacial energy is given by Equation A2,

$$\frac{F_{int}}{k_B T} = \frac{3 a_{core} N_{core} \gamma}{R_{core}} \tag{A2}$$

where $\gamma = \tilde{\gamma} a_{core}^2 / k_B T$ is the normalized surface free energy per area a_{core}^2 and $\tilde{\gamma}$ is the surface free energy per unit area (*i.e.*, surface tension). The free energy of chains in the corona is given by Equation A3,

$$\frac{F_{\text{corona}}}{k_{\text{B}}T} = \frac{\widehat{C}_{\text{F}} R_{\text{core}}^{3/2}\sqrt{\varphi}}{2\sqrt{3}p_{\text{corona}}^{3/4}N_{\text{core}}^{1/2}a_{\text{core}}^{3/2}}\ln\left[1 + \frac{2\widehat{C}_{\text{H}}p_{\text{corona}}^{1/4}N_{\text{corona}}\varphi^{1/2}a_{\text{corona}}^{2}}{\sqrt{3}R_{\text{core}}^{1/2}N_{\text{core}}^{1/2}a_{\text{core}}^{3/2}}\right] \tag{A3}$$

where $\widehat{C}_{\text{F}}$ and $\widehat{C}_{\text{H}}$ are dimensionless parameters of order unity, which depend on the solvent quality of the corona block. Equation A3 is derived assuming a θ solvent for the corona.

The corona thickness for spherical micelles is calculated directly as $L_{\text{corona}} = \langle R_{\text{h}}\rangle - \langle R_{\text{core}}\rangle$ from DLS and LP-TEM, respectively. To determine the corona thickness for a "peanut-shaped" micelle undergoing fragmentation, we assume that the corona is mostly cylindrical,

$$L_{\text{corona}} = \langle R_{\text{core}}\rangle\left[\left(1 + \frac{3}{2\sqrt{2}}\frac{\widehat{C}_{\text{H}}p_{\text{corona}}^{1/4}a_{\text{corona}}^{2}N_{\text{corona}}^{1/2}\varphi^{1/2}}{a_{\text{core}}^{3/2}\langle R_{\text{core}}\rangle^{1/2}N_{\text{core}}^{1/2}}\right)^{2/3} - 1\right] \tag{A4}$$

where N_{core} and N_{corona} are the degrees of polymerization of the core block and the corona block, respectively. The volume fraction of PB in the micelle core, φ, is assumed to be equal to 1, as there is likely a negligible amount of solvent in the core for this system. The volumetric monomer size, a, is calculated by:

$$a = \left(\frac{M_0}{\rho_{\text{P}}N_{\text{Av}}}\right)^{1/3} \tag{A5}$$

where M_0 is the monomer molar mass, equal to 54.1 g/mol for PB and 44.1 g/mol for PEO, ρ_{P} is the bulk polymer density, equal to 0.87 g/cm^3 for PB and 1.13 g/cm^3 for PEO, and

N_{Av} is Avogadro's number. From Equation A5, a_{corona} = 0.4 nm and a_{core} = 0.47 nm. The chain stiffness parameter p is given by Equation A6:

$$p = \frac{C_\infty M_0}{a^2} \tag{A6}$$

while C_∞ is the characteristic ratio, equal to 0.81 Å^{2}mol/g for PEO.[138] From Equation A6, p_{corona} = 2.20 and p_{core} = 2.15.

The parameter $\widehat{C}_H$ in the free energy model depends on the solvent quality with respect to the corona block, thus we compare the thermal blob size ξ_t and the largest blob in the corona $\xi_{largest}$. First, we estimate the excluded volume parameter for PEO in [C$_2$mim][TFSI]

$$v = (1 - 2\chi)\frac{V_{PEO}}{V_0} \tag{A7}$$

where V_0 is the reference volume chosen as 80 cm^3/mol, and V_{PEO} is the monomer volume of PEO, equal to 65 cm^3/mol. The Flory-Huggins interaction parameter χ between PEO and [C$_2$mim][TFSI] can be estimated from Equation A8,

$$\chi = \frac{V_0}{RT}(\delta_1 - \delta_2)^2 \tag{A8}$$

where R is the gas constant, T is the temperature in Kelvin, and the solubility parameters of the polymer and the ionic liquid δ are δ_1 = 9.88 MPa$^{1/2}$ and δ_2 = 21.1 MPa$^{1/2}$ for PEO[138] and [C$_2$mim][TFSI][169] at T = 303 K, respectively. From Equation A7, v = 0.63, therefore

$$\xi_t = \frac{a_{corona} p_{corona}^2}{v} = 30.7 \text{ Å} \quad \text{(A9)}$$

and

$$\xi_{largest} = \frac{R_h p_{corona}^{3/4}}{\sqrt{Q}} = 26.9 \text{ Å} \quad \text{(A10)}$$

For Equation A10, the as-prepared $\langle R_h \rangle_0$ = 108 nm for 0.25 wt % BO(53-46) in [C_2mim][TFSI] was used to approximate the largest blob size in the corona. For BO(53-46) $\xi_{largest} < \xi_t$, which means that the excluded volume interactions do not influence the corona chain conformation to a significant extent, thus the expression for $\widehat{C}_H$ in a θ-solvent was used, and $\widehat{C}_H$ was assumed to equal 0.68. For more details, see the paper from Zhulina *et al.*[36]

Table A1: Parameters for free energy model

a_{core} (nm)	a_{corona} (nm)	p_{corona}	φ	$\widehat{C}_H$
0.47	0.40	2.20	1	0.68